



Durham E-Theses

Magnetic properties of some rare earth-iron-cobalt and rare earth-cobalt-nickel compounds ;

Poldy, C.A

How to cite:

Poldy, C.A (1972) *Magnetic properties of some rare earth-iron-cobalt and rare earth-cobalt-nickel compounds ;*, Durham theses, Durham University. Available at Durham E-Theses Online:
<http://etheses.dur.ac.uk/8644/>

Use policy

The full-text may be used and/or reproduced, and given to third parties in any format or medium, without prior permission or charge, for personal research or study, educational, or not-for-profit purposes provided that:

- a full bibliographic reference is made to the original source
- a [link](#) is made to the metadata record in Durham E-Theses
- the full-text is not changed in any way

The full-text must not be sold in any format or medium without the formal permission of the copyright holders.

Please consult the [full Durham E-Theses policy](#) for further details.

Academic Support Office, Durham University, University Office, Old Elvet, Durham DH1 3HP
e-mail: e-theses.admin@dur.ac.uk Tel: +44 0191 334 6107
<http://etheses.dur.ac.uk>

MAGNETIC PROPERTIES OF SOME
RARE EARTH-IRON-COBALT AND
RARE EARTH-COBALT-NICKEL COMPOUNDS

by

G.A. Poldy, B.Sc.

Presented in candidature for the degree of

DOCTOR OF PHILOSOPHY

JUNE 1972



A B S T R A C T

The design and construction of a high field pulse magnetometer are described. This instrument was used for investigating the magnetic properties of the various pseudobinary compounds in the alloy systems $Y_x(Fe,Co)_{1-x}$ and $Y_x(Co,Ni)_{1-x}$, as well as the systems $Gd_3(Fe,Co)$ and $Gd_3(Co,Ni)$, over the entire ranges of solid solubility.

The variation of spontaneous moment in the yttrium compounds as a function of 3d electron concentration shows a continuous change in form from the YB_2 compounds to the transition metal rich Y_2B_{17} compounds, where B denotes (Fe,Co) or (Co,Ni). This change indicates a gradual progression to the well-known (Fe, Co) and (Co,Ni) moment variation of the Slater-Pauling curve. In the $Y(Co,Ni)_3$ and $Y_2(Co,Ni)_7$ compounds the spontaneous moment decreases with increasing 3d electron concentration, becoming zero for about 80% Ni, and then reappears with a small value for the compounds YNi_3 and Y_2Ni_7 . This phenomenon is very similar to that found in the compounds Y_xNi_{1-x} as x is increased.

The results are interpreted within the rigid band model and it is suggested that the disappearance of ordering in the $Y(Co,Ni)_3$ and $Y_2(Co,Ni)_7$ systems is due to a deep minimum in the density of states curve.

The 3d moment in the Gd_xB_{1-x} and Y_xB_{1-x} compounds is deduced and an attempt is made, for B = Co or Ni, to isolate it from the moment contribution due to the conduction electron polarization. A unified picture is presented in which the 3d band is gradually populated by some of the valence electrons from the tripositive Gd and Y ions, as x is increased.

The compounds for which the 3d band is filled are indicated, not by the absence of any spontaneous moment in the yttrium compounds, but rather, by the inability of gadolinium to induce a 3d moment when Gd is substituted for Y.

The magnetic results of the $Gd_3(Fe, Co)$ and $Gd_3(Co,Ni)$ systems indicate that these compounds are antiferromagnetic and the results are interpreted

quantitatively in terms of the Néel two-sublattice theory of antiferromagnetism. Values are deduced for the anisotropy and the inter- and intra-sublattice exchange coefficients. There is a close correlation between structural stability and the existence of antiferromagnetism. When the latter disappears (at 10% Fe) the structure becomes unstable for higher concentrations of iron. From this correlation, a rule is deduced for predicting when a structure might become unstable. This rule is found to be applicable also to the other stoichiometries of the gadolinium-rich compounds.

P R E F A C E

The experimental work was performed upon the transition metal-rich stoichiometric alloys Y_2B_{17} , $Y B_5$, Y_2B_7 , $Y B_3$ and the rare earth-rich Gd_3B alloys, where B denotes the 3d transition metals Fe, Co, Ni. The B component consisted of solid solutions (Fe, Co) and (Co, Ni).

The results of these two sections of the experimental work are described in Chapter 4 and Chapter 5 respectively. The various experimental techniques used are described in Chapter 2. The variation of magnetization as a function of applied field is of primary importance in this work, and a pulsed field magnetometer was designed and constructed for the purpose of measuring this variation. A detailed description of this instrument is given in Chapter 3.

In order to obtain some link between the two results sections, the discussion Chapter 6 is devoted not only to the transition metal-rich compounds with yttrium, but also deals with the gadolinium compounds of various stoichiometries, for which the data were obtained from the literature. As a consequence, the conclusions reached in Chapter 6 have some effect upon the discussion of the Gd_3B results, to which Chapter 7 is devoted. Chapter 1 is a statement of the problem.

ACKNOWLEDGEMENTS

I wish to express my gratitude to my supervisor, Dr. K.N.R. Taylor, for his guidance and encouragement. My appreciation goes to the entire Physics Department of Durham University, particularly to Professor G.D. Rochester, F.R.S., the Head of the Department, to the staffs of the workshops for their cooperation, and to my colleagues in the solid state group. I am indebted to the United States Air Force for the provision of a maintenance grant. Finally, I would like to thank Mrs. D.A. Anson most sincerely for typing the script.

C O N T E N T S

	<u>Page</u>
<u>ABSTRACT</u>	i
<u>PREFACE</u>	iii
<u>ACKNOWLEDGEMENTS</u>	iv
 <u>CHAPTER ONE - STATEMENT OF THE PROBLEM</u>	
1.1 Introduction	1
1.2 Structural Properties	3
1.3 Ferromagnetism in a Band	4
1.3.1 The Simple Band Model	5
1.3.2 The Rigid Band Model for Alloys	6
1.4 Magnetic Properties	7
1.4.1 Compounds with Nickel	7
1.4.2 Compounds with Cobalt	9
1.4.3 Compounds with Iron	10
1.4.4 Magnetic Property Variation within a given stoichiometry	11
(a) The AB ₂ Stoichiometry	11
(b) The Pure 3d Metal Alloys	14
1.4.5 The Gd ₃ (Fe,Co,Ni) Compounds	15
 <u>CHAPTER TWO - TECHNIQUES AND EXPERIMENTAL METHODS</u>	
2.1 Specimen Preparation	17
2.2 Determination of Crystal Structure and Lattice Parameters	18
2.3 Outline of the Principle of the Pulsed Field Magnetometer	18
2.4 Determination of Curie Temperatures and Néel Temperatures	19
2.4.1 A.C. Susceptibility Technique	19
2.4.2 Pulsed Field Magnetometer Technique	21
2.4.3 Comparison of the A.C. Susceptibility and Pulsed Field Magnetometer Techniques	21

CHAPTER THREE - THE PULSED FIELD MAGNETOMETER

3.1	The Magnet and the Field Producing Circuit	23
	3.1.1 Construction and Mounting of the Magnet	23
	3.1.2 Production of the Magnetic Field	24
	3.1.3 The Form of the Magnetic Field	25
	3.1.4 Theory of Secondary Fields due to Eddy Currents	26
	3.1.5 Repetition Rate	27
3.2	Magnetic Field Measurements	28
	3.2.1 The H Pick-up Coil	28
	3.2.2 Integration of the Signal and Sensitivity	28
	3.2.3 Triggering the Bright-up of the Oscilloscope Trace	29
	3.2.4 Calibration of the H Signal	30
3.3	Magnetization Measurements	32
	3.3.1 Theory of Magnetization Measurements	32
	3.3.2 The Moment Pick-up Coil System	34
	3.3.3 Eddy Current Noise and its Elimination	35
	3.3.4 Samples with Remanence	36
	3.3.5 Centering of the Sample	37
	3.3.6 The Sample and Sample Holder	38
	3.3.7 Calibration of the M Signal	39
	3.3.8 The M vs H Curve and its Analysis	40
	3.3.9 Estimation of the Ionic Moment	41
3.4	Temperature Control and Measurement	42
	3.4.1 The Cryostat	42
	3.4.2 The Heater	43
	3.4.3 Temperature Measurement	43
	3.4.4 Liquid Helium Level Detection	44
	3.4.5 Temperature Runs	44
3.5	Mechanical Considerations	45
	3.5.1 The Dewar Head and Support of Pick-up Coils	45
	3.5.2 The Vacuum System	45

3.5.3	Support of the Sample	46
3.5.4	Removing the Sample from the Pick-up Coils	46
<u>CHAPTER FOUR - RESULTS FOR $Y_x(Fe,Co)_{1-x}$ AND $Y_x(Co,Ni)_{1-x}$</u>		
4.1	Y_2B_{17}	47
4.2	YB_5	47
4.3	YB_3 and Y_2B_7	48
4.3.1	Crystal Structure	48
4.3.2	Magnetic Properties	48
<u>CHAPTER FIVE - $Gd_3(Fe,Co,Ni)$ RESULTS</u>		
5.1	Preparation of Samples	51
5.2	Structural Stability and Lattice Parameters of the Gd_3B System	51
5.3	Magnetic Measurements on $Gd_3(Fe,Co)$ and $Gd_3(Co,Ni)$	52
5.3.1	Pulsed Field Measurements at 4.2K	52
5.3.2	Magnetic Measurements as a Function of Temperature	55
	(a) A.C. Susceptibility	55
	(b) Pulsed Field Measurements as a Function of Temperature	57
5.3.3	Gd_3Ni (Magnetic Parameters as a Function of Temperature)	57
5.3.4	$Gd_3Co_{.25}Ni_{.75}$ - $Gd_3Fe_{.1}Co_{.9}$ (Magnetic Parameters as a Function of Temperature)	59
5.4	Magnetic Measurements on $Gd_3Fe_xNi_{1-x}$	60
5.4.1	Pulsed Field Measurements at 4.2K	60
5.4.2	A.C. Susceptibility as a Function of Temperature	62
<u>CHAPTER SIX - DISCUSSION OF $Y_x(Fe,Co,Ni)_{1-x}$ PSEUDOBINARIES, AND $A-Ni, A-Co, A-Fe$, WHERE A is Y OR Gd.</u>		
6.1	$Y_x(Fe,Co)_{1-x}$ and $Y_x(Co,Ni)_{1-x}$ Pseudobinaries	63
6.1.1	Structural Stability	63
	(a) The $Y(Co,Ni)_5$ and $Y(Fe,Co)_5$ Pseudobinaries	63
	(b) Effect of 3d-electron concentration	64
6.1.2	Magnetic Properties	64
	(a) The Moment Summary Graph	64

	<u>Page</u>
(b) The Low Moment Composition Range of $Y_2(\text{Co,Ni})_7$ and $Y(\text{Co,Ni})_3$	66
6.2 The 3d Moments in $Y_x\text{Ni}_{1-x}$ and $\text{Gd}_x\text{Ni}_{1-x}$	70
6.3 The 3d Moments in $Y_x\text{Co}_{1-x}$ and $\text{Gd}_x\text{Co}_{1-x}$	72
6.4 The 3d Moments in $Y_x\text{Fe}_{1-x}$ and $\text{Gd}_x\text{Fe}_{1-x}$	73
6.5 Conclusion	74

CHAPTER SEVEN - DISCUSSION OF $\text{Gd}_3(\text{Fe,Co,Ni})$ COMPOUNDS

7.1 The Néel Two-Sublattice Theory of Antiferromagnetism	76
7.1.1 The Exchange Interaction	76
7.1.2 Anisotropy	78
7.1.3 Field Induced Transitions	79
7.1.4 Some Comments on the Applicability of the Theory	81
7.2 The M vs H Curves of Polycrystalline Samples	83
7.2.1 Initial Susceptibility χ_i	83
7.2.2 The Critical Field H_c and Saturating Field H_s	84
7.2.3 Magnetization of Spin-Flop Materials for $H_c < H < H_s$	85
7.3 Interpretation of the $\text{Gd}_3(\text{Fe,Co})$ and $\text{Gd}_3(\text{Co,Ni})$ Results in terms of the Néel Theory	85
7.3.1 Relationship between H_c and χ_i at 4.2K	85
7.3.2 Spin-Flip Behaviour	87
7.3.3 Spin-Flop Behaviour	89
7.3.4 Calculation of n, the Inter-Sublattice Exchange Coefficient	91
7.3.5 Relationship between H_s and $1/\chi_i$ at 4.2K	92
7.3.6 Calculation of n', the Intra-Sublattice Exchange Coefficient	93
7.3.7 χ_{T_N} (at $T = T_N$) and its Relationship with H_c at 4.2K	95
7.4 Effects of Various Corrections	96
7.4.1 Time Dependence	96
7.4.2 The Demagnetizing Field	99
7.4.3 Temperature Variation during a Field Pulse	100
7.5 Estimation of the Magnetic Dipole Interaction between Gd Ions	101

	<u>Page</u>
7.6 Effect of the Average 3d-electron Concentration	102
7.7 The Exchange Interaction	104
7.7.1 The RKKY Theory	104
7.8 The Conduction Electrons of Gd-Rich Compounds with the 3d Elements	107
7.9 The Structural Stability of Gadolinium-rich Compounds with the 3d-Elements	108
7.9.1 Justification for the Structural Stability Rule	110
7.10 The Exchange Interaction in the Gd_3B Compounds	111
7.10.1 Applicability of RKKY Theory to the A_3B Compounds where A is a Heavy Trivalent Rare Earth	112
7.10.2 Application of RKKY Concepts to the Gd_3B Compounds	112
7.11 Conclusion	114
<u>REFERENCES</u>	116
<u>LIST OF FIGURES</u>	119
<u>LIST OF TABLES</u>	122

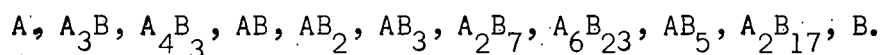


CHAPTER ONE

STATEMENT OF THE PROBLEM

1.1 Introduction

Compounds between the rare earths and 3d transition metals form only with the 3d elements to the right of chromium in the periodic table, i.e. with Mn, Fe, Co and Ni. These are stoichiometric alloys $A_x B_{1-x}$ with a fixed ratio between the number of A atoms (rare earth or yttrium) and the number of B atoms (transition metal). The discrete values of x correspond to stoichiometries of the following compositions:



The AB_2 stoichiometry is the only one which forms for all the 3d elements from Mn to Ni. The next most common stoichiometries are A_2B_{17} , existing for Fe, Co and Ni; and AB_3 , existing for Fe, Co and Ni when A is a rare earth, but only for Co and Ni when A is yttrium. As can be seen in fig. 1.1 the major overlap occurs in the $A_x Co_{1-x}$ and $A_x Ni_{1-x}$ compounds. Iron does not form intermetallic compounds for x larger than that of AFe_2 .

This work is concerned with the 3d elements Fe, Co, and Ni alloyed with Y or Gd. Fig. 1.2 shows the compounds whose existence have been established. The heavy lines along each stoichiometry show the established solid solubility regions for the pseudobinary compounds where the transition metal sites are occupied by (Fe, Co) and (Co, Ni). In general the distribution of the two types of transition metal ions is believed to be random, though some evidence (ref. 1.1) for preferential occupation of inequivalent B sites by different types of 3d ions has been found in some related compounds in the Th-Co system.

Early measurements of magnetization in the $Gd_x Fe_{1-x}$ system (refs. 1.2, 1.3, 1.4) and the $Gd_x Co_{1-x}$ system (refs. 1.3, 1.5), revealed a deep minimum in the magnetization vs x variation at $x \approx 0.2$. Fig. 1.3 shows this variation for Fe, Co and Ni compounds with Gd, using more recent data. This minimum is interpreted in terms of antiparallel coupling between the Gd spins and the transition metal spins. Work on compounds with the other rare earths

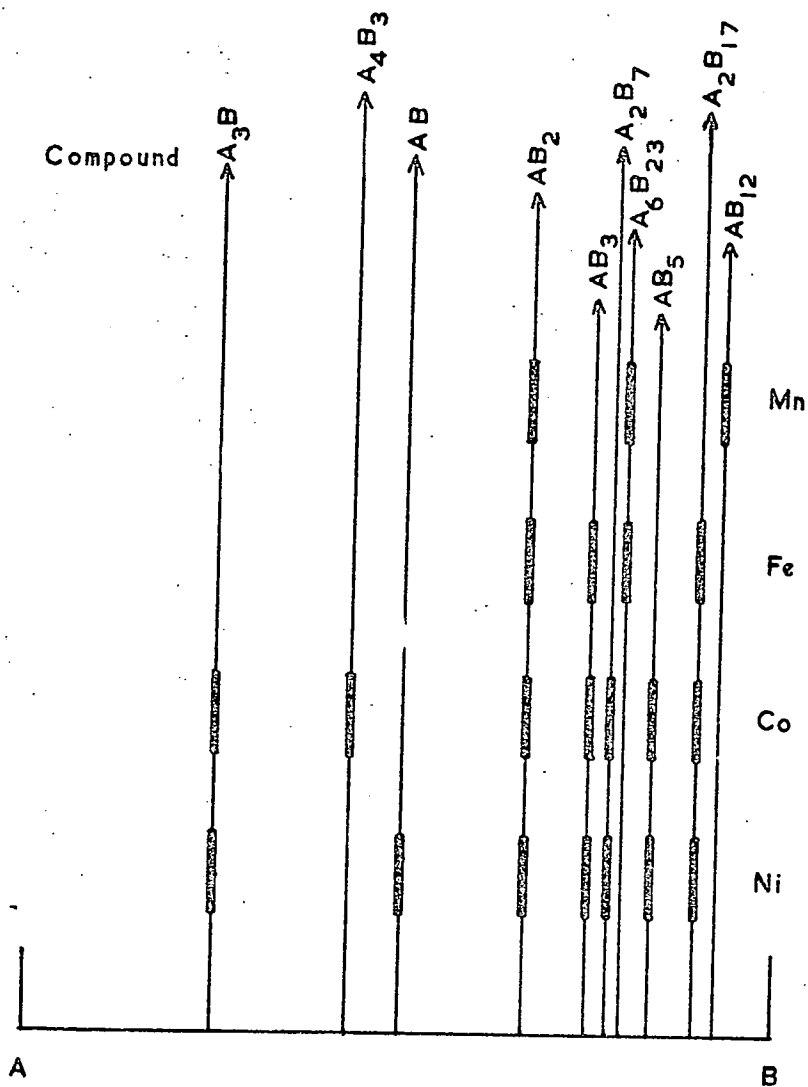


Fig. 1.1 The Existing Compounds in the AB system

A \equiv Rare Earth

B \equiv Mn, Fe, Co, Ni

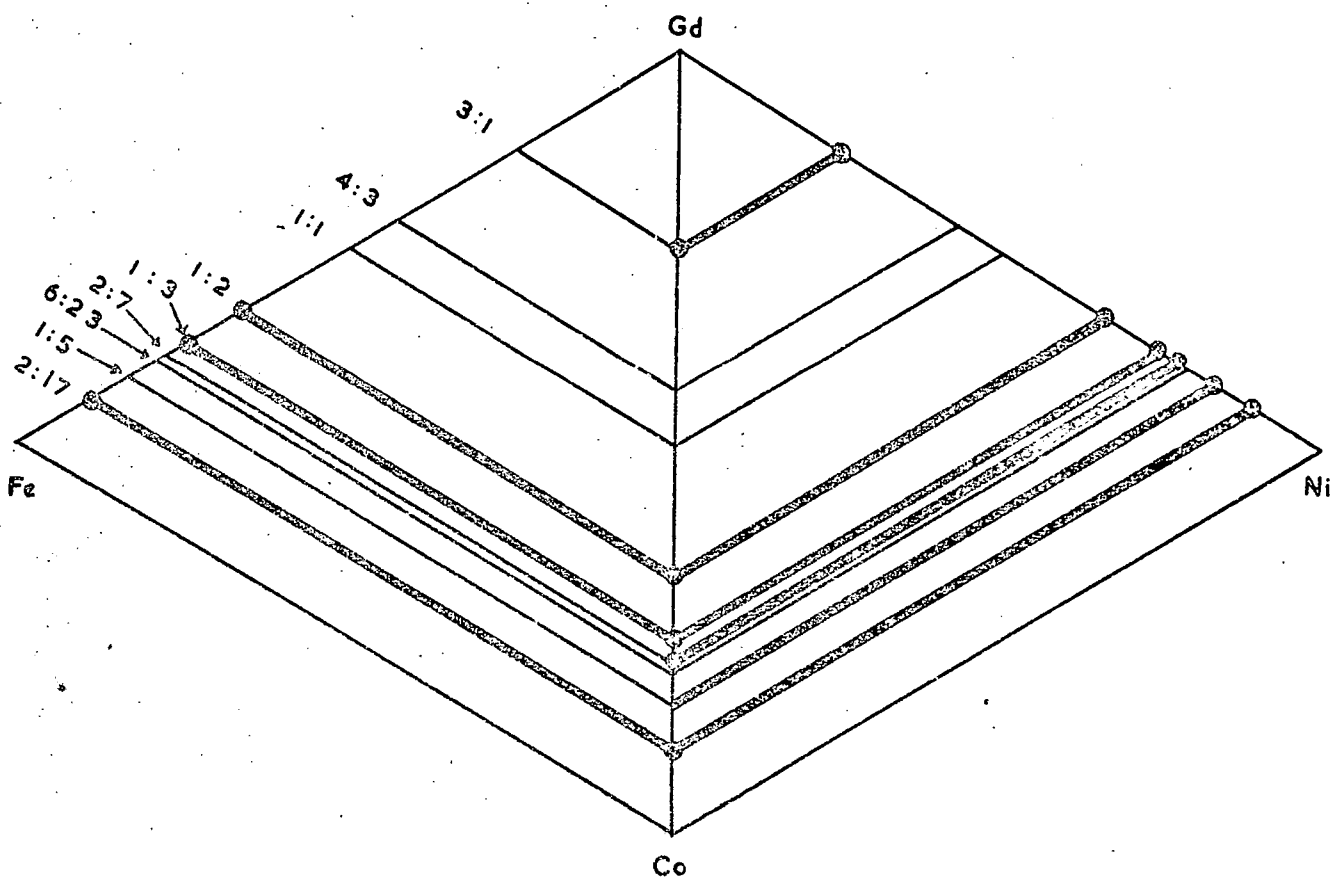
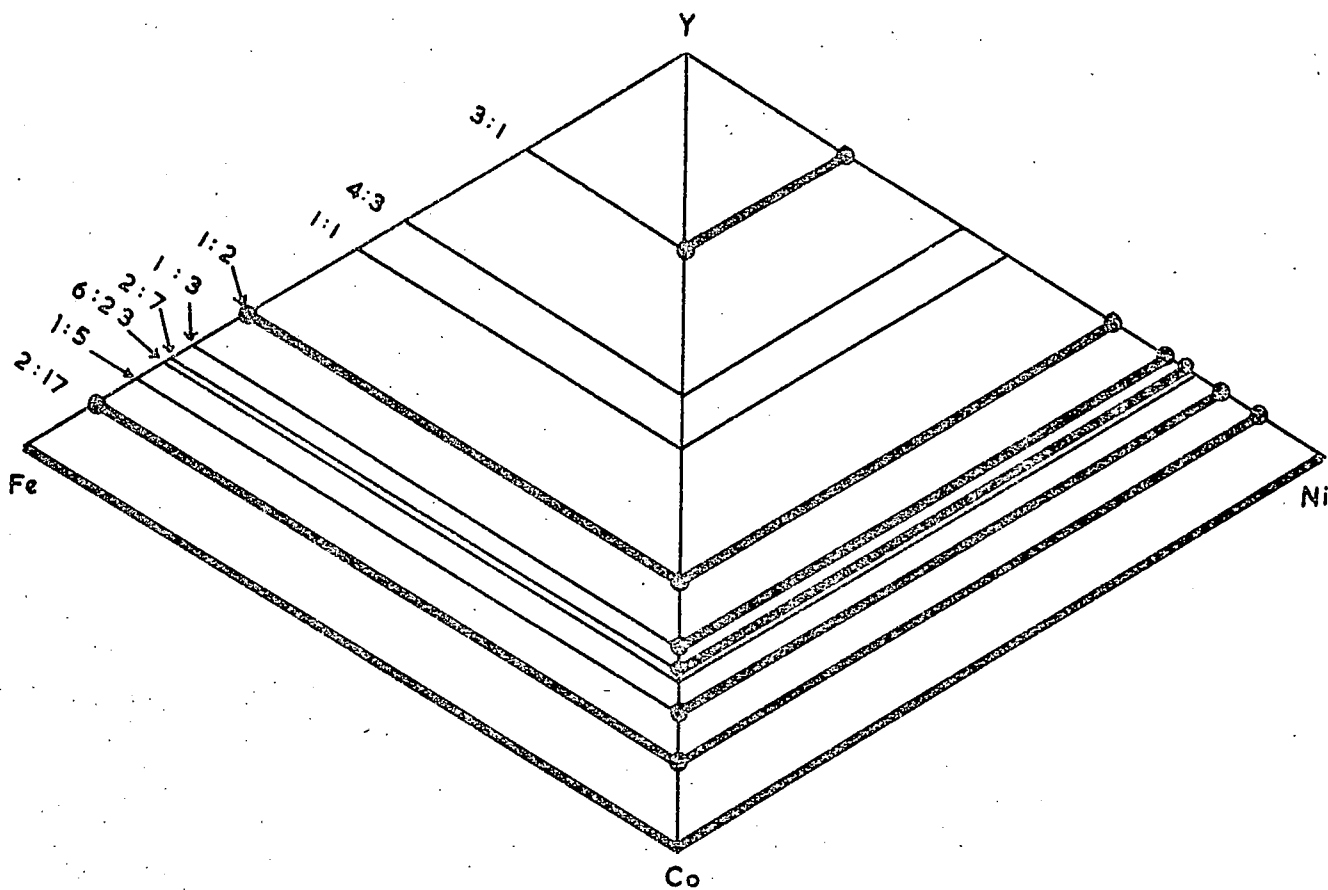


Fig. 1.2 Composition Triangles showing existing compounds (from literature) in Y-Fe-Co, Y-Co-Ni, Gd-Fe-Co, Gd-Co-Ni systems

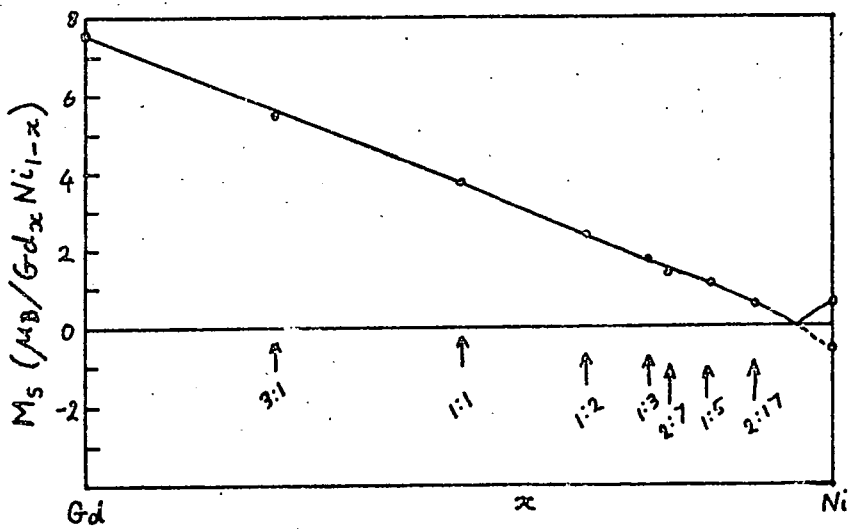
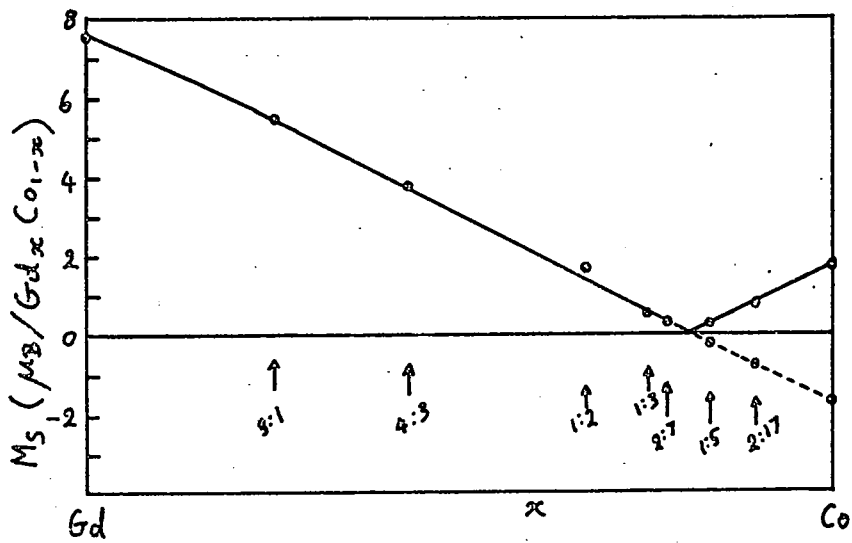
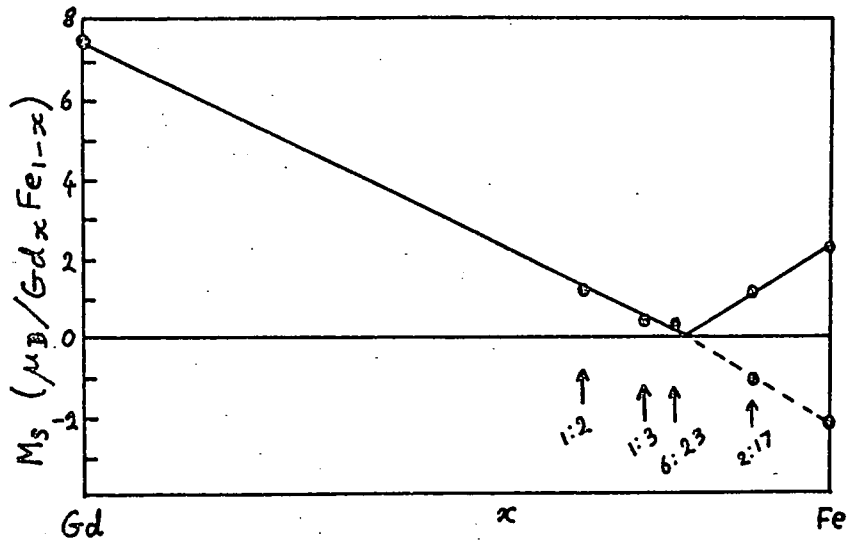
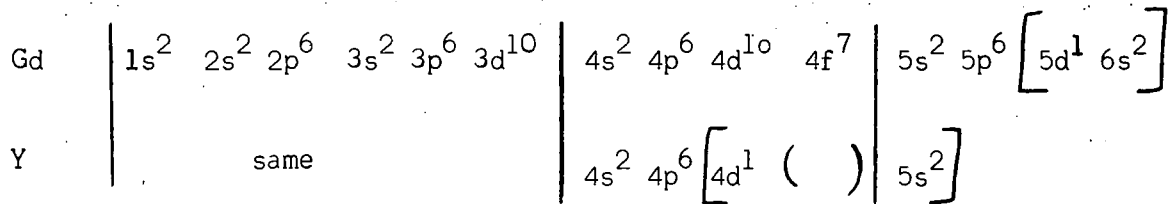


Fig. 3 Saturation Moment vs x in Gd_xB_{1-x}

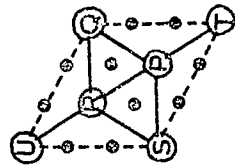
has shown this to be applicable in all the rare earths, resulting in ferrimagnetism in alloys with the heavy rare earths, and ferromagnetism in alloys with the light rare earths if $L > S$.

The electronic configurations of the Gd atom and the Y atom are shown as follows:



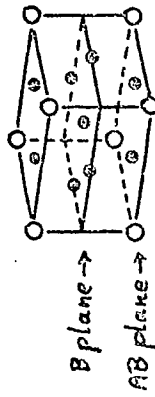
The atomic number of Gd is 64; that of Y is 39. When in the metal, the electronic states shown above in square brackets have their energy levels broadened into a band. These electrons become itinerant, and leave their respective atoms in an ionized state. It is evident that Gd and Y are very similar in that both will become tri-positive ions, the three band electrons per atom originating from levels with quantum number $n=5,6$ for Gd, and $n=4,5$ for yttrium, this being the only difference in the quantum numbers of the band electrons. As a result, in many intermetallic compounds Y can be substituted for Gd without any change in crystal structure, and with little change in the lattice parameters. The magnetism of the Gd atom originates from the 4f shell, which is half full. By Hund's rules we can deduce that Gd is an S state ion, with a magnetic moment of $7\mu_B$, which is due entirely to spin. When placed in a metallic lattice, the 4f shell is not appreciably broadened into a band, and the $7\mu_B$ per Gd^{3+} ion is an accurate value for the ionic moment. This is because of the effective screening of the 4f shell by the other filled shells, 5s and 5p which have a larger spacial extension.

Gd is the ideal rare earth to use in a study of the transition metal moment in alloys because the moment of the rare earths are generally quenched to some extent by the crystal field, and this effect is much less important in Gd. Thus the contribution of Gd to the spontaneous moment is known. Y makes a good non-magnetic substitute for Gd, as stated above. The effect of the moment of Gd upon the transition metal can be isolated from other influences,

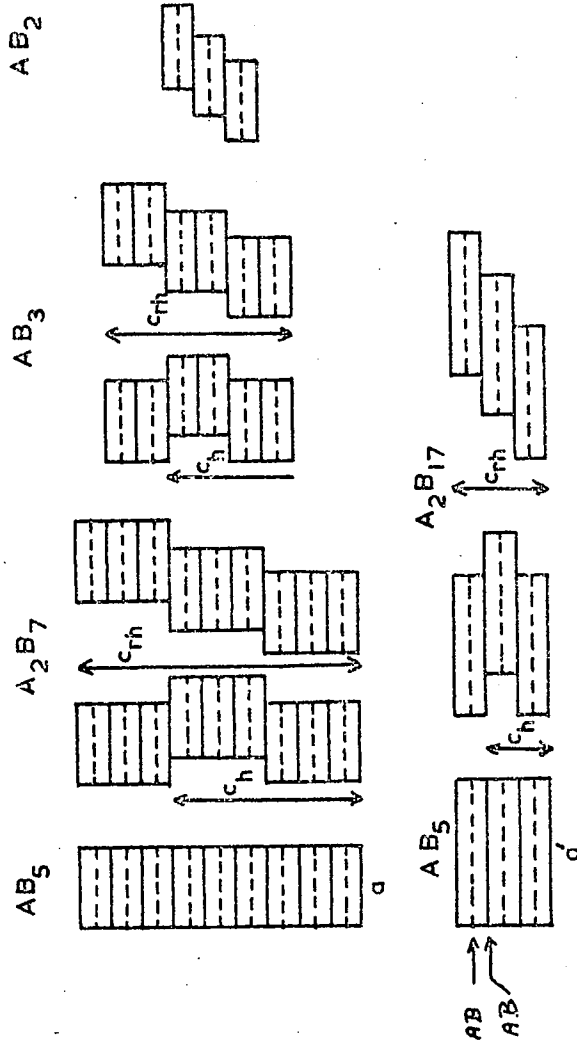


(b) The AB plane

○ B
○ A



(a) CaCu₅ (AB₅) Unit Cell



(c) Schematic representation of stacking modes for the various A_xB_{1-x} structures

Fig. 1.4 The AB₅ and related Structures

by such a substitution since most parameters remain constant, the moment on the A site being the main variable.

1.2 Structural Properties

The crystal structures of each stoichiometry are different, and some stoichiometries have more than one modification. However five stoichiometries have structures which are closely related to each other. These are AB_2 , AB_3 , A_2B_7 , AB_5 , A_2B_{17} . These can be derived from the hexagonal lattice of the $CaCu_5$ type, which is isomorphic with the AB_5 structure. These derivations arise from simple substitutions accompanied by layer shifts (ref. 1.23). The unit cell of the $CaCu_5$ type structure is shown in fig. 1.4a. The structure consists of two types of layer which are arranged alternately. One type contains only B atoms and the other contains both A and B atoms. A more extended view of the layer containing A and B atoms is shown in fig. 1.4b. Here PQRS indicates again the basal plane of the unit cell of unit cell edge a . We consider now the structure of the A_2B_{17} compounds. These arise by substitution, in the AB_5 lattice, of one third of the A atoms by a pair of B atoms, one above and one below the position of the previous A atom. The new unit cell is given by $a' = a\sqrt{3}$. If, in the basal plane, this replacement occurs at site P, then it will occur at site Q in the next layer containing A atoms. In the following layer containing A atoms it may occur again either at site P, giving a hexagonal structure, or at site T, giving a rhombohedral structure. These two possible stacking arrangements are shown schematically in fig. 1.4c.

To obtain the structures of the A_2B_7 , AB_3 , and AB_2 compounds, one must replace some B atoms by A atoms in the AB_5 lattice. For the AB_3 structure, in the top plane containing A and B atoms of every second AB_5 unit cell one of the two B atoms is replaced by an A atom, followed by a layer shift and minor rearrangements of the atoms. As in the A_2B_{17} lattice, the AB_3 has two modifications whose stacking arrangements are shown schematically in fig. 1.4c. In a similar way the structures of the A_2B_7 and AB_2 compounds can be derived, and the stacking arrangements are also shown schematically in fig. 1.4c.

The AB_2 stoichiometry forms in three modifications, known as the Laves phases. Two are hexagonal, one is cubic, the choice of which structure type the material adopts being strongly dependent upon the valence electron concentration (ref. 1.7, 1.10).

As a consequence of the close relationship of the crystal structures from A_2B_{17} to AB_2 , it is not unreasonable to expect a certain degree of continuity in the magnetic and other properties as a function of x as we cross the stoichiometries, despite the fact that x is not a continuous variable.

Of the stoichiometries other than the ones just discussed, the crystal structures can be derived from the cobalt-or nickel-centered trigonal rare earth prism. These are the A_3B , A_4B_3 and AB stoichiometries. The A_3B crystal structure, with which the second results section is concerned, is isomorphic with the orthorhombic Fe_3C structure.

The structural stability of a given stoichiometry depends upon the valence electron concentration. Although this is not the only factor affecting structural stability, it is certainly one of the factors, as has been shown to be the case for the Laves phase structures. The compounds YCo_5 , Y_2Co_7 , YCo_3 and Gd_3Co are known to exist, but the corresponding compounds with the Co replaced by Fe do not exist. The pseudobinary (Fe, Co) alloys of these four structures were prepared in order to observe at what Fe concentration the respective structures would become unstable the aim being to establish to what extent this instability is ascribable to the effects of valence electron concentration.

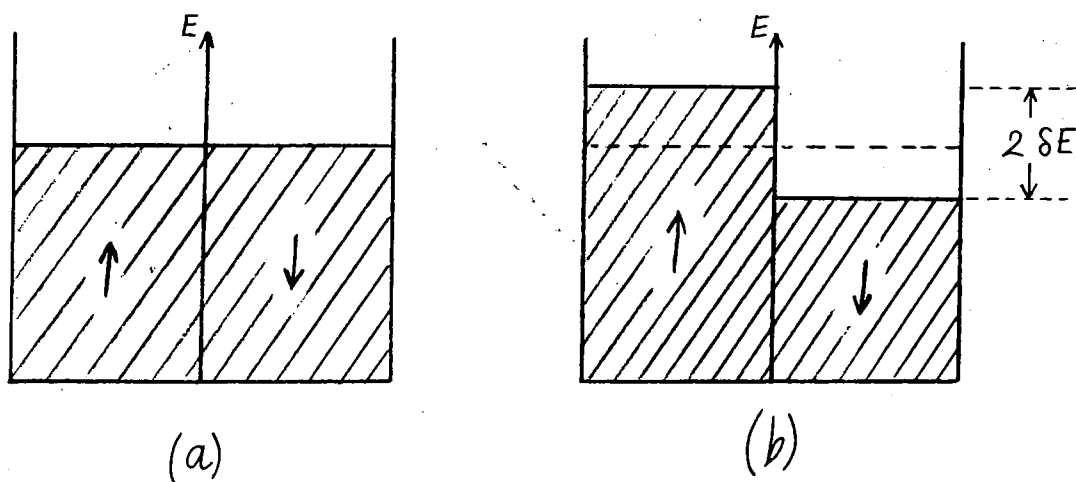
1.3 Ferromagnetism in a Band

It is generally accepted now that the age-old problem in 3d-transition metal magnetism: itinerant vs localised 3d electrons, has been resolved by a compromise between these two extremes. Whereas the itinerant model is applicable in that the 3d electron energy levels are broadened into a band which can be split by exchange to give a moment, neutron diffraction has revealed a certain amount of localization of these moments around the transition metal atoms. In the primary alloys (Co, Ni) of the pure

transition metals, this localization results in the Co sites being associated with a moment of $1.7\mu_B$ and the Ni sites with $0.6\mu_B$, these two values being those found in pure Co and pure Ni. It is thus evident that the correct theory must involve some reasoning in space, in the context of a band theory. The occurrence of spontaneous ordering within the usual band theory due to Stoner will first be described, followed by a description of the rigid band model for alloys.

1.3.1. The Simple Band Model (Stoner, ref. 1.17)

We derive a condition for the occurrence of ferromagnetism at zero degrees Kelvin in the band model, as follows. We begin with two sub-bands (spin \uparrow and spin \downarrow) which are equally populated. These are shown schematically below



Let a small number ϵ electrons/atom be transferred from the \downarrow -spin to the \uparrow -spin sub-band. This requires energy $\epsilon \delta E$ /atom, where $2\delta E$ is the energy difference between the two Fermi levels.

The exchange energy is proportional to the number of electron pairs in each sub-band so that the exchange energy as a result of the transfer is lowered by an energy of magnitude:

$$\left[\left(\frac{p}{2} + \epsilon\right)^2 + \left(\frac{p}{2} - \epsilon\right)^2 - 2\left(\frac{p}{2}\right)^2 \right] W$$

where W is the average exchange energy per pair of electrons, and p is the number of electrons per atom.

This expression reduces to

$$2W \mathcal{E}^2$$

If the total energy lowers when the band is polarized, then we have

$$2W \mathcal{E}^2 > \mathcal{E} \delta E$$

Let $N(E_F)$ be the density of states at the Fermi level. Substituting $\mathcal{E}/N(E_F)$ for δE we obtain the Stoner criterion for the occurrence of a spontaneous moment:

$$2W N(E_F) > 1$$

When this inequality holds, then one sub-band should begin to fill at the expense of the other until the total energy is a minimum. By differentiating the total energy with respect to \mathcal{E} we obtain the equilibrium condition

$$2W \overline{N(E)} = 1,$$

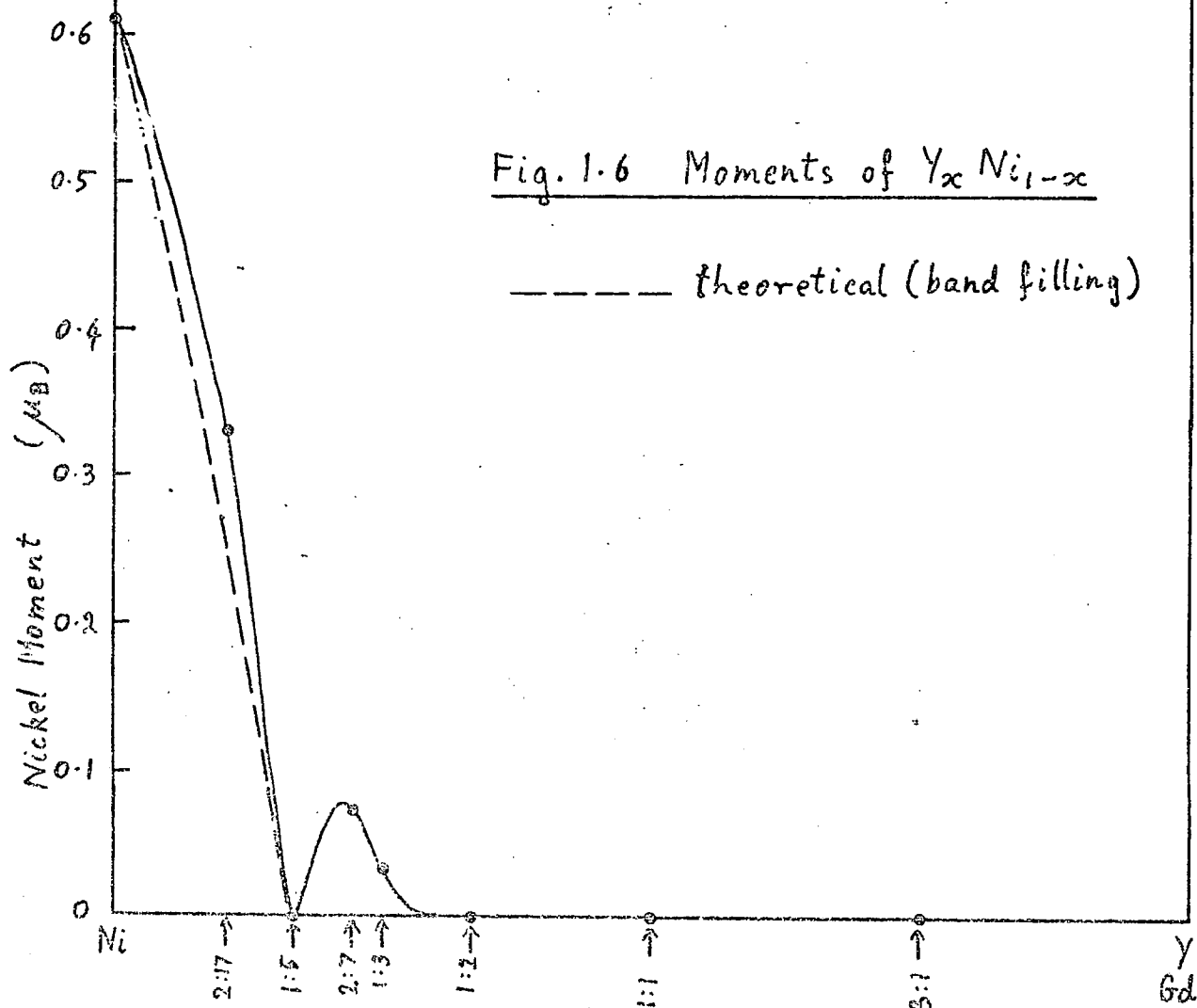
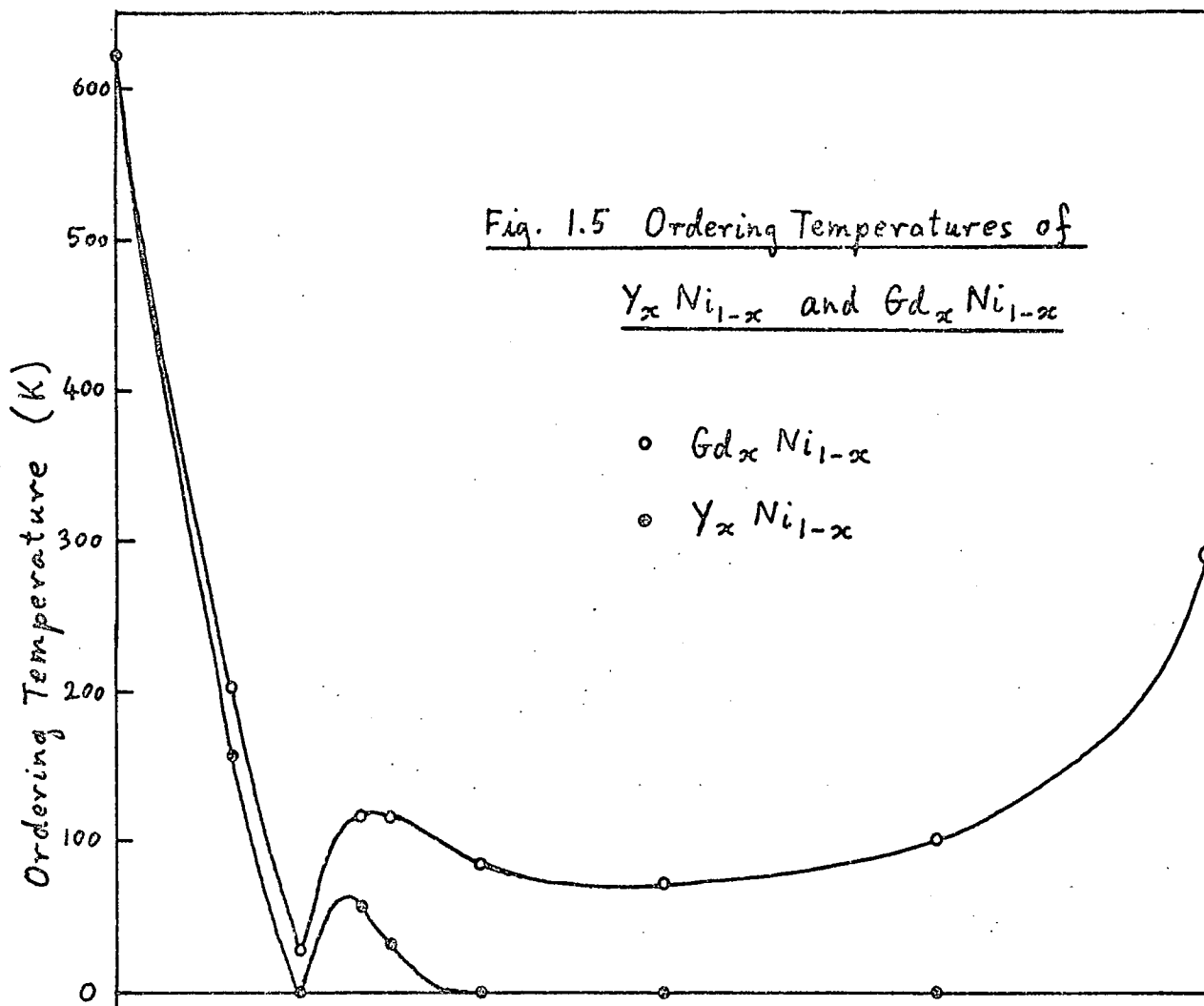
where
$$\overline{N(E)} = \frac{n}{\Delta E} = \frac{1}{\Delta E} \int_{E_1}^{E_2} N(E) dE.$$

$\overline{N(E)}$ is the average density of states between the two equilibrium Fermi levels E_1 and E_2 of the two sub-bands. ΔE is the energy of splitting between the two sub-bands, and n is the total number of electrons transferred from one sub-band to the other.

1.3.2 The Rigid Band Model for Alloys

For a pure metallic element the periodicity of the crystal lattice is almost perfect, so that the potential wells affecting the itinerant electrons also have perfect periodicity in space, resulting in a given density of states $N(E)$. When such a metal is alloyed with another metal, even if the crystal structure remains unchanged, the random distribution of the two types of ion destroys, to some degree, the periodicity of the potential energy in space.

In a dilute substitutional alloy we must consider the perturbation δV due to the solute atoms. The results of some of Friedel's calculations (ref. 1.18) will be quoted here. If δV is weak, perturbation methods can be used, with the result that the energy levels in the band must be changed by a quantity which varies only slowly with \mathbf{k} , where \mathbf{k} is the wave vector



of the band electrons. Thus, on alloying a pure metal each state of the band is shifted by a constant amount which is proportional to the concentration of solute atoms. The result is simply a shift in energy of the entire band, as if it were rigid, with little change in shape. This model works well for small δV , in other words, for alloys between neighbouring elements in the periodic table, such as (Co, Ni) and (Ni, Cu). The potential δV must of course be screened. The result is that one obtains a local piling up of band electrons near an attractive potential. If there is exchange splitting in the band then this local excess of charge near an attractive potential will be associated with a different magnetic moment than that found locally around the matrix ions. Such effects have been detected by neutron diffraction techniques. On a macroscopic scale however the alloy can be treated as if the density of states were the same as that of the pure matrix, but with a change in the Fermi level as solute atoms are substituted.

1.4 Magnetic Properties

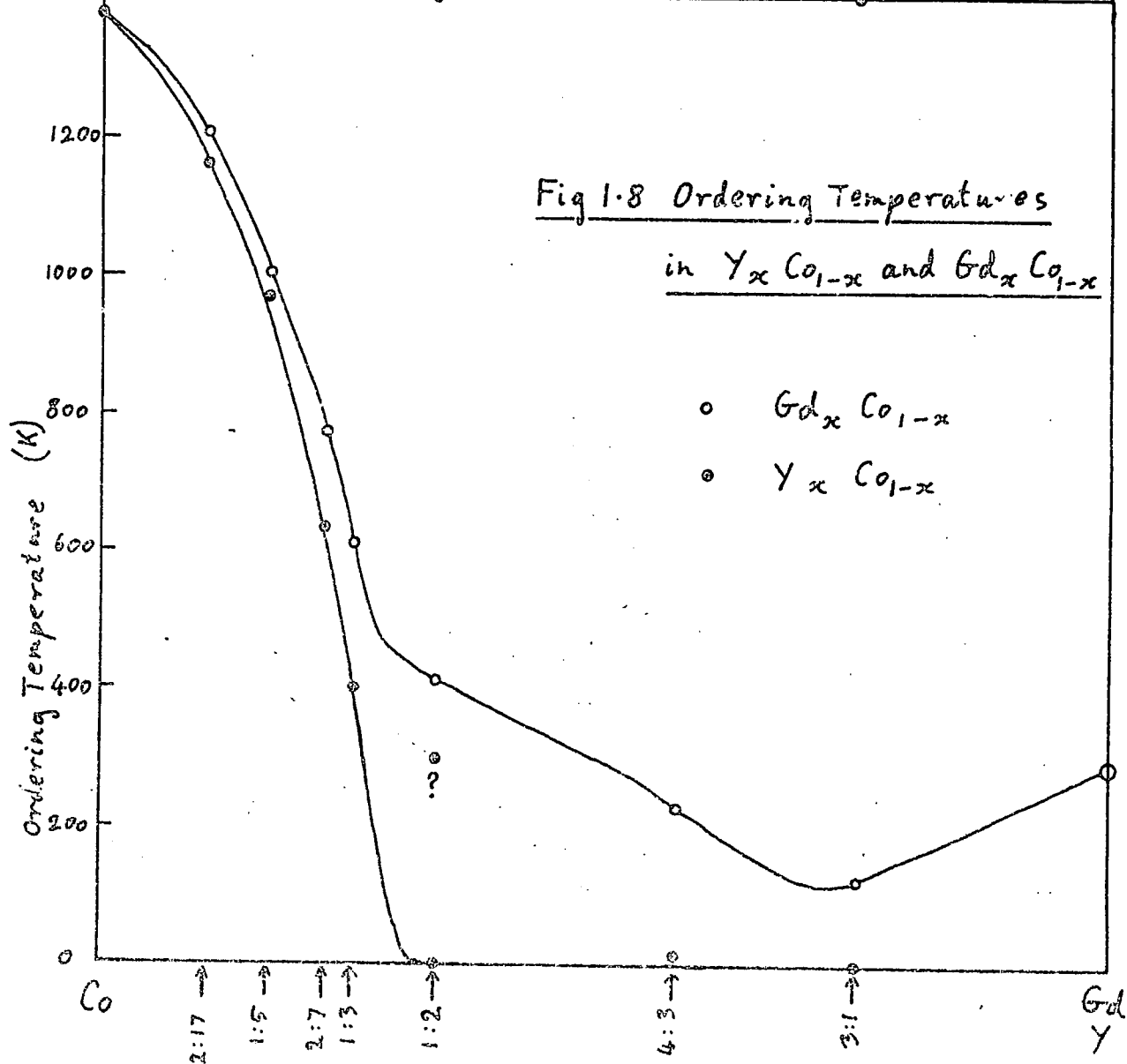
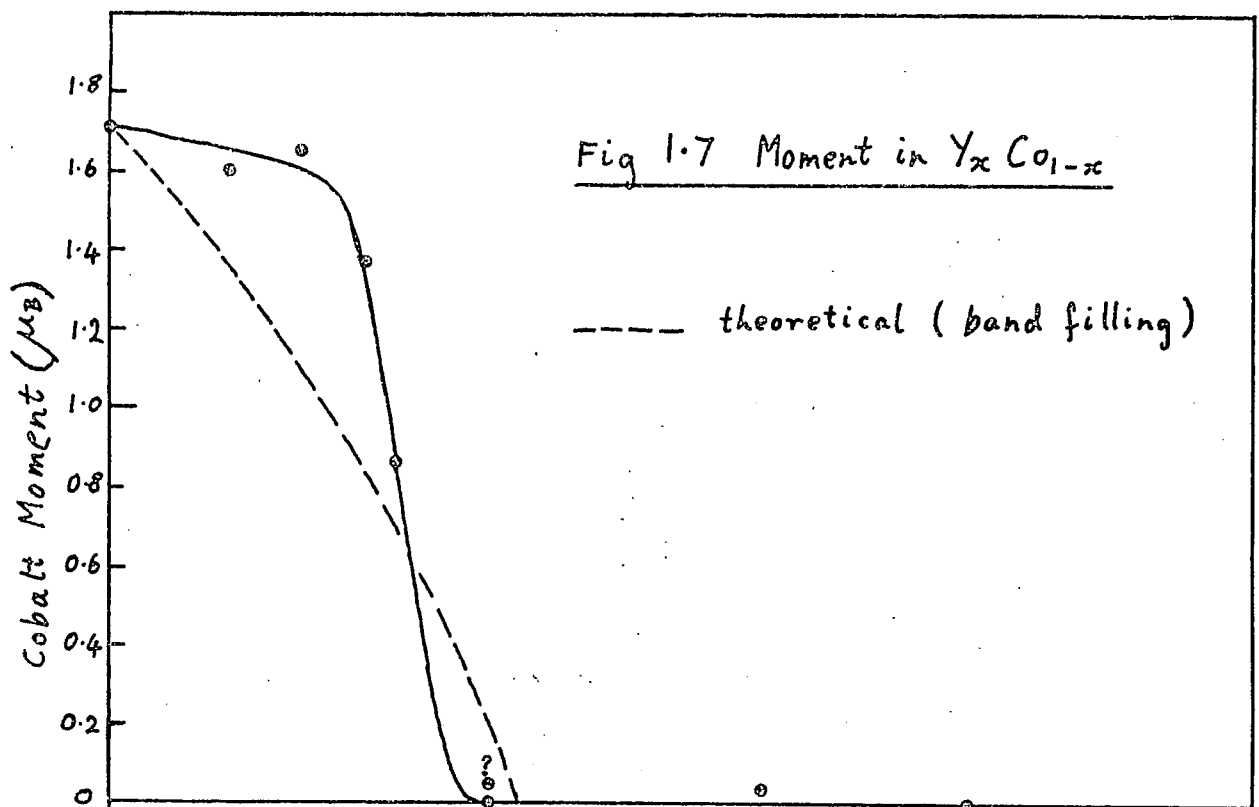
1.4.1 Compounds with Nickel

The ordering temperatures T_c of the nickel compounds $Y_x Ni_{1-x}$ and $Gd_x Ni_{1-x}$ are plotted in fig. 1.5 as a function of x . All the ordering temperatures are Curie points except that of $Gd_3 Ni$ which is a Néel point. As seen in this graph the Gd compounds have higher ordering temperatures than the Y compounds. T_c decreases rapidly from that of Ni as x increases, becoming zero for $Y Ni_5$ and very low for $Gd Ni_5$. This was interpreted by Lemaire et al (ref. 1.8) as a result of the filling of the 3d band by valence electrons from the rare earth atoms, the band becoming completely full in $Gd Ni_5$. On increasing x further, T_c rises sharply. This rise in T_c was interpreted as a result of the exchange interactions between the Gd ions inducing a moment in the 3d band of Ni. The subsequent Ni-Ni exchange interactions then contribute to a rise in T_c . T_c then decreases as x is increased further, this being due to the 3d band again becoming filled. Comparison with $Ho_x Ni_{1-x}$ showed that the same phenomenon occurred when Gd was replaced by Ho, but the increase in T_c was not as large as for the Gd compounds. Since the spin of Ho is less

than that of Gd it was evident that the increase of T_c from ANi_5 to ANi_3 was larger, the larger the rare earth spin. This interpretation, which was presented to account for the increase in T_c from ANi_5 to ANi_3 , appears to this author to be incorrect. This is because the same phenomenon occurs in the $\text{Y}_x\text{Ni}_{1-x}$ compounds where the non-magnetic Y cannot induce any moment in the Ni 3d band. The spontaneous moment per Ni atom is shown in fig. 1.6, from which it is evident that the T_c variation is directly related to the M_s variation. The reappearance of ferromagnetic ordering as we go from YNi_5 to YNi_3 cannot be caused by the A-A interaction. The A-A interaction can however amplify this effect once it has occurred. It appears therefore that this reappearance of ordering is inherently a property of the 3d electrons.

The dashed line in fig. 1.6 represents the expected decrease in moment assuming that the three valence electrons of yttrium all occupy the 3d band. The assumption is also made that one of the spin sub-bands is full. The agreement with experiment is excellent from pure Ni to YNi_5 where both the theoretical and experimental functions become zero. This is consistent with the interpretation of Lemaire et al. for this range of stoichiometries. Their interpretation is however inadequate for the compounds richer in yttrium than YNi_5 . The persistence of ferromagnetism for higher Y content than that of YNi_5 suggests that not all of the three valence electrons of yttrium occupy the 3d band. Thus the assumption in deducing the theoretical moment decrease is almost certainly incorrect.

The reappearance of a small moment on YNi_3 and Y_2Ni_7 , (after the entirely non-magnetic behaviour of YNi_5) is as yet not understood. The substitution of Co for Ni in YNi_3 (or Y_2Ni_7) may be expected to simulate the decrease in valence electron concentration or going from YNi_3 (or Y_2Ni_7) to YNi_5 . The magnetic properties of the pseudobinary systems $\text{Y}_2(\text{Co,Ni})_7$, $\text{Y}(\text{Co,Ni})_3$, and $\text{Y}(\text{Co,Ni})_5$ were therefore investigated in the hope that some understanding of the moment reappearance might be forthcoming.



1.4.2 Compounds with Cobalt

The moment per Co ion in the Y_xCo_{1-x} system is shown in fig. 1.7. It is believed (ref. 1.9) that one of the spin sub-bands of pure cobalt is full, as in nickel, and that the moment $1.7\mu_B/Co$ arises from the holes in the other sub-bands. The theoretical curve (dashed line) in fig. 1.7 shows the expected moment variation assuming that the 3 valence electrons per yttrium occupy the 3d unfilled sub-band. The discrepancy between this theoretical curve and the experimental curve is large. The cobalt moment remains at a high value between $1.5\mu_B/Co$ and $1.7\mu_B/Co$ from pure cobalt to YCo_5 . This cannot be reconciled with a simple band-filling theory. The moment collapses from YCo_5 , to become almost zero at YCo_2 which is close to the point at which the above theoretical variation becomes zero.

The Curie temperatures T_c , for the Y and Gd compounds are shown in fig. 1.8 where it can be seen that T_c decreases continually, on increasing x. The T_c values given for YCo_2 are questionable. The higher value was obtained from the measurement of M vs T by Piercy (ref. 1.15). This curve however did not show a convincing Curie point and it is generally believed that YCo_2 is a Pauli paramagnetic and shows no magnetic ordering. This latter assumption puts the T_c value very near zero.

Y_4Co_3 however does order, and its T_c value (ref. 1.11) need not be treated with reservation. On increasing x further, T_c becomes zero in Y_3Co . It appears that we may be observing here the same phenomenon as was seen to occur in the Y_xNi_{1-x} compounds where the moment and ordering temperatures collapsed to zero, with a subsequent small reappearance. In the Y_xCo_{1-x} system the collapse to zero moment and no ordering occurs as we increase x and approach YCo_2 . Then the moment reappears on further increasing x. The description of this by a continuous curve of the form used for the Ni compound is not easily justified in the Co compounds for two reasons: firstly, we have only one point to mark the reappearance of the moment, and secondly the crystal structures of the YCo_2 , Y_4Co_3 and Y_3Co are not sufficiently closely related to each other to allow us to expect continuous behaviour as we cross the

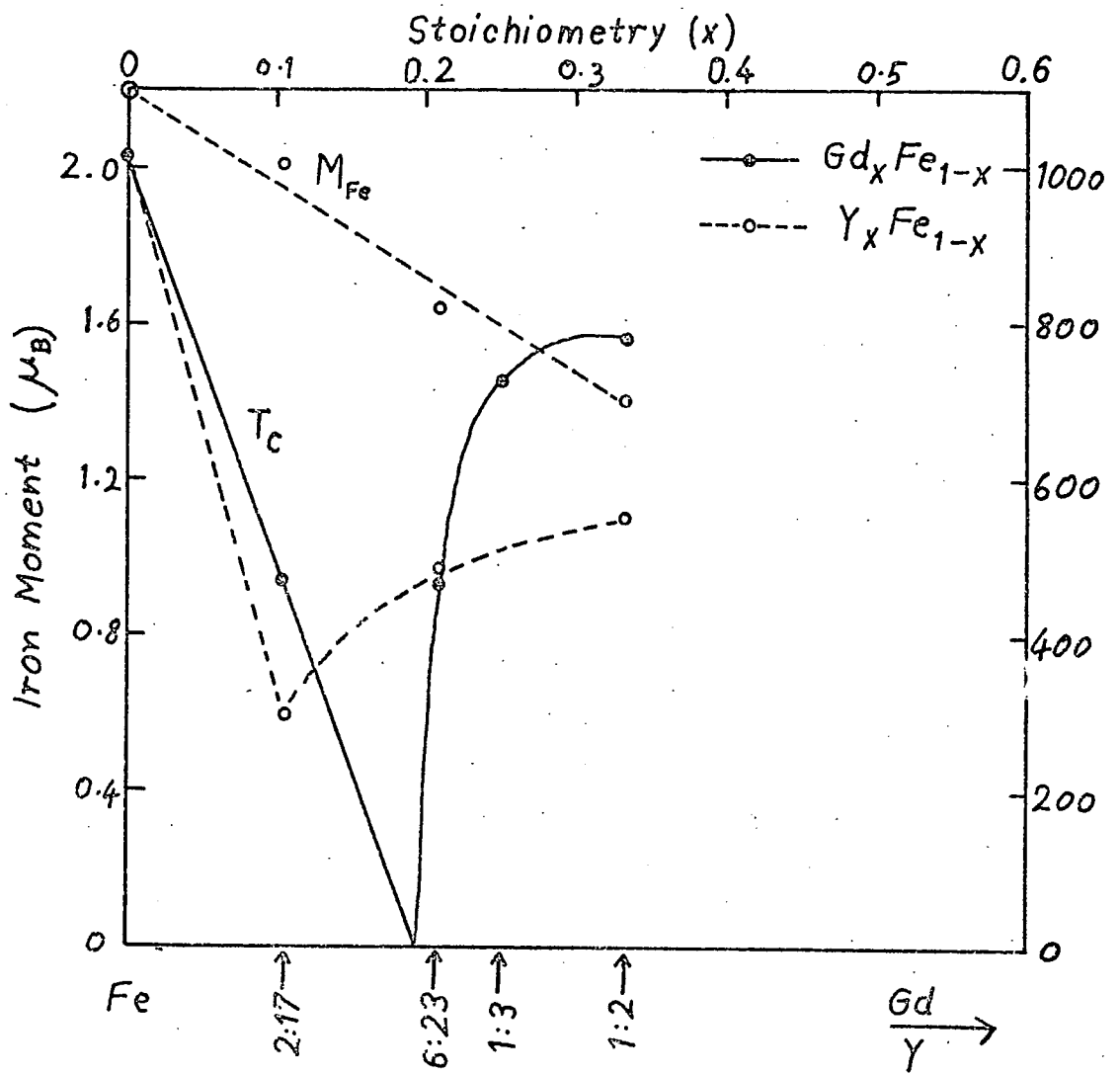


Fig 1.9. M_{Fe} and T_c in Y_xFe_{1-x} and Gd_xFe_{1-x} Compounds

stoichiometries. Neither of these objections applied in any very serious way to the Ni system in the small moment region.

The $\text{Gd}_x\text{Co}_{1-x}$ compounds (fig. 1.8) have an ordering temperature variation which can be unambiguously presented for all the stoichiometries. All the ordering temperatures are Curie points, except that of Gd_3Co which is a Néel point. The Gd compounds all have higher ordering temperatures than the corresponding Y compounds.

1.4.3. Compounds with Iron

From the foregoing it is evident that the magnetic properties of the cobalt compounds are more difficult to interpret in terms of simple band theory than the nickel compounds. The iron compounds are even more difficult to interpret in these terms.

Whereas for pure nickel and cobalt it is generally believed that one of the spin sub-bands is full, this is not the case for pure iron. Thus the number of empty 3d-states per atom in iron exceeds the number of unpaired spins. The latter quantity is 2.2 per atom (which gives the magnetic moment $2.2\mu_B/\text{atom}$), while the value suggested (ref. 1.12) for the former exceeds 3 per atom.

In fig. 1.9 it can be seen that the iron compounds with yttrium and gadolinium show a somewhat anomalous Curie temperature variation. While the moment per iron atom in $\text{Y}_x\text{Fe}_{1-x}$ is decreasing with increasing x, the Curie temperatures decrease initially very rapidly from Fe to Y_2Fe_{17} and then rise on further increasing x. In $\text{Gd}_x\text{Fe}_{1-x}$ the T_c values rise so rapidly from Y_6Fe_{23} to YFe_3 that, if one is justified in drawing a curve through these points, one is tempted to draw the one shown in this figure. This curve touches the x axis before rising rapidly to follow the T_c variation in the Gd rich Fe compounds. There is little justification for including the A_6Fe_{23} stoichiometry on this curve. This is because, unlike the other stoichiometries, the A_6Fe_{23} structure is not closely related to the CaCu_5 structure.

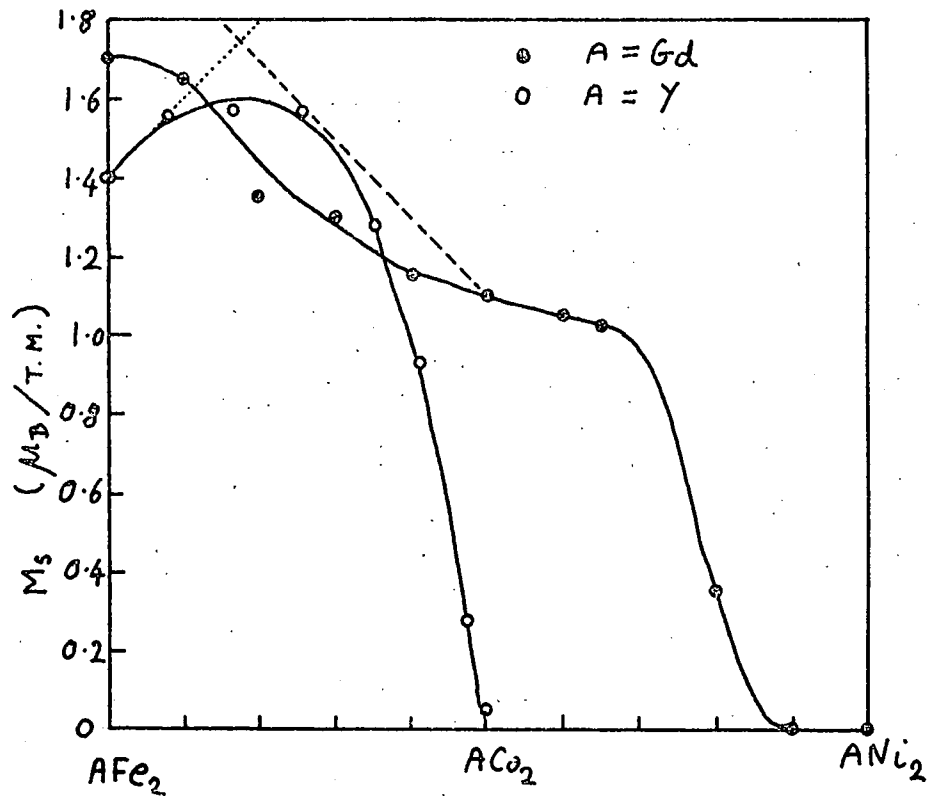


Fig.1.10 Saturation Moments in $Y(Fe,Co)_2$, $Gd(Fe,Co)_2$, $Gd(Co,Ni)_2$

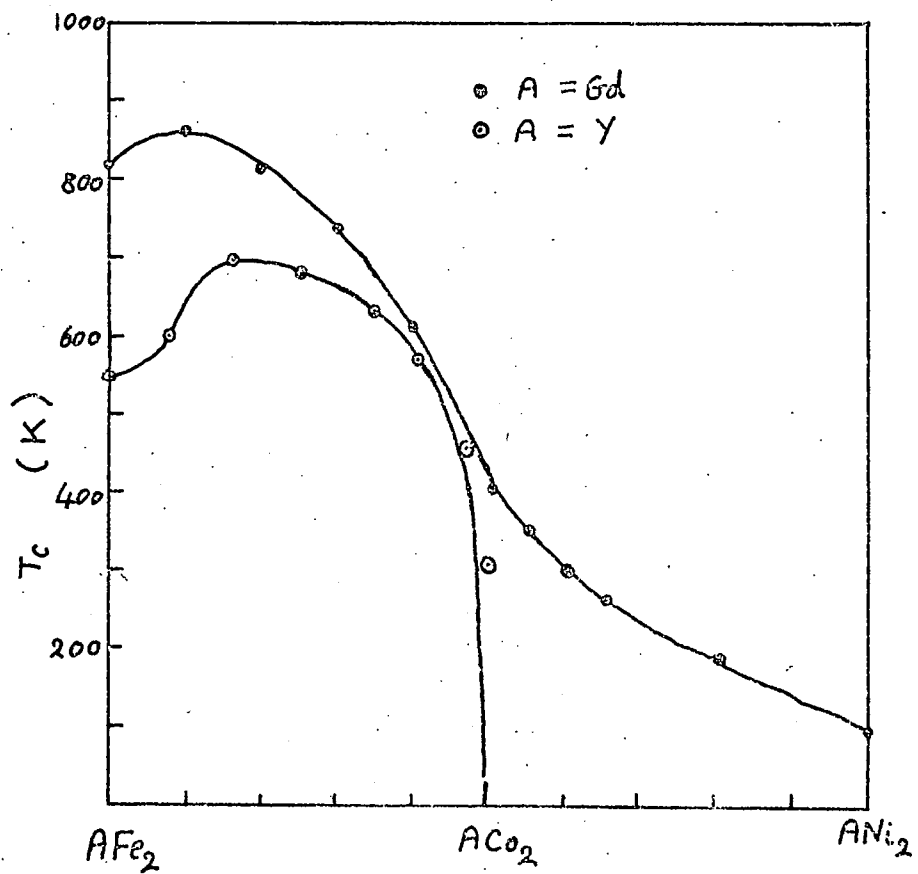


Fig.1.11 Curie Temperatures in $Y(Fe,Co)_2$, $Gd(Fe,Co)_2$, $Gd(Co,Ni)_2$

1.4.4 Magnetic Property variation within a given Stoichiometry

Within a given stoichiometry we shall consider the variation of magnetic properties on replacement of Fe with Co, and Co with Ni. Since these pairs of ion types are neighbours in the periodic table such replacements often occur without any crystal structure change. There are therefore large composition regions of solid solubility in which the lattice parameters show a smooth variation. Thus we are fully justified in drawing smooth curves through points representing magnetic properties as a function of composition within a given stoichiometry, provided that the crystal structure does not change.

(a) The AB_2 stoichiometry

The systems $Y(Fe,Co)_2$, $Gd(Fe,Co)_2$ and $Gd(Co,Ni)_2$ have already been investigated (refs. 1.13, 1.14) Figs. 1.10 and 1.11 show the variation with composition of the saturation moment M_s and Curie temperature T_c in these pseudobinary systems. Both M_s and T_c have a maximum at approximately 60% - 70% Fe substitution in the $Y(Fe,Co)_2$ system. On increasing the Co content both M_s and T_c show a collapse in the composition region of YCo_2 . As previously mentioned, the points shown for YCo_2 are questionable. It is more likely that both parameters are zero at YCo_2 .

In the $Gd(Fe,Co)_2$ and $Gd(Co,Ni)_2$ systems, the Gd moment is assumed to be $7\mu_B$ per atom. The transition metal moment was deduced by assuming an antiparallel alignment of Gd and transition metal magnetic moments. The first assumption is justified by the fact that the Gd^{3+} ion is an S state ion, and therefore not affected by the crystal field. The second assumption is justified by the considerations of section 1.1 concerning the M_s variation in gadolinium compounds with Fe, Co and Ni (fig. 1.3). This variation shows, in each case, a deep minimum which can be readily interpreted in terms of an antiparallel alignment of the Gd and transition metal moments. It is reasonable to assume that this type of alignment holds also for the pseudobinary compounds. By making the above two assumptions, the moment per transition metal atom arising from non-4f electrons can be deduced. It is uncertain, however, what fraction of

this moment can be ascribed to 3d band polarization, and what fraction to the polarization of the conduction band induced by exchange with the Gd spins.

In the $\text{Gd}(\text{Co},\text{Ni})_2$ system the moment per transition metal collapses on increasing the Ni content (fig. 1.10) in much the same way as that in the $\text{Y}(\text{Fe},\text{Co})_2$ system. On replacing Fe with Co, or Co with Ni, the valence electron concentration increases by one electron per atomic replacement. The collapse occurs on increasing the valence electron concentration. Substituting Gd for Y results in the collapse being delayed on increasing the valence electron concentration. The variation of the transition metal moment in the Y and Gd systems is very similar in the region of the transition metal moment collapse. Interestingly the moment collapse in $\text{Gd}(\text{Co},\text{Ni})_2$ is not accompanied by any abrupt decrease in the Curie temperatures, but only by a continued gradual decrease.

The transition metal moment behaviour in the Y and Gd pseudobinary AB_2 's was interpreted by Piercy (ref. 1.15) in terms of the rigid band model, assuming the 3d electrons to be itinerant. The initial rise in moment from YFe_2 on substituting Co for Fe was able to be interpreted by making the assumption that there was a minimum in the density of states $N(E)$ and that the paramagnetic Fermi level was situated at an energy above that of the minimum. On switching on the positive exchange interaction, electrons are transferred from the \downarrow -spin sub-band to the \uparrow -spin sub-band until the Fermi level of the \downarrow -spin sub-band encounters the low $N(E)$ on the high energy side of the minimum. Further transfer is then energetically unfavourable and we are left with holes in both sub-bands. On substituting Co for Fe in YFe_2 the extra valence electron of Co occupies the 3d band and decreases the number of holes. The E_F of the \downarrow -spin sub-band remains at the minimum in $N(E)$ while the extra valence electrons occupy the \uparrow -spin sub-band at the rate of 1 per Co-Fe replacement. Since the moment is given by the excess number of \uparrow -spins with respect to \downarrow -spins, and since the \uparrow -spins are increasing at the rate of 1 per Co-Fe replacement, we obtain an increase in the moment per transition

metal at the rate of $1\mu_B$ per Co-Fe replacement. This corresponds, in fig. 1.10 to the dotted line from the point $(1.4\mu_B)$ for YFe_2 with a gradient of 45° . The initial variation of the moment is seen to follow such a line. A point is reached, however, where the \uparrow -spin sub-band is filled, so that any further addition of valence electrons to the 3d-band occurs in the \downarrow -spin sub-band. This then decreases the moment at a rate of $1\mu_B$ per Co-Fe substitution. This expected variation cannot be fixed without knowing the number of holes in the 3d-band of YCo_2 . Piercy used some conclusions from an experiment of Oesterreicher and Wallace (ref. 1.16), in which it was deduced that the number of 3d holes in $GdCo_2$ was 1.1 per Co atom. This experiment consisted of substituting Al for Co in $GdCo_2$ and observing when the Co moment became zero, assuming that 3 electrons per Al atom go into the 3d band. Assuming this value for the number of 3d holes in $GdCo_2$, it was stated that there was no good reason for expecting YCo_2 to have a different number of holes in the 3d-band. Thus, if YCo_2 has 1.1 holes per atom in the 3d band, YFe_2 must have 2.1 holes per atom, and the expected decrease with a gradient of -45° is shown in fig. 1.10 as the dashed line. The actual moment variation does not follow these two lines over the whole (Fe, Co) range. The main differences are: (1) the departure begins at approximately 20% Co in Fe, and for all higher Co contents the actual moment is lower than the theoretical values. This suggests that the \uparrow -spin sub-band, while it fills up does not fill completely before the \downarrow -spin sub-band begins to be occupied. This is consistent with a low $N(E)$ near the top of the 3d-band; (2) there is a catastrophic decrease in the moment on approaching YCo_2 . This was interpreted as the result of an uncoupling of the two spin sub-bands, so that both sub-bands contain holes. The uncoupling appears to be complete at YCo_2 , though the 3d-band is not yet full, containing 1.1 holes per atom. Thus the density of states must be low at the Fermi level of YCo_2 , since no spontaneous polarization of the 3d-band exists.

The initial rise in T_c from YFe_2 , as Co is substituted, is consistent with an increased splitting of the 3d band. This would have to occur if the \downarrow -spin sub-band Fermi energy remained locked in the minimum of $N(E)$, as

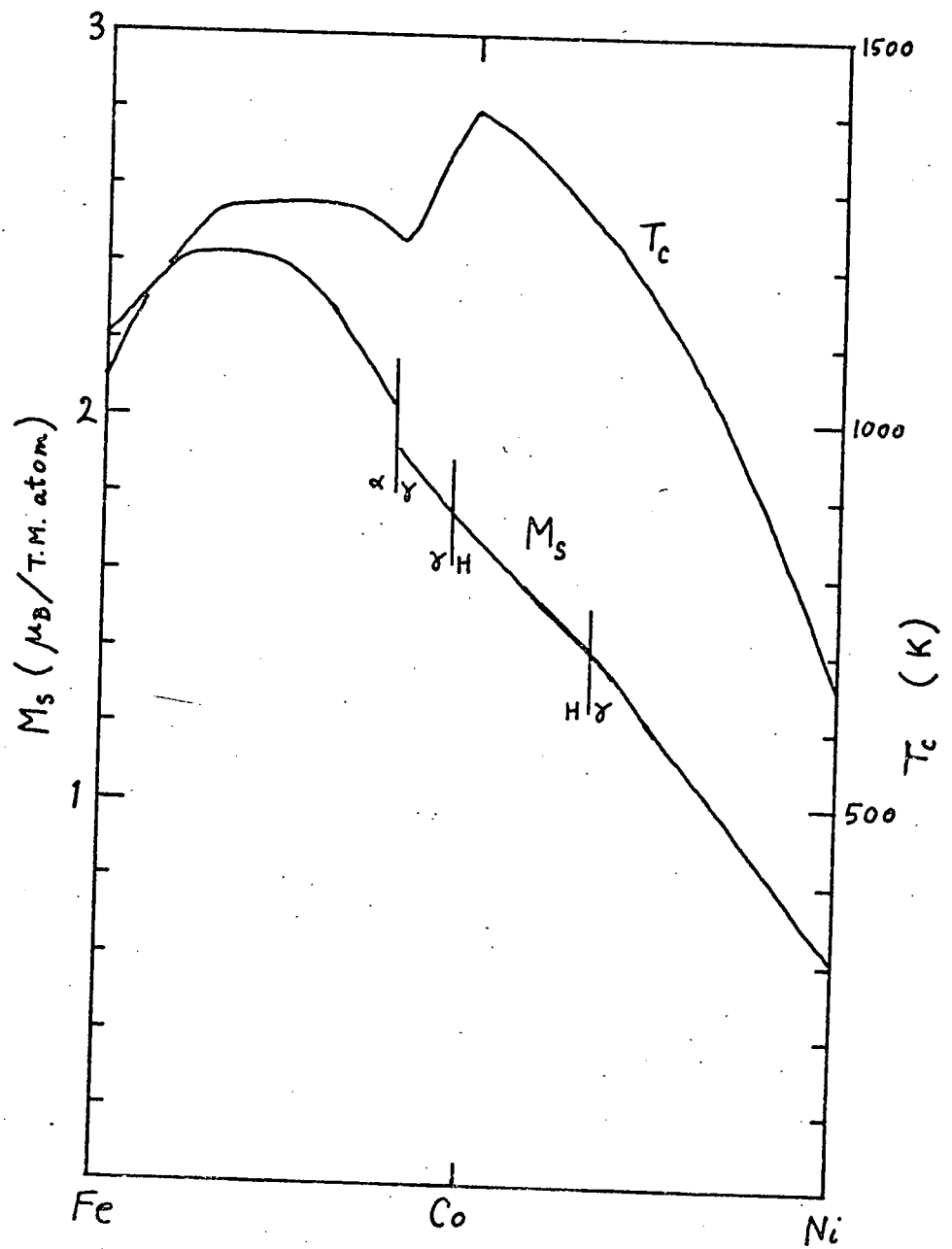


Fig 1.12 M_s and T_c for (Fe, Co) and (Co, Ni)

the above interpretation assumes, while the \uparrow -spin sub-band is being populated. The observed decrease of T_c to zero on approaching YCo_2 is consistent with the interpretation of an uncoupling of the 3d-band.

(b) The Pure 3d Metal Alloys

Fig. 1.12 shows the average spontaneous transition metal moment M_s and the Curie temperatures T_c of the alloys (Fe, Co) and (Co, Ni). These are plotted as a function of valence electron concentration, which increases by one for each step Fe to Co, and Co to Ni. The short vertical lines mark the compositions at which the crystal structure changes. The α -phase, as in iron, is b.c.c.; the γ -phase, as in Ni is f.c.c. and the H-phase is the hexagonal phase of cobalt. The Curie temperature variation has a large discontinuity at the α/γ transition. The other discontinuity occurs at the composition of pure Co. The phase change does not affect the M_s variation so drastically as it affects the T_c variation, giving only a small discontinuity in M_s .

Both M_s and T_c have a peak at the same approximate composition in the α -phase. The variation of M_s on the Fe side of the peak is a $+45^\circ$ line, and that on the Co side is a -45° line, this latter extending with a general gradient which is a little steeper than 45° , as far as Ni. On substituting Cu for Ni this line extends with a gradient of exactly -45° as far as $Cu_{.6}Ni_{.4}$, at which composition the ferromagnetism disappears. This behaviour is surprisingly close to the type of behaviour in the theoretical model used for interpreting the magnetic properties of $Y(Fe,Co)_2$. This series of compounds did not follow the theoretical behaviour very well and it was deduced that this was due to an uncoupling of the sub-bands. However, in the pure transition metals we can evidently apply the same type of model as was used in the YB_2 's, with far greater success, since no uncoupling appears to occur.

To summarise, this model involved the assumption of rigid bands for the 3d electrons, in which there is a minimum in the density of states $N(E)$. In Fe, both spin- \uparrow and spin- \downarrow sub-bands contain holes. The paramagnetic Fermi level is situated in a region of the $N(E)$ curve above the assumed minimum in $N(E)$. The exchange interaction fills the spin- \uparrow sub-band at the expense

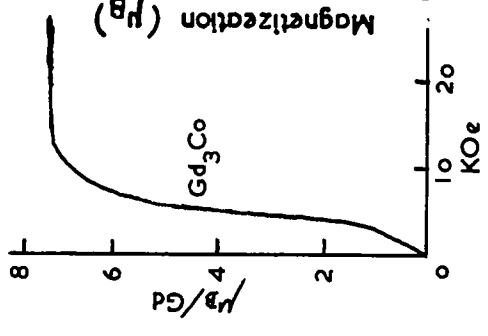
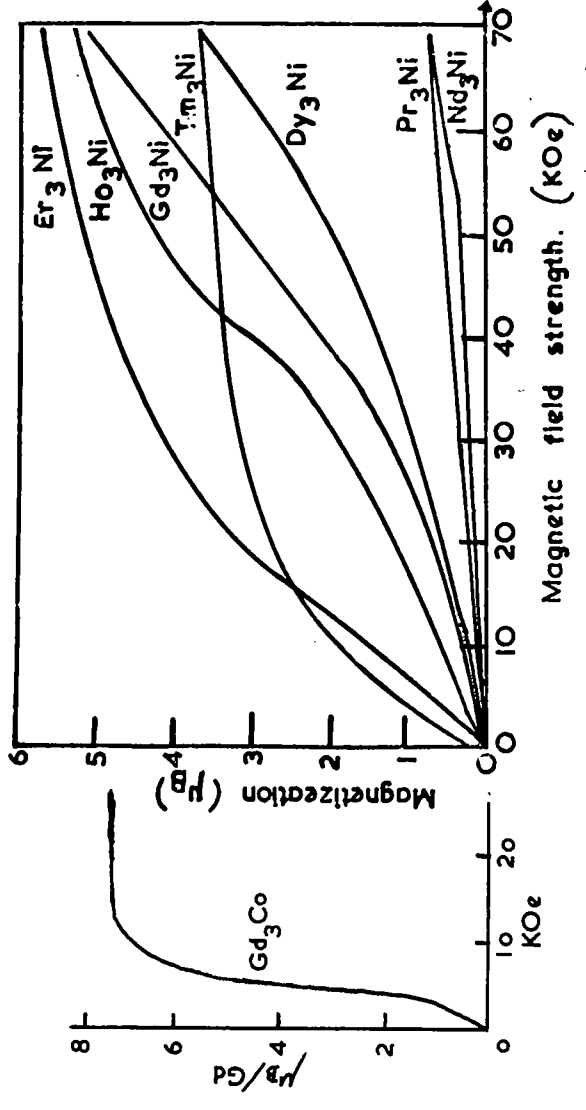
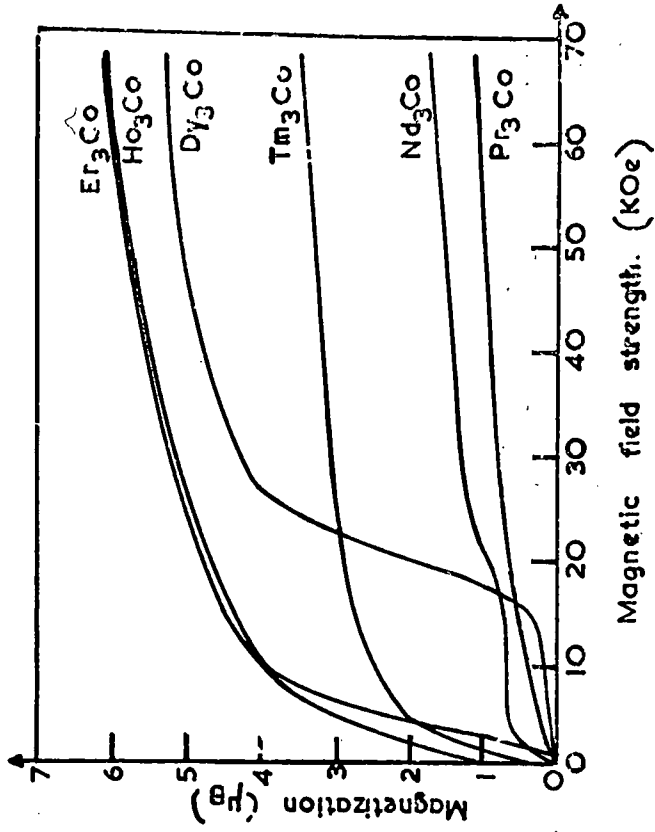


Fig 1.13 M vs H Curves of A₃Ni and A₃Co

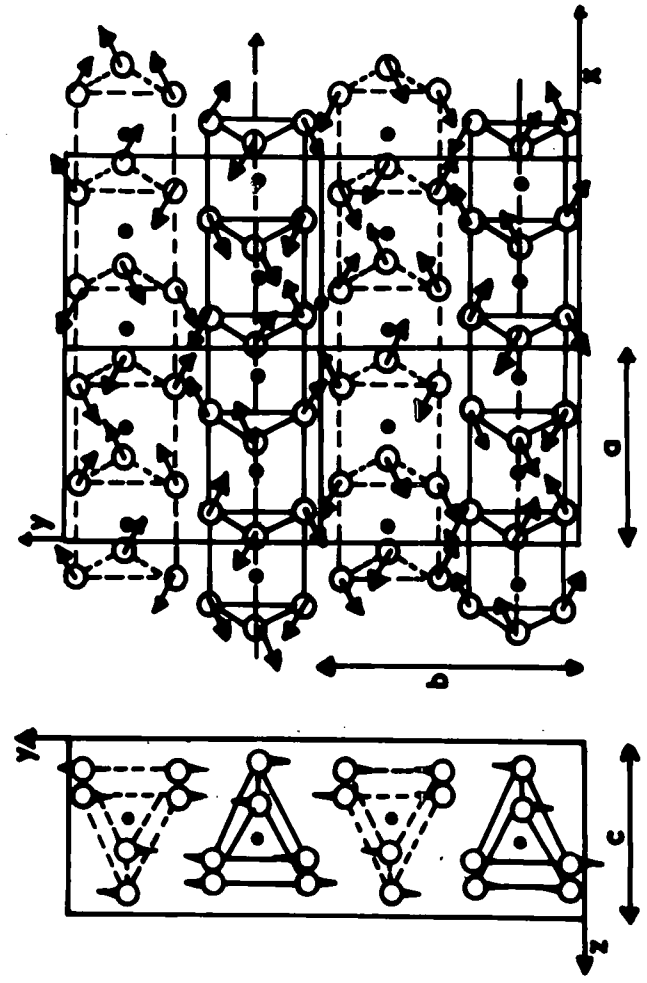


Fig 1.14

Moment Structure
of Er₃Ni

of the spin \downarrow sub-band until the Fermi level in the spin \downarrow sub-band encounters the minimum in $N(E)$. On substituting Co for Fe, the Fermi level of the spin \downarrow sub-band remains locked at the minimum and the added valence electrons populate the spin \uparrow sub-band, thus increasing the spontaneous moment at the rate of $1\mu_B$ /valence electron added. When the spin \uparrow sub-band Fermi level encounters the top of the 3d band, the spin \downarrow sub-band begins to populate, so that M_s varies now at the rate of $-1\mu_B$ /valence electron added until the 3d band is full, which occurs at 60% Cu in Ni.

1.4.5 The $Gd_3(Fe,Co,Ni)$ Compounds

To the rare earth-rich side of the $A B_2$ stoichiometry there exists a composition A_3B which occurs for both cobalt and nickel. The crystal structure is orthorhombic, isomorphic with the Fe_3C structure (ref. 1.19). Metallurgical studies show no evidence of the existence of any A_3Fe compounds.

The magnetic properties of these compounds have been investigated by Féron et al. (ref. 1.20) on polycrystalline samples down to liquid helium temperatures and by Strydom et al. (ref. 1.21), whose measurements were performed upon a Gd_3Co single crystal, but only down to liquid nitrogen temperatures (77K). Féron and his collaborators worked with magnetic field strength up to 70 KOe in static fields. Some results of Féron et al. are shown in fig. 1.13, from which it can be seen that many of the A_3Co and A_3Ni compounds show metamagnetic behaviour at 4.2K. They interpreted the critical field H_c (~ 5 KOe) and the initial susceptibility of Gd_3Co in terms of the Néel two-sublattice theory of antiferromagnetism. From this they deduced a value for the inter-sublattice molecular field coefficient and also a value for the anisotropy energy, which was of the same order of magnitude as that of metallic gadolinium. Any attempt to apply the Néel theory to the other rare earth A_3B compounds was deemed not to be worthwhile because the crystal field effects upon the rare earth moment can lead to very complex spin structures with an associated complicated variation of magnetization with field. The many varieties of M vs H curves for the different rare earths, seen in fig. 1.13, suggest that this is the case.

Neutron diffraction (ref. 1.22) revealed a complex non-collinear spin structure in Er_3Ni (fig. 1.14) as well as a non-collinear spin structure in Er_3Co .

The M vs H curve of Gd_3Ni shows an indistinct critical field at approximately 25 KOe, and measurements showed the magnetization to be still rising rapidly on increasing the field up to 70 KOe, so that saturation was not approached. The single crystal measurements of Strydom et al. showed that the critical field in Gd_3Co at 77K was observed when the field was applied in the 'b' and 'c' directions but not in the 'a' direction. Thus the sublattice magnetizations in Gd_3Co must lie in the (b,c) plane, though it is still uncertain whether or not there are only two magnetic sub-lattices.

The work, described in this thesis, on the $\text{Gd}_3(\text{Fe}, \text{Co}, \text{Ni})$ pseudobinary compounds, was performed with the aim of understanding the origin of the critical fields in the Gd_3B compounds, by observing how these changed as a function of valence electron concentration. On substituting Fe for Co, and Ni for Co, in Gd_3Co it was intended to investigate how far along these solid solution composition ranges would the Néel theory be applicable, and to investigate whether or not the anisotropy would change with valence electron concentration.

CHAPTER TWO

TECHNIQUES AND EXPERIMENTAL METHODS

2.1 Specimen Preparation

Specimens were prepared in the form of buttons of approximately 3 gm weight by melting the components together in an arc furnace. The stoichiometric quantities were weighed to an accuracy of ± 0.5 mg. The rare earth or yttrium components were obtained with a purity of 99.9% and the transition metals (iron, cobalt, and nickel) were obtained with a purity of 99.998% from Koch-light Laboratories Ltd. All the samples consisted of a rare earth or yttrium component with either one or two transition metal components.

The melting took place on a water cooled copper hearth under an argon atmosphere at a pressure of about 400 torr. The argon was obtained as 'Purargon' with an oxygen content of no more than 3 p.p.m. The arc furnace was pumped down to 10^{-3} torr then flushed with purargon to 700 torr, pumped down to 10^{-3} torr again and then filled to 400 torr with 'Purargon'. This procedure ensured that the oxygen content of the atmosphere in the furnace was down to the same order of magnitude as that of the Purargon. This oxygen content was then removed as far as possible by gettering for about half a minute with molten tantalum before melting the sample components together.

The sample melting was done at as low a temperature as possible to minimise loss of material by evaporation. This resulted in a serious loss of weight for transition metal rich stoichiometries if too high a current was used. This loss of weight was always associated with a black deposit on the cold copper hearth near the sample. The weight loss was usually no greater than 1%, and for the rare earth rich stoichiometry A_3B the weight loss was rarely greater than 0.1%. Each sample was melted and inverted three times to ensure homogeneity.

Annealing of samples was done on half-buttons wrapped in molybdenum or tantalum foil and placed in a quartz tube. Several samples were

placed in one annealing tube and each was spaced from its neighbour by a short length of quartz tube closed at one end which fit freely inside the annealing tube.

The annealing tube was filled with 'Purargon' and gettered by the same procedure as described above for preparing a sample button. The argon was then pumped out to 10^{-3} torr and the samples isolated from each other and the atmosphere by collapsing the quartz tube onto the spacers. The samples were then ready for annealing.

2.2. Determination of Crystal Structure and Lattice Parameters

The crystal structure of the end members of each pseudobinary series was obtained from the literature. X-ray photographs were obtained from a rotating powder sample using a Phillips 360 mm circumference Debye-Scherrer X-ray camera and cobalt $K\alpha$ radiation.

All of the samples could be indexed either with hexagonal or orthorhombic lattice parameters and the X-ray lines of the compounds were indexed by means of a hexagonal system Bunn Chart for all the stoichiometries studied except the A_3B . For the A_3B pseudobinary compounds the X-ray diffraction patterns of the terminal compounds were indexed with the help of the literature, in the orthorhombic system. The remaining compounds were then readily indexed.

2.3 Outline of the Principle of the Pulsed Field Magnetometer.

In a pulsed field magnetometer the specimen is subjected to an applied field which is oscillatory with an exponentially decaying amplitude. This field is produced inside a solenoid which is the inductive component of an RCL circuit. The energy stored in a charged capacitor is discharged through the magnet. The circuit is closed by a mechanical contact switch or by the use of thyratrons.

The sample is placed inside a pick-up coil system which can be principally divided into two parts: the magnetization measuring part and the field strength measuring part. The voltage induced in each part is proportional to the differential with respect to time of the magnetization of the sample and the field strength respectively.

The magnetization pick-up coil system is wound such that the applied field has no effect upon the induced voltage, the induced voltage being dependent only upon the presence of the sample. This pick-up coil system consists of a pair of pick-up coils wound in series opposition such that the output is zero in the absence of a sample. When the sample is placed inside one of these opposing coils the output is a measure of the magnetization of the sample.

The outputs of the field strength and magnetization pick-up coils are each integrated electronically. These two signals are then applied to the X and Y inputs of a cathode ray oscilloscope in order to display a magnetization-field curve on the screen.

2.4. Determination of Curie Temperatures and Neel Temperatures

2.4.1 A.C. Susceptibility Technique

The principle of this technique is described here briefly. A detailed description can be obtained from ref. 2.1. A small transformer is powered by a 500 Hz sinusoidal voltage which induces an A.C. field in the core of the transformer whose magnitude is less than 1 oersted. The core of the transformer consists of the sample in powder form. Thus the secondary of the transformer gives an output voltage which is proportional to the permeability of the core. In order to obtain a signal which is due mainly to the sample, the effect of the permeability of free space is removed by combining this transformer with a nulling transformer whose contribution to the total output can be adjusted by means of a moveable ferrite core. This is adjusted so that the total output of the two transformers is as small as possible in the absence of a sample. The output in the presence of a sample is then proportional to χ_{AC} the initial susceptibility of the sample in an A.C. field. This output is detected by a phase-sensitive detector and amplified. The amplified signal is applied to the Y input of an X-Y pen recorder. The temperature of the sample is obtained from a thermocouple whose sensing junction is placed in the powder sample. The output voltage of the thermocouple is applied to the X input of the

X-Y recorder. Thus, as the temperature varies the χ_{AC} vs T plot is traced out.

Two transformers were available, one for use at low temperatures and the other for use at high temperatures. The thermocouples used were gold-copper/copper for 4.2K to 77K, copper/constantan for 77K to 600K, and chromel-alumel for temperatures in excess of 600K.

From the form of the χ_{AC} vs T plot and from what was known about the magnetic properties of the material, one decided whether the sample was ordered antiferromagnetically or ferromagnetically. In the case of antiferromagnetic samples a sharp peak is expected, the temperature corresponding to the peak being the ordering temperature or Neel point, T_N . In the case of ferromagnetic samples it is not quite as simple to deduce the point at which ordering occurs. The ordering temperature T_C of a ferromagnet is the temperature at which spontaneous magnetization just disappears. The initial susceptibility of a ferromagnet is a function of several quantities including the spontaneous magnetization and the magnetocrystalline anisotropy. The latter term varies in a complicated manner decreasing rapidly with increasing temperature just below T_C . χ_{AC} is an inverse function of the anisotropy energy but is proportional to the spontaneous magnetization. The rapid decrease in anisotropy results in a rapid rise in χ_{AC} which peaks and then rapidly decreases due to the drop in spontaneous magnetization just below T_C . Since paramagnetic susceptibility is present above T_C the variation of χ_{AC} as a function of T is smooth on passing T_C . Thus the determination of T_C depends upon some arbitrary criterion. The generally accepted criterion is to take the point of inflection on the high temperature side of the peak to be the Curie temperature.

This is not a rigorous method of determining T_C , but it is rapid and therefore convenient when a large number of compounds is to be studied. This technique is useful also for detecting magnetic impurities in a sample since the impurities can contribute a large susceptibility even when present in very small quantities. The impurity may give rise to an extra peak in χ_{AC} which can be used in order to identify the impurity.

2.4.2 Pulsed Field Magnetometer Technique

As described briefly in 2.3 the pulsed field magnetometer gives an oscillogram displaying magnetization vs field for a sample up to high field values of the order of 100 kOe. This trace is obtained for various temperatures near the ordering temperature. In the case of antiferromagnetic ordering the initial susceptibility is measured from the oscillogram traces as a function of T and where this peaks the ordering temperature is termed the Néel point T_N . In the case of ferromagnetic ordering the region of the magnetization curve where domains are believed to be absent is used. Magnetization M vs T is plotted for various given field values in this region. The intercept $T_c(H)$ of M^2 vs T on the T axis is obtained for each field value H . $T_c(H)$ is plotted against H and the plot, which is generally linear, is extrapolated to $H = 0$. The value of $T(0)$ is the Curie temperature.

2.4.3 Comparison of the A.C. Susceptibility and Pulsed Field Magnetometer Techniques

For rigorous accurate measurements of ordering temperatures the A.C. susceptibility technique is not acceptable. This applied even to the determination of Néel points, for the following reason: The χ_{AC} vs T plots usually show some hysteresis. Thus χ_{AC} is not a unique function of temperature. The form of the χ_{AC} vs T curve depends upon the thermal history of the sample, depending upon whether the temperature of the sample is rising or lowering when passing T_N ; it also depends upon how far from the Néel point the temperature was when the temperature run was commenced. This is to be expected if one considers that the A.C. field applied to the sample is very small and is not sufficient to interfere with the spin system of the sample to any significant extent. Thus if the spin system when ordering adopts a given domain configuration just below T_N further lowering temperature might give rise to ~~some~~ new configurations. If then the temperature is raised again to the same value just below T_N it is likely that some hysteresis will result in the two domain configurations being different. Thus χ_{AC} may be different and depend upon the history of the sample. In contrast, using the pulsed field magnetometer, the effect of the field is so drastic

that within one pulse the antiferromagnetic material can undergo a transition to the ferromagnetic state and thus completely erase any memory which the spin system might have of its thermal history. Thus measurements using the pulsed field magnetometer give magnetization vs field curves which are a unique function of temperature and hence are suitable for the unambiguous measurement of Curie and Néel points.

CHAPTER THREE

THE PULSED FIELD MAGNETOMETER

3.1. The Magnet and the Field Producing Circuit

3.1.1 Construction and Mounting of the Magnet

The magnet was machined out of a solid cylinder of beryllium-copper (2%Be). This material was chosen because its high tensile strength would prevent distortion of the magnet while in operation. A helix of 10 turns per inch (total 36 turns) was cut from the cylinder (57 mm diameter) by machining a thread (width 1.27 mm) to a depth of 15 mm, leaving a core of 26 mm diameter. The threaded cylinder was potted in araldite. After allowing the araldite to harden, the one-inch core was drilled out, leaving a helix supported in araldite. The helix was then freed by burning off the araldite.

Two brass bar leads were hard-soldered to each end of the helix. A one-inch diameter steel mandril was made with screw threads at each end. This was greased and then inserted into the helix. Nylon insulation of thickness 0.5 mm was threaded between the turns. Two circular, one inch thick tufnol end plates each with a central hole of one inch were placed at either end of the helix such that the threaded ends of the mandril protruded. Two steel nuts were threaded onto either end of the mandril and were used in order to compress the helix tightly such that neighbouring turns were separated only by the insulation. The purpose of this precompression was in order to reduce any axial rebound which will occur.

There also will be large radial explosive forces due to the presence of high fields. In order to give added strength against these forces the helix was wound on the outside with glass fibre impregnated with araldite.

Each of the tufnol end plates had six O.B.A. clearance holes drilled parallel to the axis and near the circumference. **One** O.B.A. threaded rod **was** inserted into each of these holes. The helix was further

Fig 3.1 The Magnet





Fig. 3.2 The Components of
a Pulsed Magnet

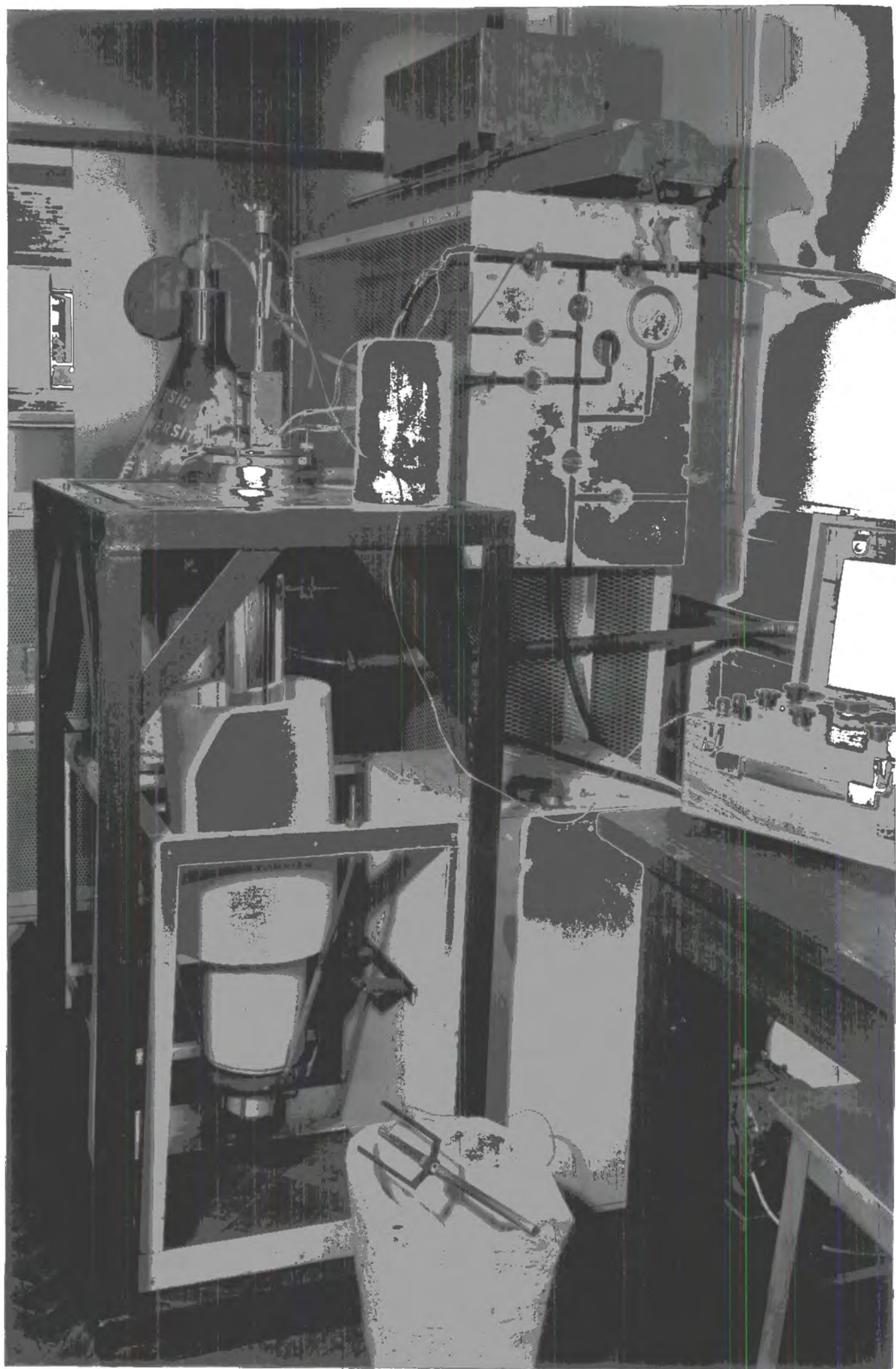


Fig. 3.3 The Pulsed Field Magnetometer

compressed by means of six O.B.A. studs passing through the end plates.

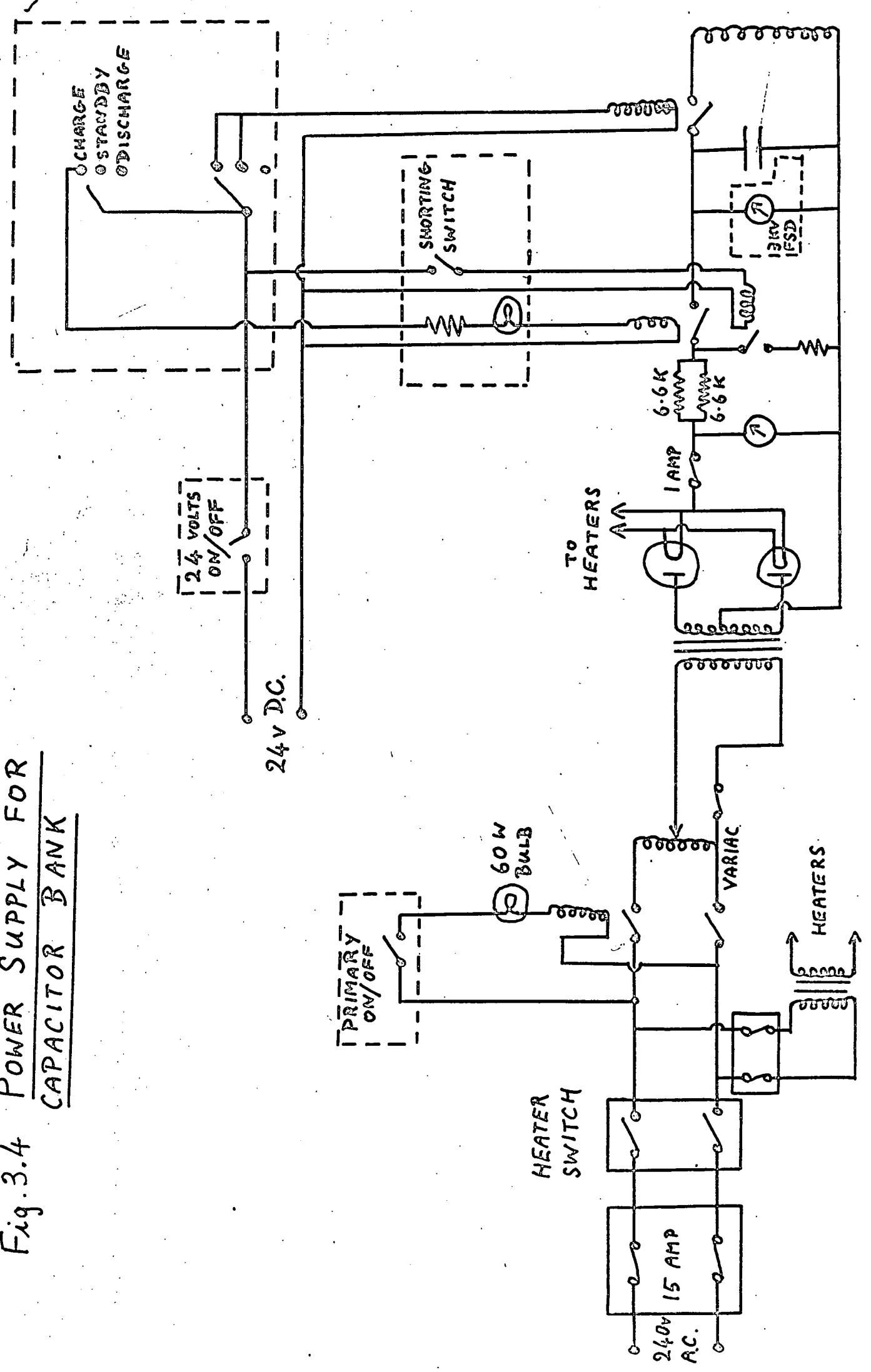
The magnet was held (fig.3.1) with its axis vertical and was supported from above via three tufnol rods whose upper ends were secured to a steel framework. The lower ends of the rods were secured by means of araldite and screws to a ring of tufnol. This ring fitted around the upper end-plate of the magnet to which it was attached by nylon screws. Thus the magnet hung down and was secured from above. This allowed the magnet to be immersed in a bath of liquid nitrogen. As will be noticed above, the magnet when mounted was surrounded in its immediate vicinity only by non-metallic material as far as was possible. This was necessary in order to reduce secondary fields due to eddy currents.

The photograph in fig.3.2 shows the parts of a similar magnet before being assembled. The difference between the magnet in the photograph and that described above are: the length of the helix, the photograph showing a magnet with fewer turns; and the end plates in the photographs being of steel. The mounted magnet can be seen in fig.3.3 which is a general photograph of the apparatus with the liquid nitrogen bath for the magnet removed.

3.1.2 Production of the Magnetic Field

A capacitor bank (2000 μ F) is charged to a maximum of 2KV by means of a power supply whose circuit is shown in fig.3.4. The energy stored in the capacitor is discharged through the magnet via thick brass leads and by means of a mechanical contact switch consisting of two molybdenum plates in air. The plates are brought into contact by means of a D.C. solenoid whose core is mechanically connected to one of the plates. The magnet is immersed in liquid nitrogen when being operated in order to decrease the resistance contributed to the circuit by the magnet, thus increasing the field.

Fig. 3.4 POWER SUPPLY FOR CAPACITOR BANK



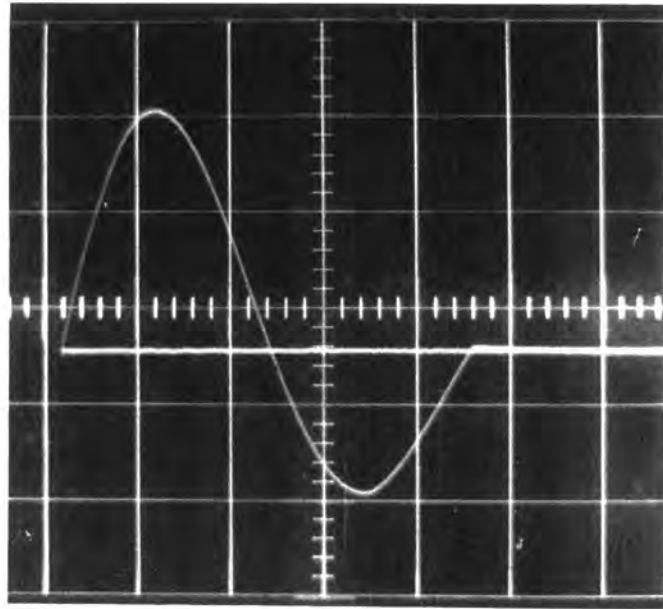


Fig. 3.5 H vs t illustrating sudden cut-off
 (in this pulse the peak field was small)

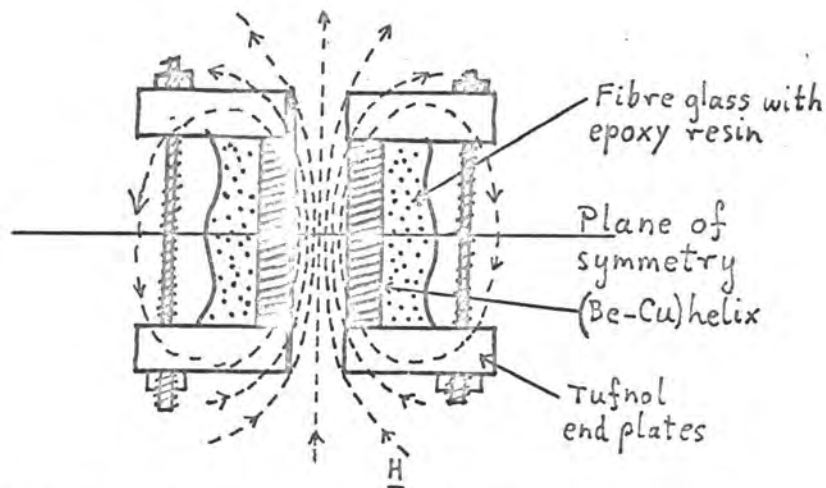


Fig 3.6 Schematic cross-section of Magnet
showing plane of symmetry of Field

3.1.3 The Form of the Magnetic Field

The form of the field as a function of time is ideally given by the solution of the RCL circuit differential equation to obtain the current;

$$I = I_0 e^{-\lambda t} \sin \omega t \quad \dots \dots \dots (1)$$

where $\lambda = R/2L$

and $\omega^2 = \left(\frac{1}{LC} - \frac{R^2}{4L^2} \right)$

The magnetic field is therefore given by

$$H(z,t) = H_0(z) e^{-\lambda t} \sin \omega t \quad \dots \dots \dots (2)$$

at a given position z on the axis. The period of the field is 1.25 ms and the peak field is 160 kOe. The second half cycle has a peak value of -120 kOe.

In practice the form in time of the magnetic field is different from the ideal form for three reasons:

- 1) The Joule heating varies the resistance R during the pulse.
- 2) Eddy currents induced in the metallic helix by the oscillating field contribute to other components of the magnetic field.
- 3) Varying current distribution in the conducting cross-section of the turns may contribute to a further departure from the ideal variation of H as a function of t .
- 4) The switch only conducts when the voltage across it is greater than a threshold voltage. Each oscillation involves a progressively decreasing peak voltage across the switch and when this drops below the threshold value the oscillation is cut off as seen in the oscillogram (fig.3.5). This cut-off can occur as the field approaches zero either negatively or positively. The result is that one rarely obtains more than seven oscillations, the ultimate having a peak of about 3kOe.

The form of the field in space shows a plane of symmetry (fig.3.6). Where this plane of symmetry intersects the magnet axis the field has its maximum uniformity and magnitude.

3.1.4 Theory of Secondary Fields due to Eddy Currents

We must add to the ideal form of the field given in equation (2) extra terms to take into account the secondary magnetic fields due to eddy currents in the metallic helix. The total magnetic field can then be represented approximately by

$$\begin{aligned} H(z,t) &= H_0(z,t) + H_1(z,t) - H_2(z,t) \\ &= H_0(z)e^{-\lambda t} \sin \omega t + H_1(z)e^{-\lambda t} \sin (\omega t + \phi) - H_2(z)e^{-\lambda t} \end{aligned}$$

The first term is the largest and represents the ideal RCL discharge.

The second term is very small compared with the first and has a phase shift of ϕ . The eddy currents are proportional to the voltage induced in any metallic cross-sections and these are given by the differential with respect to time of the main applied field $H_0(z,t)$. Thus the form of the term $H_1(z,t)$ in time is obtained by differentiating $H_0(z,t)$ with respect to time.

The third term is a small arbitrary term which was added in order to maintain the condition $H(z,t) = 0$ for $t = 0$ and $t = \infty$. Thus $H_2(z) = H_1(z) \sin \phi$. A detailed analysis of higher order terms would give a more complicated term for $H_2(z,t)$ than is given here.

All these amplitude terms $H_0(z)$, $H_1(z)$, $H_2(z)$, are a function of the vertical position z on the axis of the magnet. We shall confine ourselves to the axis for the present purposes because that is the region of the field to be used.

Let us examine in this paragraph the situation for which the ratio $H_0(z)/H_1(z)$ and also $H_1(z)/H_2(z)$ is a constant for all z .

The total field can be written:

$$H(z,t) = H_0(z) e^{-\lambda t} \left[\sin \omega t + h_1 \sin (\omega t + \phi) - h_2 \right] \dots \dots (3)$$

h_1 and h_2 are the ratios $H_1(z)/H_0(z)$ and $H_2(z)/H_0(z)$. Simplifying the above equation we obtain:

$$H(z,t) = H_0(z) e^{-\lambda t} (1 + \delta) \sin (\omega t + \phi') - h_2$$

where ϕ' is a function of ϕ and h_1 ; δ is a small quantity, also a function of ϕ and h_1 . As could be seen from equation (3) the variables z and t can be separated and $H(z,t)$ is a product of two functions, one of z and one of t .

The shape of the time variation of the field will not be a function of position. The eddy currents simply contribute to a total phase shift ϕ' .

However, since $H_0(z)$ and $H_1(z)$ have entirely different origins ($H_0(z)$ arises from the main current through the solenoid, $H_1(z)$ arises from eddy currents in the elementary circuits within the cross-section of the turns of the helix depending critically upon the dimensions and orientation of the turns) the ratio $H_0(z)/H_1(z)$ is not likely to be a constant for all z . If it is not a constant for all z then we cannot separate $H(z,t)$ into a product of a function of z and a function of t as we could above. h_1 above will then be a function of z , thus ϕ' the phase shift will be a function of z also. Thus the field as a function of time will not have the same form for different positions z .

The form of H as a function of t may also vary for differing z as a result of another effect; the current distribution within the conducting cross-section of the turns of the helix is not constrained to be of a given form and may vary during the pulse. If it varies in a different way for different parts of the helix then this will give rise to another component of $H(t)$ whose shape in time depends upon z . Either of these two effects could contribute to the difficulty of electronically balancing the pick-up coils as will be seen later.

3.1.5 Repetition Rate

Due to Joule heating during a pulse the magnet will be warmer at the end of the pulse. Thus the resistance will vary. This affects the main field to a very small extent but it has a large effect upon the secondary fields. As will be mentioned later these secondary fields give rise to noise signals, for which corrections are made. In order that these noise signals may be repeatable the magnet must be at the same temperature at the beginning of each pulse. The magnet is immersed in liquid nitrogen while in operation and it was found that a repetition rate of one pulse every 2 minutes was sufficient to render the results repeatable for 160 kOe pulses. For smaller pulses higher repetition rates were admissible, it being sufficient to listen to the boiling of the liquid nitrogen and wait until

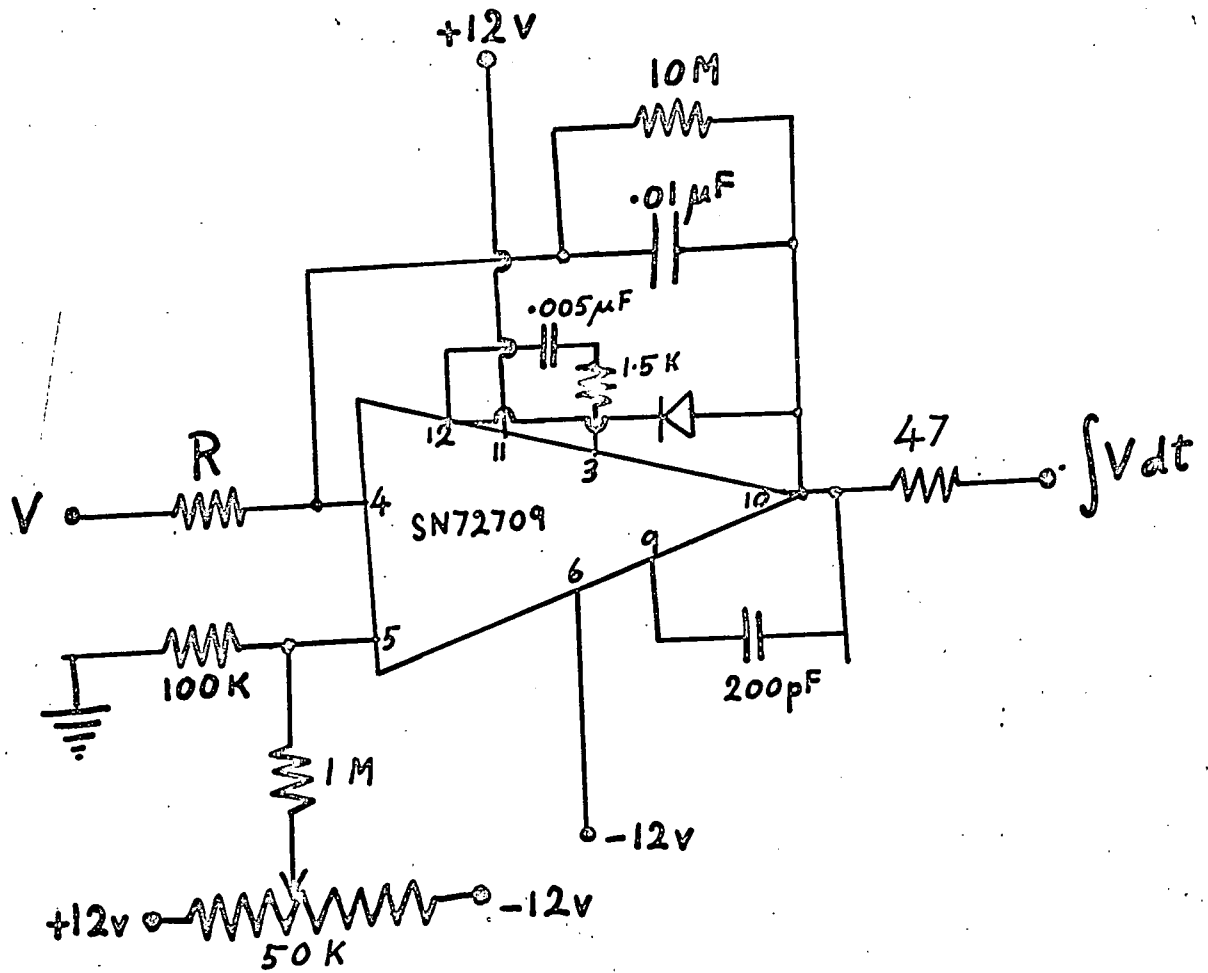


Fig. 3.7 The Integrating Circuit
 $R = 100K$ in the M integrator
 $R = 200K, 100K$ OR $50K$ in the H integrator.

it has dropped to the normal boiling rate before firing the next pulse.

3.2. Magnetic Field Measurements

3.2.1 The H pick-up Coil

The strength of the field applied to the sample is obtained by means of a pick-up coil situated near the sample but not so near as to be affected by the magnetization of the sample. This pick-up coil consists of a total of 30 turns of 44 S.W.G. insulated copper wire wound on a quartz tube of diameter 7.5 mm coaxial with the magnet. The coil is not in the region of maximum field since the sample is in the maximum field region. However since the main component of the magnetic field has a time dependence which is not a function of position the field at a given time t in the H coil is proportional to the field applied to the sample at the same time t .

The H coil is divided into two halves: 15 turns wound above the plane of symmetry of the field and 15 turns wound below this plane. This eliminates any first order dependence of the H signal upon slight vertical movements of the H coil in the magnetic field. Thus if the pick-up coil system is raised slightly the increase of flux in the lower coil is balanced out to first order by an equal and opposite decrease of flux in the upper coil. The signal is therefore not sensitive to slight vertical displacements. The distance between the two halves of the H coil is 3.75 cm.

3.2.2 Integration of the Signal and Sensitivity

The output of the H coil which is proportional to dH/dt is electronically integrated (fig.3.7) to give a signal proportional to the field strength H .

The 50K potentiometer is used in order to adjust the D.C. level of the output. However, it was found necessary to shunt the 0.01 μ F capacitor with a 10 M resistor in order to stabilize the D.C. level of the output. In the absence of the 10 M resistor adjustment of the D.C. level was very difficult and when adjusted to zero it would drift either positively or negatively and within a few minutes would drive itself to a saturating voltage at which the circuit ceased to behave as an integrator. The 10 M Ω shunt allows a

continual leakage of charge to earth so that equilibrium can be set up more easily and the D.C. voltage can be maintained at the desired level. The $10M\Omega$ in combination with the $0.01\mu F$ capacitor results in a charge leakage with a time constant of 100 ms and this is sufficiently long not to distort the required signal during the pulse of period 1.25 ms.

There are three settings for the resistance R in the H integrating circuit: 200K, 100K, and 50K. These influence the attenuation of the H signal, the magnitude of the output being inversely proportional to R. In practice the following H signal sensitivities are obtainable:

CRO X axis setting	R (Ω)	H sensitivity (kOe/cm)
X 1	200 K	34
X 1	100 K	17
X 1	50 K	8.5
X 5	200 K	7.45
X 5	100 K	3.73
X 5	50 K	1.86

As will be noticed the real ratio of the two X-axis sensitivity settings is 4.56 rather than 5 as claimed by the manufacturers.

3.2.3. Triggering the Bright-up of the Oscilloscope Trace

The spot on the oscilloscope screen (Cossor CDU 110) was required to bright up for the duration of the pulse. However it was found that when the mode switch was in the 'X-amp' position the trace was always unblanked so that the brilliance of the spot could only be varied by the brilliance control.

Before triggering bright-up was possible the following modification was required: The blanking circuit was connected to the single sweep time-base, thus blanking the trace until the single sweep is triggered by a signal into the X-amplifier input. The unblanking period is 10 X setting on the time-base control.

The spot will bright up for a trace if the X-coordinate of the spot is set, by adjusting the DC level of the H integrator, to be just to the left of the point at which it will unblank.

Information about the position of the origin of the H axis is obtained by adjusting the unblanking time such that the spot remains bright for a short time after the end of the pulse.

3.2.4 Calibration of the H Signal

Two methods of calibration were used. One consisted of observing the M vs H curve for a substance which has a known critical field. A powder sample of ZnCr_2Se_4 was used. The magnetization of this material rises linearly with increasing field until a critical value of the field (64 kOe) at which it saturates. This behaviour occurs in both pulsed and static fields (ref.3.1). From the magnetization trace the sensitivity of the H signal was directly deduced:

$$34 \pm 1.3 \text{ kOe/cm on (x1, 200K) setting.}$$

From this value was deduced the maximum attainable field:

$$160 \pm 6 \text{ kOe.}$$

The other method which is much less direct consisted of calculating the sensitivity of the H signal from first principles. This required the measurement of many quantities. The accumulation of large errors is therefore inherent to this method which is described as follows.

The relation between $V(t)$ and $v(t)$ the input and output signals of the integrating circuit is given by:

$$v(t) = \frac{1}{K} \int_0^t V(t) dt.$$

K has dimensions of time, and was calculated as follows:

An AC voltage was applied to the input.

$$V(t) = V_0 \cos wt$$

$$v(t) = v_0 \sin wt = \frac{V_0}{wK} \sin wt$$

$$K = \frac{V_0}{w v_0}.$$

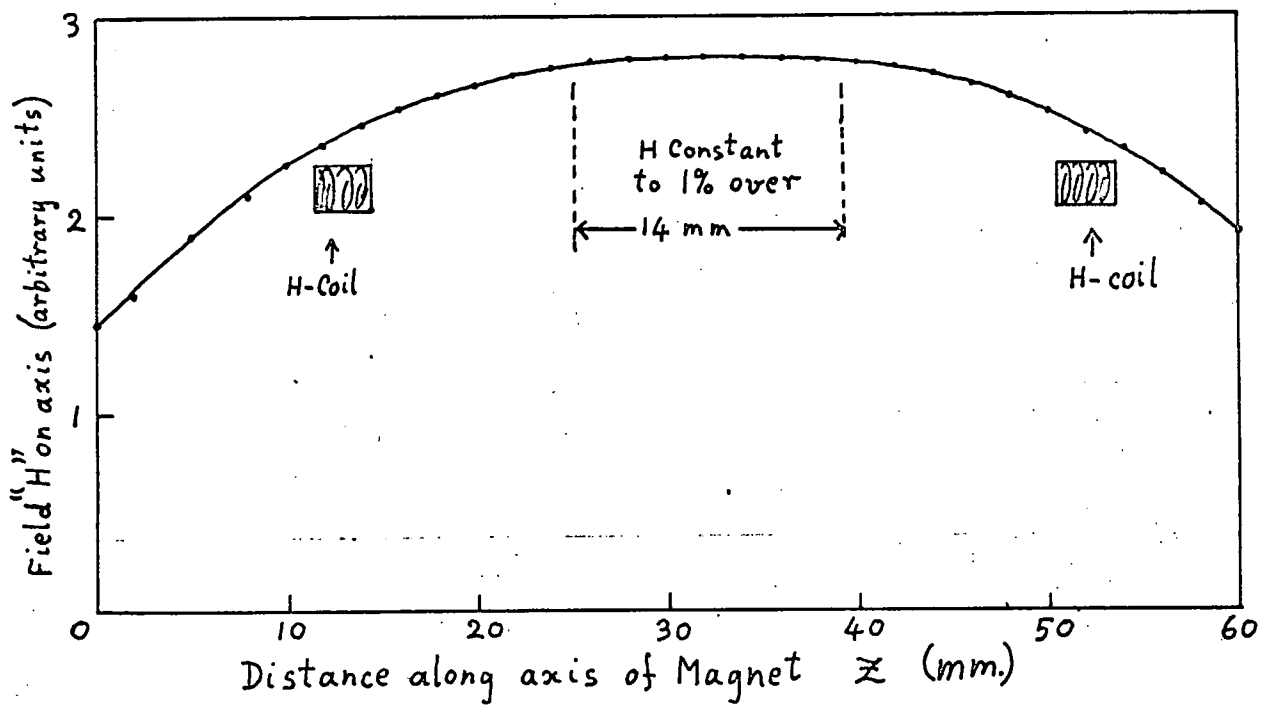


Fig. 3.8 Plot of H vs z along axis of magnet

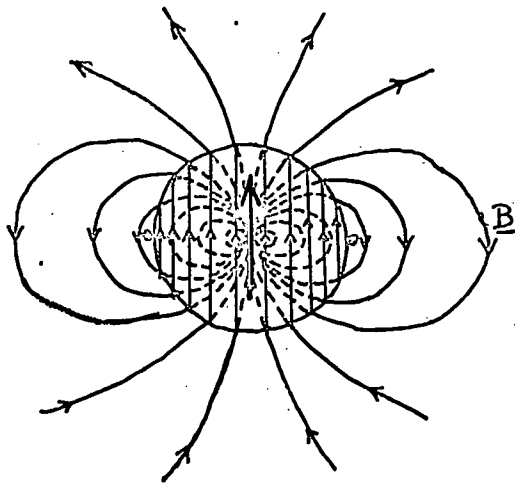


Fig 3.9 Lines of \underline{B} in and around a spherical sample with uniform magnetization \underline{M}

V_o and v_o were measured on the oscilloscope whose sensitivity settings had been checked by a digital voltmeter. The following result was obtained:

$$K = 2.22 \times 10^{-3} \text{ s. } (\pm 10\% \text{ error}).$$

The turn-area nA of the H coil was measured geometrically and was found to be

$$nA = 1.37 \times 10^{-3} \text{ m}^2 (\pm 3\% \text{ error})$$

The field along the axis of the magnet was plotted using a simple pick-up coil with 20 turns. The magnet was powered by AC (50 Hz) and the voltage induced in the pick-up coil was proportional to the amplitude of the field. The voltage was noted for various positions z of the pick-up coil on the axis of the magnet.

The plot of field in arbitrary units as a function of z (fig.38) was used in order to estimate the ratio R which is given by:

$$R = \frac{\text{Field at the sample}}{\text{Field at the H coils}}$$

The value obtained is:

$$R = 1.17 (\pm 4\% \text{ error}).$$

The sensitivity S (volts/cm) of the X input to the oscilloscope was determined by using a digital voltmeter:

$$S = 1.44 \text{ V/cm } (\pm 3\% \text{ error}).$$

The sensitivity (kOe/cm) of the H axis of the oscillogram is given by:

$$\frac{\text{Field}}{\text{X-deflection}} = \frac{K S R}{nA} \times 10 \text{ (kOe/cm)}$$

The result obtained is:

$$27.3 \text{ kOe/cm } (\pm 22\% \text{ error})$$

$$\text{i.e. } 27.3 \pm 6 \text{ kOe/cm.}$$

Since the maximum attainable field corresponded to 4.7 cm deflection:

$$\text{Maximum field} = 128 \pm 29 \text{ kOe.}$$

This is to be compared with the value obtained by the more direct method:
 $160 \pm 6 \text{ kOe.}$

3.3 Magnetization Measurements

3.3.1 Theory of Magnetization Measurement

The flux in a pick-up coil containing a sample is the result of:

- a) The applied field
- b) The magnetic moment of the sample
- c) The demagnetizing field of the sample.

Before the output voltage can be regarded as a measure of the magnetization of the sample the effect of the applied field must be removed such that the total voltage is a result of the presence of the sample only. It must then be ascertained that this voltage, which is a result of the moment and demagnetizing field (both inside and outside the sample) is proportional to the moment. The magnetization can then be determined after calibration if the mass of the sample is known.

The effect of the applied field is removed by putting in series with the pick-up coil containing the sample another pick-up coil wound in opposition to the first such that the total output is zero when no sample is present. The output is then a result only of the presence of the sample.

This section will be devoted to a theoretical consideration of the flux in a coil arising from a spherical sample. The purpose of this is to establish whether the contribution to the flux in the coil due to the sample is proportional to the magnetic moment σ irrespective of the size of the sample. The effect upon this proportionality of varying the shape can only be treated empirically and will be done in the section on calibration. The definition of σ used is

$$\sigma = \mu_0 I S$$

where I is the current in amperes flowing in an elementary circuit of area S in m^2 . (In some literature μ_0 is omitted).

The contribution to the output of the pick-up coil due to the sample depends on the rate of change of the lines of induction due to the sample. These are shown in fig 3.9 for a spherical sample of magnetic moment σ and uniform magnetization M parallel to the axis of a coil of one turn placed

concentrically with the sample. Let the radius of the coil be R and that of the sample be a .

The flux contribution from inside the sample is given by

$$\begin{aligned}\Phi_i &= \int_0^{\pi a^2} \underline{B} \, dS \\ &= \frac{2}{3} M \times \pi a^2 \\ &= \frac{2}{3} \frac{\sigma}{\frac{4}{3}\pi a^3} \times \pi a^2 \\ \Phi_i &= \frac{\sigma}{2a}\end{aligned}$$

since the demagnetizing field inside a spherical sample is $-\frac{1}{3}\underline{M}$ so that \underline{B} within the sample is given by

$$\underline{B} = \mu_0 \underline{H} + \underline{M} = -\frac{1}{3}\underline{M} + \underline{M} = \frac{2}{3}\underline{M}.$$

The flux contribution from the area between the sample and the coil is given by

$$\Phi_o = \int_a^R \underline{B} \, dS.$$

To obtain a value of the field outside the spherical sample of moment σ one can imagine the entire sample to be replaced by a small dipole of moment σ situated at the centre of the sample. Therefore

$$\Phi_o = - \int_a^R \frac{\sigma}{4\pi r^3} 2\pi r \, dr$$

where r is the distance from the centre of the sample in the plane of the coil.

$$\begin{aligned}\Phi_o &= -\frac{\sigma}{2} \int_a^R \frac{1}{r^2} \, dr = \frac{\sigma}{2} \left[\frac{1}{r} \right]_a^R \\ \Phi_o &= \frac{\sigma}{2R} - \frac{\sigma}{2a}.\end{aligned}$$

Therefore the total flux in the coil is given by

$$\begin{aligned}\Phi &= \Phi_i + \Phi_o = \frac{\sigma}{2a} + \frac{\sigma}{2R} - \frac{\sigma}{2a} \\ &= \frac{\sigma}{2R}\end{aligned} \quad \text{--- Eqn. 3.1}$$

This is independent of the size of the sample.

This could have been deduced considering only the dipole field outside the sample and not considering the flux inside the sample, by recalling that lines of \underline{B} are continuous. Thus all the lines of \underline{B} which thread the coil must be conserved outside the coil as well.

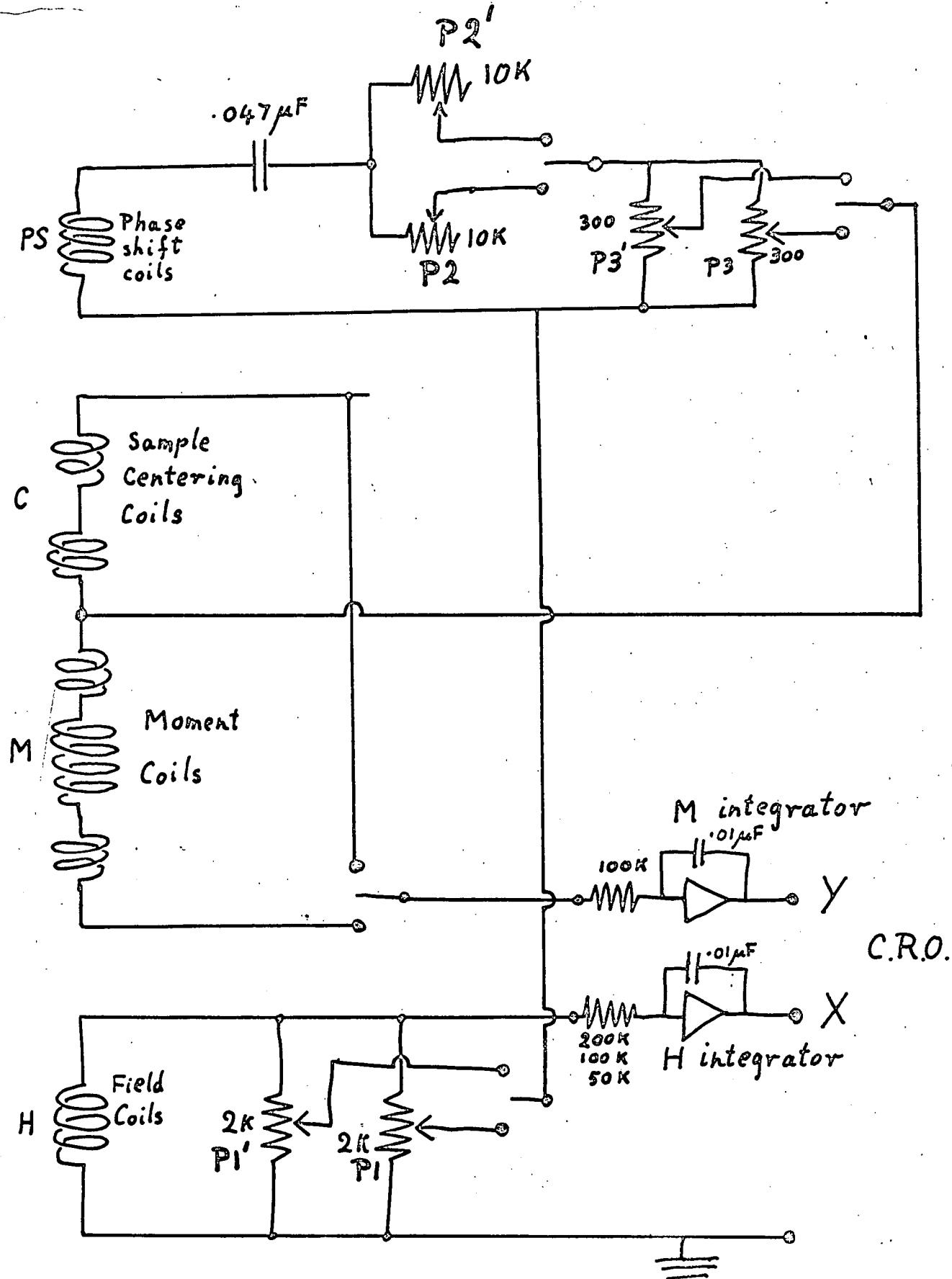
Thus the same answer should be obtained in integrating \underline{B} from the coil to infinity:

$$\begin{aligned}\Phi &= \int_R^\infty \frac{\sigma}{4\pi r^3} 2\pi r dr \\ &= \frac{\sigma}{2} \int_R^\infty \frac{1}{r^2} dr = -\frac{\sigma}{2} \left[\frac{1}{r} \right]_R^\infty \\ \Phi &= \frac{\sigma}{2R} .\end{aligned}$$

It has been shown that, despite the demagnetizing field, the induced signal in the pick-up coil is a measure of the moment. In fact it is evident that this fortunate state of affairs is due to the demagnetizing field. It is only because of the demagnetizing field that the two terms in equation 3.1, depending on the size of the sample, cancel out. Thus it is conceivably possible that, for samples of various sizes which are not spherical the voltage induced in the pick-up coil might be a measure of σ . This can only be investigated empirically by a calibration experiment, as was done later.

3.3.2. The Moment Pick-up Coil System

The moment pick-up coil system consists of two coils A and B wound in series and in opposition. This is wound between the two components of the H coil already described. The fluxes in coils A and B are balanced to give approximately zero output in the absence of a sample. The sample is placed in the centre of coil A in the field region of maximum strength and uniformity. Since coil B occupies a different position on the axis the coil B is in a region with a field gradient. It was therefore divided into two halves and each half placed symmetrically above and below coil A, for the same reason for which the H coil was divided, i.e. to reduce the sensitivity of the signal to slight vertical displacements of the pick-up coil system.



Magnetization and Field Detection System (Fig.3.10)

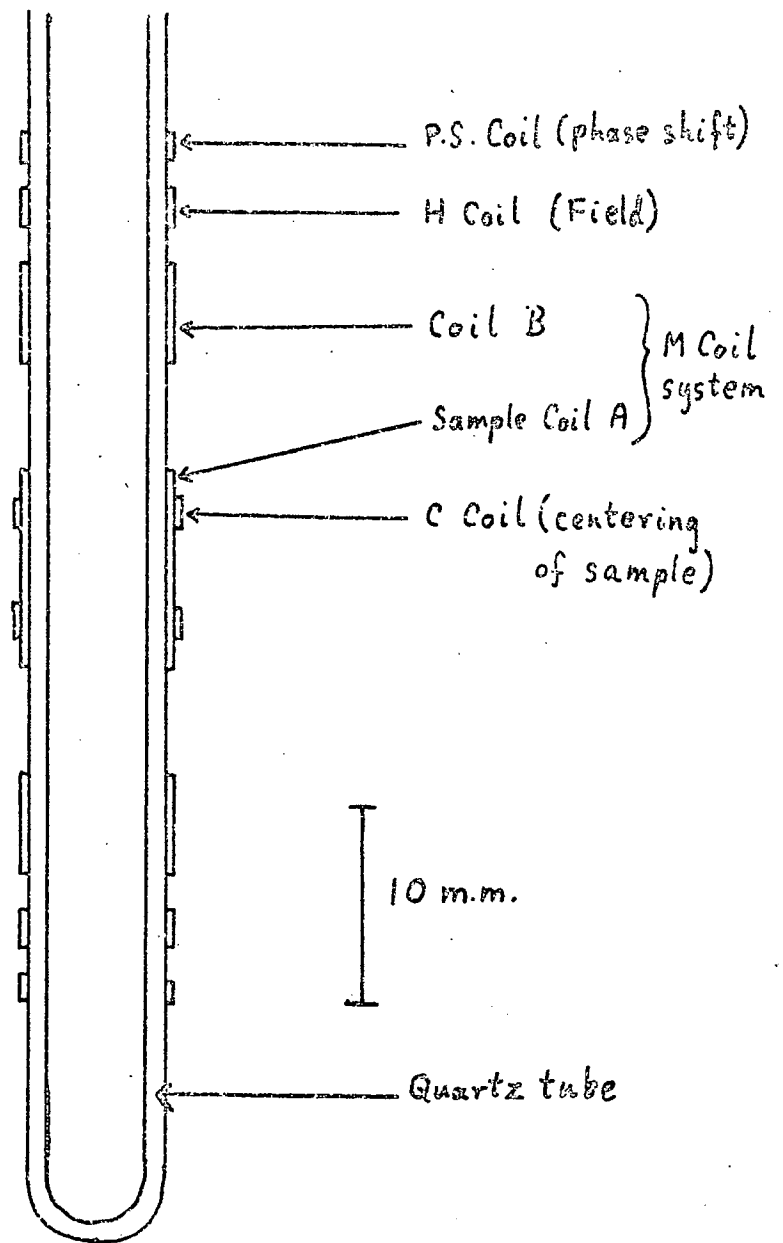


Fig. 3.11 Pick-up Coil System (drawn to scale)

As regards the shape of the coils the only coil whose shape matters is coil A. It was made sufficiently long (8 mm) for the M signal not to be too sensitive to the vertical position of the sample.

The balancing of coils A and B was only done approximately: by winding 70 turns for coil A and 35 turns for each half of coil B. The final balancing was done electronically by tapping off from potentiometer P1 the required quantity of signal from the H coil and adding this to the M signal as shown in fig.3.10 which gives the entire circuit for the M and H detection system.

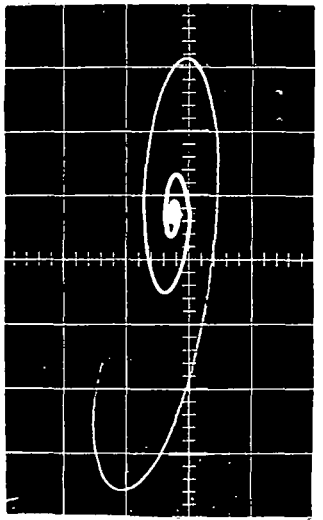
Coil B is not as far from the sample as the H coil since it does not matter if coil B is influenced by the moment of the sample, the result will only be a slight reduction in the M signal which will be taken into account by calibration. All that is required is that coil A be more strongly affected by the sample than coil B. Fig.3.11 gives the dimensions of the pick-up coil system.

3.3.3 Eddy Current Noise and its Elimination

As shown in 3.1.4 the shape of the H vs t function varies from place to place along the axis of the magnet when one takes into account the effect of eddy currents. Hence accurate balancing of the signal from coil A against the signal from coil B is impossible since one is attempting to balance out two signals of different shape in time.

The desired M vs H display in the absence of a sample is a horizontal straight line, the gradient of the trace being adjusted to be horizontal by fine balancing using the H potentiometer P1. However, as a result of eddy currents in the magnet the no-sample trace has an elliptical appearance as shown in fig.3.12. This is consistent with a phase difference of the field in coil A with respect to coil B.

This elliptical component is eliminated by opposing it with an equal and opposite signal. This signal is obtained by shifting the phase of the output of another pick-up coil (the phase-shift coil). The output of this PS coil is applied to a phase shift circuit (see Fig.3.10) which consists



Y-Sensitivity
 ← 10mV/cm →

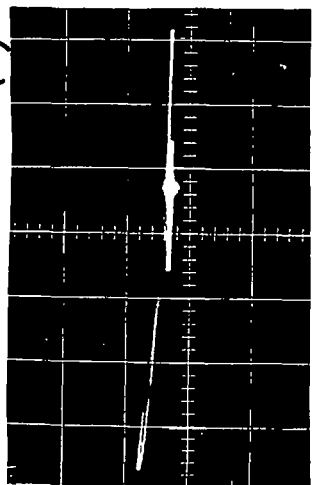
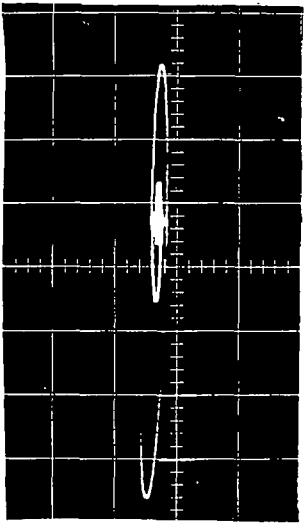


Fig. 3.13 M vs H with Phase Correction
 (a)(b) No Sample (4.2K)
 (c) Fe Sample at 4.2K (93.5 mg Powder)



Y-Sensitivity
 ← 50mV/cm →

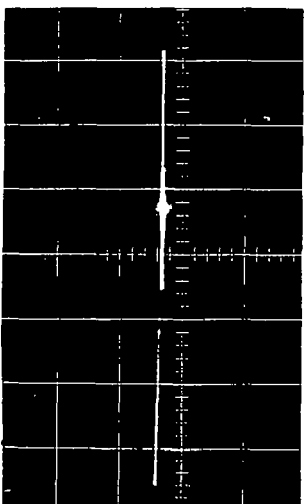


Fig. 3.12 M vs H with No Phase Correction (no sample) (T = 4.2K)

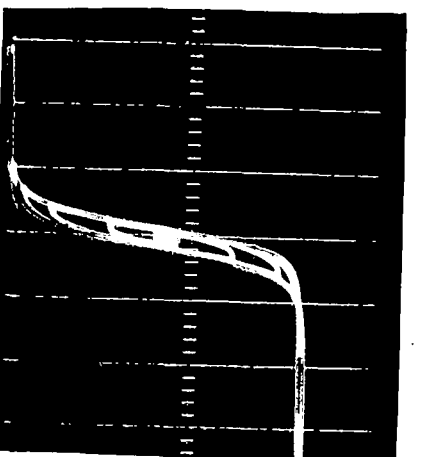
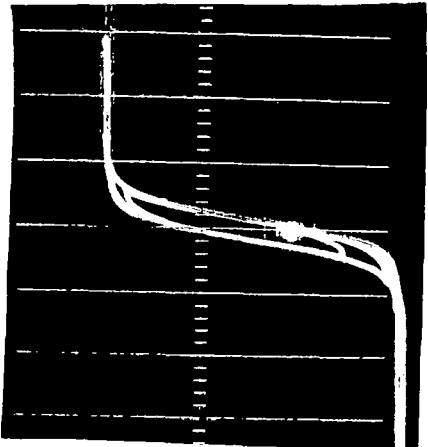
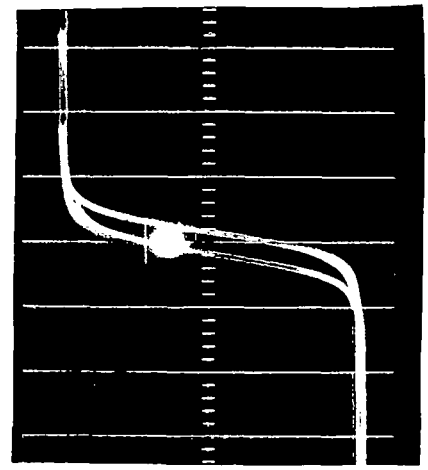
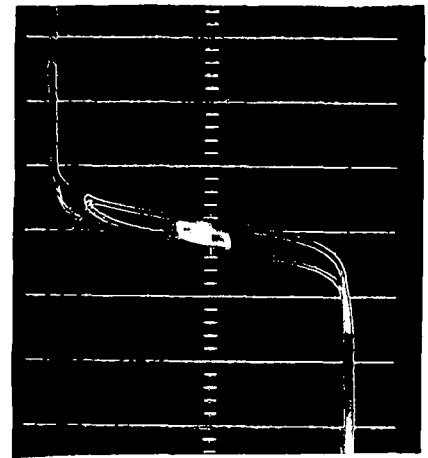
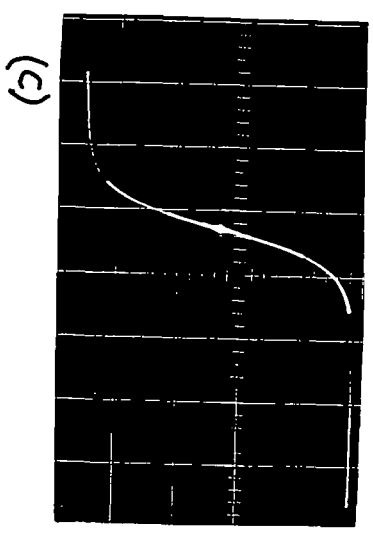


Fig. 3.14 Sequence of M vs H Curves of YCo₃Ni₂ (4.2K, Powder) illustrating effect of Remanence

of an R and C in series. The PS signal is taken from a potentiometer which is part of the R component of the phase-shift circuit. This RC circuit is a differentiator if $RC \ll 1$. However since we do not require strict differentiation, the phase shift (less than $\pi/2$) is set to the required value by adjusting the R of the circuit by means of the potentiometer P2. The amplitude of the phase correction signal is adjusted by P3. P2 and P3 are adjusted to give a no-sample trace which is as close to a horizontal straight line as possible. This optimum situation is shown in fig 3.13 which is on the same sensitivity ranges as fig 3.12. It was not possible to reduce the eddy current noise any further. This noise is superposed upon the magnetization vs field trace when a sample is inserted into the M coil system and was subtracted from the trace to obtain the M vs H graph for every sample studied (see section 3.3.8). For samples of large moment the sensitivity of the Y axis could be reduced such that the noise signal was negligible.

3.3.4 Samples with Remanence

As shown earlier the magnetic field oscillates a finite number of times finally approaching zero either positively or negatively at which point the oscillation ceases. Thus a ferromagnetic sample will be left with a remanence which can be positive or negative. The final position of the spot at the end of a pulse is a measure of this remanence but if the brightness of the spot is continued for a time greater than 100 ms after the end of the pulse it will be seen to drift exponentially down to its normal position due to the leakage of charge from the output of the M integrator down to earth as mentioned earlier.

Now if this sample with a remanence is subjected to another pulse the spot starts at the normal position but this normal position now represents the remanence and the origin of the M vs H curve will not be coincident with the normal position of the spot. Thus from pulse to pulse the M vs H curve may be displaced by a vertical distance which cannot be predicted, and is a result of the sign and magnitude of the remanence after each subsequent pulse. Such a sequence of magnetization curves is shown in fig 3.14.

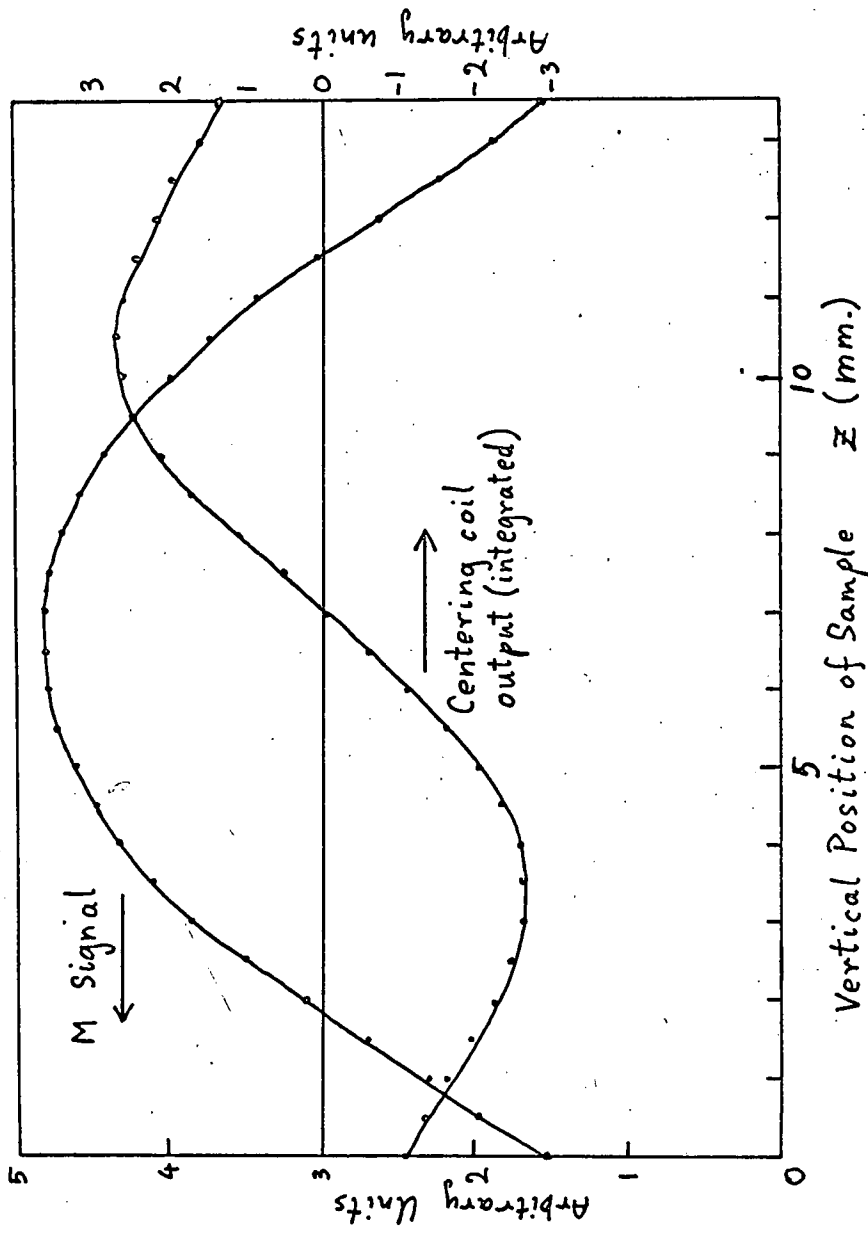


Fig 3.15 M-signal and Centering Coil Output vs Z

(Sample used was $Y_2(Fe_4Co_6)_7$ whose remanence was negligible, the M-signal was that for saturation)

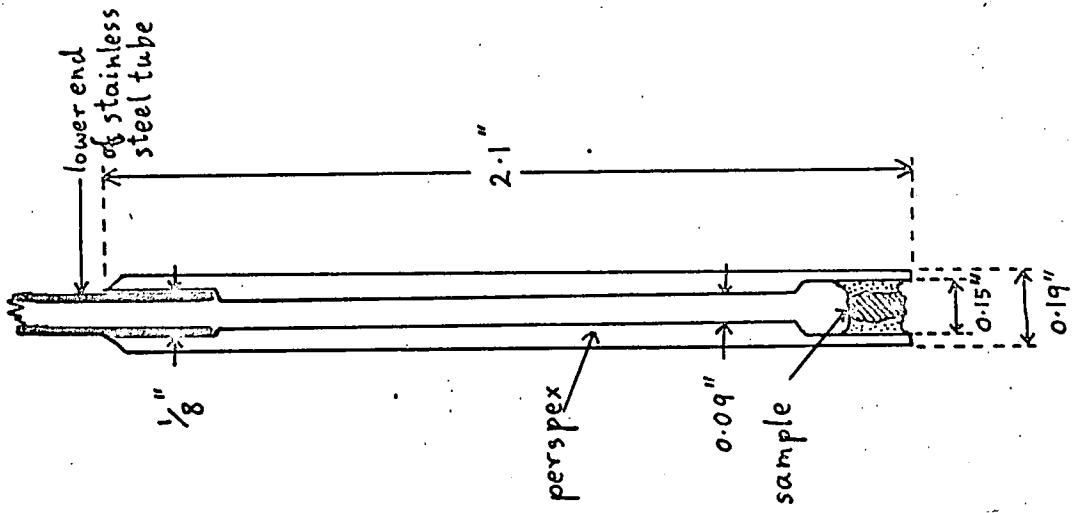


Fig 3.16 The Sample Holder

The reason for this phenomenon lies in the method of measuring M . The induction of a voltage in the pick-up coil gives a measure only of changes in M during a pulse and hence does not give a measure of the absolute value of M .

3.3.5 Centering of the Sample

The use of the calibration factor of the M coil system is meaningful only for a sample in the centre of coil A where the induced voltage due to the sample is a maximum and unique. It was found to be very tedious to adjust the sample position to give a maximum M signal before taking a photograph of the M vs H curve. The spot had to be placed to the left of the ordinate of the graticule and the vertical reading of where the trace crossed the ordinate was noted for different positions z of the sample on the axis of the magnet. The position had to be adjusted to give a vertical reading corresponding to a maximum signal.

In addition to being tedious this method was impossible for samples with remanence, since the vertical reading was apparently random and changed when the position of the sample had not been altered.

The method adopted for centering the sample is based upon the fact that it is easier to detect when a signal is zero than to detect when it is a maximum. This method also made possible the centering of samples with remanence. A pair of coils each with 15 turns were wound in opposition on top of coil A such that they were symmetrically above and below the intended position of the sample.

When centering the sample the M integrating circuit is switched from the moment coils to this pair of coils. The output of these centering coils (C coils) after integration is displayed on the Y axis of the oscilloscope instead of the M signal. When the sample is at the desired position in the centre of coil A the Y signal from the C coils is zero. The reliability of the C coils was checked by means of a sample with negligible remanence. The position of the sample for which the M coil gave maximum response was found to coincide closely with the C coils giving zero response (fig 3.15). When using

the C coils the trace appears as a $+M$ vs H curve if the sample is too high and $-M$ vs H if too low. Consequently the correct position is found with ease. When the output has been nulled the Y axis is switched back to the M coil and a photograph of the M vs H curve taken.

The output of this centering coil is also subject to eddy current noise. The gradient of the trace sometimes has to be corrected to zero in the absence of a sample. Thus the C coil has its own three potentiometers equivalent to P_1 , P_2 and P_3 for the corresponding corrections of the M signal. These are P_1' , P_2' , and P_3' (fig. 3.10). Switching between using the M coil and using the C coil is done by simultaneous operation of the four switches (fig. 3.10). The eddy current noise corrections and gradient corrections to the centering signal are not very important, since it is not difficult to observe where the sample ceases to have any effect upon the trace, even when a noise signal is present.

3.3.6 The Sample and Sample Holder

Two types of sample were used: bulk polycrystalline material of unspecified shape or powder samples of cylindrical shape.

The sample holders (fig. 3.16) were made from $3/16$ inch diameter perspex rod. A hole was drilled down the centre to allow access for the thermocouple. The top end fitted tightly over the end of a $1/8$ inch diameter stainless steel tube. The sample was placed in the lower end of the sample holder.

Bulk samples were obtained by breaking a button to obtain a sample piece whose length was no greater than 4 mm, and which fitted into the sample holder. This was weighed and then secured by Durofix cement into the sample holder.

In some cases powder samples were required. Various reasons were:

(a) Eddy currents induced in a bulk sample whose conductivity was high would interfere with the magnetization-field trace giving rise to a false hysteresis. This was of the same form as the eddy current noise and always resulted in increasing the area of a genuine hysteresis loop.

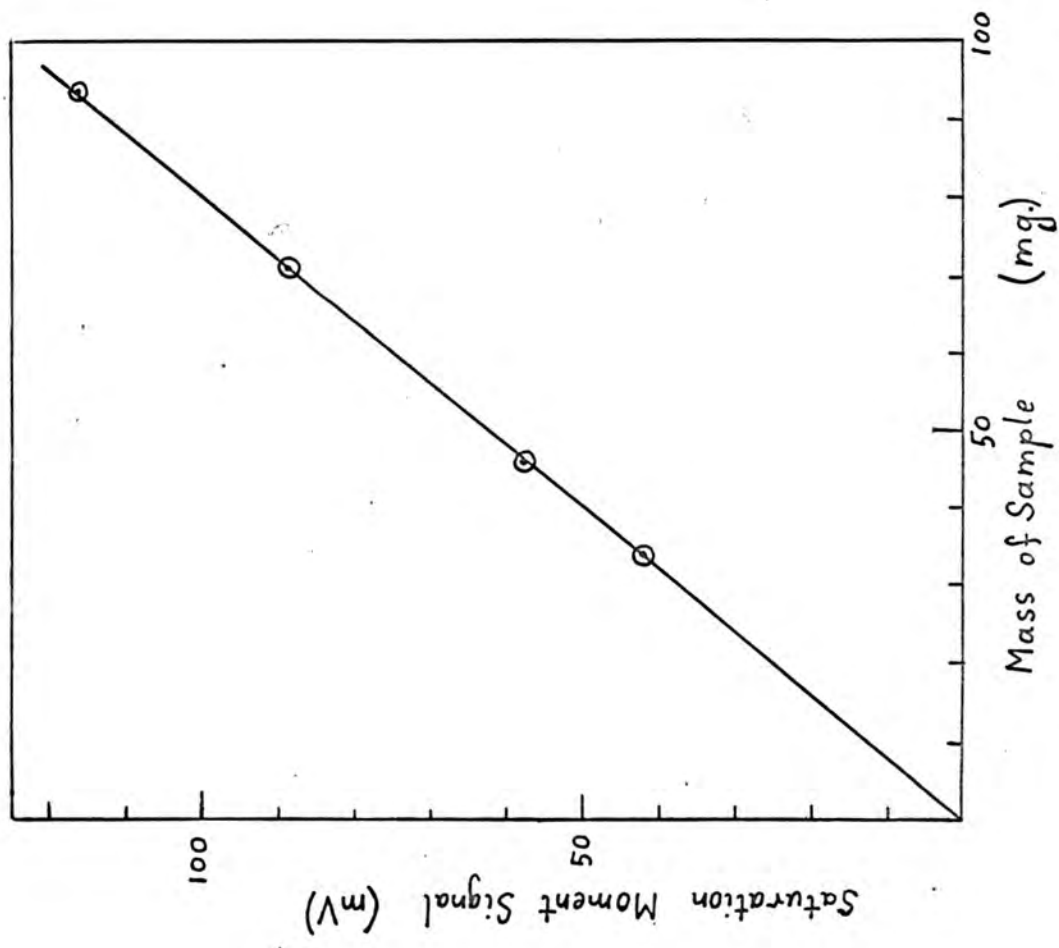
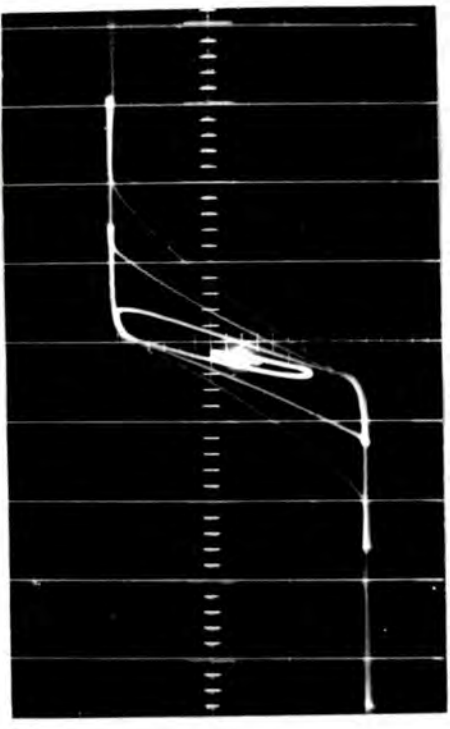
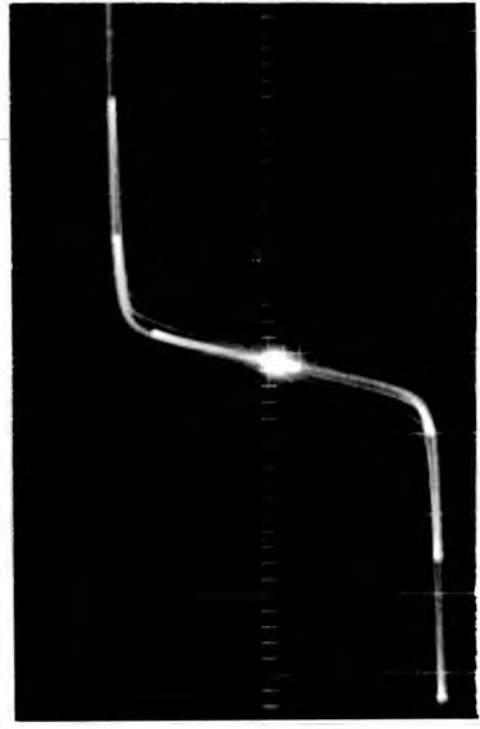


Fig. 3.17a Calibration Graph (sample = Fe Powder at 4.2K length of 93.5mg sample ~ 3mm)



Pure Iron



YFe₃ (multiphase)

Fig. 3.17b M vs H for two Bulk Samples containing free Iron (4.2K, l cm = 7.45 KOe)

(b) For strongly anisotropic samples a magnetization vs field curve could only be made to approach saturation by powdering the sample in the hope that each grain would be a single crystal which could orient its easy direction with the applied field if it was free to move.

The method of mounting a powder sample was as follows: The upper end of the sample cavity was blocked with a small pellet of plasticene which was squeezed, in order to present a flat surface to the sample cavity, by means of a perspex piston which just fitted into the diameter of the specimen cavity. The sample holder with plasticene was weighed. Then the powdered sample was poured into the sample holder to a depth of no more than 4 mm.

The sample holder with powder was then reweighed to obtain the weight of the sample. A short perspex stopper was lowered into the sample cavity till it just touched the powder but without compressing the powder, so that the grains were still free to orient themselves. This stopper was then secured by Durofix cement.

3.3.7 Calibration of the M signal

Calibration was done using samples of iron whose saturation moment is known (ref. 3.1). Due to eddy currents in iron at low temperatures bulk samples could not be used. Powder samples were used instead. In 3.3.1 it was mentioned that the effect of the shape of the sample upon the calibration factor could only be determined empirically. The following calibration experiment was therefore performed.

Several cylindrical samples whose shapes were varied by varying the length-to-diameter ratio were made with constant diameter equal to that of the sample cavity. A trace of M vs H was photographed for each of this series of samples and the signal corresponding to the saturation moment was measured for each sample. The voltage corresponding to the saturation moment of each sample was plotted against the mass of each sample (fig. 3.17a). The useful region of the curve is the linear part and the maximum length of a sample is 4 mm if one is not to depart from linearity by more than 1%. The eddy current effect for solid iron samples is evident in fig. 3.17b.

From the gradient the calibration factor 0.0317 was deduced and was used in the following formula:

$$M = \frac{0.0317 \times (\text{Molecular Weight}) \times (\text{Signal in mV})}{(\text{Mass in mg.})}$$

where M is the magnetization of the specimen in Bohr magnetons per molecule of the sample. The molecular weight is taken to be the weight per formula unit.

On further increasing the length of the sample the signal vs Mass curve reaches a maximum after which the signal decreases as the sample enters the coils B which are wound in opposition to coil A.

3.3.8 The M vs H curve and its Analysis

The photograph of the M vs H curve is obtained together with the corresponding photograph of a base-line curve (ie. with no sample). The two photographs are projected onto graph paper and the base-line curve subtracted from the sample curve in order to obtain a graph of M vs H. There is however still some uncertainty as to the position of the level corresponding to $M = 0$. The position corresponding to $H = 0$ is known from the final position of the spot. The vertical position of the origin can be obtained as follows: If the moment of the sample saturates positively and negatively in the applied field then the level for $M = 0$ is half way between the two saturation levels $+M_{\text{sat}}$ and $-M_{\text{sat}}$. If the moment of the sample does not reach saturation then use is made of the symmetry of the high field **position** of the magnetization curve in order to deduce geometrically the position of the origin.

Errors in measuring the moment arise from the following factors: Parallax in the apparent position of the trace with respect to the graticule as seen by the camera gives rise to an error of +2% at most. Distortion of the trace due to projection of the photograph results in an error which is small compared with the graticule markings. The largest error arises from the finite thickness of the trace, this thickness depending on the speed at which the spot traces out the curve. This error is of the order of the

distance between the graticule markings and is about 1mm in measuring the position of the trace. This contributes a $\pm 4\%$ error in measuring a typical magnetization signal.

For measurements of critical fields the main error arises from the original calibration of the H axis.

3.3.9 Estimation of the Ionic Moment

The spontaneous magnetization at absolute zero gives a measure of the magnetic moment on the magnetic ions in a given sample. This magnetic moment is a quantity of primary interest in this work. Since the magnetic ordering temperatures of the majority of the samples studied were well above 4.2K, the temperature at which measurements were made, the spontaneous magnetization at 4.2K was equated to the spontaneous magnetization at absolute zero with little error.

If the magnetization saturated within the range of the available field values then the saturation magnetization was equated to the spontaneous magnetization. In the case of the magnetization-field curve not showing saturation the cause of the non-saturation was suspected to be either (a) high magnetocrystalline anisotropy preventing alignment of domain magnetizations with the applied field or (b), that the applied field was increasing the value of the magnetization within a domain before having aligned it completely. In the latter case on increasing the field after having aligned all the domains the magnetization would further increase, exceeding the value of the spontaneous magnetization.

In many cases saturation was achieved by performing magnetization-field measurements on powdered samples whose grains were free to rotate. It was then assumed that the powder was sufficiently fine for each grain to be a single crystal whose easy axis was free to orient itself with the applied field, and that the cause of the non-saturation of the corresponding bulk specimen was (a) above.

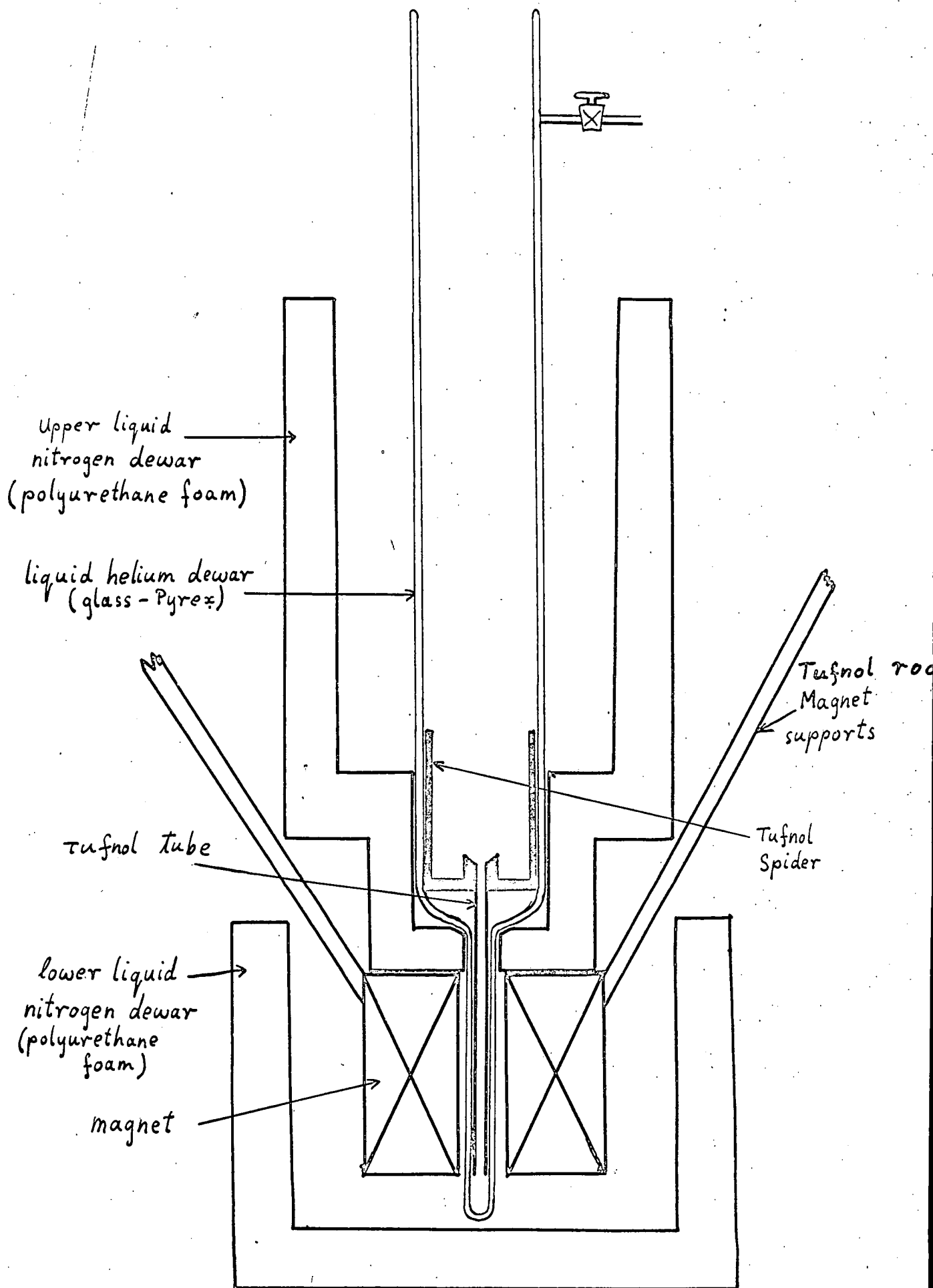


Fig. 3.18 The Dewar System

When saturation was not attained with a powder sample it was possible that the powder was not sufficiently fine to be of single crystal grain-size. Thus either or both (a) or (b) could be applicable. The estimation of the spontaneous magnetization depended upon a decision between these two possibilities.

The usual procedure for a non-saturating sample is to plot M against $1/H$ or $1/H^2$. If such a plot shows linearity in the high field region then the extrapolation to $H = \infty$ gives the saturation magnetization. This extrapolation is not valid for very high fields since contributions to the magnetization arising from increasing the modulus of the domain magnetization or paramagnetic contributions can cause departure from linearity. It is thus difficult to decide in which range of field values such extrapolation is valid.

If it is suspected that the only cause of non-saturation of a sample is (b) then the procedure is to examine the high field portion of the M vs H curve. If a linear portion up to the highest applied field is observed then the extrapolation of this portion to $H = 0$ gives the value of the spontaneous magnetization.

The choice of which of these two extrapolations to use for a given sample requires some knowledge of the magnetic properties of the sample. The relevant properties are the strength of exchange interactions, the magnitude of magnetocrystalline anisotropy and the magnitude of the ionic moment. Therefore justification for the employment of a given extrapolation for a sample will be given in the relevant part of the results section.

3.4. Temperature Control and Measurement

3.4.1. The Cryostat

The cryostat (fig. 3.18) was designed for containing liquid helium in order to measure the magnetic properties of a sample from 4.2°K up to room temperature. Because the magnet was operated while immersed in liquid nitrogen the liquid helium dewar tail was designed to fit closely into the magnet. There was no need for a nitrogen dewar tail to fit into the magnet which would have required a larger field volume and consequently lower field strengths. The

tail of the glass liquid helium dewar protruded through a hole in the bottom of the upper nitrogen dewar which was required for keeping the liquid helium dewar surroundings as cold as was practical to prevent a large boil-off rate of helium.

The upper liquid nitrogen dewar was machined out of polyurethane foam. Leakage of liquid nitrogen through the hole in the bottom through which protruded the helium dewar tail, was eliminated by the application of vacuum grease which froze at liquid nitrogen temperatures and was an effective seal.

The lower liquid nitrogen dewar was used for surrounding the magnet with liquid nitrogen. This dewar was also made of polyurethane foam. When in operation the liquid level in the lower dewar reached to the upper nitrogen dewar.

3.4.2. The Heater

Because of the need to wait 2 minutes between every 2KV discharge it was essential in a temperature run to be able to control the rate of temperature rise. This was possible by means of the heater coil which was of constantan wire wound non-inductively upon a tufnol tube which fitted around the outside of the pick-up coil system. The tufnol tube was attached to the centre of a spider (fig.3.18) which rested at the bottom of the helium dewar just above the tail. Voltage for the heater coil was obtained from a 6-volt filament transformer powered by a variac. The heater contributed some 50 Hz pick-up to the M signal but this was too small to be troublesome. The power was adjusted by the variac and could give a maximum of 7 watts. An ammeter was used for monitoring the current in the heater coil.

3.4.3 Temperature Measurement

This was done by means of thermocouples. Two thermocouples were available. One was of copper: constantan for use at temperatures above 77°K. The other was of gold-copper: copper for use between 4.2°K and 77°K. The reference junction was in liquid nitrogen and the thermo-emf was measured by a Pye Portable Potentiometer in conjunction with an external Scalamp galvanometer.

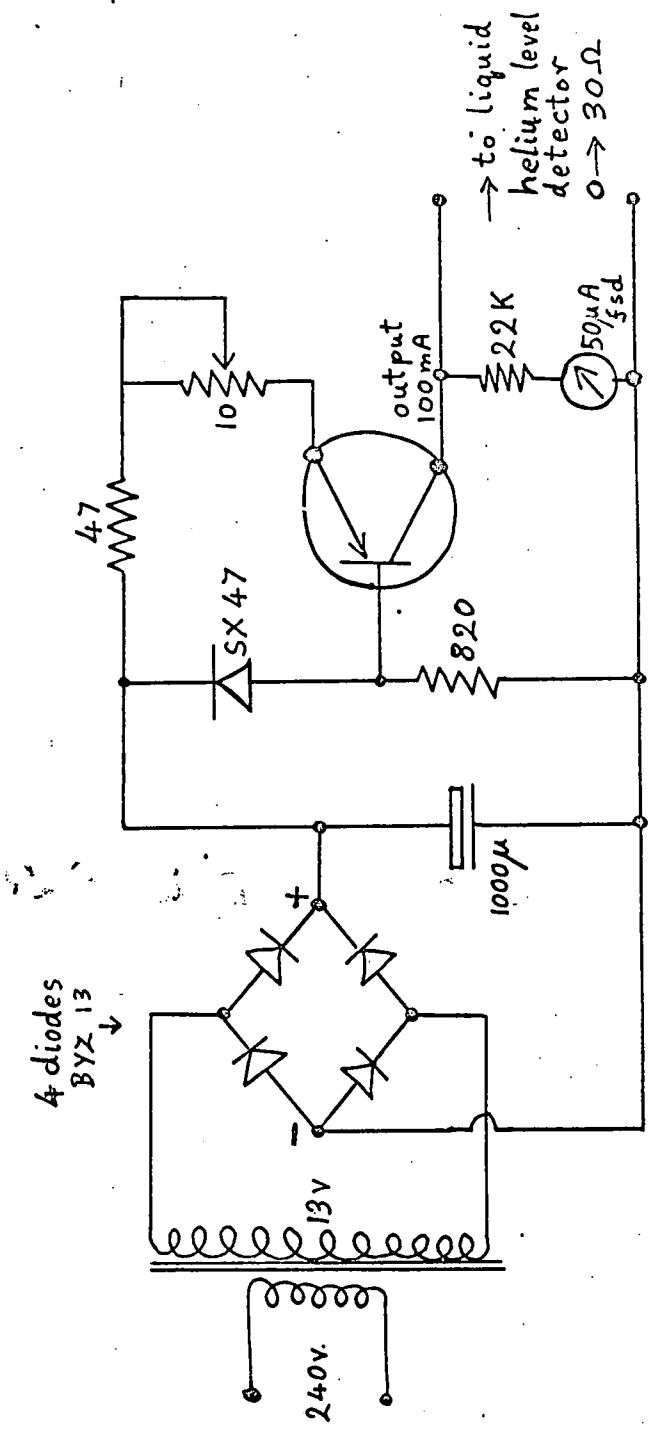


Fig 3.19 Constant Current Supply for Liquid Helium Level Detector

When high M signal sensitivities were used an eddy current noise signal appeared due to the presence of the thermocouple near the sample in the pick-up coil system. This could be eliminated by lifting the thermocouple junction out of the pick-up coils so that it was a few inches from the sample. This method was of course useful only when making measurements at a constant temperature, for example, at 4.2K so that one could be sure that if the thermocouple was below the liquid helium level and reading 4.2K then the sample, also below this level, was at 4.2K.

3.4.4 Liquid Helium Level Detection

This was done either by raising the sample to detect the liquid surface by means of the thermocouple or by using a superconducting wire connected to a constant current supply (fig.3.19) such that the superconducting wire was in parallel with a 22K resistor. The onset of superconductivity was detected by the micro-ammeter in series with the 22K resistor, the current in the 22K then dropping to zero when the entire wire became superconducting. The superconducting wire was made by coating a constantan wire with soft solder, which is a superconductor below the temperature of liquid helium. This wire extended 10 cm up one of the three spider legs (fig.3.18) and a measure of quantity of liquid helium in the cryostat could be obtained from the micro-ammeter reading. Due to temperature cycling the superconducting wire deteriorated and required frequent replacement.

3.4.5 Temperature Runs

Reliable temperature runs were possible only for samples in bulk form. For a powder sample close contact between sample and thermocouple was not possible due to the form of the specimen holder (3.3.6). Temperature runs were performed while the sample was warming, the rate of warming being controlled by the heater coil. A photograph of the M vs H curve was taken every few degrees. It was sometimes found that the base line to the M vs H curve changed slightly in gradient as the temperature rose. However, taking a photograph of the base line trace between every M vs H trace as the temperature rose involved raising the sample out of the pick-up coils. This disturbed the temperature equilibrium and was therefore not the adopted procedure.

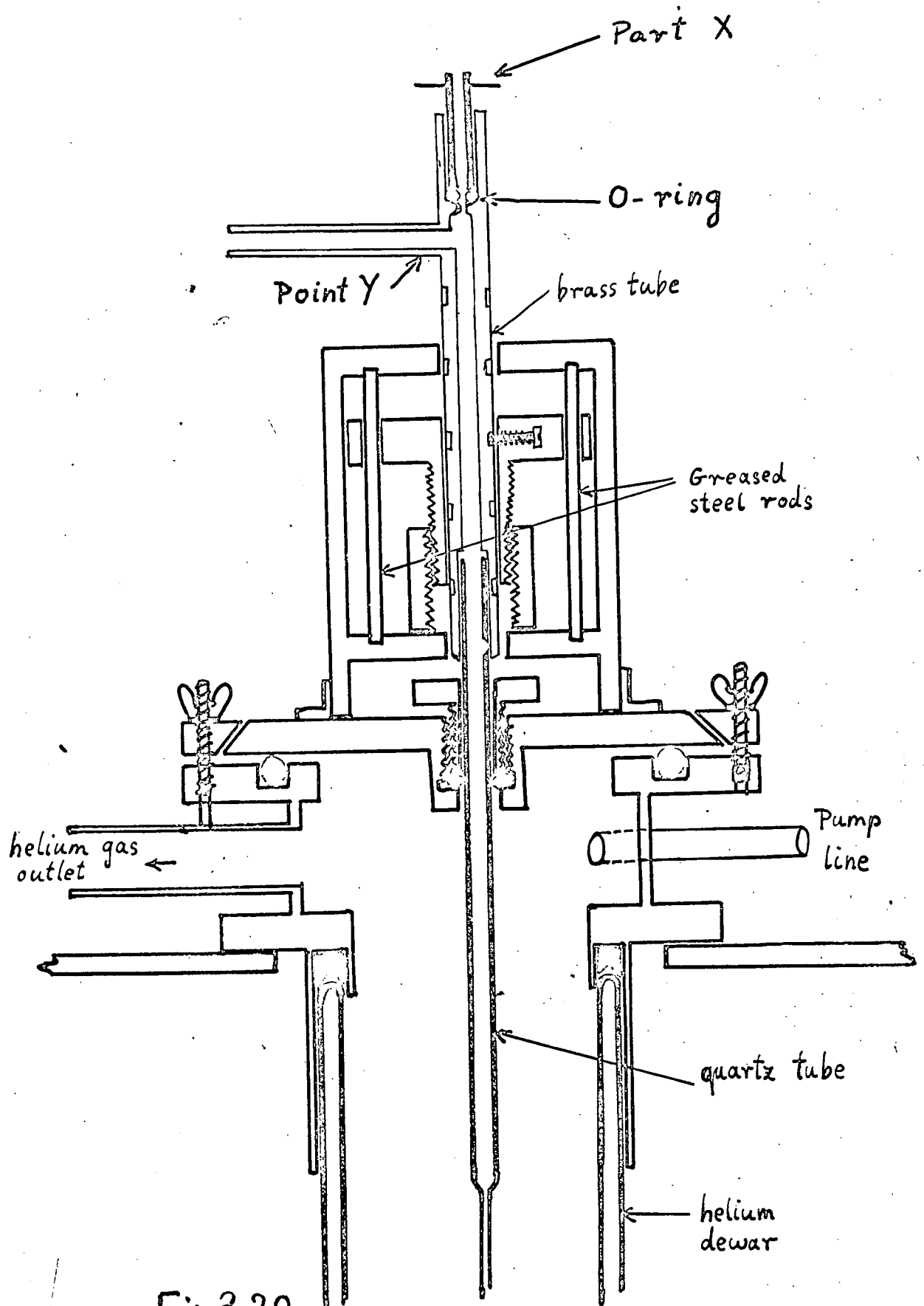


Fig.3.20

Dewar Head and Height Adjuster

It was considered preferable to take a base line photograph before and after the temperature run and assume a linear relationship between the gradient of the base line trace and the temperature.

The gradient change was due to a movement of the pick-up coil system as a result of the thermal expansion of the quartz tube supporting the pick-up coils. Since quartz has a low thermal expansion coefficient, this gradient change with temperature was never very large. If necessary a base line signal could be obtained part way through a run.

The error in temperature measurement depends upon the rate of temperature rise. This was adjusted to be always less than 1K per minute. Reproducible results were obtained and the error was estimated to be $\pm 1K$.

3.5 Mechanical Considerations

3.5.1 The Dewar Head and Support of Pick-up Coils

The dewar head rested upon the top of a steel bridge (fig.3.20). To the top plate of the dewar head was attached a mechanism of brass (the height adjuster) whose function was to adjust the vertical position of the quartz tube upon which the pick-up coils were wound. The lower end of this quartz tube was confined to the axis of the magnet by means of a hole through the spider (fig.3.18). This quartz tube was of narrow diameter in order to confine the sample to the magnet axis also. This narrow diameter extended from the lower closed end for 70 cm, above which the tube continued with $\frac{1}{2}$ " outer diameter. The top of this tube fitted into a brass tube (fig.3.20) and was secured to this by araldite to give a vacuum-tight seal. The upper end of the sample tube was attached to the top of this brass tube and sealed by an O-ring. This brass tube could be evacuated via a side tube near the top thus evacuating the region around the sample prior to filling with helium as an exchange gas. The brass tube had notches at intervals of an inch along its length into which a small screw from the height adjuster could fit in order to give a coarse adjustment of height. The fine adjustments of height was done by means of the large screw in the height adjuster.

3.5.2 The Vacuum System

Vacuum and gas flow were controlled through an all glass system shown

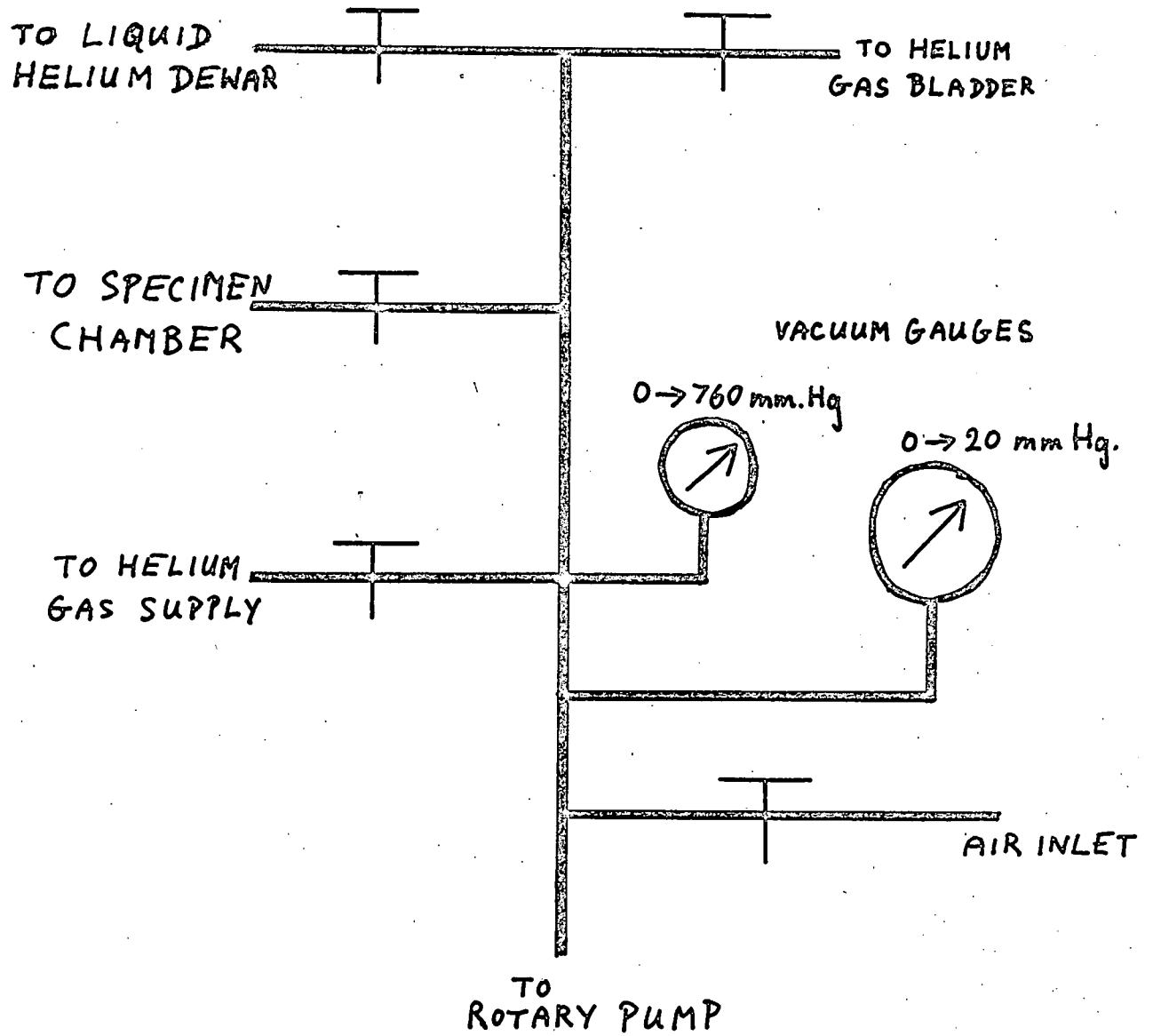


FIG. 3.21 VACUUM SYSTEM

schematically in fig. 3.21. It was used in conjunction with a rotary pump for evacuating the walls of the helium dewar and for evacuating the inner volume of the dewar and specimen region prior to filling with helium gas. The helium gas was obtained either from a helium cylinder or from the boiling of helium in the external liquid helium dewar.

3.5.3 Support of the Sample

The upper end of the sample holder fits over the lower end of the long stainless steel tube which is soldered at the top to a thin brass tube. This thin brass tube is smooth over a region where the O-ring is to be situated and is sealed to the other brass tube by this O-ring. This other brass tube is secured to the pick-up coil tube by means of araldite (3.5.1). Above the smooth part, the thin brass tube is threaded and a wing nut is used for adjusting the height of the sample. This wing nut rests upon Part X which, by means of a rubber band attached to Point Y, squeezes the O-ring, thus isolating the sample from the atmosphere.

3.5.4 Removing the Sample from the Pick-up Coils

When it is required to remove the sample momentarily from the pick-up coils to take a photograph of a base line trace, the sample is lifted a few inches, well out of the coil system, so that the O-ring is still in contact with the smooth portion of the sample tube and still isolates the sample from the atmosphere.

Removing the sample entirely in order to change it for another sample while liquid helium is in the dewar requires care in order not to allow air to enter the specimen cavity, as it would freeze and block up the cavity. This is done by connecting the external helium dewar to the vacuum system during a helium run in such a way that an excess pressure of helium gas is always maintained in the sample cavity due to boiling of helium in the external dewar.

Thus when a sample is removed a continuous flow of helium gas out of the top of the sample cavity prevents any air from entering the cavity. The top is then stopped up with a small rubber bung until one is ready to insert the next sample, when the same precaution is taken.

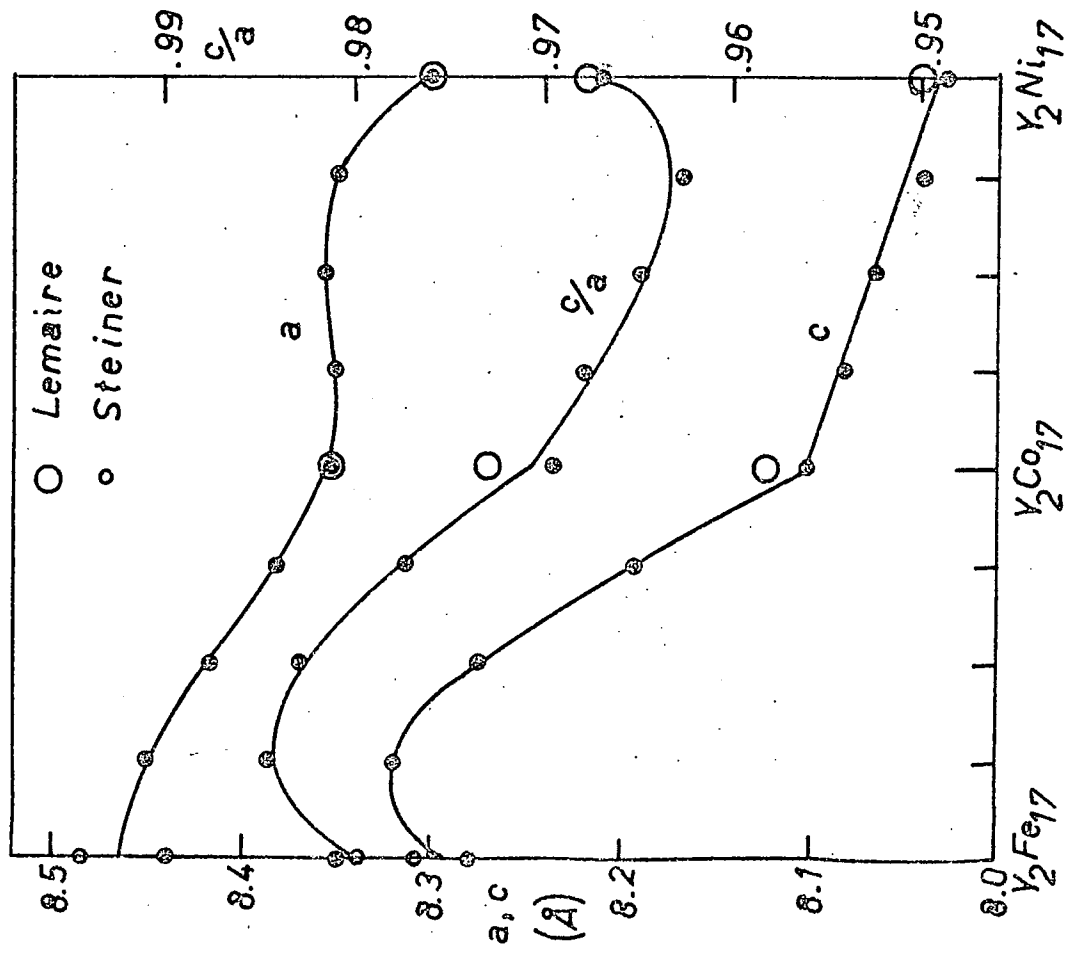


Fig. 4.1 Lattice Parameters of Y_2B_{17}

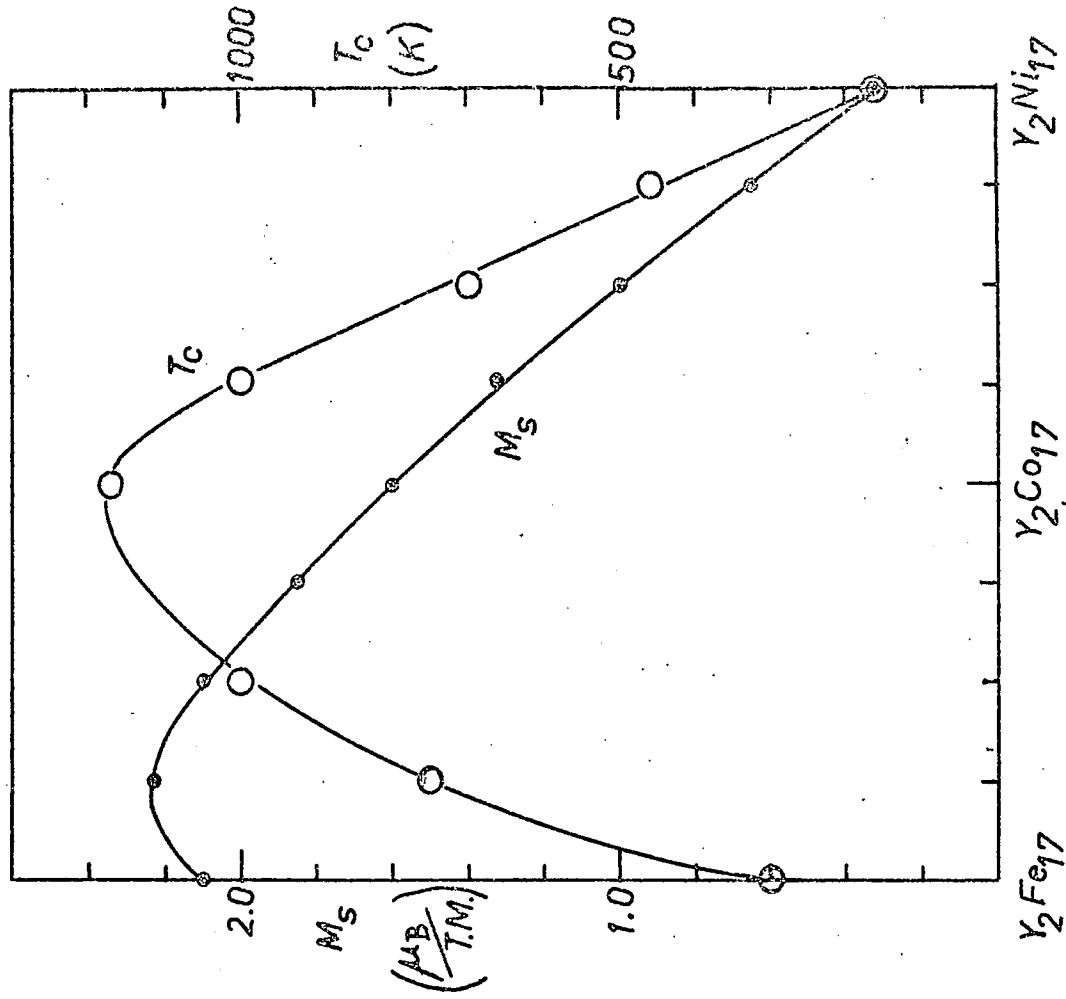


Fig. 4.2 M_s and T_c for Y_2B_{17}

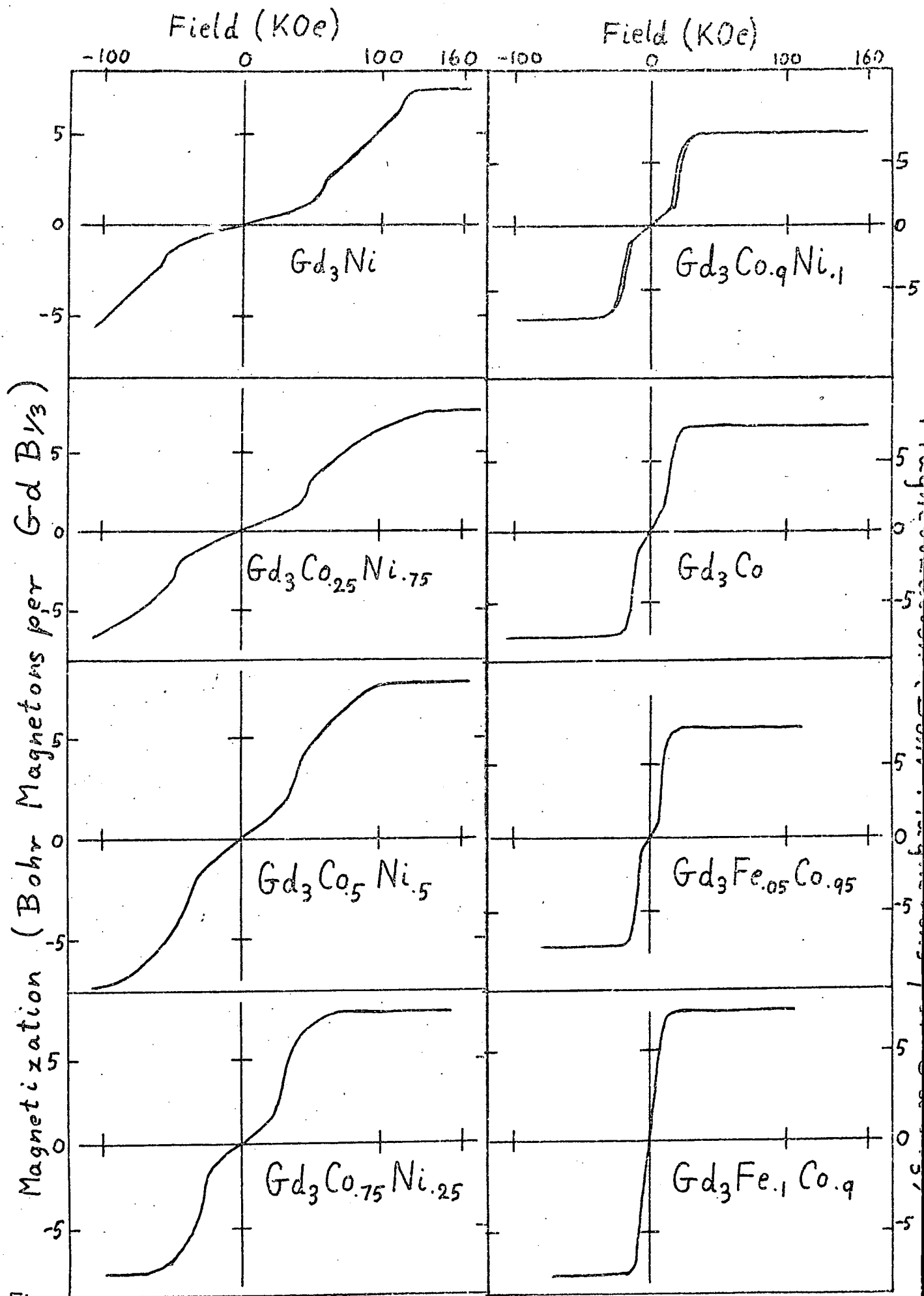


Fig. 5.2 Pulsed Field Magnetization Curves for $Gd_3(Fe,Co)$ and $Gd_3(Co,Ni)$ at 4-2

In the $Gd_3(Fe,Ni)$ system, on substituting Fe for Ni, the Fe_3C lines remained distinct but slowly deteriorated in definition up to and including $Gd_3Fe_{.5}Ni_{.5}$.

In $Gd_3Fe_{.3}Ni_{.7}$ a line appeared which had not been observed in Gd_3Ni . This line, which increased in intensity on further substitution of Fe into Ni, corresponded to the (231) line for Gd_3Ni calculated by Lemaire and Paccard (ref 5.2) to have a value of $\theta = 23^\circ 49'$, for cobalt radiation, but whose observed intensity was zero. The line appearing in $Gd_3Fe_{.3}Ni_{.7}$ had a value of $\theta = 23^\circ 47'$. It is possible that the substitution of Fe for Ni into the Fe_3C structure modified the scattering intensities to cause the appearance of the (231) reflection. Beyond $Gd_3Fe_{.5}Ni_{.5}$ the Fe_3C lines broadened rapidly becoming very indistinct for $Gd_3Fe_{.6}Ni_{.4}$. If the instability of the Fe_3C structure is postulated to occur at a critical average 3d electron concentration then, noting that this occurs at $Gd_3Fe_{.1}Co_{.9}$ in the $Gd_3(Fe,Co)$ system, this allows us to predict a corresponding break-down of the structure at approximately $Gd_3Fe_{.55}Ni_{.45}$ in the $Gd_3(Fe,Ni)$ system which appears, from the X-ray diffraction patterns, to occur.

The lattice parameters a, b and c (fig. 5.1) were calculated from the deflections of a selection of the indexed lines, the lines being selected according to their sharpness. This same set of lines was used for lattice parameter determinations for the entire range of compounds studied. From Fig. 5.1 it is apparent that the break-down of the Fe_3C structure is not accompanied by any significant lattice distortions.

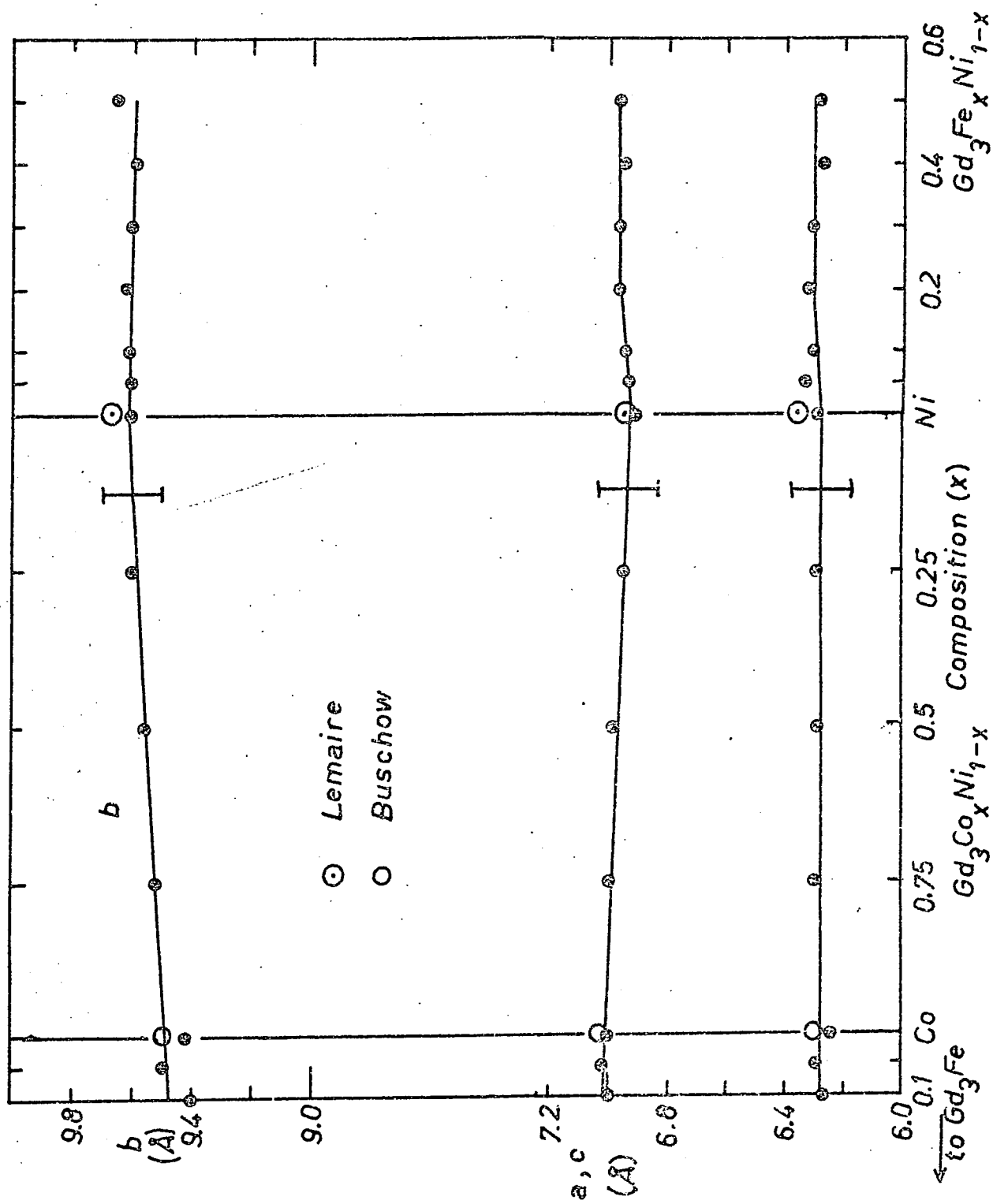
5.3. Magnetic Measurements on $Gd_3(Fe,Co)$ and $Gd_3(Co,Ni)$

5.3.1 Pulsed field measurements at 4.2K

Magnetization vs applied field curves were obtained using the pulsed field magnetometer. Measurements were performed up to 160 kOe and at 4.2K which was well below the ordering temperatures of the compounds.

The magnetization vs field curves for some bulk samples of the $Gd_3(Fe,Co)$ and $Gd_3(Co,Ni)$ series are shown in fig. 5.2 to 5.3. A general feature of these curves is an initial linear rise in magnetization with applied field up to a

Fig. 5.1 Lattice Parameters for $Gd_3(Fe,Co,Ni)$ Compounds at 300 K.

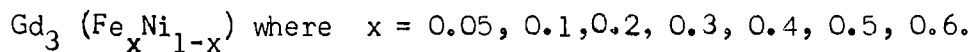
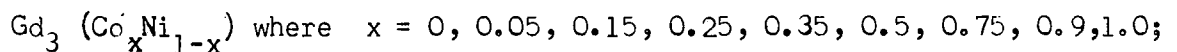
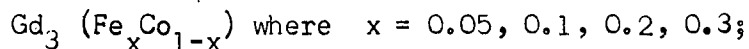


CHAPTER FIVE

Gd₃(Fe, Co, Ni) RESULTS.

5.1 Preparation of Samples

Using the arc-furnace techniques as described in section 2.1, specimens were produced of the pseudobinary compounds with the basic formula Gd₃B where B is the transition metal component. The following specimen compositions were prepared:



Each sample button was melted three times, inverting it between melts in order to improve its homogeneity. The average weight lost during specimen preparation was 0.07% and in many of the samples the weight loss was too small to be determined (i.e. <0.01%).

5.2 Structural Stability and Lattice Parameters of the Gd₃B system

Debye-Scherrer photographs of the samples at 300K were obtained using cobalt ~~K~~ radiation. The diffraction lines in the series Gd₃Co to Gd₃Ni indicated that the whole series of compounds adopted the same crystallographic structure. Homogenization annealing at 700°C for two weeks had no effect upon the X-ray diffraction patterns. The diffraction patterns of the compounds Gd₃Co and Gd₃Ni were compared with those already reported in the literature (refs. 5.1 and 5.2) and the lines were indexed in the orthorhombic Fe₃C structure. These lines showed a linear variation of deflection between the two end compounds and could be indexed throughout the series Gd₃(Co,Ni).

In the Gd₃(Fe,Co) system the lines broadened and became indistinct for Fe concentrations greater than that of Gd₃Fe_{0.1}Co_{0.9}. This was taken to indicate that the Fe₃C structure of the desired composition was not stable beyond this point.

the extrapolation intercepting the M axis at $M = 0$ for these two compounds with linear M vs H curves.

(b) For powder samples of low moment to the Co side of these minima there appears a critical field H_c (fig. 4.5) similar to that found in YCo_2Ni_3 . Saturation was not attained for any of the samples showing a critical field. For field oscillations of amplitude less than H_c there appeared a conventional non-saturating hysteresis loop. The spontaneous moment was obtained from the linear portion of the M vs H curve above the critical field.

The saturation moments, fig. 4.7 and fig. 4.8, were obtained from solid samples for $Y(\text{Fe}_{.8}\text{Co}_{.2})_3$, $Y(\text{Fe}_{.6}\text{Co}_{.4})_3$, $Y(\text{Fe}_{.4}\text{Co}_{.6})_3$, $Y\text{Ni}_3$ and $Y_2\text{Ni}_7$ which saturated in the available field. All the other samples of the $Y\text{B}_3$ series and the $Y_2\text{B}_7$ series were powdered, because of high magnetic anisotropy not allowing a close approach to saturation. The spontaneous moment in the powder samples was obtained by extrapolating the high field linear portion of the M vs H curve back to $H = 0$ since it was believed that the application of the high field may have been distorting the magnitude of the spontaneous moment. The maximum value of the moment attained at 160 KDe is also given in fig. 4.7 and fig. 4.8. For the samples which show complete saturation the error is that inherent in the measurement of magnetization. It is therefore $\pm 4\%$ for all the saturated samples.

The solid sample of $Y\text{Fe}_3$ showed the same eddy current effect, in the M vs H curve (fig. 3.17b), as was found for a solid sample of pure iron (fig. 3.17b) at low temperatures. This is consistent with the presence of free iron in the sample, thus further confirming that $Y\text{Fe}_3$ does not exist as a single phase.

Two other interesting features are noteworthy. (a) There is a deep minimum in both the Curie temperatures and the spontaneous magnetizations for compounds with approximately 20% Co substitution in Ni for both the $Y\text{B}_3$ and the $Y_2\text{B}_7$ series. These minima may indicate a complete disappearance of any spontaneous magnetic ordering for these compositions. The M vs H curves of $Y_2(\text{Co}_{.2}\text{Ni}_{.8})_7$ and $Y(\text{Co}_{.2}\text{Ni}_{.8})_3$ at 4.2K were linear, with a low susceptibility. Any extrapolation of M vs $1/H$ to $H = \infty$ for such samples is clearly not a measure of the spontaneous magnetization. It is reasonable to assume that the slight susceptibility may be of a Pauli paramagnetism type, with zero spontaneous magnetization. This is consistent with the method used for estimating the spontaneous magnetization. This method consisted of extrapolating the linear portion of M vs H to $H = 0$,

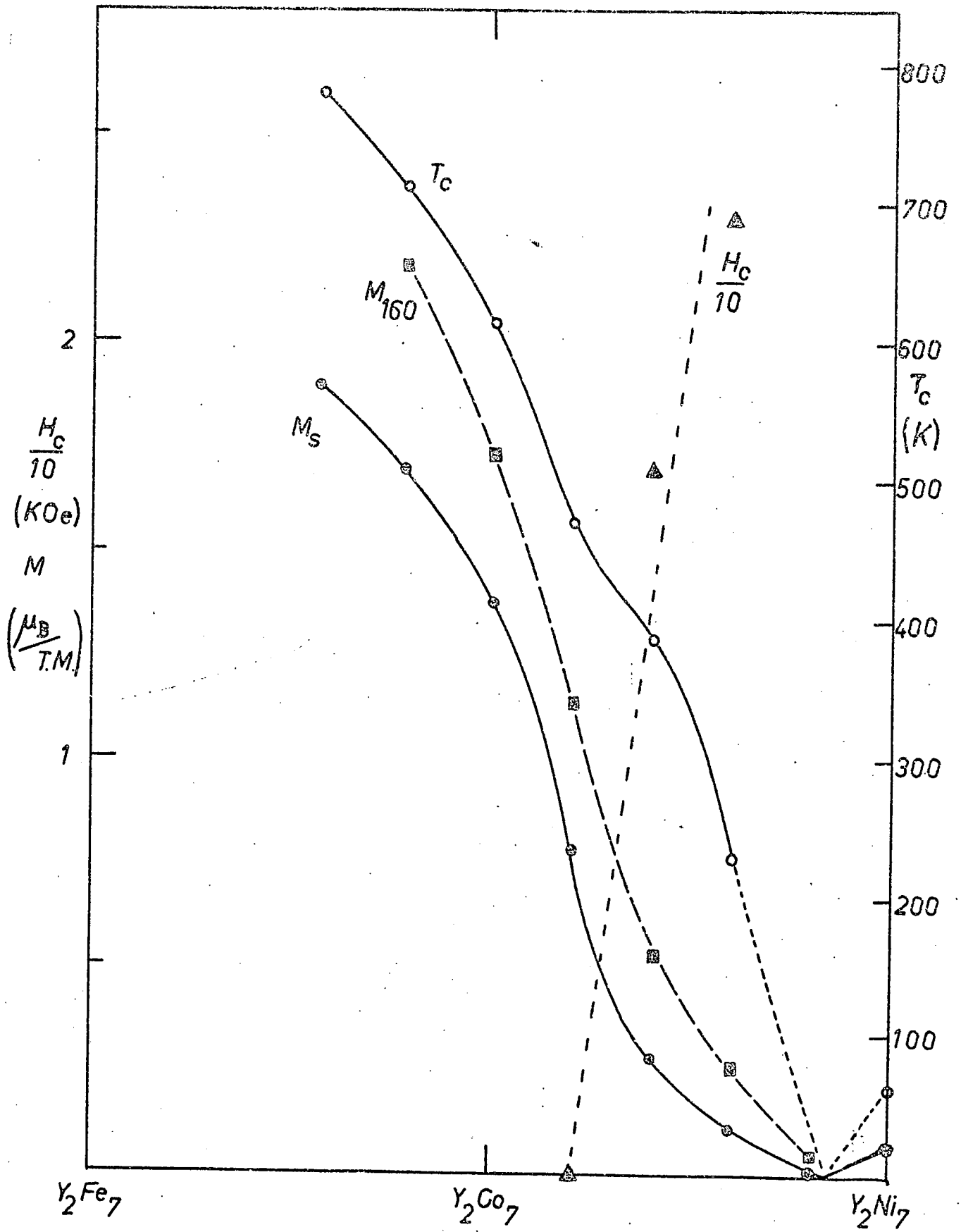


Fig. 4.8 M_s , M_{160} , T_c and H_c for Y_2B_7

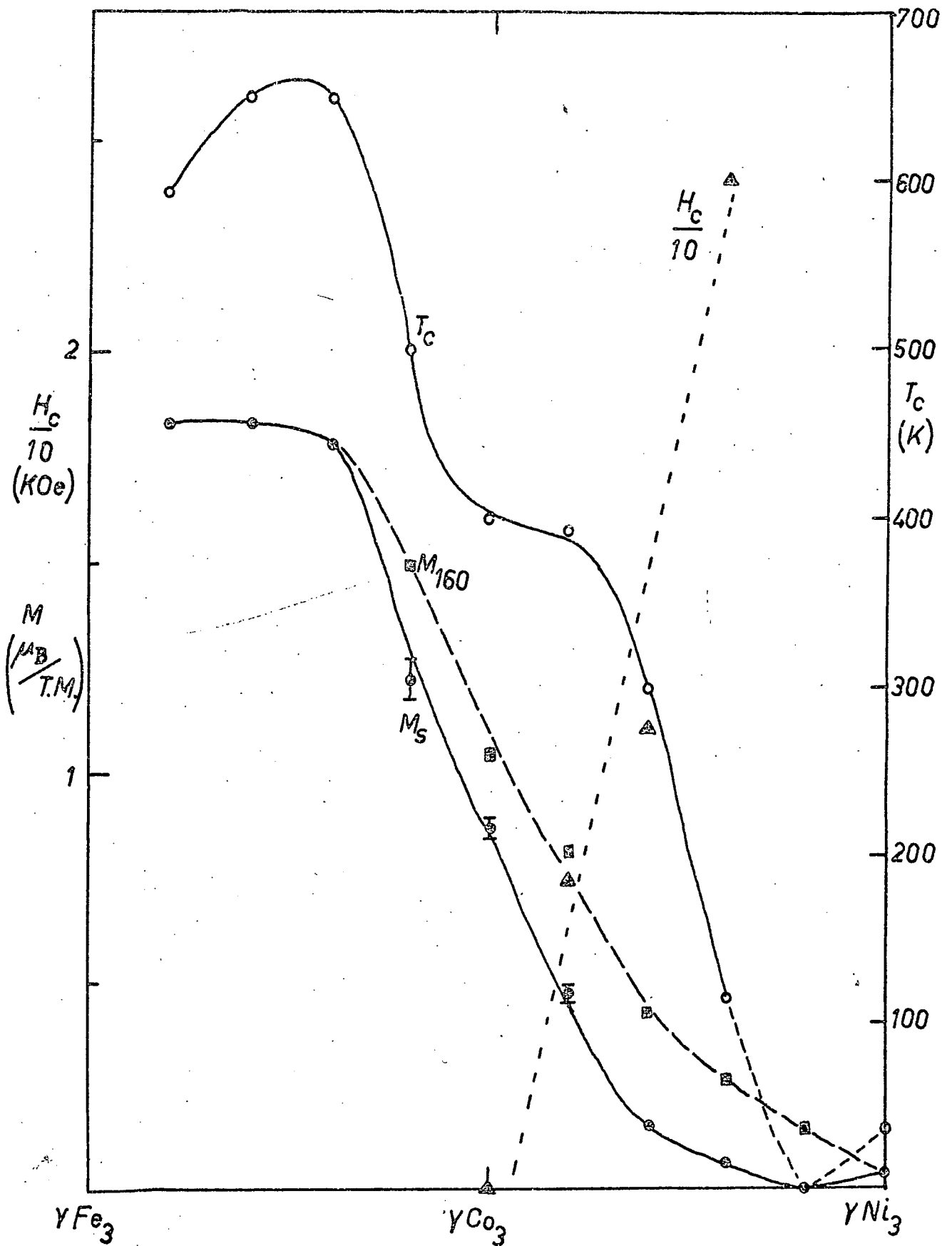


Fig. 4.7 M_s , M_{160} , T_c and H_c for YB_3

magnetization rose more steeply and then settled down at the same gradient as that of the smaller return oscillations. The return for a high field showed no sign of any positive critical field and had the same gradient as the smaller return oscillations. On reversing the field M decreased rapidly and then the same phenomenon was seen for large negative fields. Powder samples of the other $Y B_5$ compounds showed no critical fields.

4.3 YB_3 and Y_2B_7

4.3.1 Crystal Structure

The X-ray photographs of the $Y B_3$ series showed a similar structure for all of the compounds from Ni to Co to $Y(Fe_{.8}Co_{.2})_3$. The sample corresponding to $Y Fe_3$ showed a totally different type of structure and is believed not to exist as a single phase. This is confirmed by other workers (ref. 4.1). The $Y Fe_3$ sample rusted after a few weeks, whereas all the other samples did not, suggesting the existence of large quantities of free iron in the sample.

The YB_3 stoichiometry is rhombohedral but the X-ray lines were indexed in the hexagonal system with lattice parameters as shown in fig. 4.6.

The Y_2B_7 compounds showed the same pattern of X-ray diffraction lines for the range Ni to Co to 40% Fe substitution in Co. It is assumed that higher concentrations of Fe than 40% in Co do not form the Y_2B_7 phase. The phase Y_2Fe_7 has not been shown previously to exist. The X-ray photographs for the range in which the Y_2B_7 phase is believed to exist were not analysable due to the lines not being sharp. The large number of lines suggested the presence of other phases. No improvement was found upon annealing for 2 weeks at $1000^\circ C$. Therefore no reliable estimates of the lattice parameters were obtained for the Y_2B_7 compounds.

4.3.2 Magnetic Properties

The Curie temperatures of the YB_3 and Y_2B_7 compounds were obtained from the A.C. initial susceptibility vs temperature, fig. 4.7 and fig. 4.8.

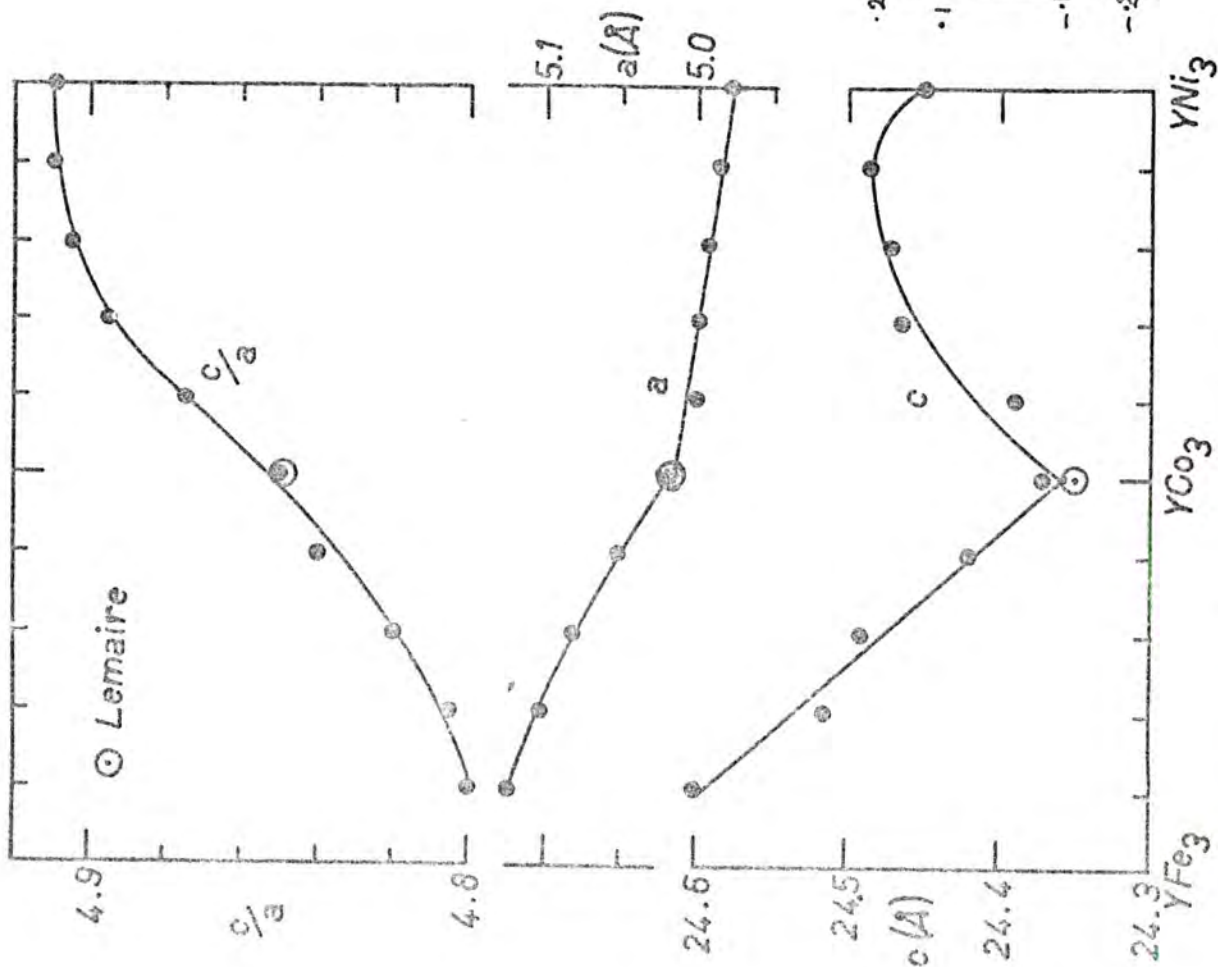


Fig. 4.6 Lattice Parameters of YB_3

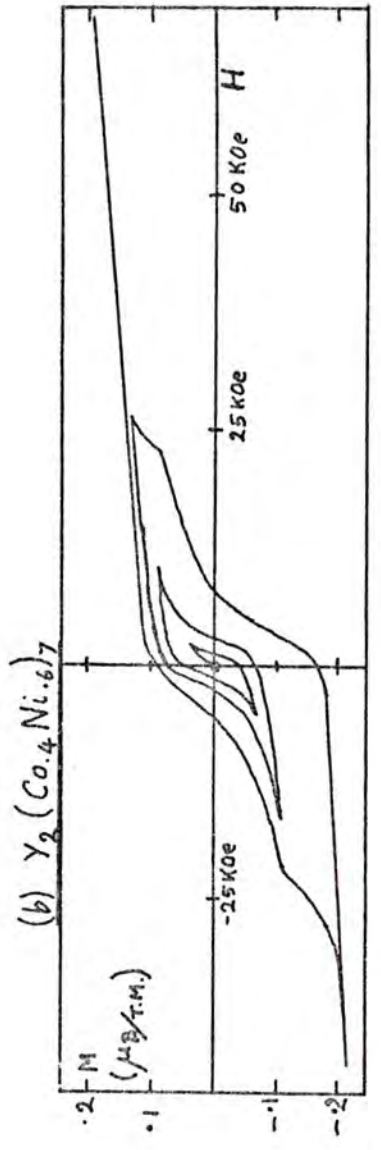
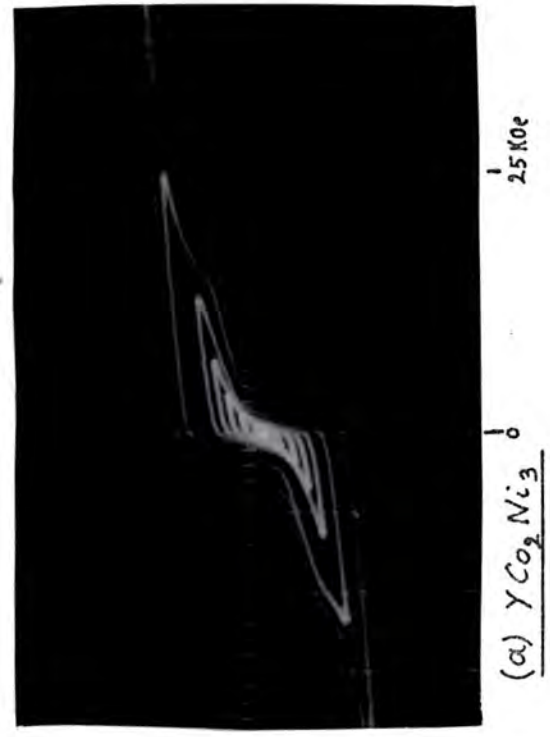


Fig 4.5 M vs H for two Powder Samples at 4.2 K

illustrating the Critical Field for large pulses.

CHAPTER FOUR

RESULTS FOR $Y_x(Fe,Co)_{1-x}$ AND $Y_x(Co,Ni)_{1-x}$ 4.1 Y_2B_{17}

The as-cast samples of $Y_2(Fe,Co)_{17}$ and $Y_2(Co,Ni)_{17}$ were single phase. They were indexed hexagonally with lattice parameters a and c as shown in fig. 4.1, together with the c/a ratio.

The magnetic properties measured were the Curie temperatures and the saturation moments (fig. 4.2). The saturation moments at 4.2K were directly obtained from the magnetization vs field oscillograms of solid samples because complete saturation was achieved in the available field from the pulse magnet for all the samples in the series (except Y_2Fe_{17} which approached the saturation value within 5% as deduced by extrapolating M vs $1/H$ to $H = \infty$).

4.2 YB_5

Lattice parameters were obtained from the X-ray photographs of the as cast samples which were indexed hexagonally (fig. 4.3). On substituting iron for cobalt in YCo_5 the ratio c/a of lattice parameters burgeoned and compounds with higher iron concentrations than that of $YFeCo_4$ could not be made in the single phase form.

Due to high magnetic anisotropy the Curie temperatures were not easily determined because the initial susceptibility was low in many of the samples. However slight peaks in χ_i vs T were just visible in most of this pseudobinary series and the Curie temperatures obtained are shown in fig. 4.4.

The saturation moments (fig. 4.4) were obtained from powder samples because solid samples did not show any tendency to saturate in the available fields, except $YCoNi_4$ which showed complete saturation.

A powder sample of YCo_2Ni_3 gave a magnetization curve with a critical field (fig. 4.5) of 16 ± 0.4 KOe. For field oscillations of amplitude less than 16 KOe a conventional non-saturating hysteresis loop was seen, with a return to $H = 0$ of constant gradient. Above the critical field the

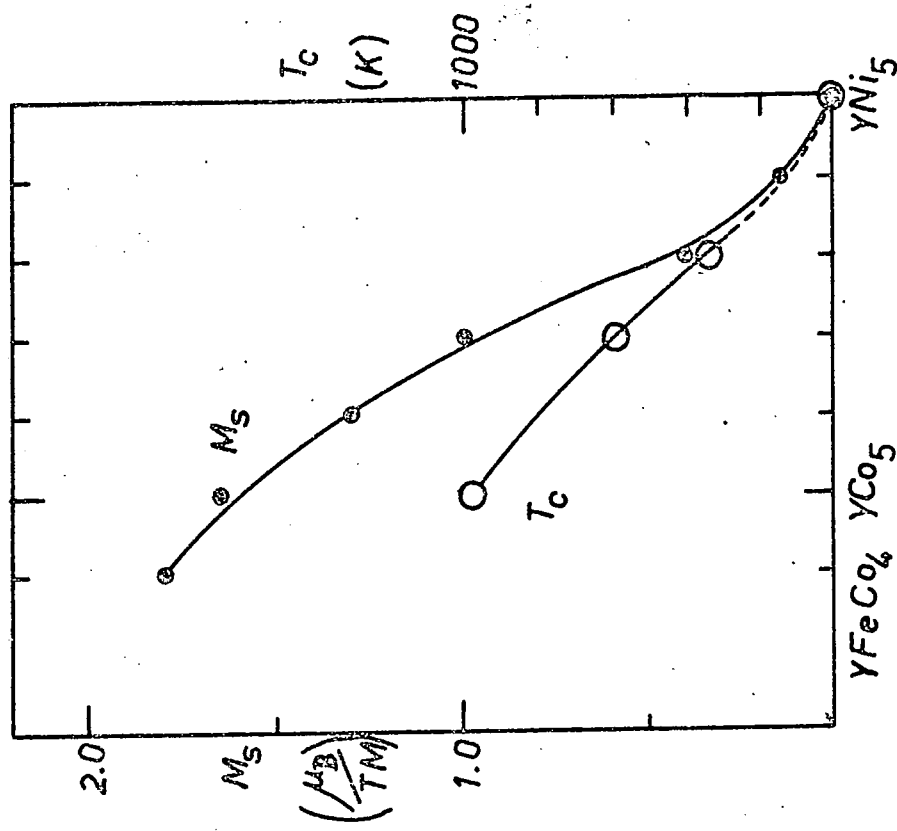


Fig.4.4 M_s and T_c for YB_5

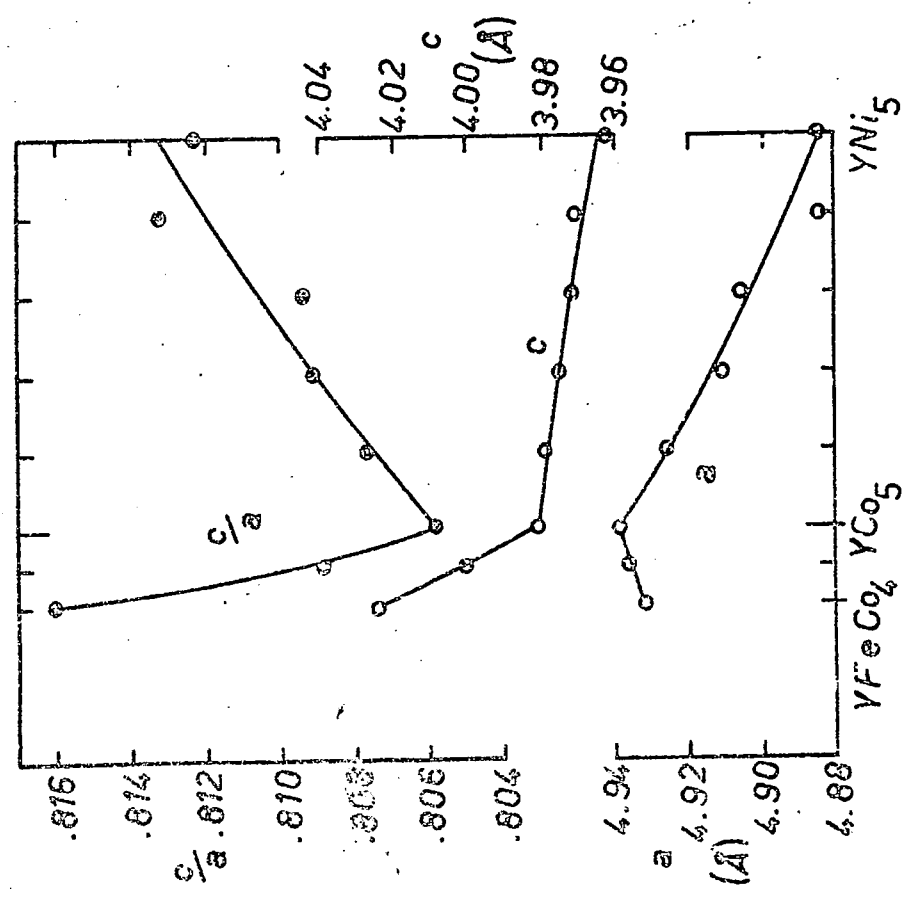


Fig.4.3 Lattice Parameters of YB_5

critical field value H_c at which point the magnetization rises more rapidly subsequently approaching saturation. Hysteresis above H_c is also evident.

The curves for $Gd_3Co_{0.05}Ni_{.95}$ and Gd_3Ni have a distinctly different shape from those for the other compounds of the series and show a second critical field H_c' just below the field value required to saturate the magnetization. H_c' has a value approximately double that of H_c . These compounds are also different from the others of the series in that the linear portion between H_c and H_c' when extrapolated has a negative intercept on the magnetization axis, whereas the extrapolation of any existing linear portion above H_c in the other compounds has an intercept near zero on the magnetization axis.

The measurement of the critical fields was performed on the initial field rise for a pulse of 160 kOe, by extrapolating the M vs H curves above and below the transition, as shown in fig. 5.3. The critical field was defined to occur at the intersection of the two extrapolated sections.

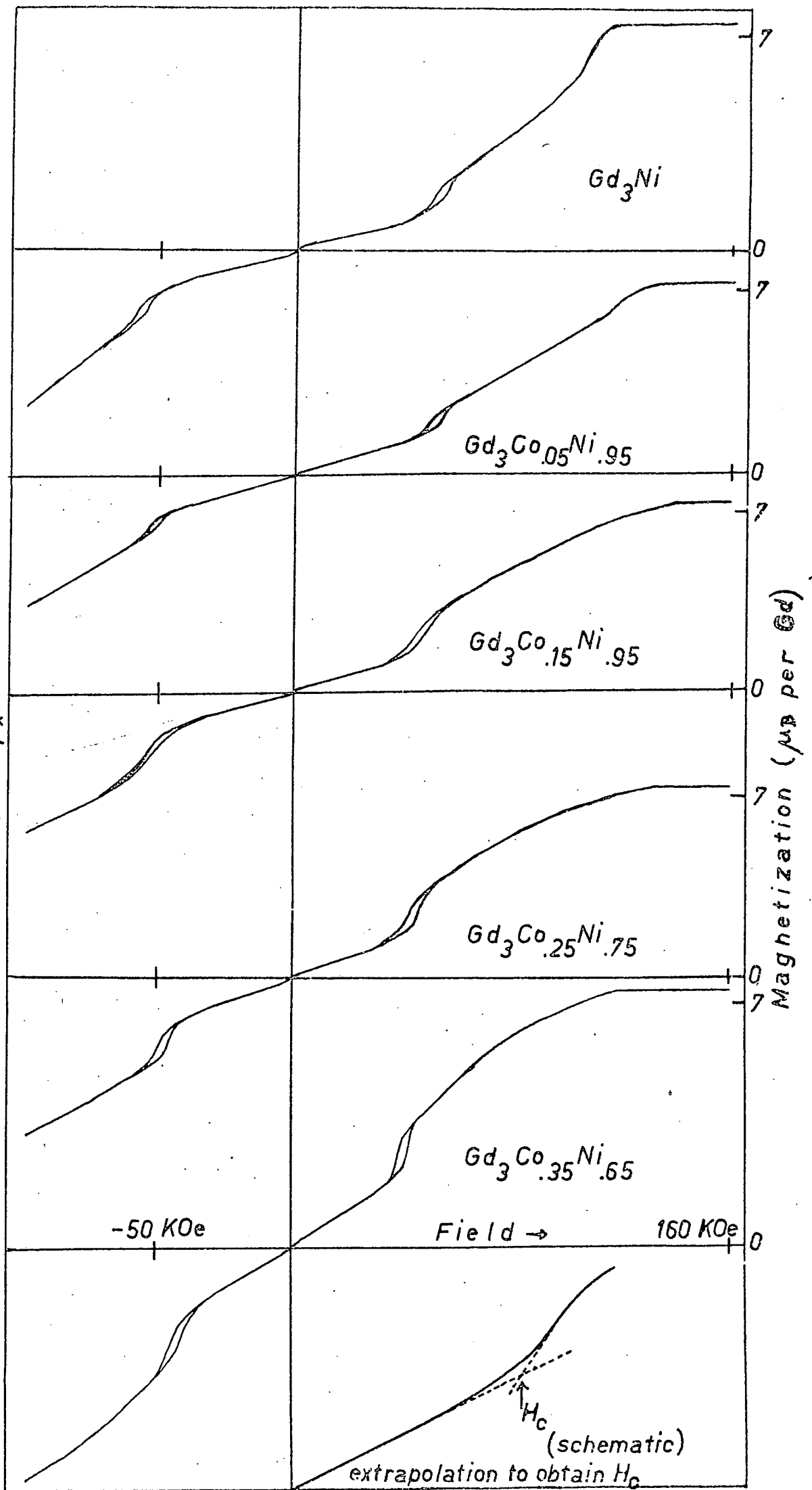
The critical field H_c is shown as a function of composition in fig. 5.4 such that the composition axis represents the 3d-electron concentration per Gd_3B formula unit. H_c varies smoothly with composition for composition ranges near Gd_3Co and becomes zero just beyond $Gd_3Fe_{.1}Co_{.9}$. This is the same point beyond which the Fe_3C structure appears to break down.

The initial susceptibility χ_i was measured directly from the magnetization vs field curves and is shown in fig. 5.5 plotted against composition.

The initial susceptibility χ_i is here expressed in μ_B per kOe per Gd. This should rigorously be expressed per $GdB_{\frac{1}{3}}$ where B is the transition metal component, but the simpler notation will be used and no ambiguity should arise. Some of the M vs H curves show a small kink near the origin. This kink, which sometimes has hysteresis is presumed to arise from the presence of small quantities of impurity. For these curves the initial susceptibility χ_i was measured from the linear portion of the M vs H curves on either side of the kink.

In fig. 5.5 are plotted also M_{160} , the magnetization at 160 kOe; H_s , the field value at which the magnetization saturates and H_c' . H_c' appears only in the samples Gd_3Ni and $Gd_3Co_{.05}Ni_{.95}$. When a line through these two values

Fig. 5.3 M vs H Curves of $Gd_3Co_xNi_{1-x}$ at 4.2 K (Ni-rich compounds)



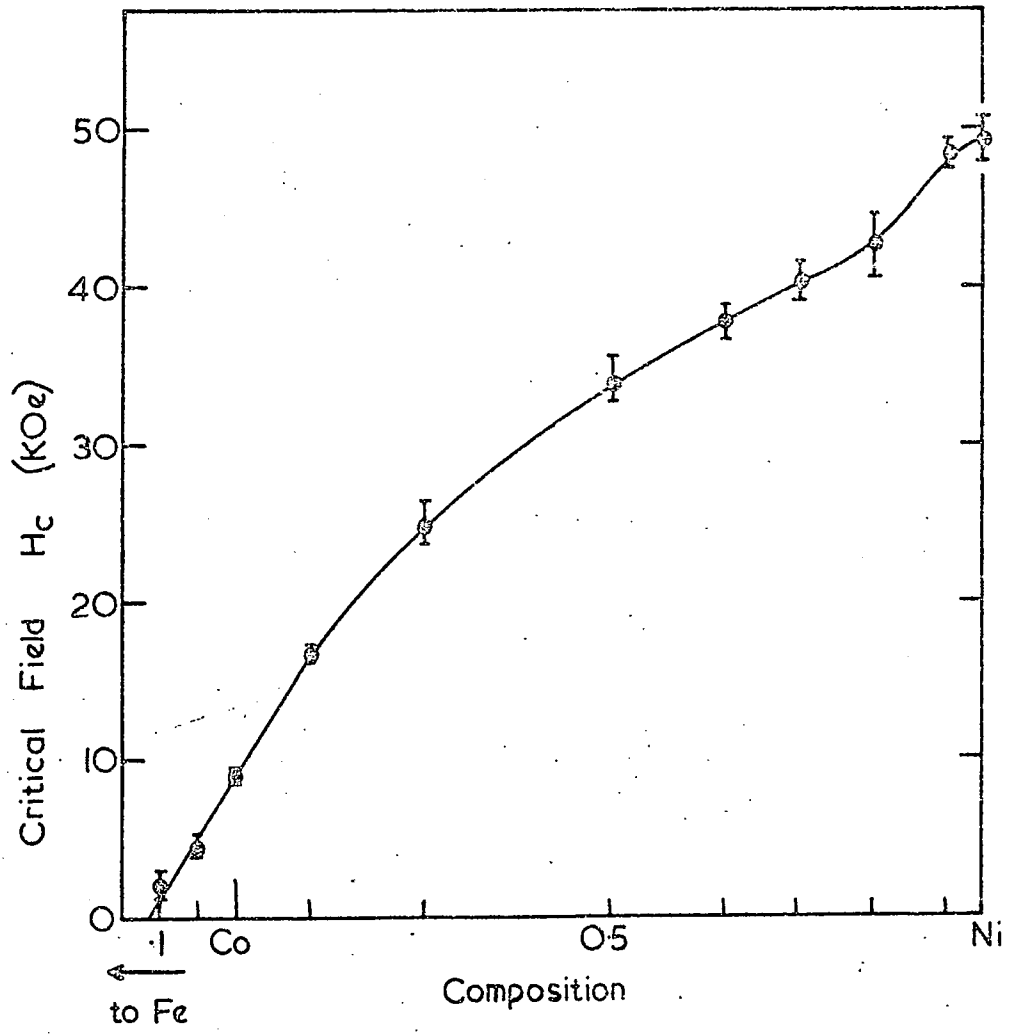


Fig. 54 H_c vs Composition at 4.2 K

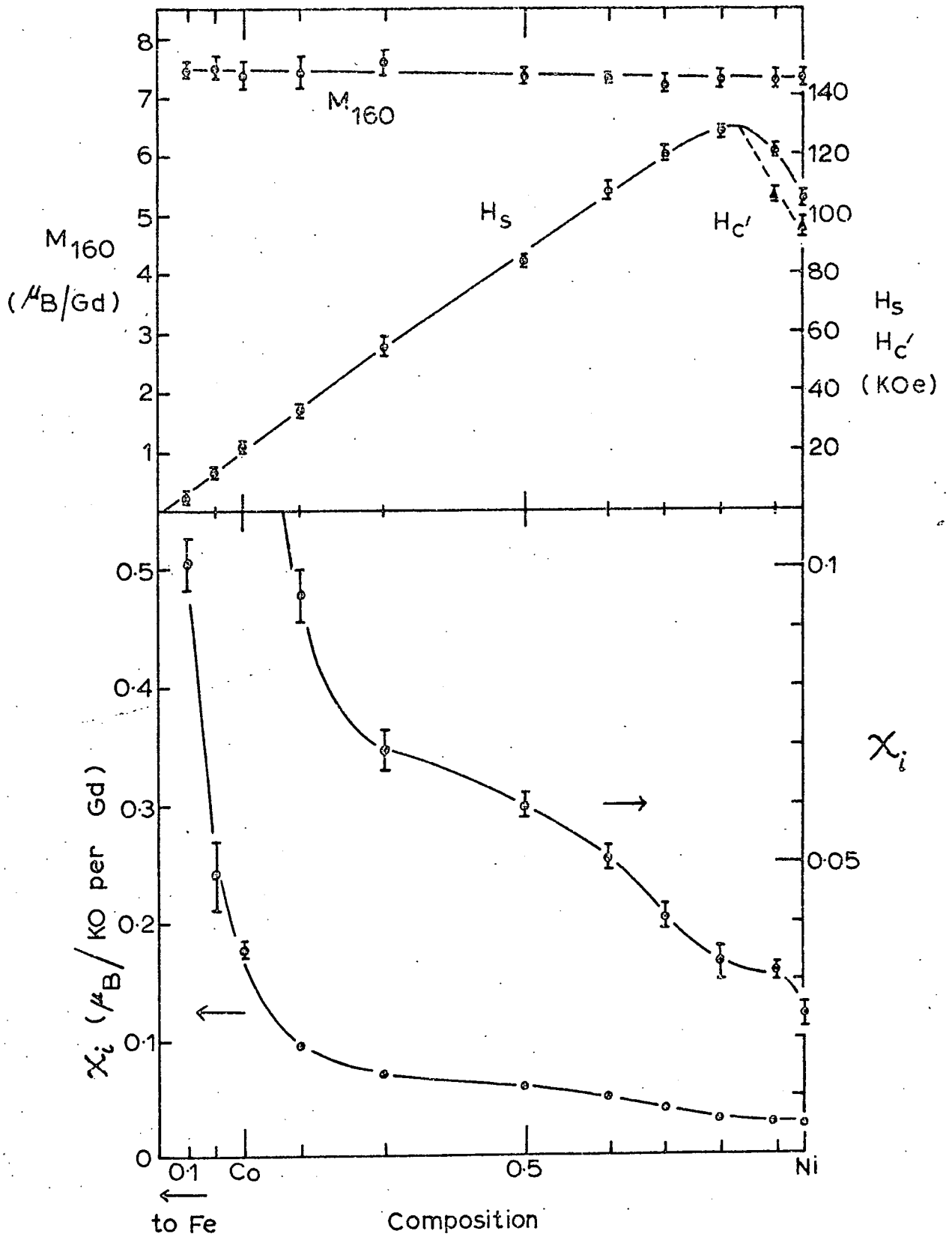


Fig.5.5 $\chi_i, H_s, H_{c'}, M_{160}$ at 4.2 K

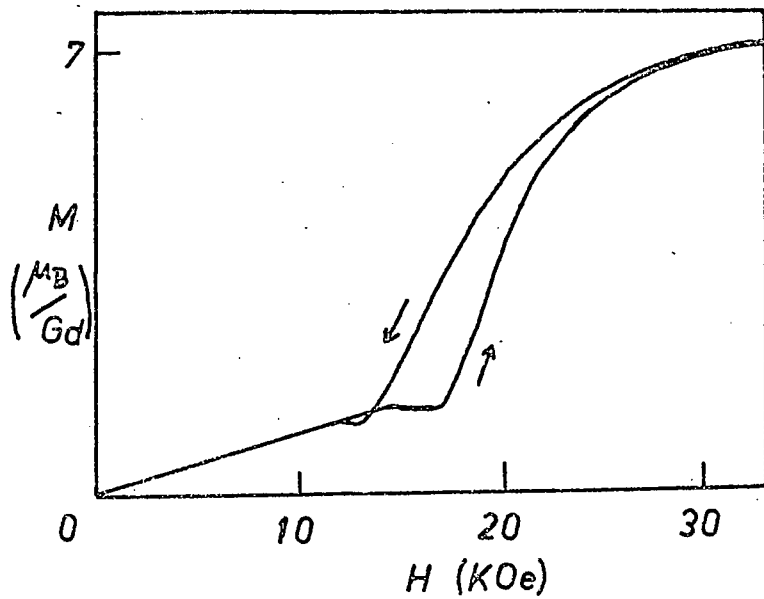


Fig. 5.6 a M vs H ($H_0 = 160$ KOe) for $Gd_3Co_9Ni_1$ at 4.2 K

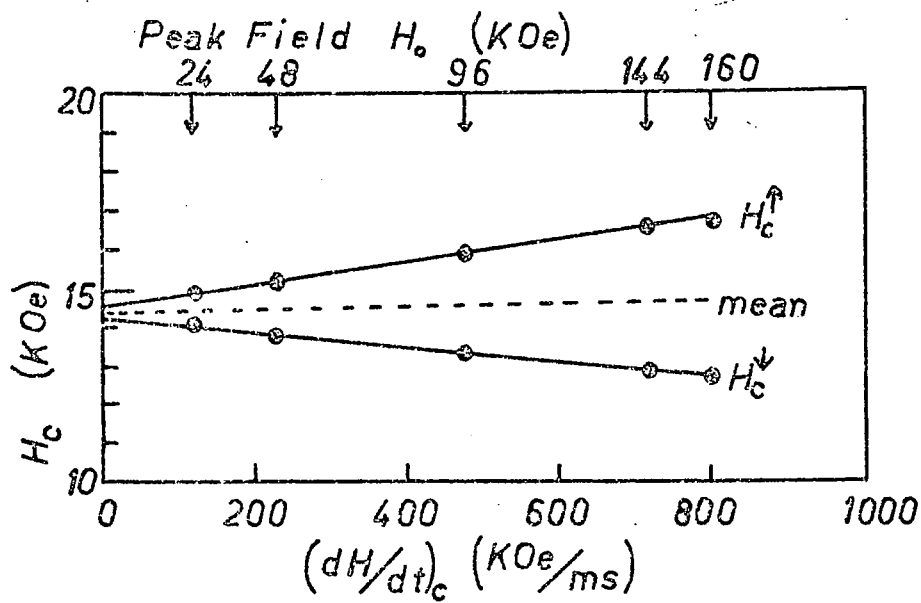


Fig. 5.6 b H_c vs Rate of change of field at $H = H_c$ ($T = 4.2$ K)

is extrapolated to higher cobalt concentrations, the next sample prepared $\text{Gd}_3\text{Co}_{.15}\text{Ni}_{.85}$ would have a value of H_c' greater than H_s . Therefore H_c' does not manifest itself in this sample, the shape of whose M vs H curve is different from that of $\text{Gd}_3\text{Co}_{.05}\text{Ni}_{.95}$ or Gd_3Ni .

The average value of M_{160} is $7.38\mu_B$ per $\text{GdB}_{\frac{1}{3}}$ which is well in excess of the gJ value for Gd ($7\mu_B$ per Gd ion). The excess molecular moment $1.14\mu_B$ per formula unit Gd_3B may arise from parallel alignment of the conduction electron moments and/or 3d electron moment. Without neutron diffraction techniques there is no way of deciding at present between these possibilities.

Some time-dependence of the magnetization was observed, which resulted in a small variation in the value of the critical field H_c with increasing pulse height. A large pulse height results in the field sweeping through the H_c value faster than does a small pulse height.

The critical field for the sample $\text{Gd}_3\text{Co}_{.9}\text{Ni}_{.1}$ was observed for various pulse heights H_0 . We use the notation H_c^\uparrow for increasing fields and H_c^\downarrow for decreasing fields. On increasing H_0 it was found that H_c^\uparrow increased and H_c^\downarrow decreased thus making the hysteresis more prominent. Between $H_0 = 96$ kOe, and $H_0 = 144$ kOe the type of critical field changed its character (fig. 5.6(a)). At the top of the initial linear portion the magnetization suddenly started to remain constant, until a critical field H_c^\uparrow at which it rose sharply with increasing field. This critical field increased in magnitude with increasing H_0 . In fig. 5.6(b) is plotted H_c^\uparrow and H_c^\downarrow as a function of $(dH/dt)_c$, the rate of change of field value at the critical field. The corresponding peak fields are also indicated. From this figure it can be seen that H_c^\uparrow increases, and H_c^\downarrow decreases with increasing $(dH/dt)_c$. The average value of H_c^\uparrow and H_c^\downarrow remains almost constant at 14.6 kOe, increasing very slightly with increasing $(dH/dt)_c$. By extrapolating the two lines to $(dH/dt)_c=0$ it becomes apparent that the hysteresis would be almost zero in a static experiment if this linear extrapolation were valid. The possibility arises that the hysteresis observed in these compounds may be due almost entirely to time dependence of the magnetization vs field behaviour.

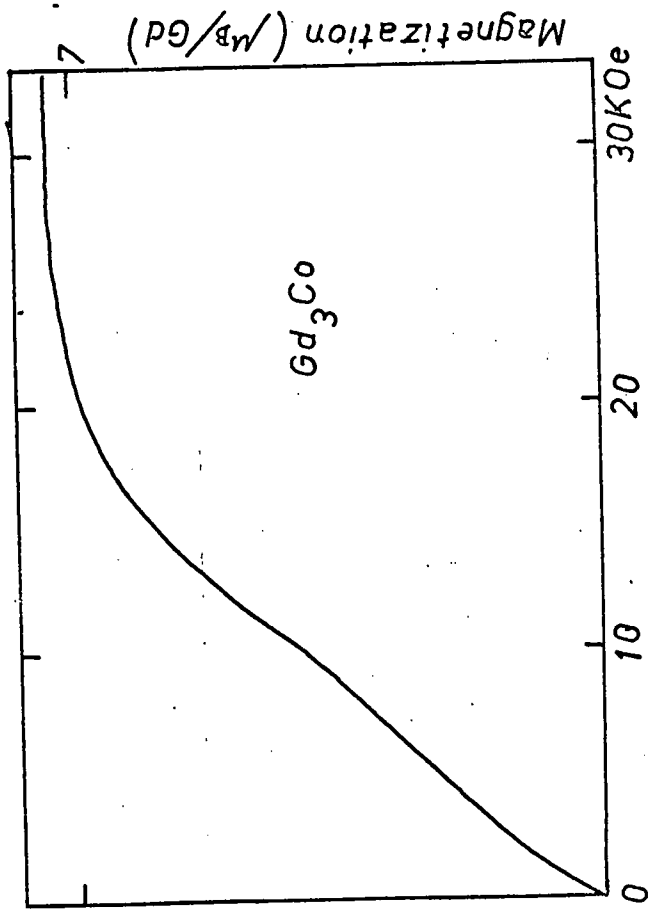


Fig:5.7 M vs H for Gd_3Co Powder at 4.2 K.

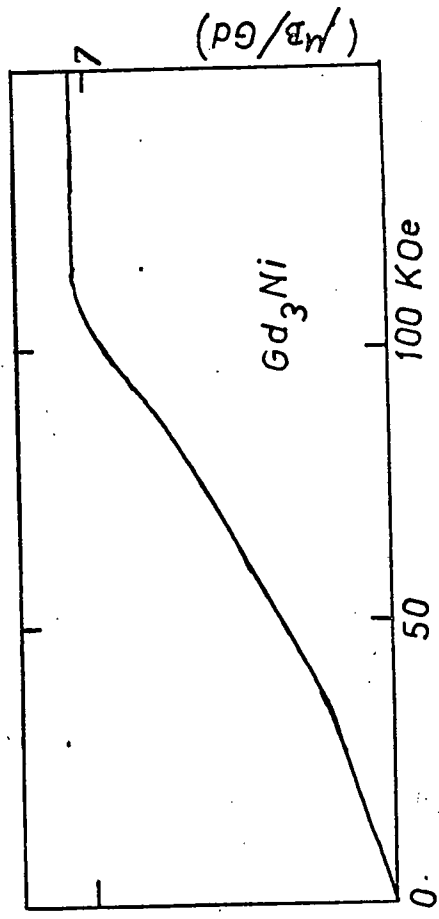


Fig.5.8 M vs H for Gd_3Ni Powder at 4.2 K.

Observations were made upon powder samples of Gd_3Co and Gd_3Ni and these gave magnetization vs field curves which were almost linear right up to saturation. The critical field had almost disappeared as a result of powdering (fig. 5.7). The small kink near the origin is believed to be an impurity effect. The kink was also observed in the bulk sample magnetization vs field curve of Gd_3Ni but not the bulk sample of Gd_3Co .

The just perceptible critical field for powdered Gd_3Ni was 14% less than that in the bulk sample. For Gd_3Co the critical field for the powdered sample was equal to that for the bulk sample.

The critical fields in the two types of sample of Gd_3Co are identical within the experimental error, since the critical field for the powder sample is hardly perceptible. The susceptibility measured from the magnetization vs field curve on the linear portion just above the impurity kink has values which are about 1.6 times those in the corresponding bulk samples. An antiferromagnetic material is expected to give a ratio of $3/2$ between the free powder and bulk sample initial susceptibilities. The closeness between these two numbers shows that the results are not inconsistent with an interpretation based upon antiferromagnetic theory.

The magnetization vs field curves were also investigated for a number of other powder samples in the range of compositions between the end points Gd_3Co and Gd_3Ni . In all cases where the sample was powdered, it was found that the critical field had become very much less sharp, and the initial susceptibility was increased by a factor of approximately $3/2$ above the value for the corresponding bulk sample.

5.3.2 Magnetic Measurements as a Function of Temperature

5.3.2a A.C. Susceptibility

The transformer method for plotting A.C. susceptibility as a function of temperature (see section 2.4.1) was used in order to estimate the ordering

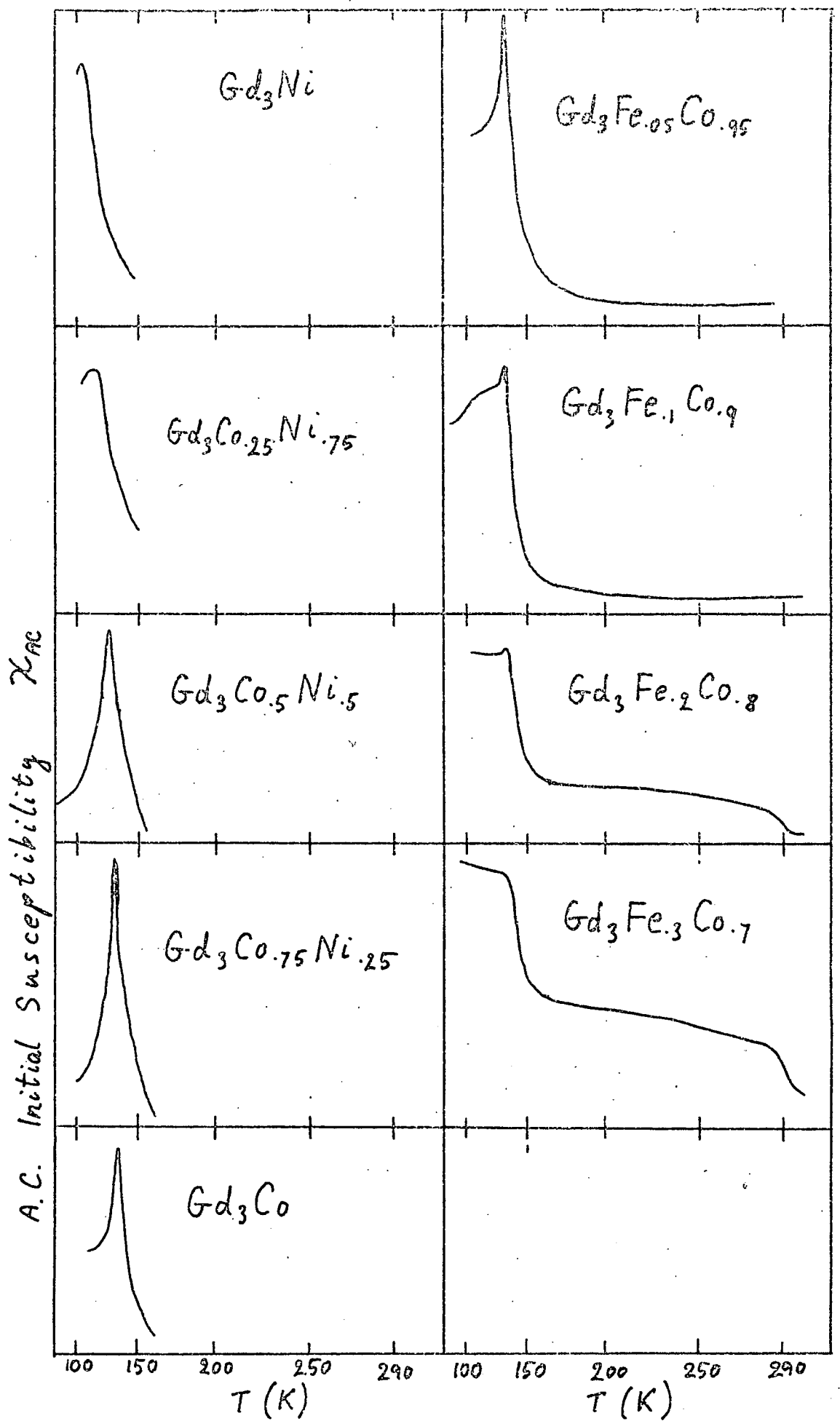


Fig. 5.9 Néel Peaks of χ_{AC} vs T for $Gd_3(Fe,Co)$ and $Gd_3(Co,Ni)$

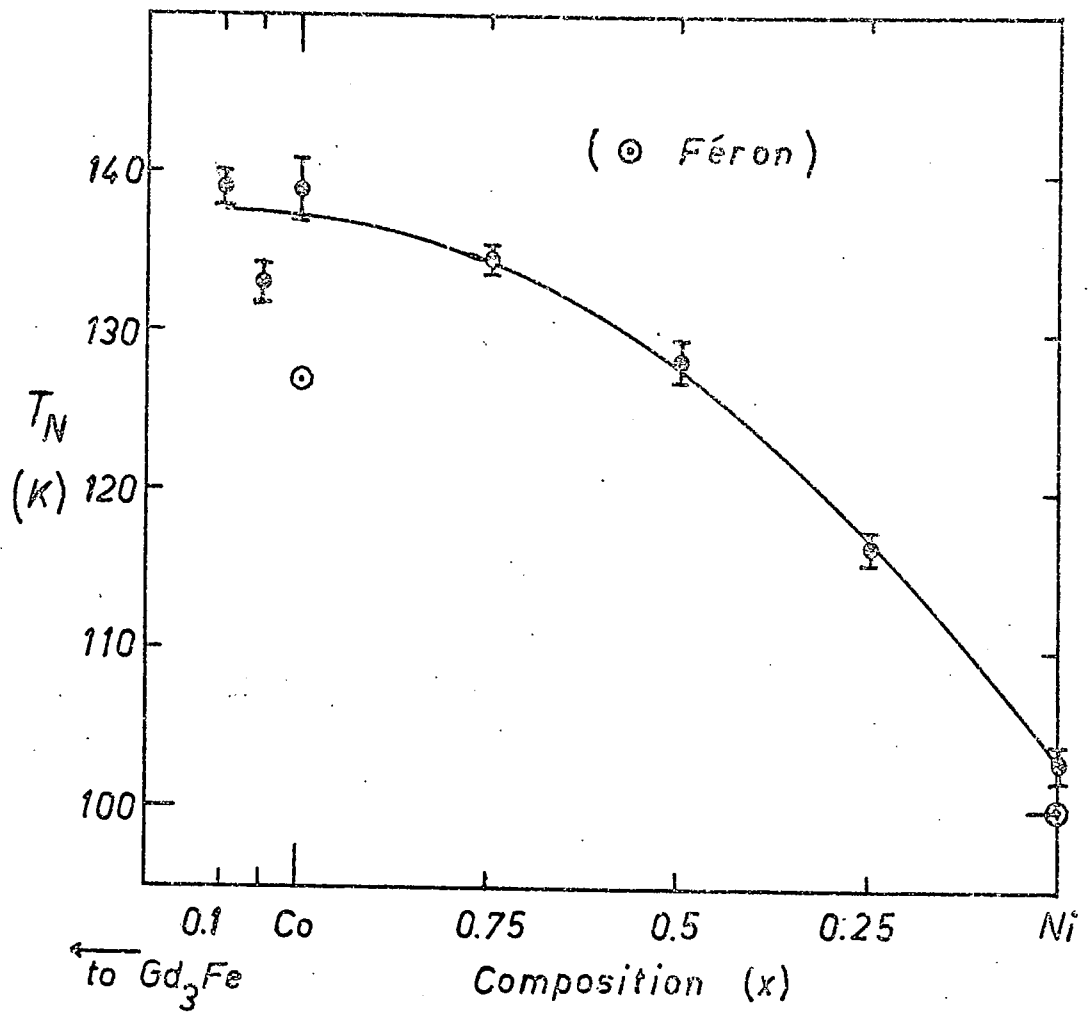


Fig.5.10 T_N vs Composition (from χ_{AC})

temperatures of the compounds. The results are shown in fig. 5.9 where the horizontal axis, indicating the copper-constantan thermo-couple voltage, has been calibrated in degrees Kelvin. Vertical deflections are proportional to χ_{AC} the A.C. initial susceptibility of the sample which was in the form of a powder. The sample was cooled by liquid nitrogen and the temperature was raised by lowering the dewar gradually.

The existence of sharp peaks in the susceptibility suggests that we may be dealing with antiferromagnetic materials. The temperatures T_N at which these peaks occurred were obtained while warming and are plotted in fig. 5.10 as a function of composition.

The position of the peak in the χ_{AC} vs T plot for a given sample was not reproducible. The plot obtained while warming was considerably different from that obtained while cooling. This is believed to be partly due to a temperature lag between the sample and thermocouple junction and partly due to a genuine hysteresis in χ_{AC} vs T for the sample. This latter cause is suspected to give a large contribution because the irreproducibility was more for some compounds than for others. The compound $Gd_3Fe_{.1}Co_{.9}$ for example, showed a χ_{AC} vs T plot which was completely reproducible as far as could be seen, irrespective of whether the temperature was rising or lowering. For the other compounds the behaviour depended very much upon the magnetic history of the sample, i.e. whether it was going from the ordered to the disordered state, or vice-versa, or how far the temperature was from the Néel point when the temperature run was commenced.

Even though the ordering temperatures are denoted by T_N , conforming with the notation used for antiferromagnetic materials, the possibility should be borne in mind that these compounds might not be antiferromagnetic. However, in view of the results given so far, there is a strong likelihood of T_N being a genuine Néel point. The symmetry of the Néel peak is seen to show a systematic variation with 3d-electron concentration in the range of compositions with high 3d-electron concentration. From $Gd_3Co_{.5}Ni_{.5}$ which presents a symmetrical peak, the curve on the left of the peak appears to be approaching a level, whose height increases until, at $Gd_3Fe_{.2}Co_{.8}$ it is almost level with

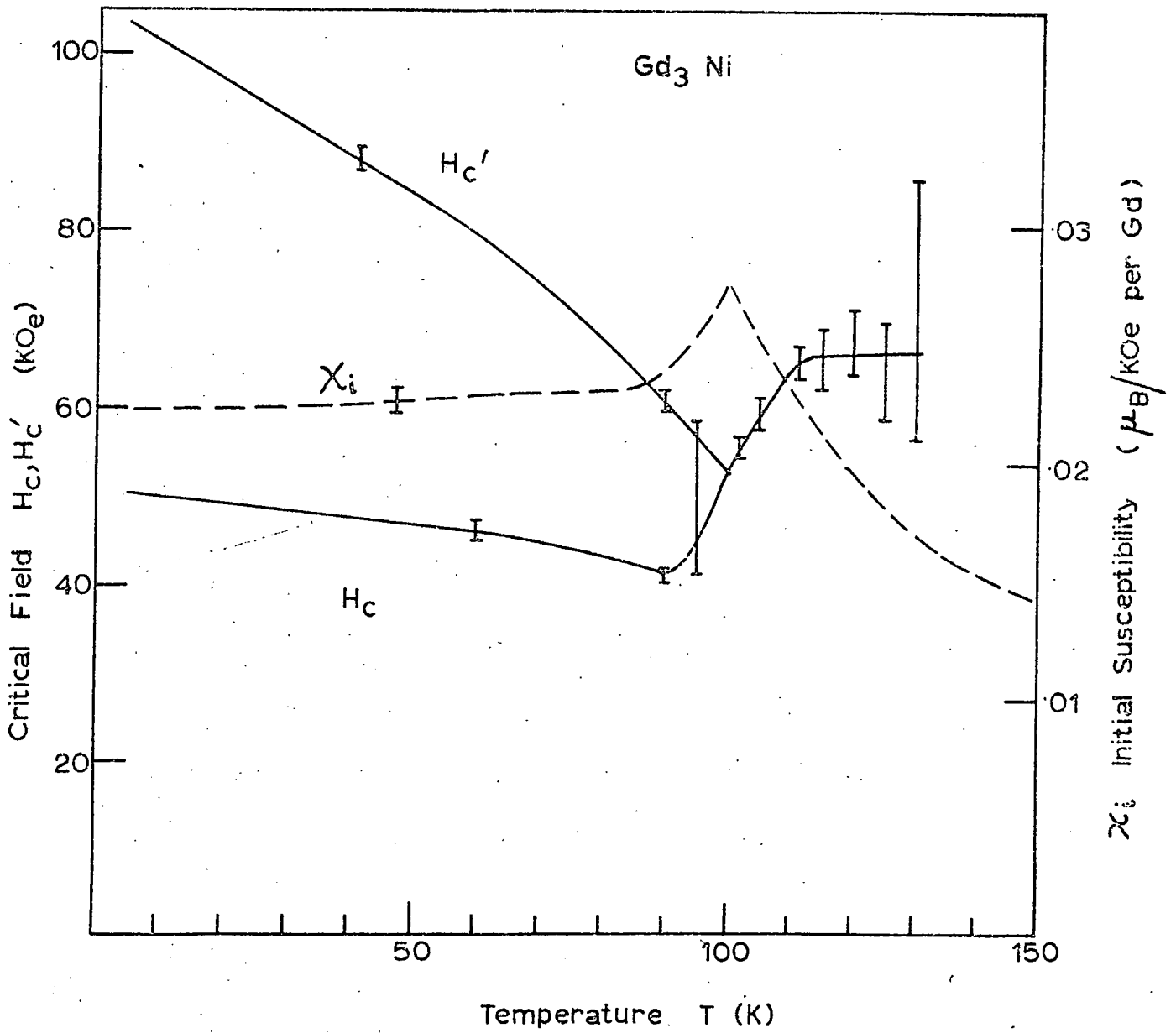


Fig. 5.11 χ_i, H_c, H_c' vs T for $Gd_3 Ni$

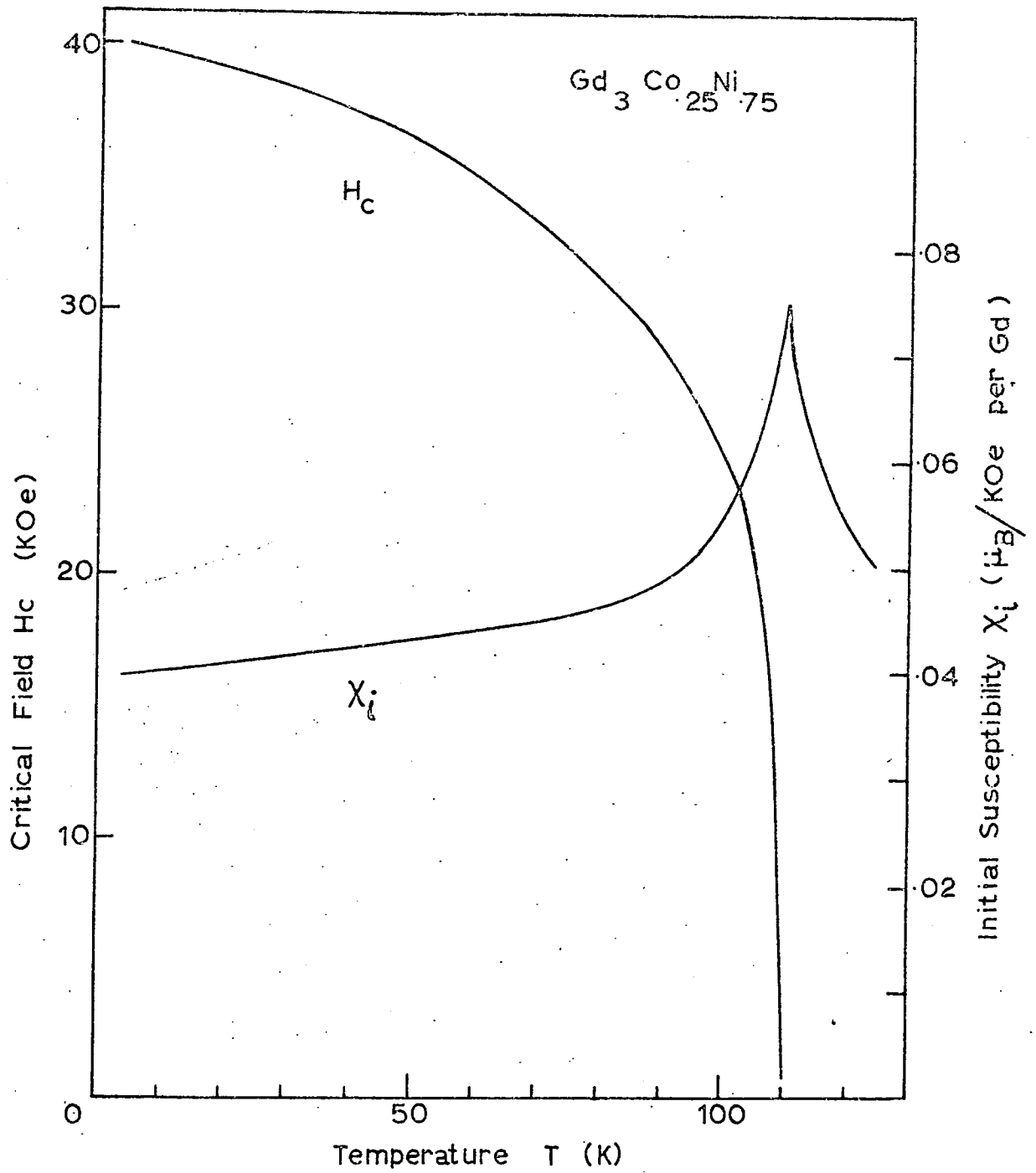


Fig. 5.12 χ_i, H_c vs T for $Gd_3Co_{.25}Ni_{.75}$

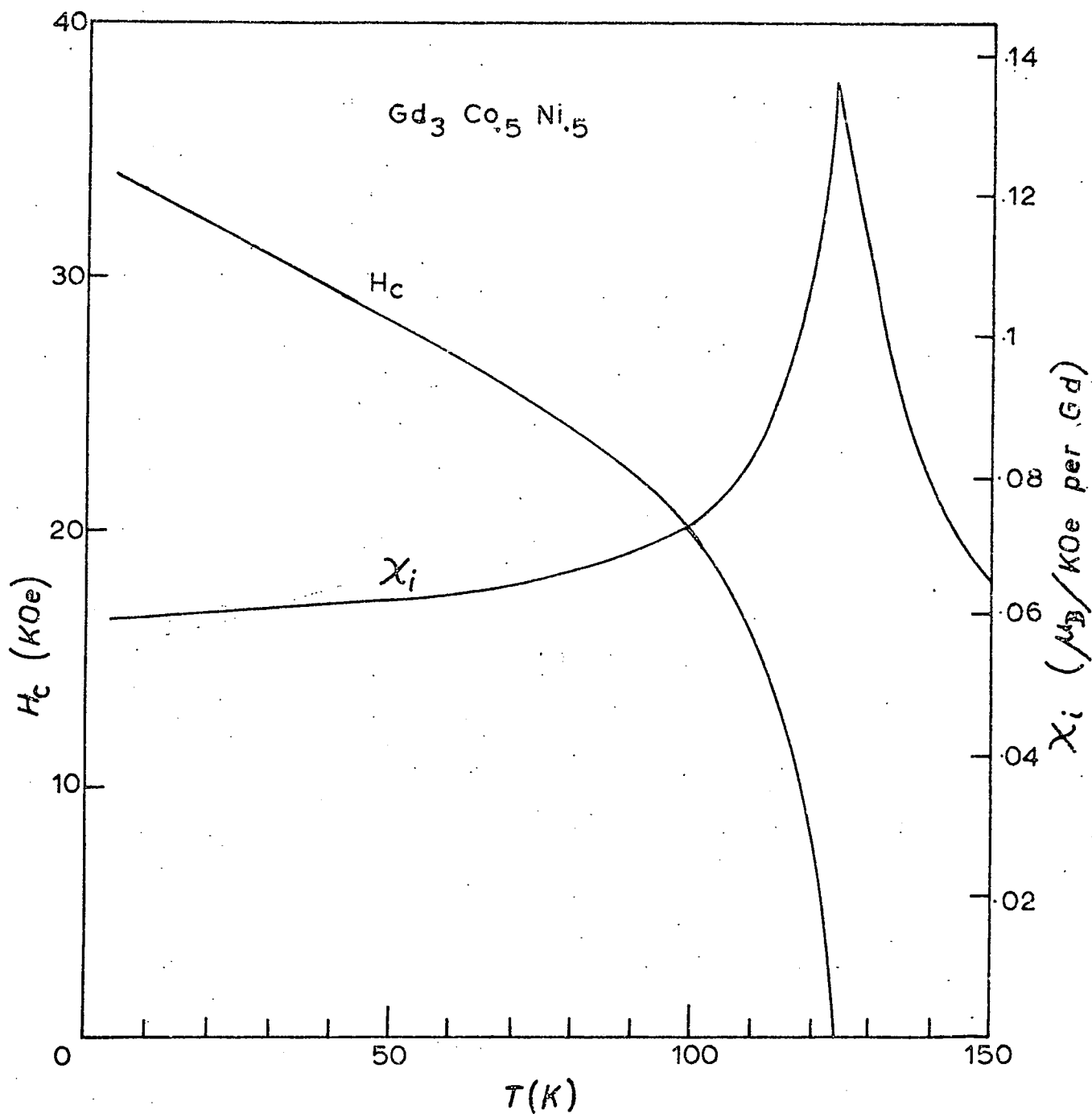


Fig. 5.13 χ_i , H_c vs T for $Gd_3 Co_5 Ni_5$

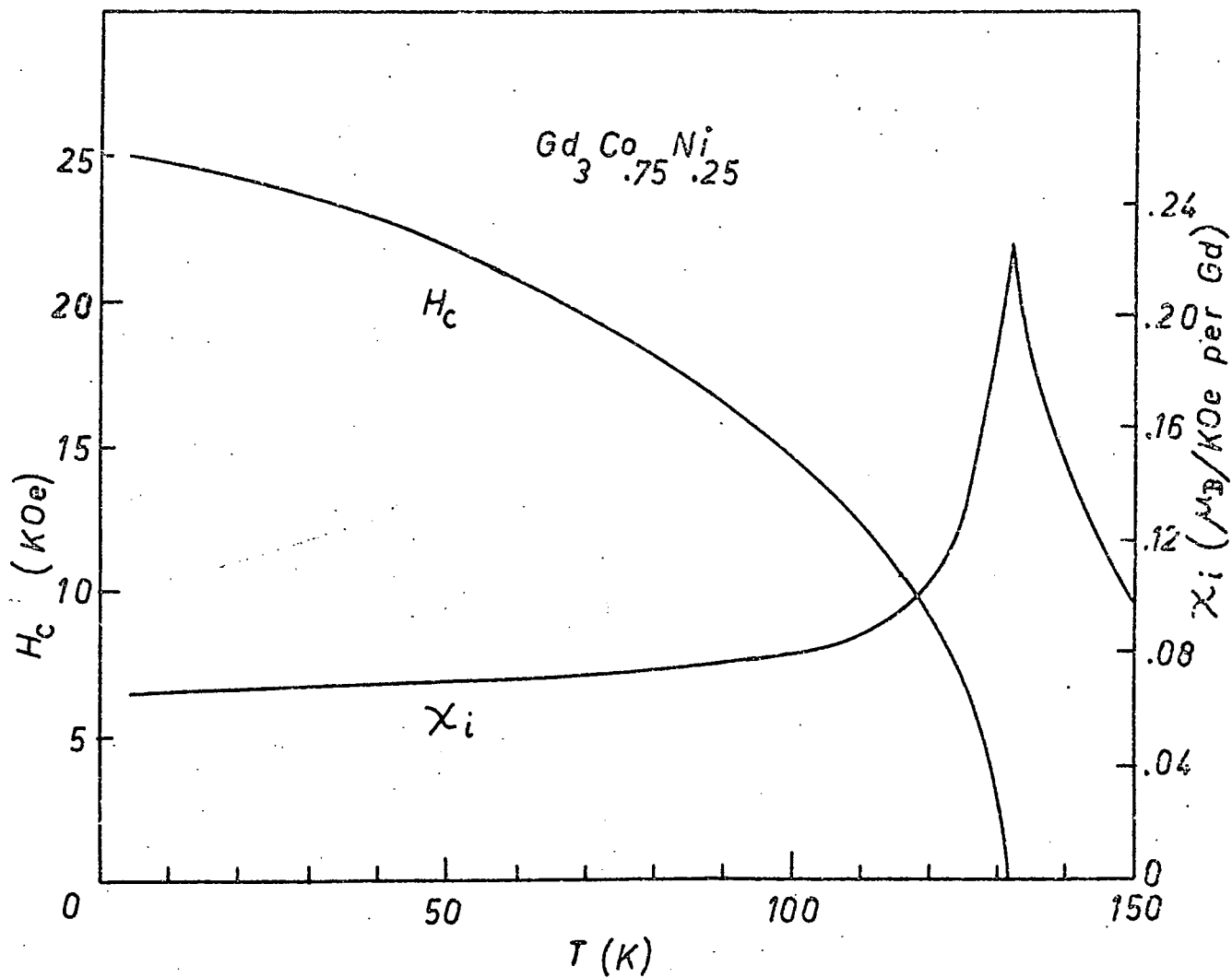


Fig. 5.14 χ_i , H_c vs T for $Gd_3Co_{.75}Ni_{.25}$

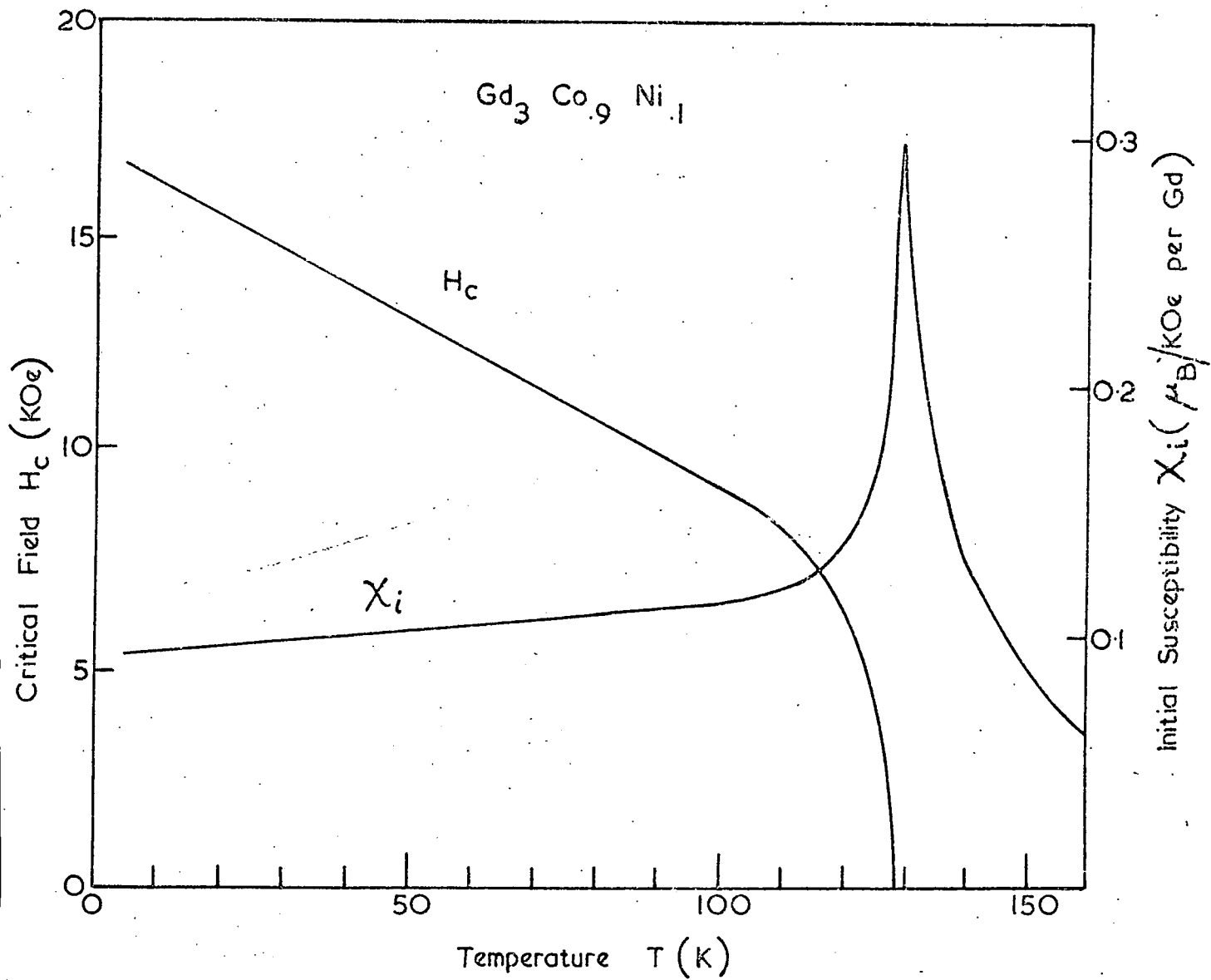


Fig. 5.15 H_c, χ_i vs T for $Gd_3 Co_9 Ni_1$

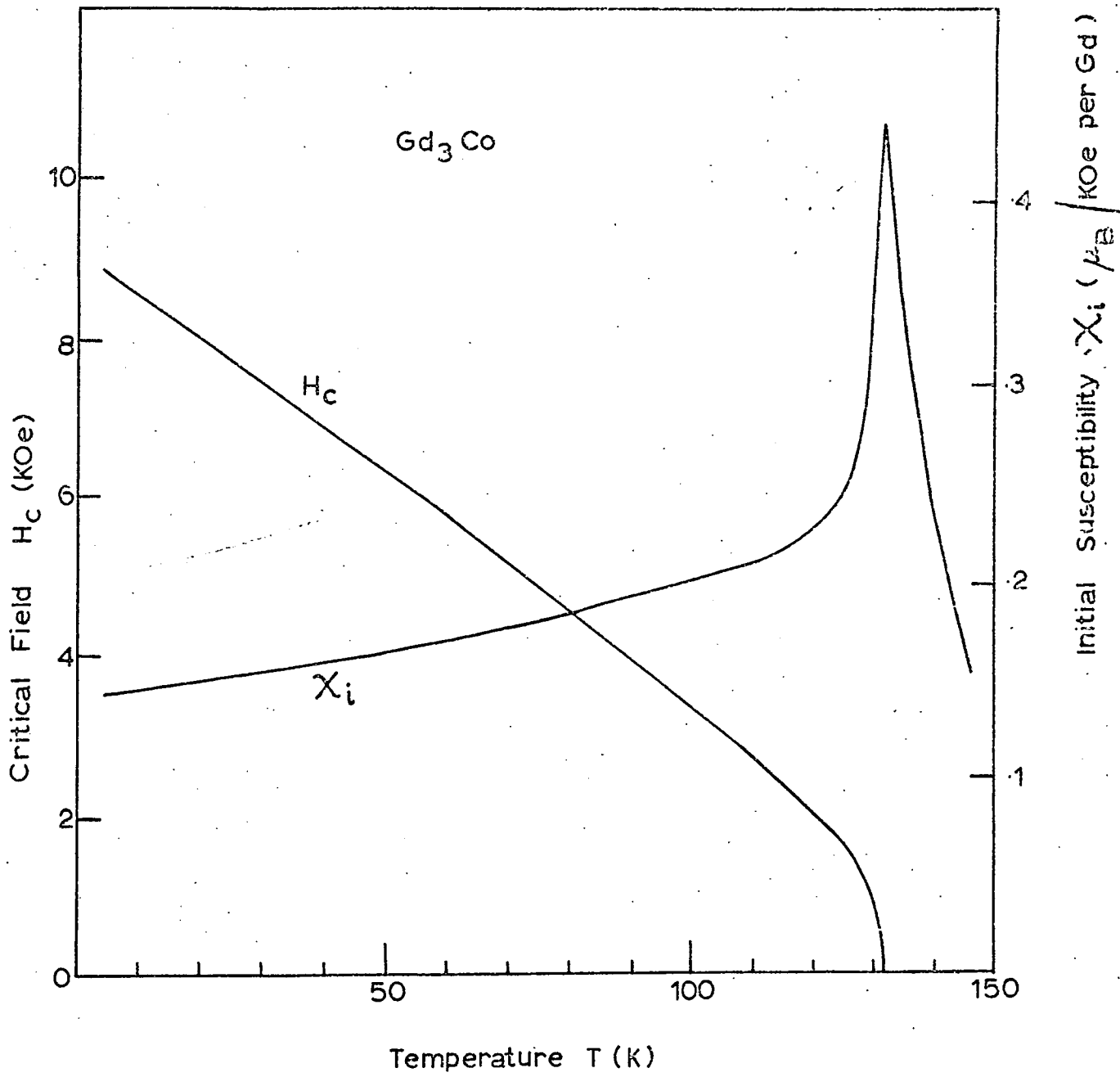


Fig.5.16 χ_i , H_c vs T for Gd_3Co

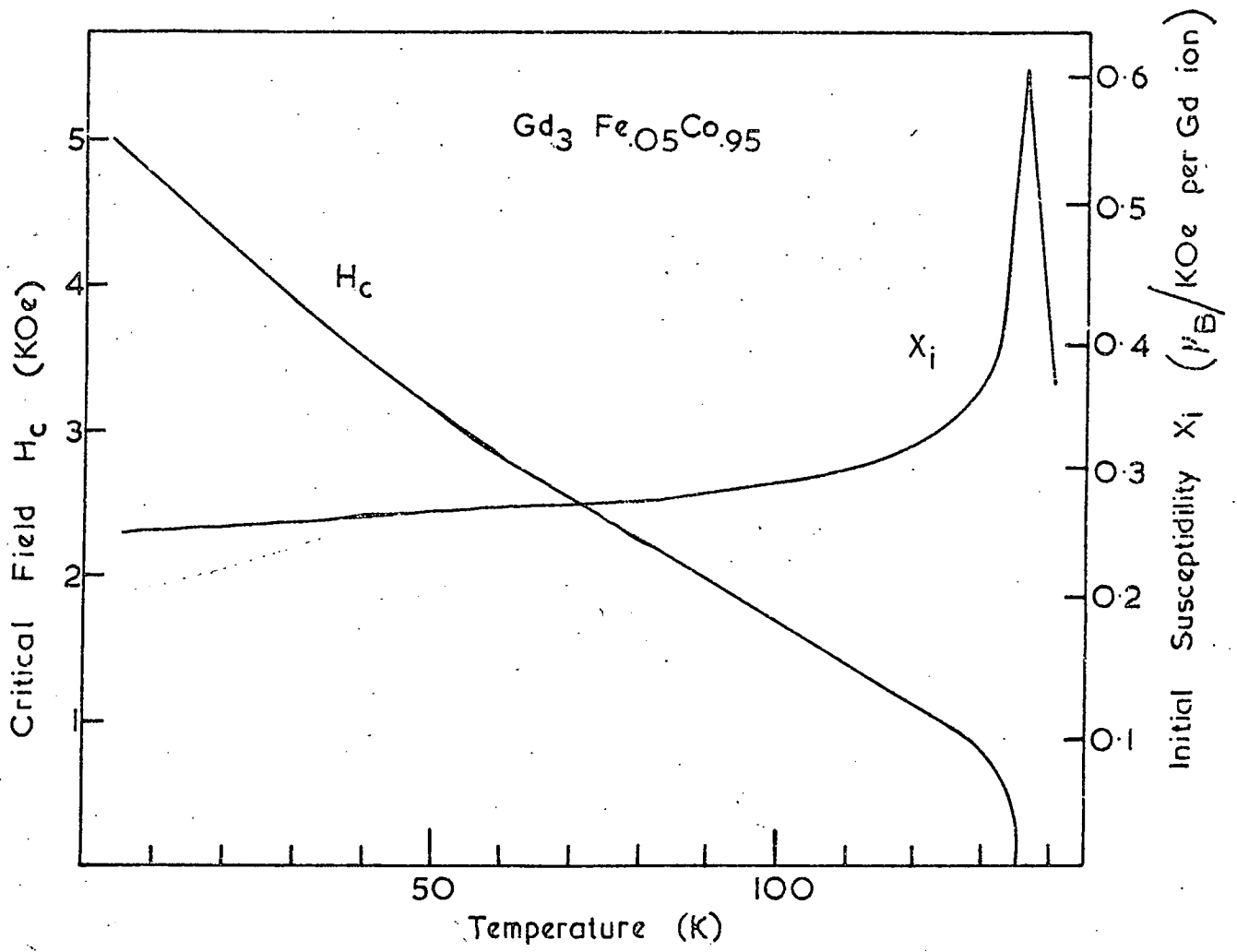


Fig. 5.17 X_i , H_c vs T for $Gd_3 Fe_{0.05} Co_{0.95}$

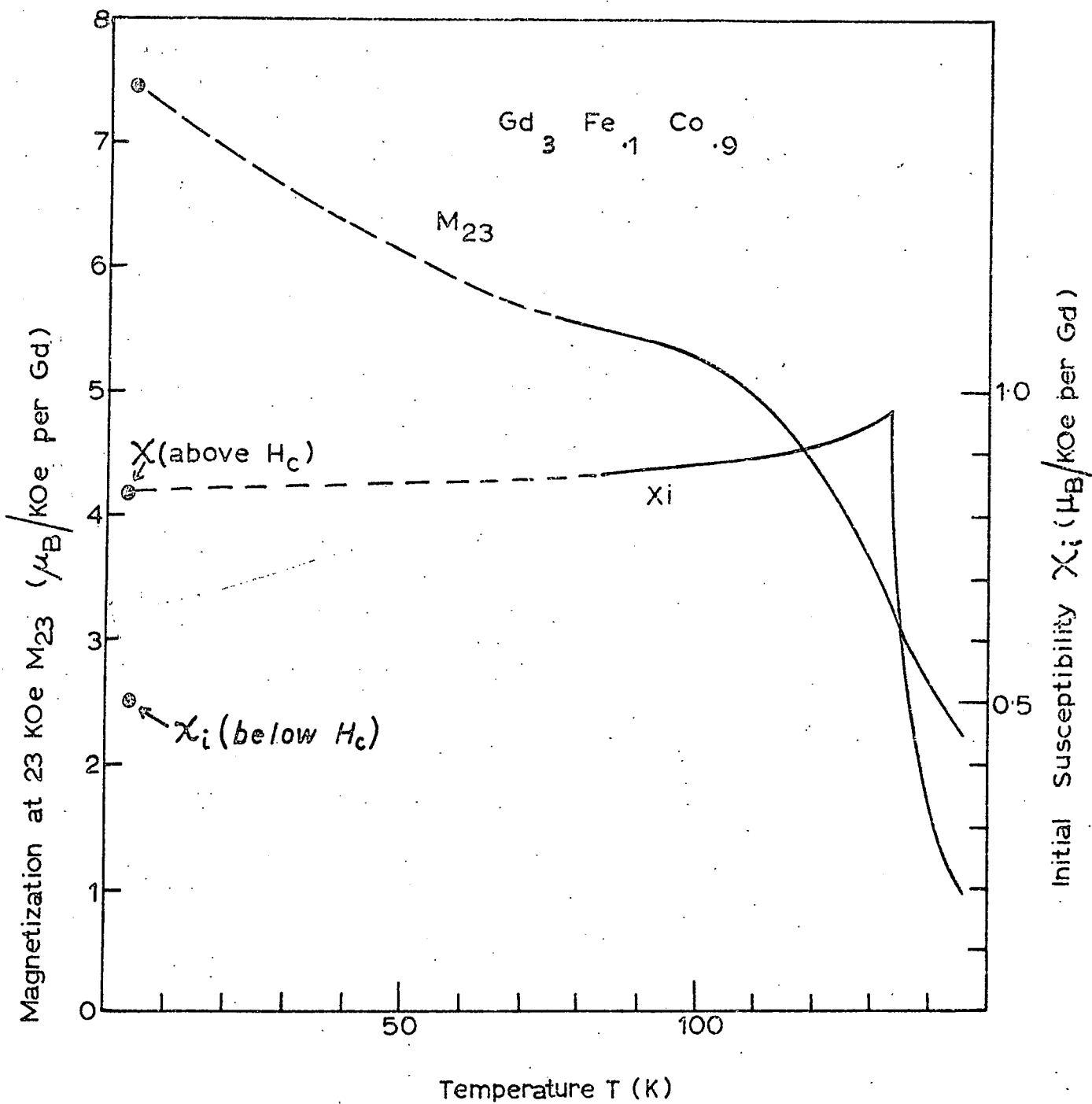


Fig. 5.18 χ_i, H_c, M_{23} vs T for $Gd_3Fe_{.1}Co_{.9}$

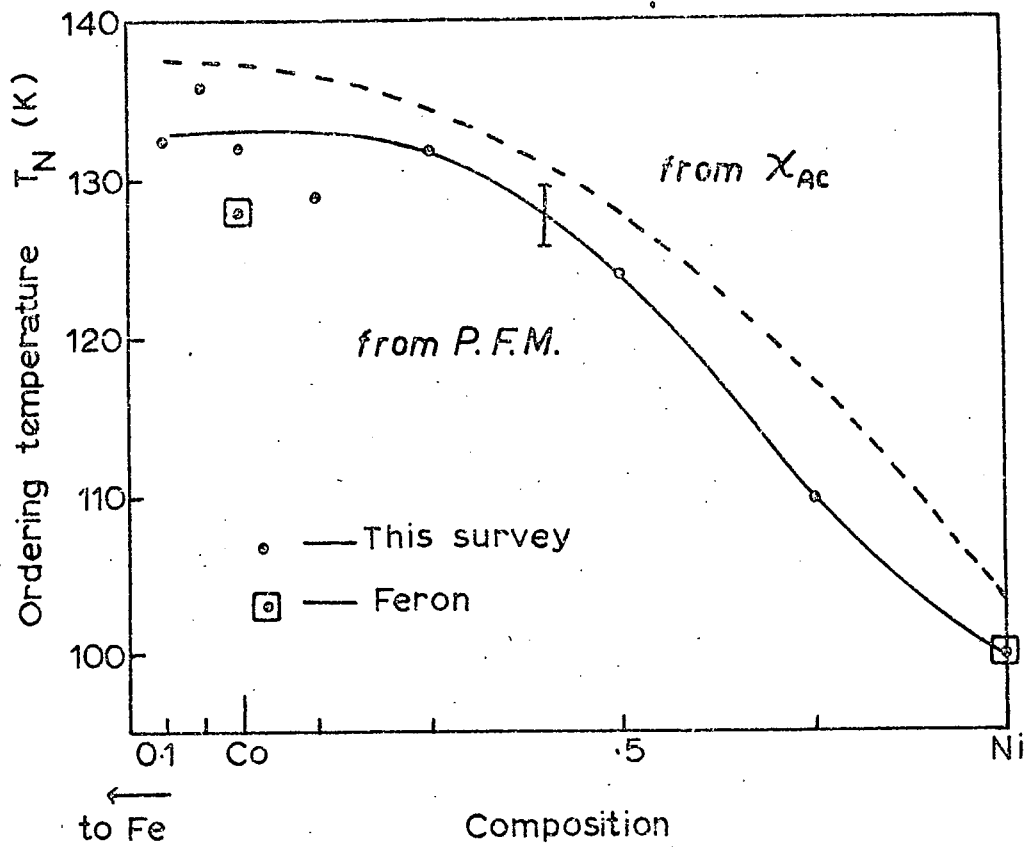


Fig. 5.19 T_N vs Composition for $Gd_3(Fe,Co)$, $Gd_3(Co,Ni)$

the peak. In the $\text{Gd}_3\text{Fe}_{.3}\text{Co}_{.7}$ composition the peak has disappeared altogether.

For $\text{Gd}_3\text{Fe}_{.2}\text{Co}_{.8}$ a Curie point at 290 K is evident and this becomes more prominent on further Fe substitution. This coincides with the Curie point of metallic gadolinium and indicates that we have more than one phase in $\text{Gd}_3\text{Fe}_{.2}\text{Co}_{.8}$ and $\text{Gd}_3\text{Fe}_{.3}\text{Co}_{.7}$. This is consistent with the apparent instability of the Fe_3Co structure for greater than 10% Fe substitution, as deduced from the X-ray diffraction data.

5.3.2b Pulsed Field Measurements as a function of Temperature

A magnetization vs field oscillogram was photographed for various temperatures from 4.2 K up to about 160 K, thus observing the variation of critical fields, susceptibility, and high field magnetization of bulk samples while passing between the magnetically ordered and the disordered state. The results are plotted in figs. 5.11 to 5.18. χ_i is seen to pass through a sharp peak at the temperature T_N . This is considered to be a more accurate measure of T_N than was obtained from the A.C. susceptibility, for the reasons given in section 2.4.3. The values of T_N from this method and the A.C. susceptibility technique are plotted in fig. 5.19. T_N appears to be constant for 3d electron concentrations less than that of $\text{Gd}_3\text{Co}_{.75}\text{Ni}_{.25}$. The critical field H_c is seen from the figures 5.11 to 5.18 to decrease continuously with rising temperature, finally dropping rapidly to zero at the Néel point T_N , except in the compound Gd_3Ni .

5.3.3 Gd_3Ni - (Magnetic parameters as a function of T)

In fig. 5.11 for Gd_3Ni χ_i , H_c , H_c' are plotted as a function of temperature. H_c decreases slowly with rising temperature while H_c' decreases more rapidly. The two critical fields H_c and H_c' approach each other and become unresolvable at about 5 degrees below T_N (=100K). Above T_N the critical field still exists and increases with increasing temperature, finally becoming imperceptible at about 130 K. It is not known whether the final disappearance of the critical field is effected by its approaching zero or by its remaining a large value. In the latter case it can disappear by decreasing the sharpness of its perturbation upon the magnetization vs field curve until it is not longer present.

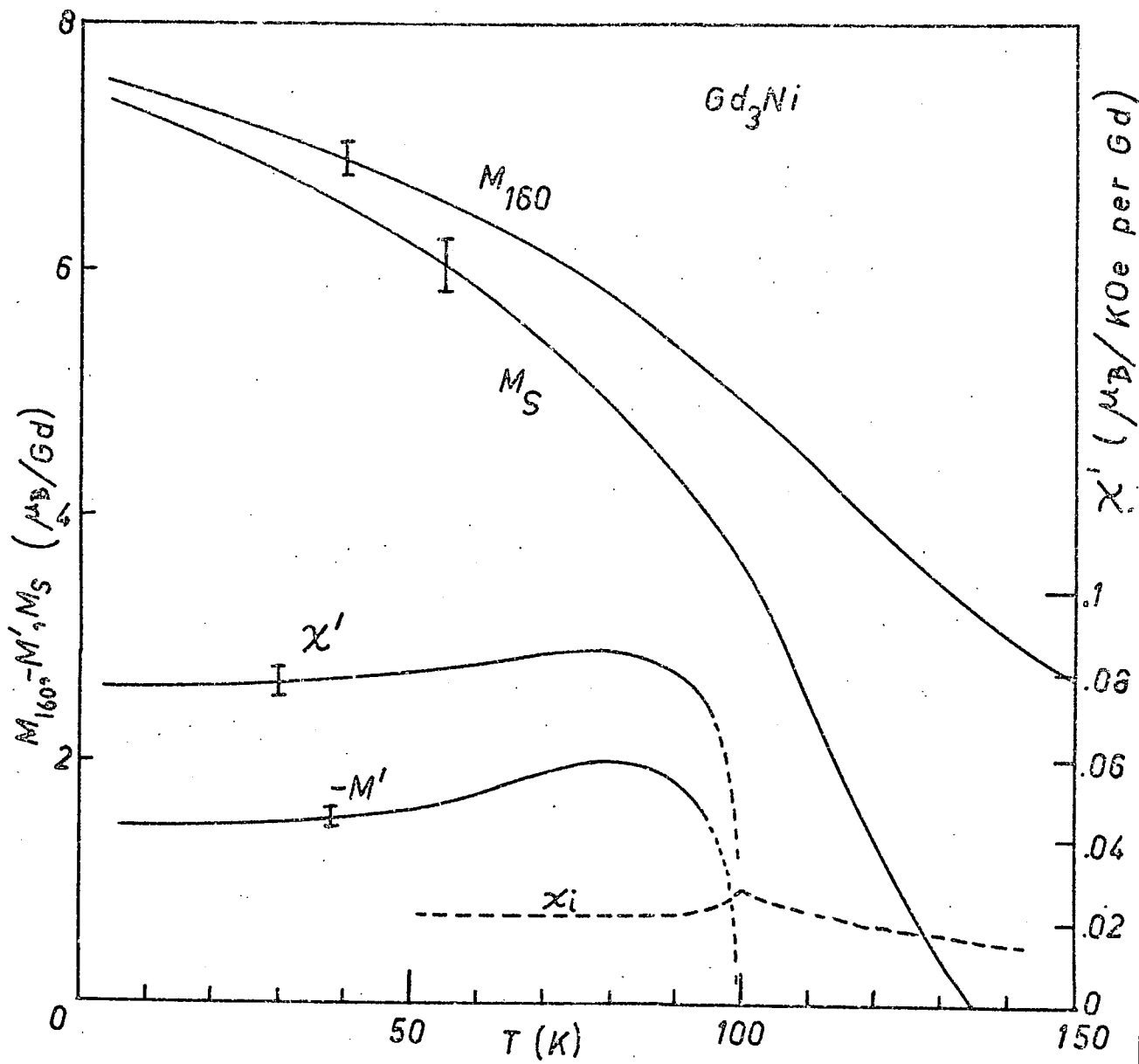


Fig. 5.20 $\chi_i, M_{160}, -M', M_S$ for Gd_3Ni

It is also not known whether the critical field above T_N is a continuation of H_c or H_c' or both of these. When H_c ceases to be resolvable from H_c' it is possible that it has dropped rapidly to zero between measurements. It is also possible that H_c has risen to continue along the values of critical field above T_N . If this is the case, then it is observed that the extrapolation of H_c' from the region where it is distinguishable intersects H_c at the Néel point; it could also be that H_c' drops to zero at T_N with H_c rising to continue above T_N . Two other possibilities remain: H_c could drop between measurements becoming zero at T_N while H_c' suddenly rises at T_N to continue above T_N . The other possibility, which is less likely, is that both H_c and H_c' drop rapidly, becoming zero at T_N , and that the new critical field above T_N has its origin in an entirely different mechanism than that which gives rise to H_c or H_c' .

In fig. 5.20 M_{160} , χ' , M' and M_s are plotted for Gd_3Ni . M_{160} , the magnetization at 160K Oe does not show any sharp decrease at the Néel point and is still large at 150K. The M vs. H curve is linear at 150K where the sample is evidently paramagnetic.

In order to obtain some measure of the spontaneous magnetization within a sub-lattice of Gd_3Ni , the parameter M_s was obtained from M_{160} . The M vs H curve was extrapolated from the highest field portion near 160K Oe back to $H = 0$. A linear M vs H curve gave a value of $M_s = 0$. Since a paramagnet in this high temperature region is expected to give a linear M vs H curve, the disappearance of any spontaneous magnetization is consistent with $M_s = 0$. The value of M_s as a function of T is also plotted in fig. 5.20 where it can be seen that M_s becomes zero at $T = 135K$. This is the point at which the critical field becomes imperceptible.

Also seen in fig. 5.20 is χ' , the susceptibility in the linear part of the M vs H curve between the two critical fields H_c and H_c' . When H_c and H_c' approach each other near the Néel point, χ' becomes a meaningless concept. It is therefore not certain whether it is tending to zero at T_N or whether it tends to the value of χ_i at the Néel peak. The extrapolation to $H = 0$

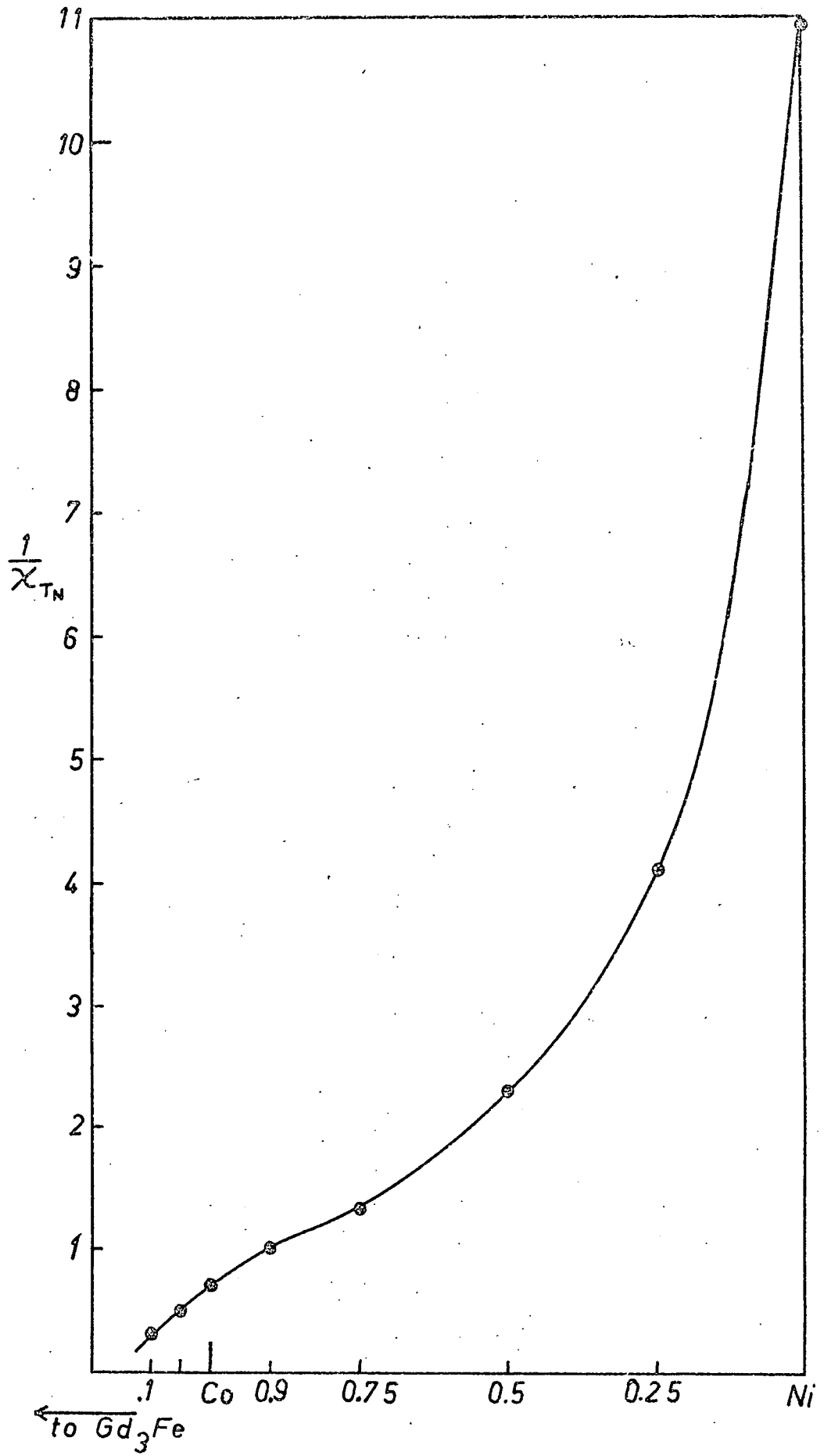


Fig. 5.21 $(\chi_{TN})^{-1}$ vs Composition for $Gd_3(Fe,Co)$, $Gd_3(Co,Ni)$

of the linear portion of the M vs H curve from which χ' is measured, gives M' , the negative intercept on the M axis. This is seen to have the same type of variation as χ' and its value at T_N is similarly uncertain.

5.3.4 $Gd_3Co_{.25}Ni_{.75} - Gd_3Fe_{.1}Co_{.9}$ (Magnetic Parameters as a function of T)

The curves of H_c vs T for the compounds other than Gd_3Ni show a systematic trend with increasing 3d-electron concentration. Near the $Gd_3Fe_{.05}Co_{.95}$ end of the range of compositions H_c drops rapidly as soon as T rises from 4.2K, giving an H_c vs T plot which is concave upwards. Near the nickel rich end of the range H_c remains high until near T_N where it drops rapidly. In Gd_3Ni itself H_c not only remains almost constant but might even rise in the region of T_N as described above. The ratio $\chi_{T_N}/\chi_{4.2}$ between the initial susceptibility at the Néel peak and that at 4.2K is well in excess of 3/2, that expected from a simple two-sublattice antiferromagnet with no anisotropy.

The M vs H curves for $Gd_3Fe_{.1}Co_{.9}$ as a function of temperature were obtained from 77K upwards. The curve at 4.2K showed a critical field, but this had disappeared entirely at 77K, so that only the parameters χ_1 and M_{23} (at 23 kOe) were measurable. These are shown in fig. 5.18 where the dashed line links the results at 4.2K with those at 77K. The values of the susceptibility above and below the critical field at 4.2K are shown. Since H_c has dropped to very near zero at 77K it is impossible to measure χ_1 below H_c . The M vs H curves for $T > 77K$ are linear near the origin and the apparent initial susceptibility corresponds to the ferromagnetic phase above H_c . It is therefore reasonable to connect the results for $T > 77K$ with χ at 4.2K measured above the critical field, as shown in fig. 5.18. The rapid fall of H_c as T rises from 4.2K in $Gd_3Fe_{.1}Co_{.9}$ is consistent with the increasing upward concavity of the H_c vs T curves when substituting Fe for Co in Gd_3Co . M_{23} decreases rapidly on increasing T from 4.2K with no discontinuities at the Neel point. The M vs H curves are not linear even at 145K which is in the paramagnetic region above T_N . Fig. 5.21 shows the variation with composition of $1/\chi_N$.

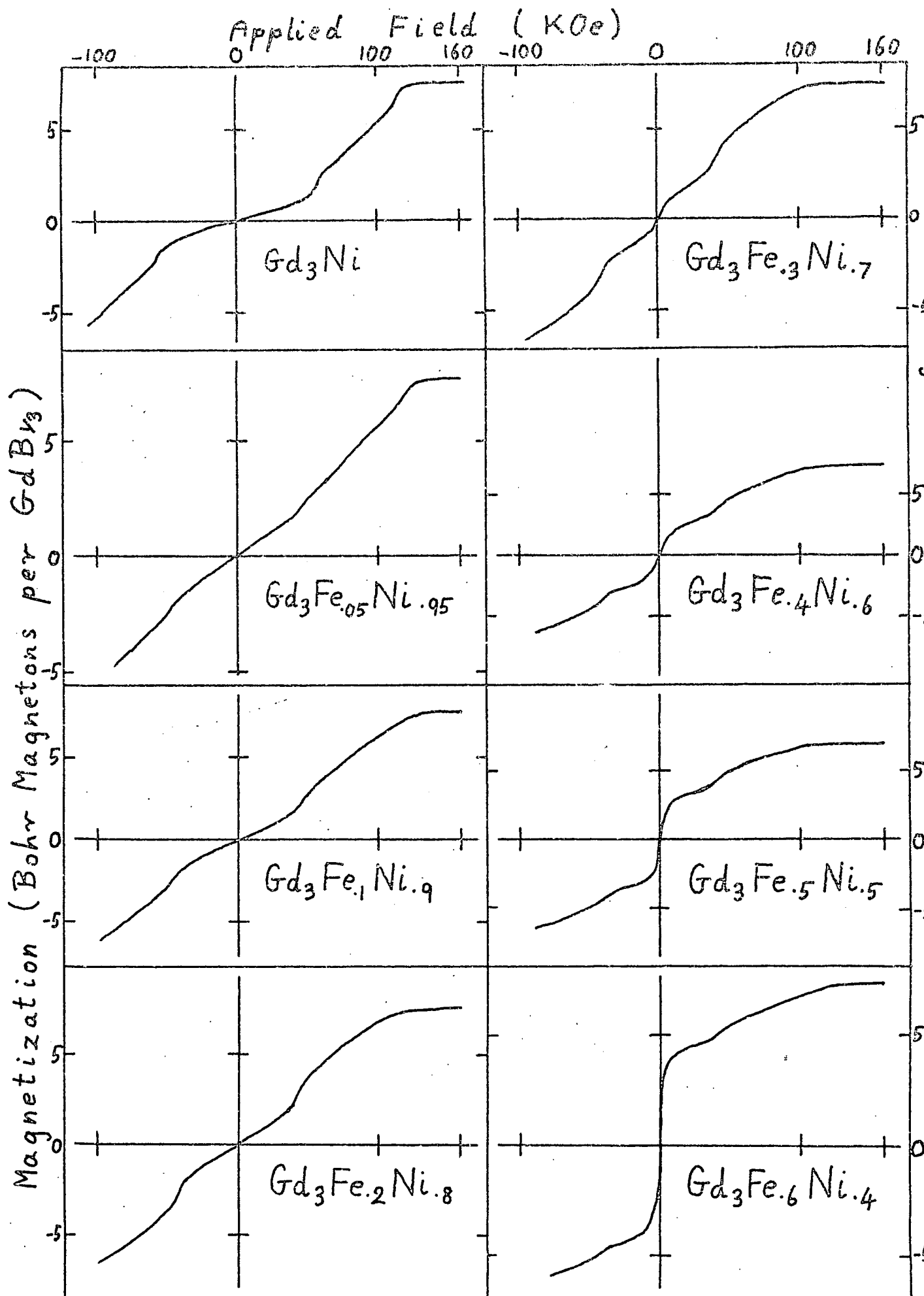


Fig. 5.22 Pulsed Field Magnetization Curves for $Gd_3(Fe,Ni)$ at 4.2

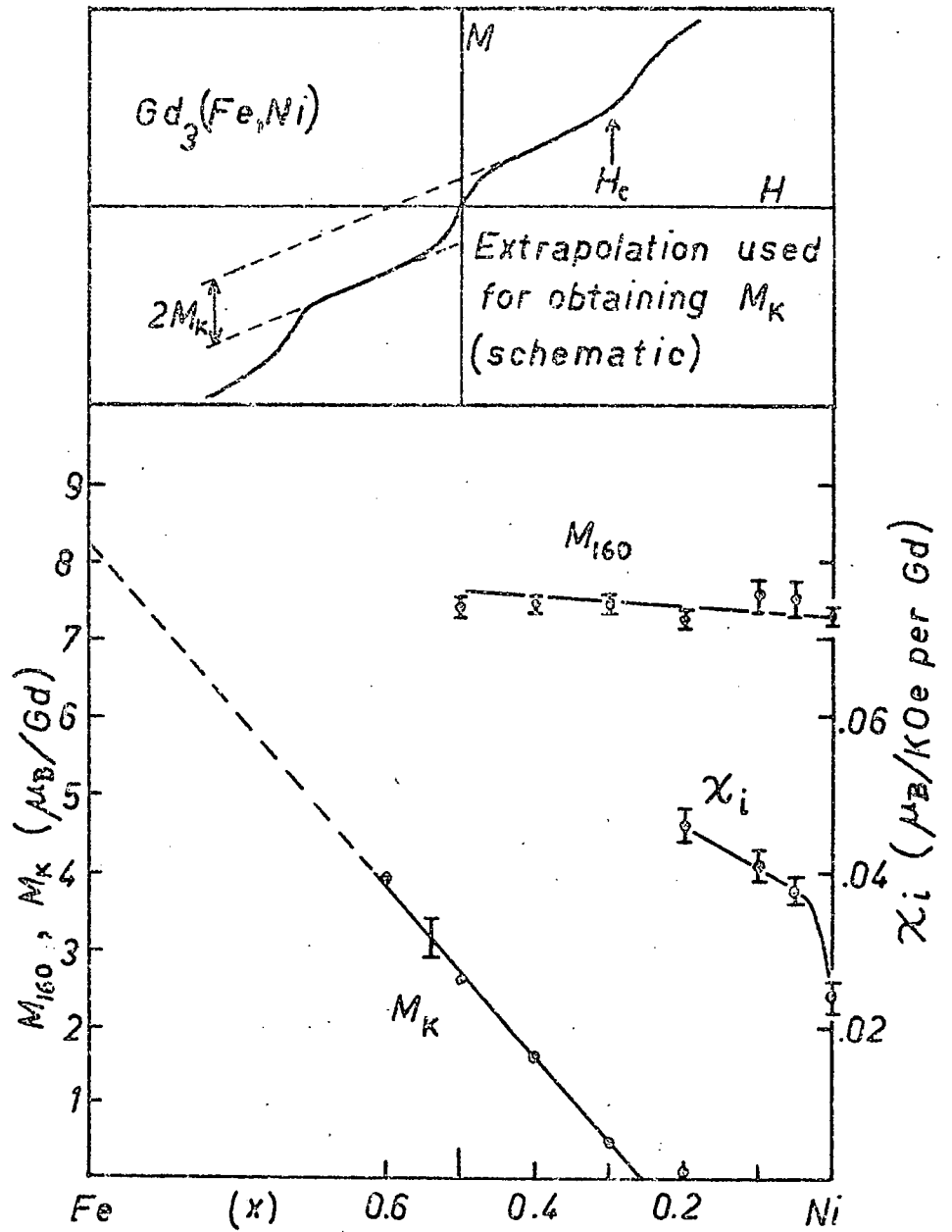


Fig. 5.23 M_{160} , M_K , χ_i vs Composition at 4.2 K

5.4 Magnetic Measurements on $Gd_3Fe_xNi_{1-x}$

5.4.1 Pulsed Field Measurements at 4.2K

The M vs H curves of the compounds $Gd_3(Fe_xNi_{1-x})$ from Gd_3Ni up to 60% Fe substitution are shown in fig. 5.22. The left hand column of curves up to $x = 0.2$ is believed to represent genuine compounds.

From $x = 0.3$ a large kink near the origin appears and gradually increases in size on further iron substitution. Let us assume that this kink is the result of a foreign phase contribution which is ferromagnetic and that this is superposed upon the Gd_3B contribution to the M vs H curve. It would then appear that Fe substitution forming single phase Gd_3B occurs up to $x \approx 0.2$. For $x > 0.2$ the contribution from the foreign phase is proportional to the Fe content (fig. 5.23). In this figure is shown M_K versus composition. The quantity M_K is the saturation magnetization of the ferromagnetic foreign phase. This was estimated by assuming saturation was attained in fields less than the critical field. If this is valid, then the slope below the critical field is due to the initial susceptibility of the Gd_3B phase. This region was extrapolated (fig. 5.23) linearly back to $H = 0$ in order to estimate the value of M_K superposed on the Gd_3B contribution. The intercept on the M axis was taken as M_K . In Fig. 5.23 M_K is seen to vary linearly with composition. This straight line, when extrapolated to the Gd_3Fe composition gives a value of $8.2 \mu_B/Gd$ for Gd_3Fe . Gd_3Fe does not form as a single stoichiometric compound. If the Gd and Fe metals are assumed to contribute to the saturation moment of Gd_3Fe , the value of $8.3 \mu_B/Gd$ is to be expected. Considering the rudimentary method by which M_K was estimated this is very close to the extrapolated value $8.2 \mu_B/Gd$. The straight line variation of M_K with composition intersects the composition axis at approximately $x = 0.25$. If our original assumption is correct, that the kink near the origin of the M vs H curve is due to the appearance of a ferromagnetic foreign phase, then it would seem that this phase first appears at $x = 0.25$. It is therefore likely that the Fe_3C structure is stable up to $x = 0.25$. This is consistent with the X-ray diffraction data for which the diffracted lines started to deteriorate in quality for the sample

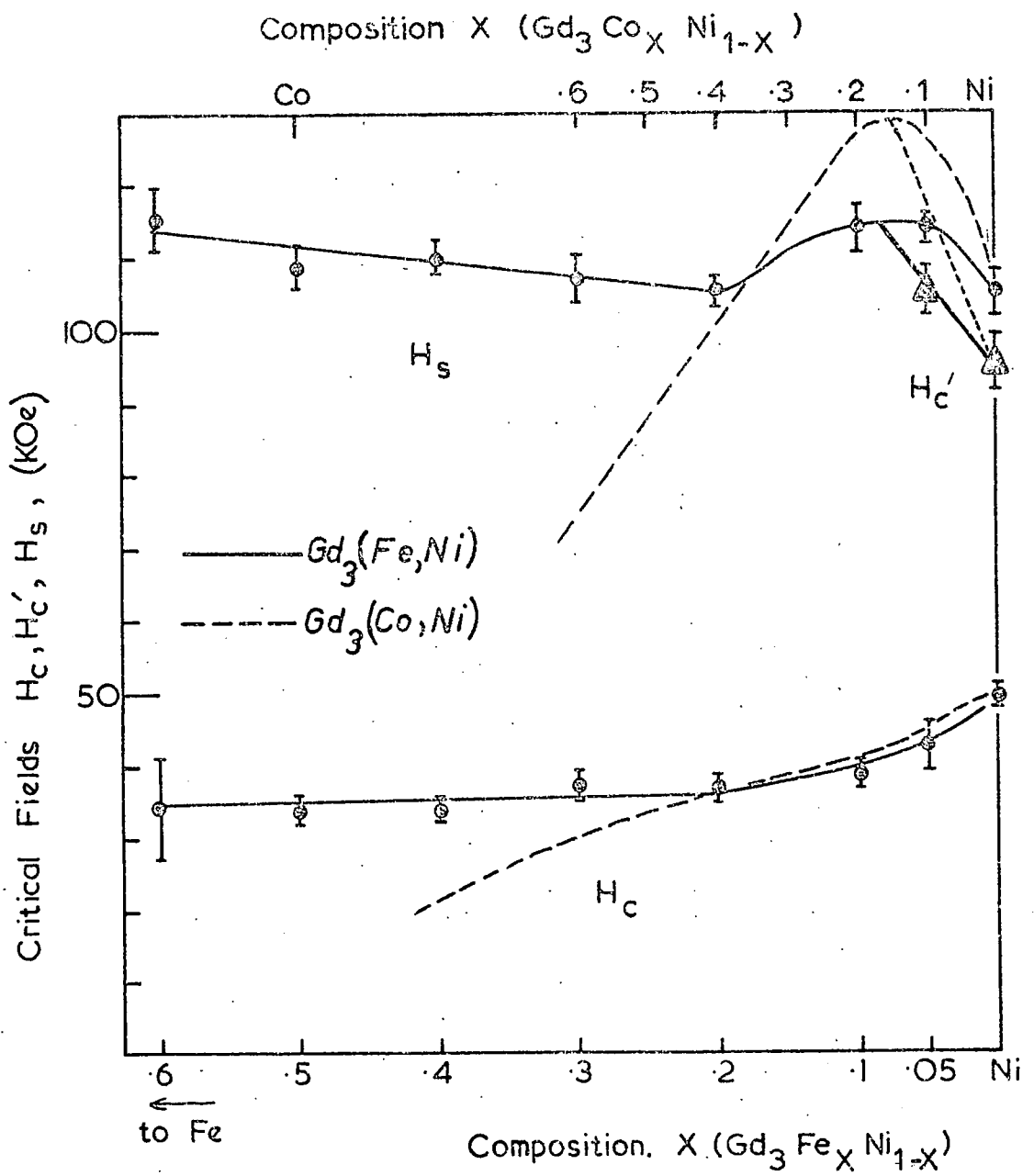


Fig. 5.24 H_c, H_c', H_s vs Composition (x)

with $x = 0.3$. The Fe_3C phase existing in samples with $x > 0.25$ is expected to correspond to the composition $\text{Gd}_3\text{Fe}_{.25}\text{Ni}_{.75}$, hence any magnetic properties which are characteristic of the Gd_3B component of the multiphase samples are expected to remain constant for $x > 0.25$.

In fig. 5.23 is shown also M_{160} and χ_1 . M_{160} probably increases slightly from the value at $x = 0$ for increasing Fe concentration. The increased expected theoretically assuming that the Fe contributes 2 holes per atom to the 3d band more than does nickel, is shown by the straight line. χ_1 could be measured reliably only for the single phase samples from $x = 0$ to $x = 0.2$. The variation is similar to that found in the $\text{Gd}_3(\text{Co},\text{Ni})$ system with the value of χ_1 for Gd_3Ni being much less than that for the neighbouring compositions.

In fig. 5.24 is shown the variation of the various critical fields with composition x . As in the $\text{Gd}_3(\text{Co}_x\text{Ni}_{1-x})$ the form of the M vs H curves for $x = 0$ and $x = 0.05$ lies in a class of its own, showing two critical fields H_c and H_c' . For the samples with $x \geq 0.1$ the critical field H_c' is no longer present. The line through H_c' intersects the curve of H_s between $x = 0.05$ and $x = 0.1$ at the point where H_s is a maximum. H_s decreases from $x = 0.1$ to $x = 0.2$. H_c decreases from $x = 0$ to $x = 0.2$. This behaviour is similar to that shown for the $\text{Gd}_3(\text{Co}_x\text{Ni}_{1-x})$ system, whose behaviour is also shown on the same figure for comparison. The behaviour of the compounds $\text{Gd}_3\text{Co}_x\text{Ni}_{1-x}$ is shown by the dashed lines in the figure, and is plotted in such a way that the abscissa represents the average 3d-electron concentration for the (Fe,Ni) and for the (Co,Ni) pseudobinaries alike. The assumption has been made that an Fe ion contributes one less 3d electron than a Co ion, and that a Co ion contributes one less 3d electron than a Ni ion. It is apparent that the curve for H_c in the (Fe,Ni) compounds is the same as that for H_c in the (Co,Ni) compounds when plotted as a function of the average 3d-electron concentration. The curves for H_s in the two systems are different but they both peak at the same value of the 3d-electron concentration. For samples with $x > 0.2$ the quantity H_c remains constant at approximately the value for $x = 0.2$, as expected from what was indicated two paragraphs above. It is uncertain whether H_s increases or remains constant for increasing x in

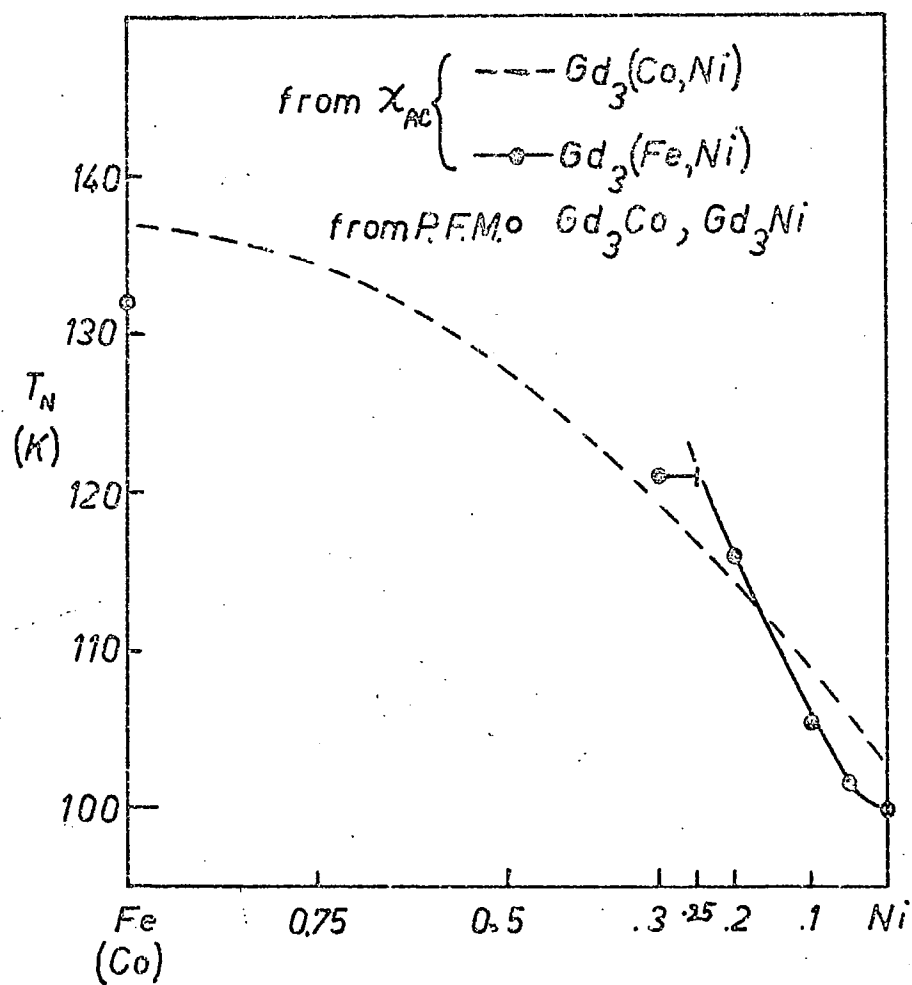


Fig. 5.25 T_N vs Composition for $Gd_3(Fe,Ni)$

this range.

5.4.2 A.C. Susceptibility as a Function of Temperature

The A.C. susceptibility vs temperature curves of the $\text{Gd}_3\text{Fe}_x\text{Ni}_{1-x}$ system were used in order to deduce the Néel temperatures T_N . The results are shown in fig. 5.25 together with the corresponding results for the $\text{Gd}_3\text{Co}_x\text{Ni}_{1-x}$ system. The two sets of results give almost coincident curves. It appears therefore that T_N is a function of x rather than a function of 3d-electron concentration. In other words, if one substitutes a given fraction of the Ni, the effect upon T_N is the same whether the substitution is done by Fe or by Co. The sample in the $\text{Gd}_3\text{Fe}_x\text{Ni}_{1-x}$ system with $x = 0.3$ gave a value of $T_N = 121\text{K}$. Since this was the first multiphase sample in the series and since the Gd_3B phase in this sample is expected to be the compound with $x = 0.25$ (as already indicated in section 5.4.1) the point for this composition (where $x = 0.3$) has been shifted to $x = 0.25$. The X_{AC} vs T curves for $x \geq 0.3$ indicated a Curie point at about 290 K which is the Curie temperature of metallic gadolinium. The sample with $x = 0.2$ gave a slight indication of a Curie temperature at 290K. This was to be expected since the M vs H curve at 4.2K showed a slight kink at the origin for this composition (fig. 5.22) The samples with $x > 0.3$ had a large quantity of foreign phase, which contributed to a larger initial susceptibility. Therefore measurements of T_N of the Gd_3B component in these multiphase samples was impossible because the contribution to the initial susceptibility was obscured by the contribution from the metallic gadolinium, so that no distinct Néel peak was distinguishable.

CHAPTER SIX

DISCUSSION OF $Y_x(Fe,Co,Ni)_{1-x}$ PSEUDOBINARIES, AND

A-Ni, A-Co, A-Fe, where A is Y OR Gd.

6.1 $Y_x(Fe,Co)_{1-x}$ and $Y_x(Co,Ni)_{1-x}$ Pseudobinaries

6.1.1 Structural Stability

On substituting Fe for Co in the Compounds YCo_5 , Y_2Co_7 , and YCo_3 , a composition was reached in each stoichiometry where the crystal structure of that stoichiometry became unstable, and was replaced by more than one phase.

(a) The $Y(Co,Ni)_5$ and $Y(Fe,Co)_5$ Pseudobinaries

The variation of the lattice parameters (a and c) in $Y(Co,Ni)_5$ follow Vegard's Law, showing a linear variation between the terminal compounds, as expected by this law for substitutional solid solutions. On substituting Fe for Co however, an increase in 'c' and a decrease in 'a' results in a large increase in the c/a ratio. The samples were single phase, with the $CaCu_5$ structure for iron substitution up to 20%, but the sample with 30% substitution of Fe was multiphase. The distortion of the hexagonal crystal structure, associated with the rapid increase of the c/a ratio, would appear to be the cause of the onset of structural instability. However the cause of the axial expansion itself is less certain. The agreement with Vegard's law on going from YNi_5 to YCo_5 suggests that there is substitutional replacement of Ni by Co on the B sites in the AB_5 structure. On substituting Fe for Co in YCo_5 the rapid axial expansion suggests that there may be a tendency for a more complex type of substitution.

Buschow et al. have investigated the stoichiometry $ErCo_6$. (ref. 6.1). X-ray photographs show this compound to be of single phase, the diffraction lines having the same pattern as those of the $CaCu_5$ structure. Buschow et al. have interpreted the structure of $ErCo_6$ to be derived from the AB_5 structure by a partial replacement of Er atoms on the A sites by pairs of Co atoms

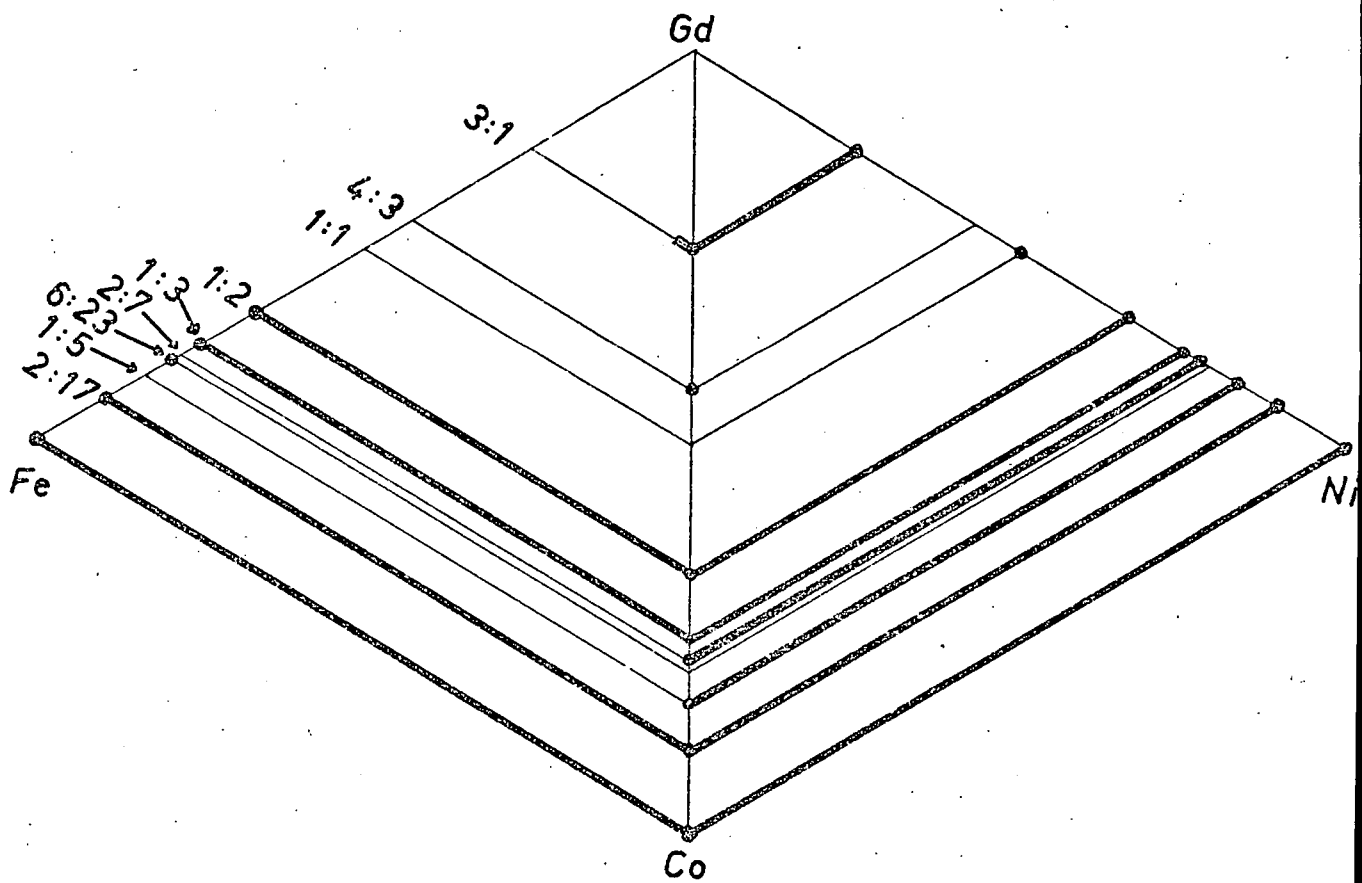
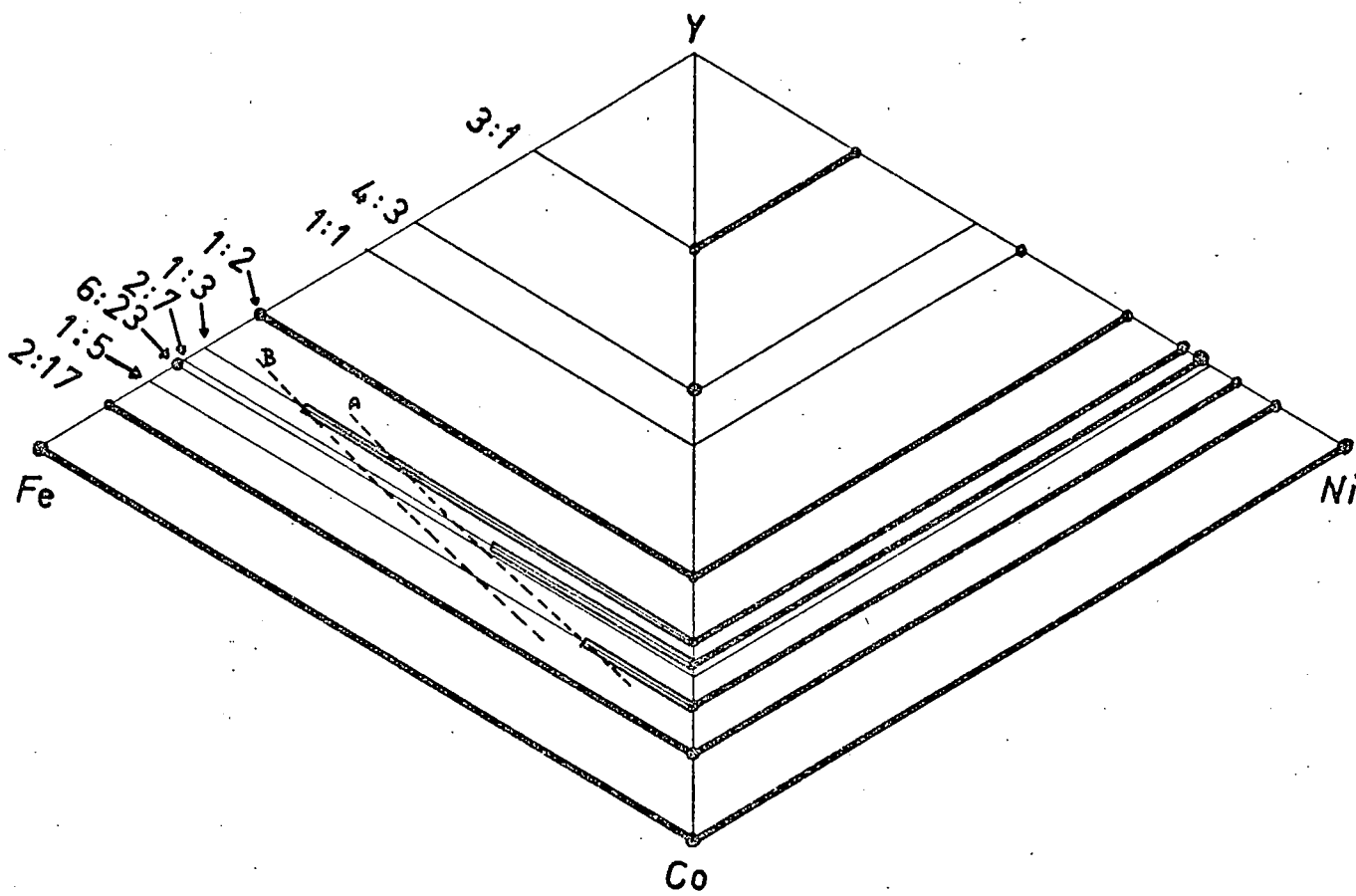


Fig 6.1. Composition Diagrams showing Range of Existence of Stoichiometries

arranged along the c axis direction. It is tentatively suggested that, in the $Y(Fe,Co)_5$ pseudobinaries, there may be a similar partial substitution of some Y atoms by pairs of Fe atoms in the axial direction. This might account for the large axial expansion as we substitute Fe for Co in YCo_5 .

(b) Effect of 3d electron concentration

Fig. 6.1 illustrates which compositions in the various pseudobinary systems exist. The compositions which were known to exist before the commencement of this work are marked by the thick lines in fig. 6.1 on each stoichiometry. The compositions which have been shown to exist in this work are marked by a pair of thin lines.

The lines labelled A and B in the yttrium diagram are two contours of constant 3d electron concentration, which were deduced with the following assumptions: Firstly it was assumed that the substitution of an atom of Co for an atom of Fe increased the 3d electron concentration by one. Secondly, it was assumed that all the valence electrons from yttrium (3 per Y atom) occupy the 3d band. What is meant by "3d electron concentration" is the average number of 3d electrons per transition metal atom. Thus the 3d electron concentration will equal 10 when the 3d band is full. The lines A and B cannot be labelled with their respective values of 3d electron concentration, since this is not known in an absolute sense. The difference in 3d electron concentration between contours A and B is 0.2 electrons per transition metal atom. It is evident that the limit of solid solubility of Fe in Co for each of the stoichiometries YB_5 , Y_2B_7 and YB_3 , correspond to the same value of 3d electron concentration, with an error of ± 0.1 3d electrons per transition metal atom. If our assumptions about the three valence electrons of yttrium occupying the 3d band is correct, then it would appear that the onset of structural instability occurs at a critical 3d electron concentration.

6.1.2 Magnetic Properties

(a) The moment summary graph

Fig. 6.2 is a summary graph of the spontaneous moment per transition

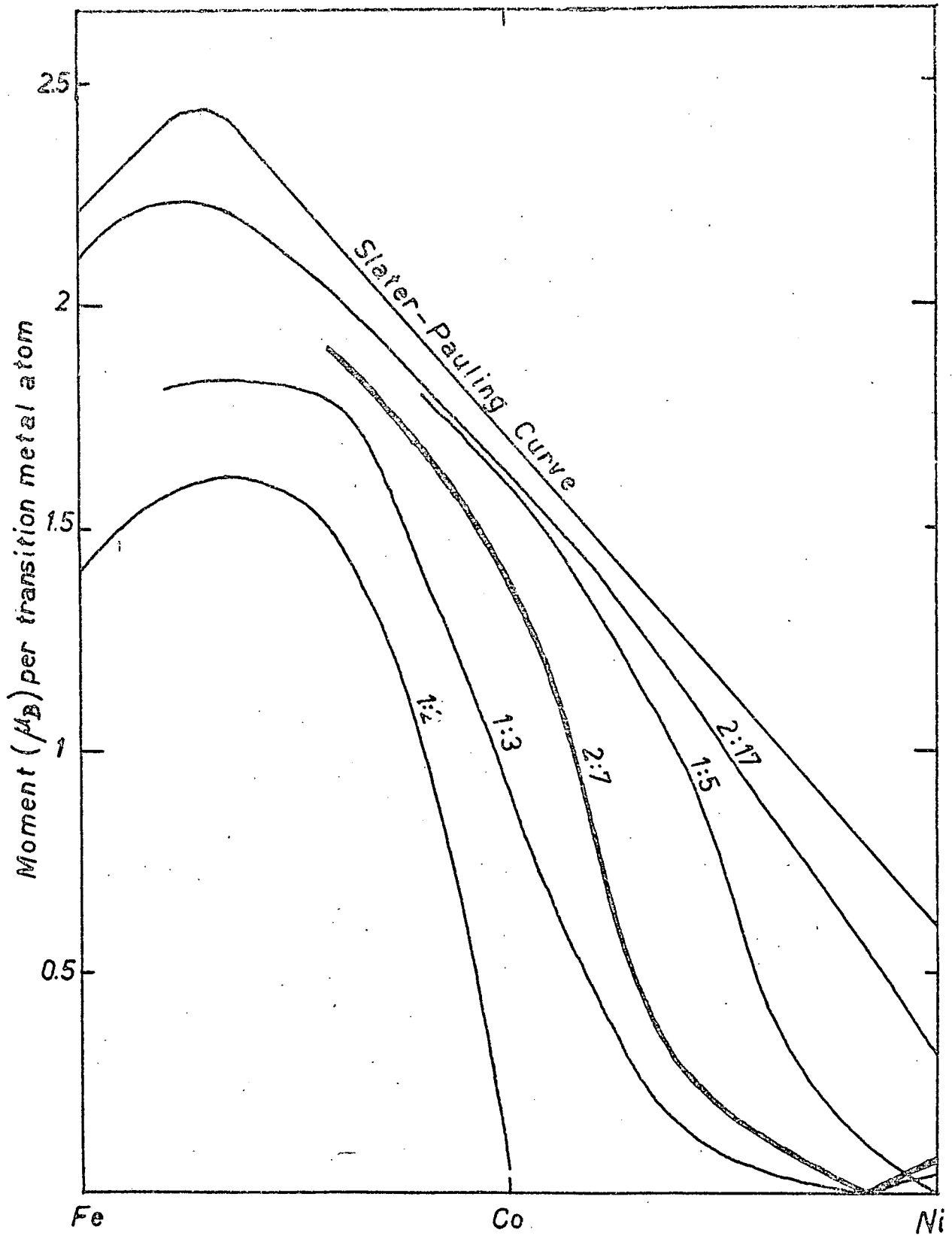


Fig. 6.2 Summary Graph of Moments in $Y_x(\text{Fe}, \text{Co})_{1-x}$ and $Y_x(\text{Co}, \text{Ni})_{1-x}$

metal atom for each of the stoichiometries studied. The pure transition metals (Fe, Co) and (Co, Ni) are represented schematically as the Slater-Pauling Curve. The $Y(Fe,Co)_2$ results, discussed in chapter one are also included.

One striking feature of this graph is the way in which the moment variation changes very gradually from one stoichiometry to the next as we increase the Y content from zero (Slater-Pauling Curve) to that of YB_2 . Since the 3d moment must depend to a considerable extent upon the density of states in the 3d band, this smoothness of the change from one stoichiometry to the next suggests that there may be some similarity in the density of states curve between the different stoichiometries. The crystal structures of all the yttrium-transition metal compounds here are related to each other (fig. 1.4), as described in chapter one. Because of this it is reasonable to expect the density of states curves, for each of these stoichiometries, to have some similar features, and therefore give rise to some continuity in magnetic behaviour as we cross stoichiometries.

Each of the stoichiometries which show a peak in the moment, do so at approximately the same Fe:Co concentration ratio. Piercy (see Chapter one, section 1.4.4) interpreted the peak in moment of the $Y(Fe,Co)_2$ compounds by assuming the existence of a minimum in the density of states curve. In this model the moment initially increases from YFe_2 at the rate of $+ \mu_B / Fe-Co$ substitution until one of the spin sub-bands is almost full, then on further substitution the other sub-band is occupied, decreasing the moment at the same rate. The fact that the actual moment variation falls below this pair of theoretical curves and then collapses to zero, was attributed to a decoupling of the two sub-bands. Such a pair of theoretical curves can be constructed for the pure 3d transition metals and it is evident that the moment variation in the pure transition metals is in very close agreement with this theoretical interpretation, where there is no decoupling of the spins in the two sub-bands. The moment behaviour as a function of 3d electron concentration in each of the stoichiometries YB_3 , Y_2B_7 , YB_5 , Y_2B_{17} also shows evidence of decoupling of the spin sub-bands, but the moment collapse becomes progressively less abrupt as we increase the transition metal content. This is consistent

with the decrease in the distance between the transition metal ions, giving rise to stronger ferromagnetic coupling.

In the $Y(Fe,Co)_2$, $Y(Fe,Co)_3$, and (Fe,Co) systems the moment shows a peak. This peak occurs at the same composition in each stoichiometry as that for which the Curie Temperature is a maximum. This is consistent with the model proposed to account for the peak. This is not the case, however, in the Y_2B_{17} compounds where the Curie temperature reaches a maximum at Y_2Co_{17} , and the moment has its maximum for 75% Fe substitution in Co.

(b) The low moment composition range of $Y_2(Co,Ni)_7$ and $Y(Co,Ni)_3$

In both of these stoichiometries the moment collapses on increasing the 3d electron concentration. As already stated, this collapse is due to an uncoupling of the 3d spin sub-bands, with the result that the Fermi levels in the sub-bands become equalized. However, when the moment finally becomes zero (at 20% Co) a further increase in 3d electron concentration causes a moment to reappear. The initial susceptibility of both the 20% Co compositions was measured down to 55K. No ordering temperature was observed in either stoichiometry. The Curie temperatures of the two 20% Co compositions can therefore be represented by an error bar from 0 to 55K, in fig. 4.7 and fig. 4.8. We shall assume that the composition with no moment at 4.2K also does not order. The variation of the Curie temperatures to the Co rich side of the 20% Co composition appears to support this assumption, the extrapolated T_c variation intersecting the composition axis very close to the 20% Co composition.

The minimum in the moment cannot therefore be interpreted in terms of the compensation of two opposing sub-lattices, since it corresponds also to a minimum in the Curie temperatures. Therefore the minimum in the moment corresponds to the disappearance of magnetic ordering.

The following model is proposed in order to interpret this disappearance of ordering at the 20% Co composition. It is postulated that there is a deep minimum in the density of states curve near the top of the 3d band. On increasing the Ni content from YCo_3 or Y_2Co_7 the Fermi level is being raised

and gradually approaches this minimum in $N(E)$. The two 3d sub-bands, each of which is unfilled, therefore gradually uncouple, with a resulting lack of polarization when the Fermi level encounters the minimum in $N(E)$. See fig. 6.3, below.

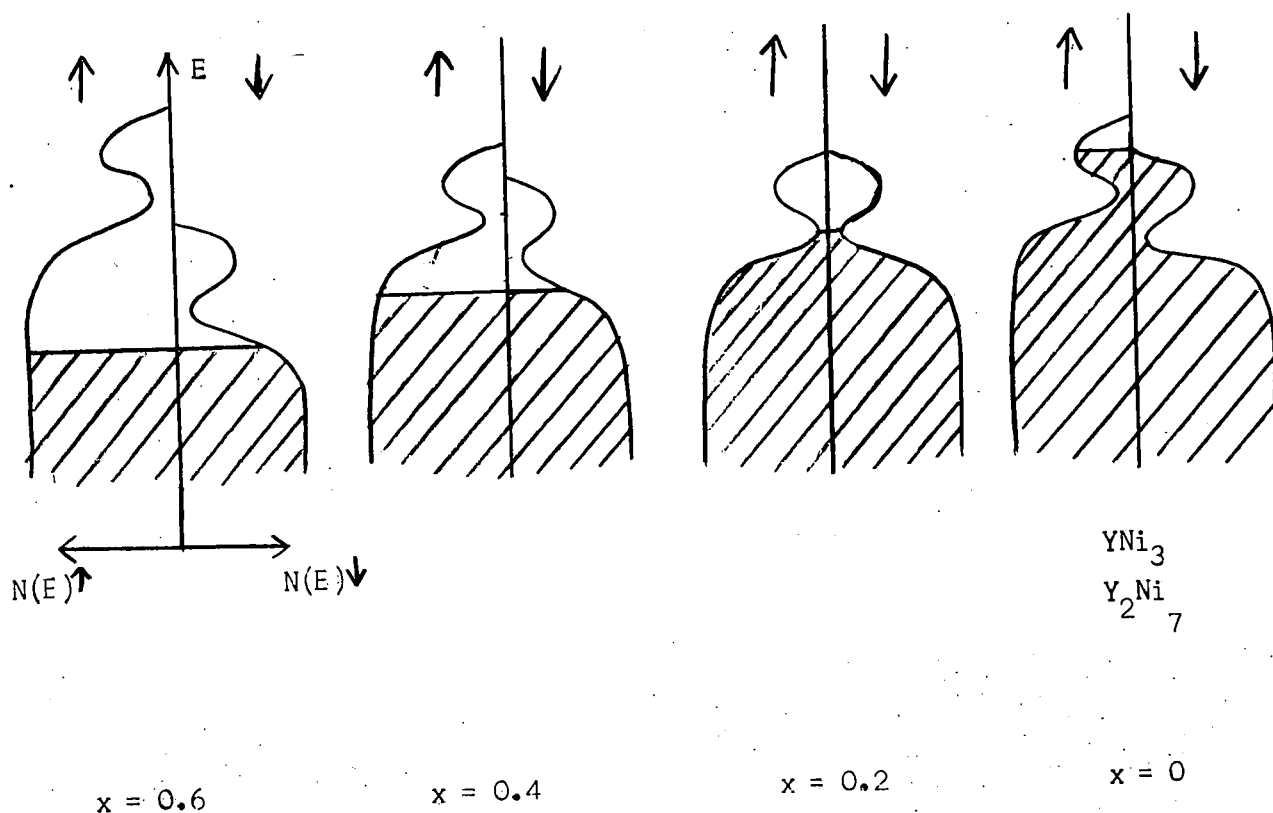


Fig. 6.3 Model (schematic) to account for disappearance of ordering in $\text{Y}(\text{Co}_x\text{Ni}_{1-x})_3$ and $\text{Y}_2(\text{Co}_x\text{Ni}_{1-x})_7$.

The value of $N(E)$ at this minimum must be sufficiently low for the Stoner criterion for ferromagnetism (section 1.3.1) to be no longer fulfilled. On adding more electrons to the 3d band, from this point of no ordering, the Fermi level rises above the minimum in $N(E)$ and then finds itself at an energy value with a higher $N(E)$. Spontaneous polarization then reasserts itself, with the resulting reappearance of a spontaneous moment, as in YNi_3 and Y_2Ni_7 . It is proposed that the minimum in $N(E)$ is sufficiently near the top of the 3d band for the polarization in YNi_3 and Y_2Ni_7 to be complete. The polarization obviously cannot be complete for samples with greater than 20% Co since the exchange cannot cause electrons to occupy the energy states above the minimum in $N(E)$ in either sub-band. This has two consequences: 1) The M vs H curves of samples with Co content greater

than 20% will not saturate. This is because the spontaneous moment arises from the difference in population between two incompletely filled sub-bands which are split by a weak exchange interaction. On applying a field H , the domains of spontaneous moment will initially line up parallel to H . On increasing H the two sub-bands will be split further. Since the exchange is weak the field required to simulate the order of magnitude of the exchange field need not be large. This increased splitting will result in a larger population difference between the sub-bands which will enhance the moment. This enhanced moment will be proportional to the applied field and will result in saturation not being approached. (2) For YNi_3 and Y_2Ni_7 , on the other hand, the polarization is already complete, and any further splitting of the sub-bands cannot give any further population difference. Thus the sample magnetization will saturate completely.

These two effects (1) and (2) are observed experimentally. The moment of powder samples with greater than 20% Co do not saturate, but show a linear magnetization rise with field, at high fields. Assuming the above model to be applicable it appears that this non-saturation is a result of the applied field increasing the magnitude of the moment, rather than a result of magnetocrystalline anisotropy impeding alignment of domains. The latter might be suspected to be ineffective if the powder grains were not sufficiently small. Thus the method used for determining the spontaneous moment (i.e. extrapolating $M(H)$ to $H = 0$ from high fields) was probably correct.

The above effect (2) is observed in YNi_3 and Y_2Ni_7 . Both of these samples in bulk and powder form, saturated completely in fields of less than a few kilo-oersted.

Critical fields were observed in the low moment composition range for greater than 20% Co substitution in Ni. These critical fields were observed only for powder samples. The cause of this occurrence may be that the exchange/anisotropy energy ratio is small. The powder samples might consist of single domain particles for which a critical field is required to reverse the magnetization direction. For low moment samples the domain size

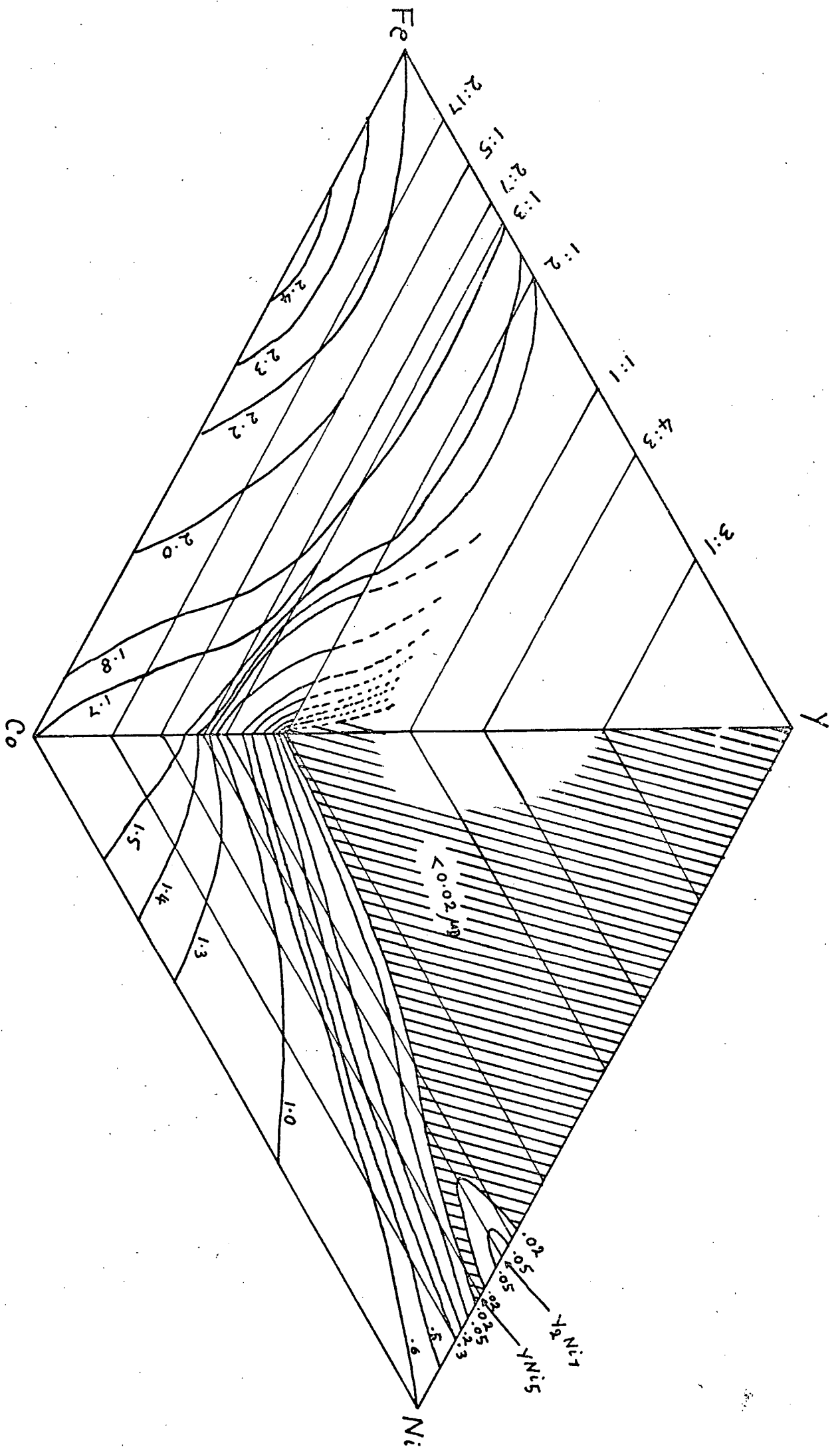


Fig. 6.4 Moment Contour Diagram in the Y-Fe-Co and Y-Co-Ni Systems

is large and may be of the order of the powder grain size.

In fig. 6.4, the data of the summary diagram (fig. 6.2) are plotted in an alternative form. The contours of moment value per transition metal atom are plotted in the Y-Fe-Co and Y-Co-Ni composition triangles. The general downhill trend of the moment with increasing 3d-electron concentration and with increasing Y content is obvious. The zero moment compositions are represented tentatively by the shaded regions, since this region has not been fully investigated. It is convenient and vivid to resort to geographical terms and refer to this shaded region as a 'sea' and the high moment region as the 'mainland'. It will be noticed that the small moment on Y_2Ni_7 represents the top of a small 'island' separated from the 'mainland' by a narrow 'estuary' of zero moment which extends through the non-ordering compositions $Y(Co_{.2}Ni_{.8})_3$, $Y_2(Co_{.2}Ni_{.8})_7$, as far as YNi_5 . It is clear therefore that the disappearance of magnetic ordering in each of these three compositions originates from the same cause. Thus, any model which accounts adequately for this phenomenon on varying the composition within onestochiometry must be applicable also when the composition varies while crossing stoichiometries. The rigid band model proposed for $Y_2(Co,Ni)_3$ and $Y_2(Co,Ni)_7$ in which a minimum in the density of states was assumed is therefore applicable also in the Y_xNi_{1-x} system.

Thus it is probably valid to assume that this same minimum in $N(E)$ exists for the compositions Y_2Ni_{17} , YNi_5 , Y_2Ni_7 and YNi_3 . This suggests that there is a transfer of valence electrons from Y to the 3d band of Ni. This transfer probably involves only a fraction of the 3 valence electrons per yttrium atom. On going from the 20% Co in Ni composition to the pure Ni composition of either of the stoichiometries YB_3 or Y_2B_7 the 3d electron concentration increases by 0.2 per T.M. atom. The zero moment composition in the Y_2B_7 alloys appears to be slightly to the Ni-rich side of the 20% Co composition. The zero moment composition in the YB_3 alloys appears to be exactly at the 20% Co composition. We shall therefore assume that $Y(Co_{.2}Ni_{.8})_3$ has the same 3d electron concentration as YNi_5 . We can then calculate how

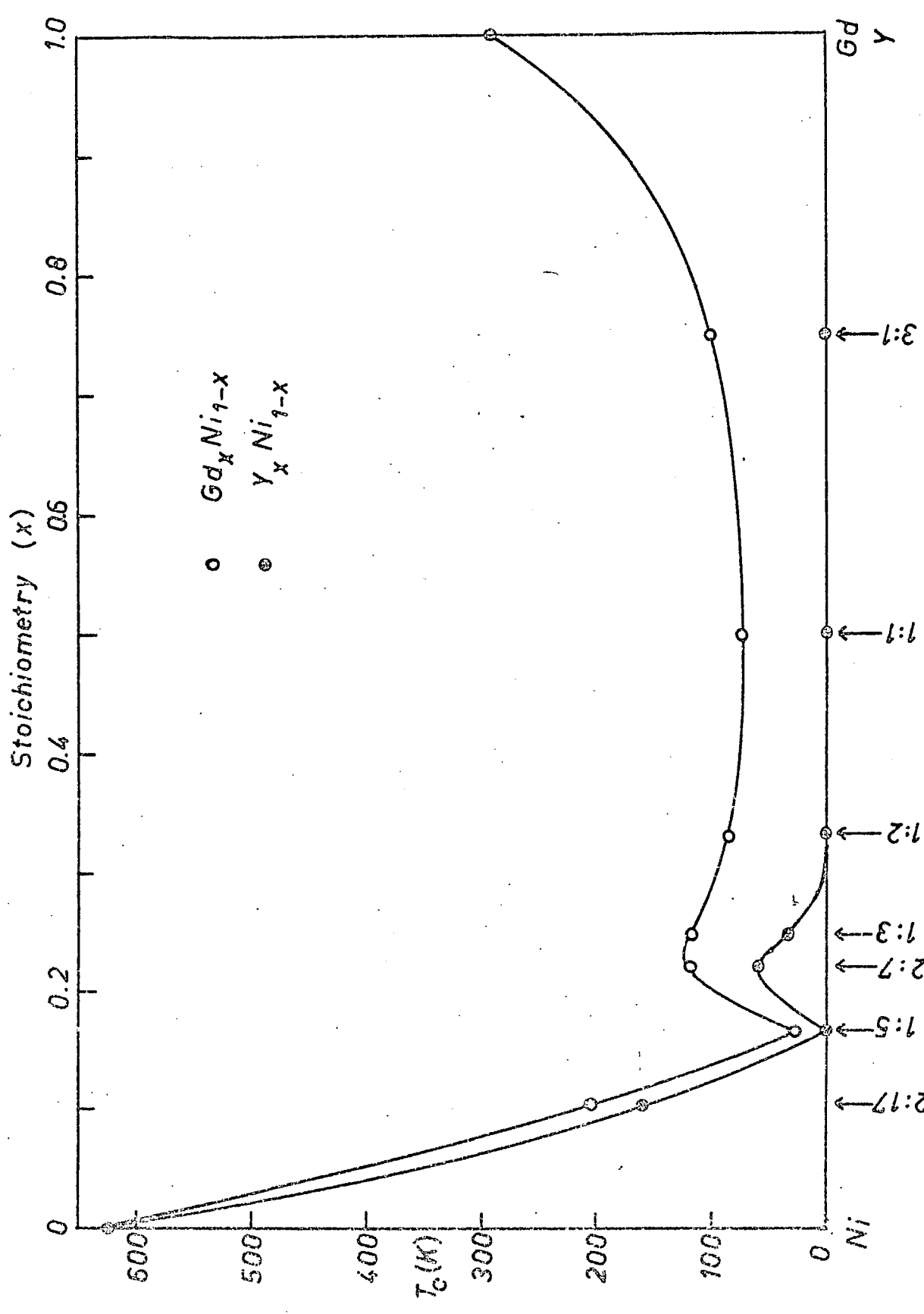


Fig 6.5 Curie Temperatures in Gd_xNi_{1-x} and Y_xNi_{1-x}

many of the valence electrons of Y^{3+} are donated to the 3d band. The value obtained is 1.5 per Y^{3+} ion. Thus only about half of the valence electrons of Y^{3+} occupy the 3d band. This same value need not necessarily be applicable over the whole Y_xNi_{1-x} range of compounds. If it were applicable over the whole range, however, this would predict a completely full 3d band for some composition between YNi_3 and YNi_2 , assuming pure Ni to have 0.61 holes per atom.

6.2. The 3d Moment in Y_xNi_{1-x} and Gd_xNi_{1-x}

Fig. 6.5 shows the ordering temperatures of the compounds of nickel with yttrium and with gadolinium. The yttrium compounds have already been discussed partially in chapter one and in section 6.1. The nickel moment in the yttrium compounds was seen to follow closely the Curie temperature variation. The problem in this section is to attempt to deduce when the 3d band is full. Since it is possible to have a partially full 3d band with the Fermi level at a low $N(E)$ the absence of a spontaneous moment does not necessarily mean that this band is full. However, if the band is unfilled, the replacement of yttrium by gadolinium can induce a 3d moment where none exists spontaneously. If the Gd is found not to induce any 3d moment, this may be considered as some evidence of the 3d band being full. In attempting to calculate the 3d moment we must find some way of separating this from the moment due to the polarization of conduction electrons. The latter polarization is induced by exchange of the RKKY type (see section 7.7.1) between the localized Gd ions and the conduction electrons. We make the following assumptions: (1) The moment due to the conduction electron polarization per Gd (M_{ce}) is oriented parallel to the gadolinium moment. The saturation moment of Gd metal is $7.55 \mu_B$ per atom. The $0.55 \mu_B$ excess is attributed to conduction electron polarization, and is parallel to the Gd^{3+} ionic moment and in the same direction. It is not unreasonable to assume therefore that, in the alloys, M_{ce} is also in the same direction as the Gd moment inducing it. (2) The value chosen for M_{ce} is assumed constant for all the alloys. This assumption is admittedly a bad one, but in the absence of any more reasonable assumption we shall adopt it here.

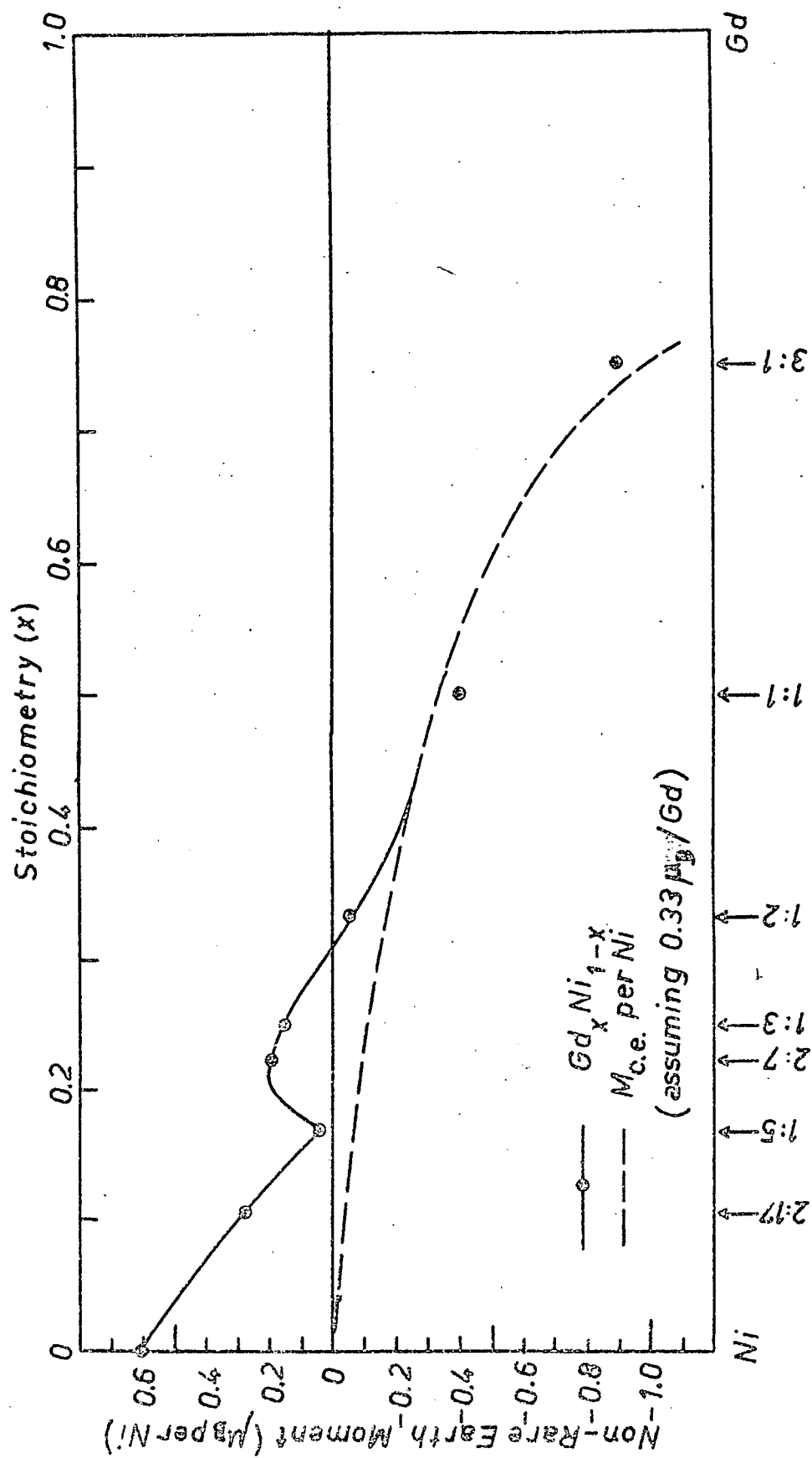
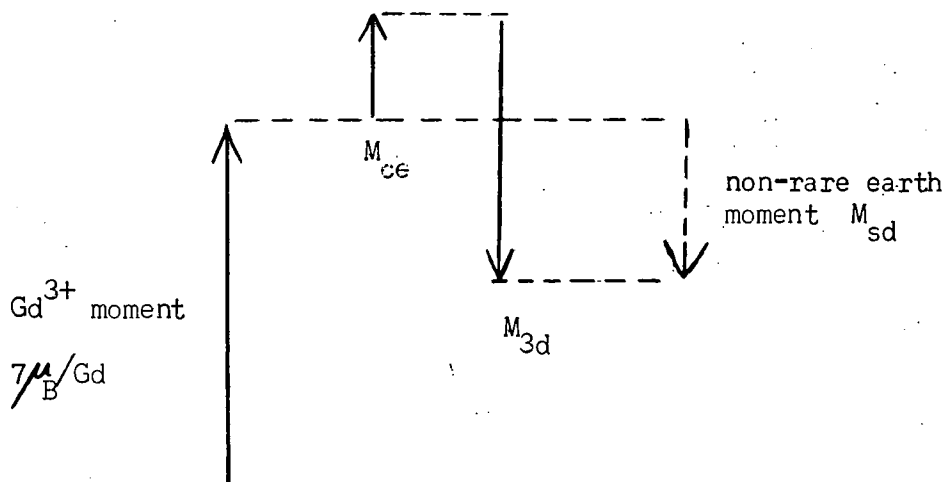


Fig. 6.6 Non-Rare Earth Moment in $Gd_x Ni_{1-x}$ Compounds

(3) The 3d moment is oriented antiparallel to the Gd moment. From section 1.1 it was seen that this was the most convenient way of interpreting the saturation moment of the Gd compounds with Fe, Co, or Ni. No evidence against this rule has been found. It is therefore reasonable to adopt it.

The ordering temperatures of the gadolinium compounds decrease initially from that of pure Gd, as would be expected when the Gd-Gd distance increases on adding Ni. The Curie temperatures then rise slightly from that of GdNi, on further Ni addition, to that of GdNi₂, and continue to rise more rapidly on approaching GdNi₃, whose 3d band is known already to be unfilled. Though the rise in the T_c from the 1:1 to the 1:2 compounds is small, it probably indicates the appearance of a 3d moment induced on the Ni atoms by the Gd in GdNi₂. It may be recalled, from chapter 1 (section 1.4.4) that the number of holes in the 3d band of GdCo₂ is 1.1 holes per Co atom. Since Ni has one more valence electron than Co, the number of holes in the 3d band of GdNi₂ is probably 0.1 per Ni atom. Thus it appears to be possible that the 3d band in GdNi₂ is not quite full. This is consistent with the consideration above, where T_c rises from the 1:1 to the 1:2 composition.

Fig. 6.6 shows the variation (continuous line) of the non-rare earth moment M_{sd} per Ni atom. By this is meant that the $7\mu_B$ per Gd³⁺ ion has been subtracted from the saturation moment as shown here:



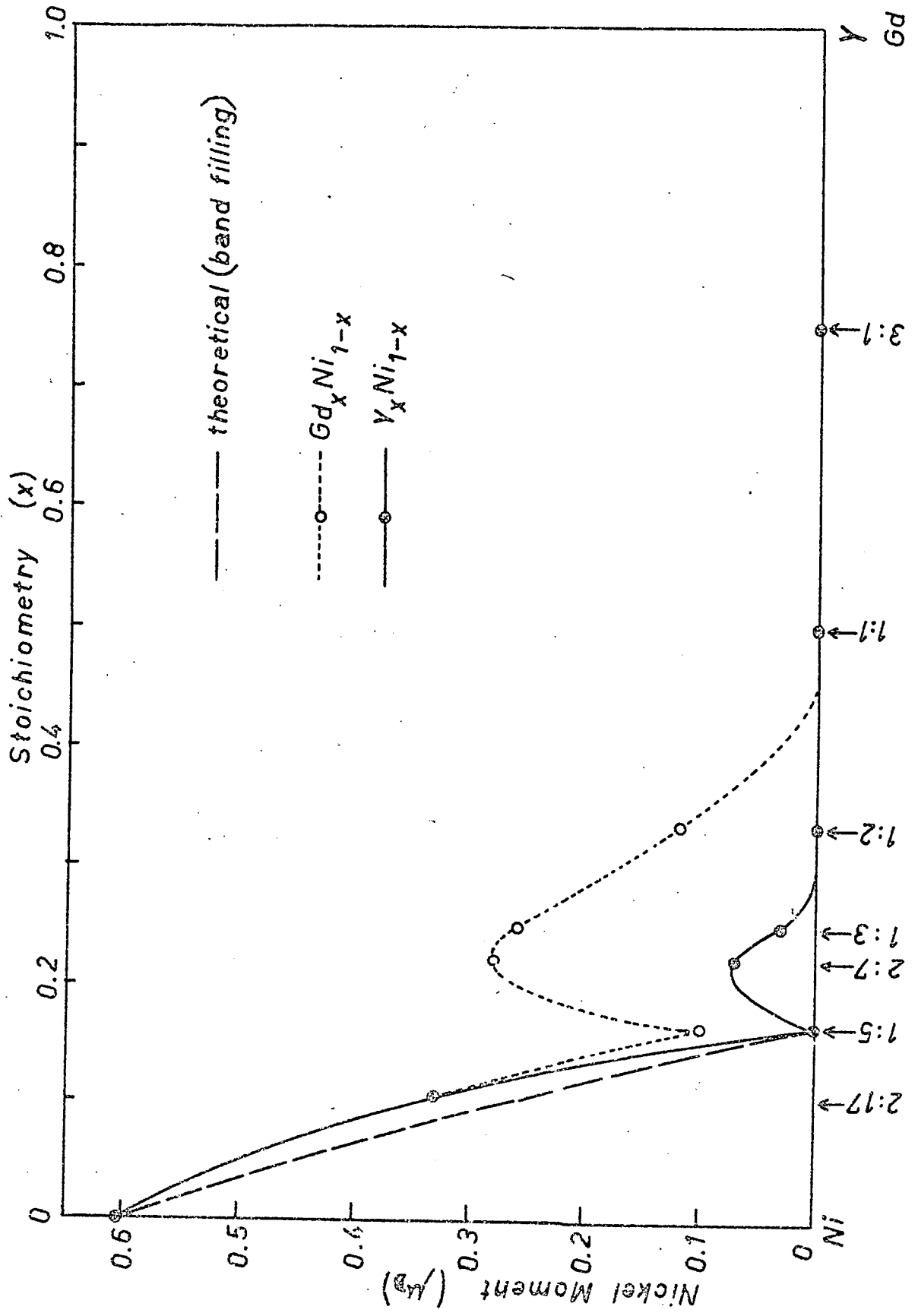


Fig 6.7 Nickel Moment in Gd_xNi_{1-x} and Y_xNi_{1-x}

Thus M_{sd} is the 3d moment minus the conduction electron polarization moment. If the 3d moment is larger than the conduction electron moment, M_{sd} will be positive and antiparallel to the Gd^{3+} moment. If the saturation moment of the alloy is exactly $7\mu_B$ per Gd atom, then this suggests that M_{ce} is equal to M_{3d} and does not necessarily indicate that the Ni moment is zero.

It appears, from the variation of the ordering temperature that the top of the 3d band is encountered by the Fermi level somewhere between the 1:1 and 1:2 compositions. Therefore the compounds $GdNi$ and Gd_3Ni have no 3d moment and their non-rare earth moment must be due purely to conduction electron polarization. Making the above three assumptions leads to the dashed line in fig. 6.6, and this represents the theoretical variation of the conduction electron moment (per Ni atom), assuming that M_{ce} is $0.33\mu_B$ /Gd atom. This dashed line is the best fit to the non-R.E. moment values of the compounds $GdNi$ and Gd_3Ni . The 3d moment is given by the difference between the continuous line and the dashed line in fig. 6.6. This is plotted in fig. 6.7 together with the values of the Ni moment in the Y compounds, and the theoretical variation from pure Ni, assuming the three valence electrons from Y^{3+} occupy the 3d band. We see that the presence of Gd in place of Y amplifies the 3d moment on the Ni atoms, and also induces a small moment on the Ni atoms of the inherently non magnetic YNi_5 and YNi_2 compounds. The fact that the 3d band is unfilled at YNi_5 shows that only a fraction of the three valence electrons of Y^{3+} occupy the 3d band of Ni.

6.3. The 3d moments in YCo_x and $GdCo_x$

By means of the identical argument as used in section 6.2, we derive the 3d moment on the Co atoms in the $GdCo_x$ compounds. The relevant graphs are figs. 6.8, 6.9 and 6.10 which are the equivalents of figs. 6.5, 6.6 and 6.7 for the Ni compounds. The result is that the 3d band is full in Gd_3Co and Y_3Co , but that both these compounds have their Fermi level very near the top of the 3d band. Y_4Co_3 is more strongly ferromagnetic than YCo_2 and it may be that we are observing the same type of reappearance of ordering on going from YCo_2 to Y_4Co_3 as we observed in the Ni system on going from YNi_5

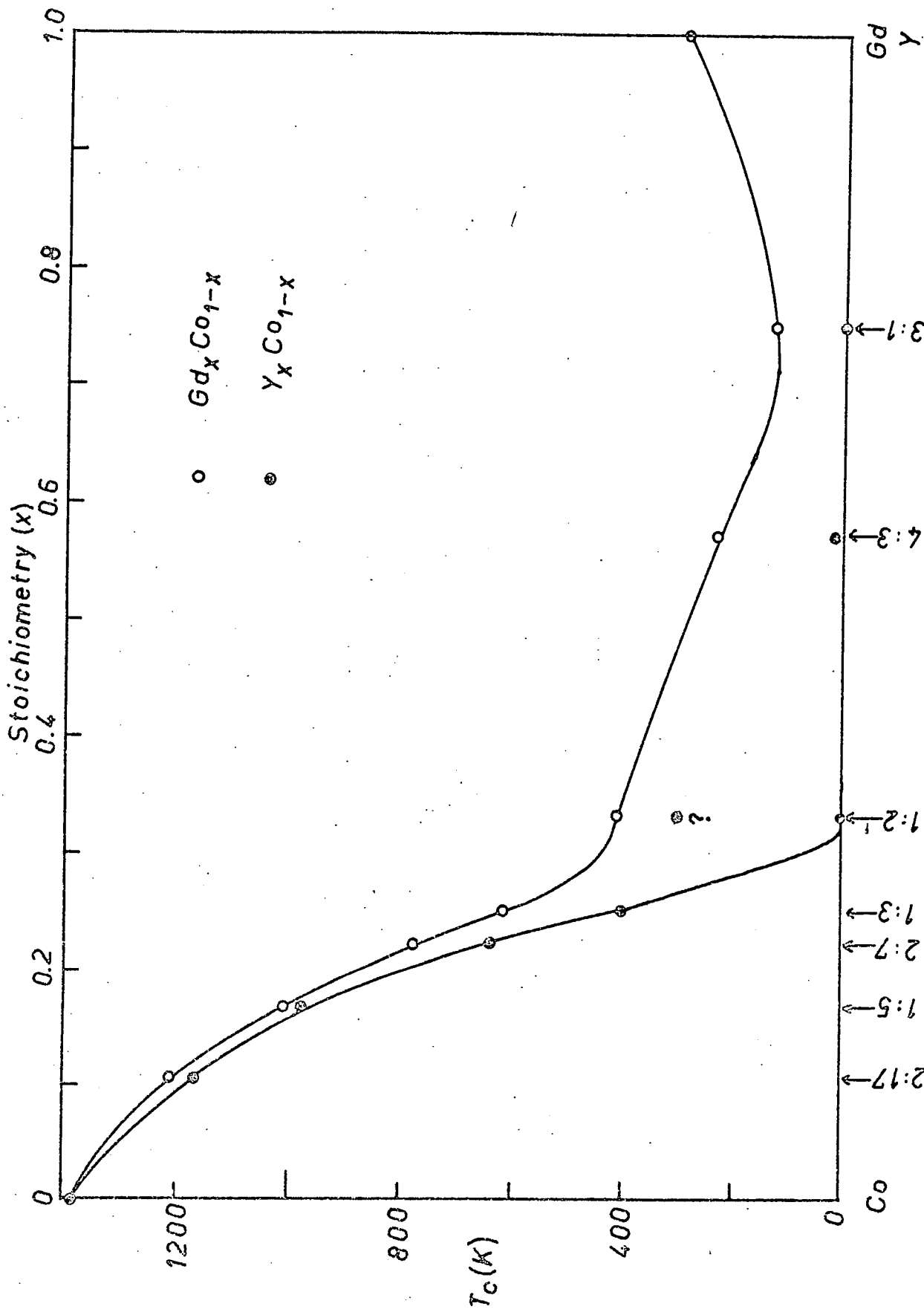


Fig 6.8 Curie Temperatures of Gd_xCo_{1-x} and Y_xCo_{1-x}

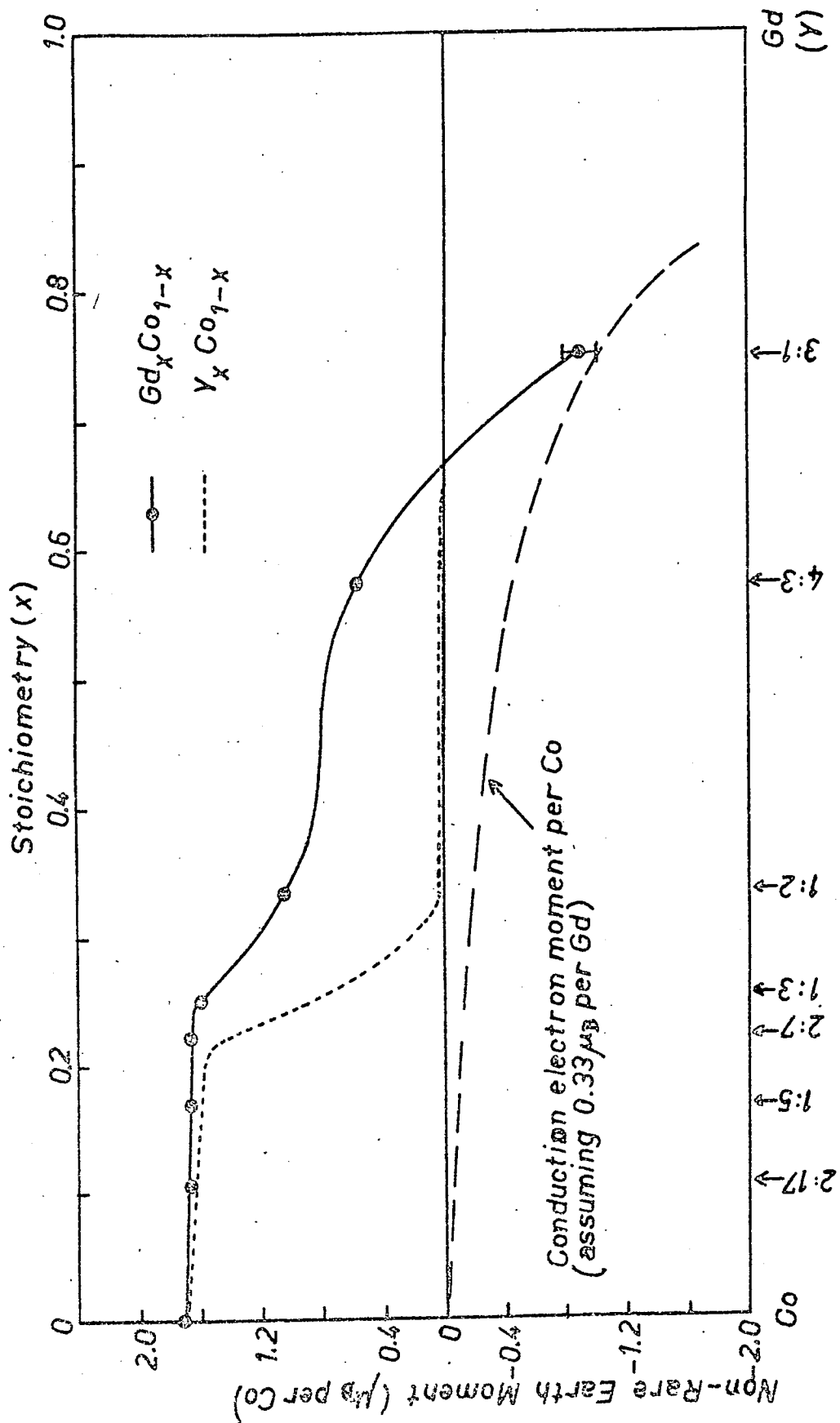


Fig. 6.9 Non-Rare Earth Moment in Gd_xCo_{1-x} Compounds

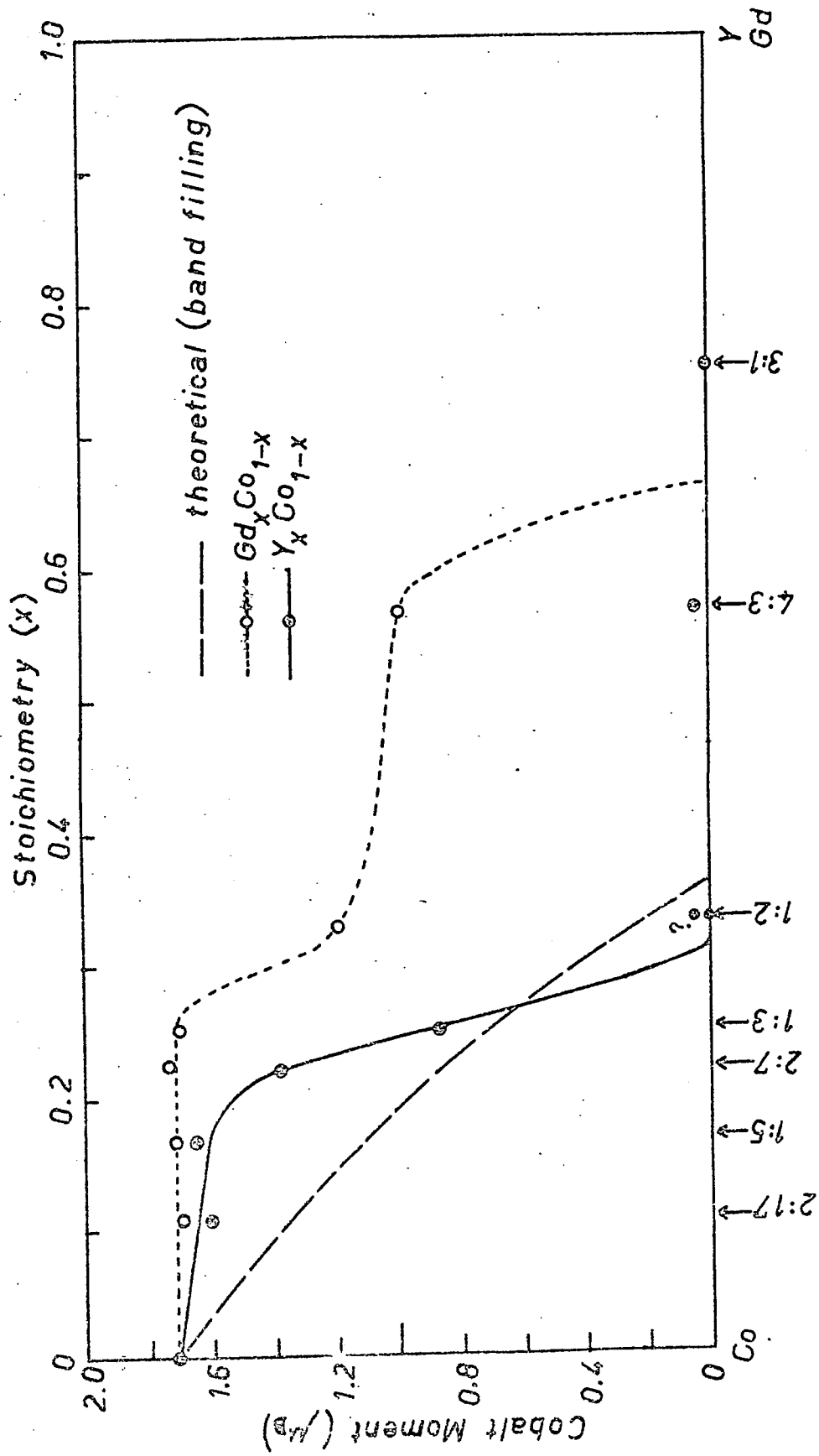


Fig 6.10 Cobalt Moment in Gd_xCo_{1-x} and Y_xCo_{1-x}

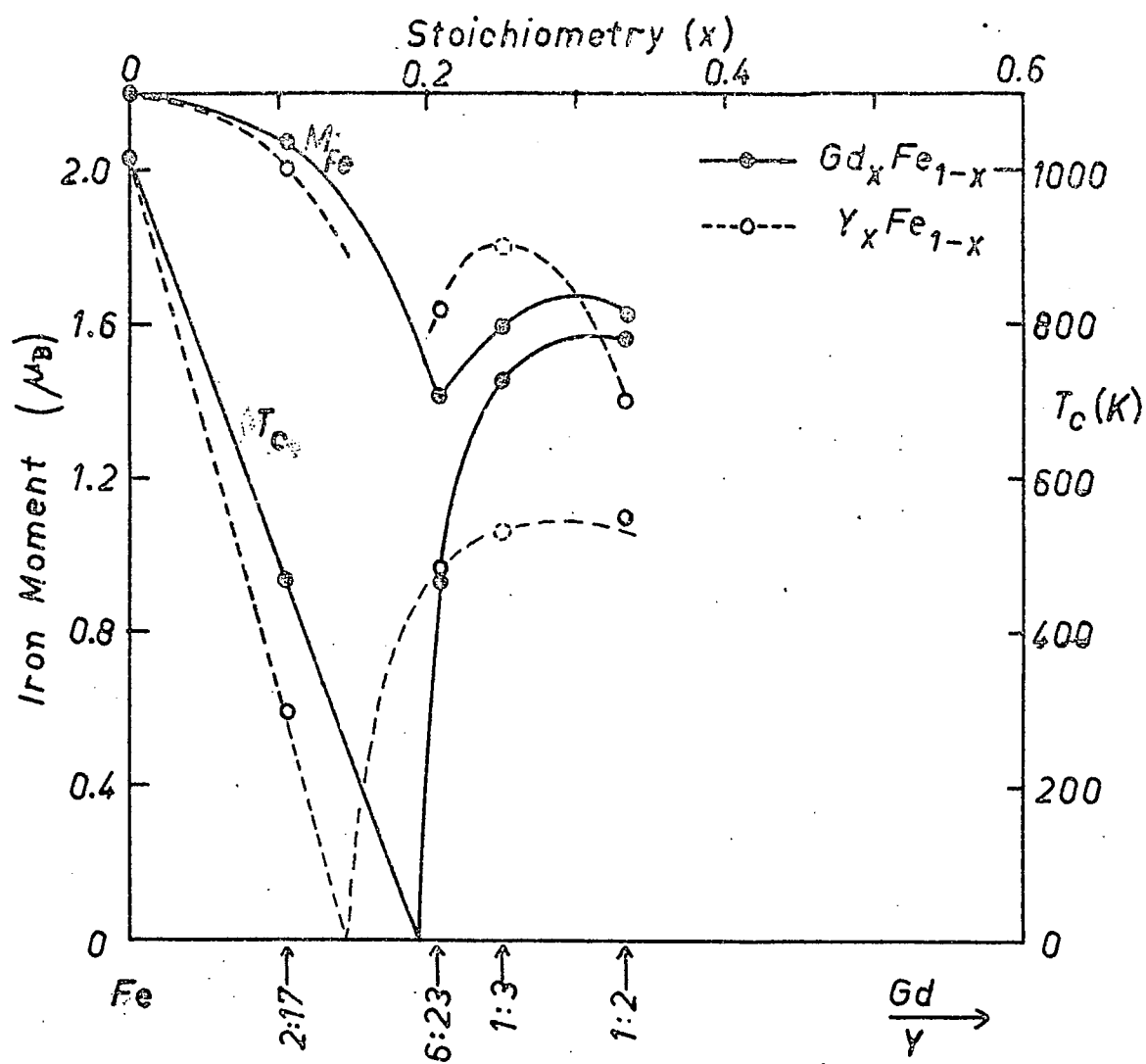


Fig 6.11 Iron Moments and T_c in Y_xFe and Gd_xFe

to Y_2Ni_7 . This is however very conjectural since there is only one composition to mark the reappearance of ordering.

6.4 The 3d moments in Y_xFe_{1-x} and Gd_xFe_{1-x}

In chapter one (section 1.4.3) it was stated that the moment per iron atom, in the Y compounds with Fe decreased progressively on increasing x from that of pure Fe, while the Curie temperature decreased rapidly from Fe to Y_2Fe_{17} and then increased on increasing x further. From the results of the $Y(Fe,Co)_3$ system the situation appears to be rather different. The YB_3 structure existed up to 80% Fe substitution and the Fe moment was approximately constant at its maximum from 40% to 80% Fe substitution (fig. 4.7). The multiphase sample of YFe_3 had a measured moment ($1.8\mu_B/Fe$) which was close to this maximum value. The moment of YFe_3 , if this compound were to exist, would therefore be close to this value. The Curie temperatures varied more rapidly in the 40% - 80% Fe substitution range. The Curie temperature of YFe_3 , if it were to exist, was deduced by extrapolating the T_C values of the 60% and 80% Fe compositions of $Y(Fe,Co)_3$ to 100% Fe. This T_C value (530K) is plotted in fig. 6.11, and the new T_C variation of the Y_xFe_{1-x} compounds is also shown as a function of composition. It has a similar deep minimum as the Gd_xFe_{1-x} compounds. The existence of these deep minima are not purely fanciful, and are consistent with the magnetic results of the $Y_6(Mn,Fe)_{23}$ and $Gd_6(Mn,Fe)_{23}$ substitutional alloys, obtained by Kirchmayr and his collaborators (refs. 6.2, 6.3). The above value ($1.8\mu_B/Fe$) of moment in the hypothetical YFe_3 compound is also plotted in fig. 6.11. On comparing the moment variation in Y_xFe_{1-x} with the iron moment variation in the Gd_xFe_{1-x} compounds we see that the iron moments, in the two sets of compounds, have the same type of variation.

The Fe moments in the Gd compounds were deduced by assuming antiparallel alignment of Fe and Gd moments, and assuming that the Gd moment is $7\mu_B/Gd$. No correction for conduction electron polarization was made, for two reasons: (1) The non-R.E. moments (i.e. Fe moments) are generally large and any conduction electron polarization would be small compared with the Fe moment.

(2) No Fe compounds exist for any Gd-rich compositions, where the conduction electron polarization would have the largest effect upon any such corrections.

The moment variation in $Y_x Fe_{1-x}$ now shows more resemblance to the Curie temperature variation as well as the M_{Fe} variation in $Gd_x Fe_{1-x}$. The oscillatory form of the variation of T_c and M_{Fe} suggests that the Fe-Fe interactions might be understood in terms of semi-localized 3d moments whose interactions depend critically on interatomic distance. The model was developed originally by Friedel (ref. 6.4) for discussing the interactions of impurity ions in a lattice. The model involves polarizations of the 3d electrons, which are localized about the impurity ion, these polarizations having an oscillatory variation in space.

6.5 Conclusion

The variation of the transition metal moment in the yttrium-3d metal pseudobinary compounds within a given stoichiometry can be understood qualitatively in terms of the rigid band model. The decrease of the average moment is a result of a combination of the 3d band filling on increasing the 3d electron concentration, and the decoupling of the spin up-spin down sub-bands. The disappearance and reappearance of magnetic ordering in the $Y(Co, Ni)_3$ and $Y_2(Co, Ni)_7$ systems can be explained by assuming the existence of a minimum in the density of states curve. This same model can be used in order to interpret the same phenomenon in the $Y_x Ni_{1-x}$ system as x is increased. Thus this same detail in the density of states curve is present in each of the different stoichiometries of the $Y_x Ni_{1-x}$ system from $Y_2 Ni_{17}$ to YNi_3 . The close relationship between the crystal structures of these stoichiometries renders such a possibility not unreasonable.

The yttrium and gadolinium ions in cobalt and nickel compounds contribute a fraction of their valence electrons (3 per Y or Gd ion) to the 3d band in nickel or cobalt. The 3d band of the nickel compounds becomes filled on increasing the A content, between ANi_2 and ANi . That of the cobalt compounds becomes filled between $A_4 Co_3$ and $A_3 Co$, but the Fermi level of $A_3 Co$ lies close to the top of the 3d band.

The spin of the Gd ions in the Co and Ni compounds induces a moment in the 3d band if that band is unfilled. The fractional increase in the moment, on substituting Gd for Y, is large when the spontaneous 3d moment is small in the corresponding yttrium compounds.

CHAPTER SEVEN

DISCUSSION OF $Gd_3(Fe,Co,Ni)$ COMPOUNDS

The results are interpreted here in terms of the two-sublattice theory of antiferromagnetism due to Néel (ref. 71). An outline of the theory follows.

7.1. The Néel two-sublattice theory of Antiferromagnetism

7.1.1 The Exchange Interaction

In this theory the molecular field approach is used. The lattice of magnetic ions is divided, in zero applied field, into two sublattices A and B. Each sublattice has a spontaneous magnetization which is equal and opposite to the other sublattice. These two spontaneous magnetizations are \underline{M}_a and \underline{M}_b

$$\underline{M}_a = - \underline{M}_b$$

The interactions of exchange are represented by the molecular fields \underline{H}_a and \underline{H}_b . An ion in the sublattice A experiences an exchange field $n'\underline{M}_a$ by interaction with other ions in the same sublattice. This interaction within the sublattice tends to align the magnetic moments of the sublattice ferromagnetically if n' is positive. This ion also experiences an exchange field $-n\underline{M}_b$ by interaction with ions in the opposing sublattice. If n is positive, this part of the exchange field tends to cause antiferromagnetic alignment of the two sublattices. The quantities n' and n are the two molecular field coefficients and are dimensionless quantities. The total molecular field acting on an ion in sublattice A and B respectively are:

$$\underline{H}_a = n'\underline{M}_a - n\underline{M}_b, \quad \underline{H}_b = n'\underline{M}_b - n\underline{M}_a.$$

At high temperatures the material obeys the classical Curie-Weiss law, where the paramagnetic Curie temperature θ_p is given by

$$\theta_p = \frac{1}{2}C(n'-n) \dots \dots \dots (1)$$

C is the Curie constant.

Below a certain temperature T_N the antiferromagnetic ordering establishes itself. Let the magnitude of the magnetization of each sub-

lattice be $M/2$, which will be a function of temperature. If both n' and n are positive, then the ferromagnetism in one sublattice is encouraged both by the intersublattice molecular field and by the intra-sublattice molecular field, so that each adopts the spontaneous magnetization $M/2$ under the action of the molecular field $(n'+n)M/2$. The spontaneous magnetization of a sublattice drops to zero at the temperature T_N which by analogy with the relation for T_c (Curie temperature) as a function of the molecular field in the Weiss theory of ferromagnetism, is given by:

$$T_N = \frac{1}{2}C(n'+n) \quad (2)$$

At the temperature T_N the susceptibility is given by

$$s = \frac{1}{n'} \quad (3)$$

For the present purposes we require a theory from which the existence of critical field transitions from the antiferromagnetic (af) to the ferromagnetic (f) state follows. In addition, provision must be made for these critical fields to be small without requiring the total molecular field to be small. The theory due to Néel, with the requirement $n' \gg n$, is therefore useful. Small critical fields of the order of the inter-sublattice exchange field will cause the two sublattices to decouple and align ferromagnetically, parallel to the applied field. This weak coupling can be associated with a high ordering temperature since T_N depends now mainly upon n' .

This assumption considerably simplifies the theory because the ions within one sublattice are so strongly coupled to each other that the sublattice can be treated as a magnetically rigid entity.

The exchange field gives rise to an energy of orientation between the two sublattices. The theory considers only uniaxial crystals. Therefore the directions of \underline{M}_a and \underline{M}_b can be specified by the angles θ and θ' between the axis and \underline{M}_a and \underline{M}_b respectively. Since a uniaxial crystal has

cylindrical symmetry the direction of any components of \underline{M}_a or \underline{M}_b in the basal plane does not enter into the energetics of the problem. The exchange energy is expressed as:

$$E_W = \mu_0 n \underline{M}_a \cdot \underline{M}_b \quad (4)$$

$$= \mu_0 n \frac{M^2}{4} \cos(\theta - \theta')$$

where $|\underline{M}_a| = |\underline{M}_b| = \frac{M}{2}$.

7.1.2 Anisotropy

In order to account for critical field transitions from the (af) to the (f) state, it is necessary to introduce anisotropy. An anti-ferromagnetic in the absence of anisotropy has no mechanism for the occurrence of finite critical fields of this type.

The anisotropy results in the appearance, in the expression for the total energy, of a term which depends upon the orientation of the magnetization of a sublattice with respect to the crystal axis. Since the Néel theory considers only uniaxial crystals the anisotropy energy expression used is:

$$E_{K_0} = -\frac{1}{2} K_0 (\cos^2 \theta + \cos^2 \theta') \quad (5)$$

This may be a magnetocrystalline anisotropy.

In addition it is necessary to take into account the magnetic dipole interaction between the magnetic ions. Unlike the exchange interaction, which is isotropic, depending only on the angle between two interacting magnetic moment directions, the dipole interaction also depends upon the angles between these moments and the line joining them. This gives rise to an anisotropy energy which can be expressed in the form:

$$A \cos \theta \cos \theta' + B \sin \theta \sin \theta'$$

A and B are constants which depend upon the nearest neighbour configurations.

$$\text{Since } \cos(\theta - \theta') = \cos \theta \cos \theta' + \sin \theta \sin \theta'$$

the above expression can be rewritten:

$$(A - B) \cos \theta \cos \theta' + B \cos(\theta - \theta').$$

The second term is isotropic, depending only on the angle between \underline{M}_a and

\underline{M}_b , but not on their directions with respect to the crystal axis. This term can therefore be incorporated into the exchange energy, thus modifying the value of n . The total anisotropy energy can then be expressed:

$$E_K = -\frac{1}{2} K_0 (\cos^2 \theta + \cos^2 \theta') - K_1 \cos \theta \cos \theta' \quad (6)$$

where $A-B = -K_1$. For an antiferromagnet with this form of uniaxial anisotropy there are two types of spin configuration, the (af) direction being directed either parallel or normal to the axis. The conditions are as follows:

Antiferromagnetism direction	Conditions
Parallel to axis (A_p)	$K_0 - K_1 > 0$
Normal to axis (A_n)	$K_0 - K_1 < 0$

7.1.3 Field Induced Transitions

When a magnetic field \underline{H} is applied, an extra term, due to magnetostatic energy, must be incorporated in the total energy expression.

$$E_H = -(\underline{M}_a + \underline{M}_b) \cdot \underline{H} \mu_0 \quad (7)$$

Calculations have been made only for the two situations: \underline{H} parallel to the (af) direction, and \underline{H} normal to the (af) direction. For fields normal to the (af) direction there is a finite susceptibility s_n which is independent of H up to a value H_1 at which the magnetization suddenly saturates (fig. 7.1).

For an applied field normal to the (af) direction we have a gradual field induced transition from the (af) to the (f) state as the magnetization direction of each sublattice gradually folds up into the direction of the applied field, as the field strength increases.

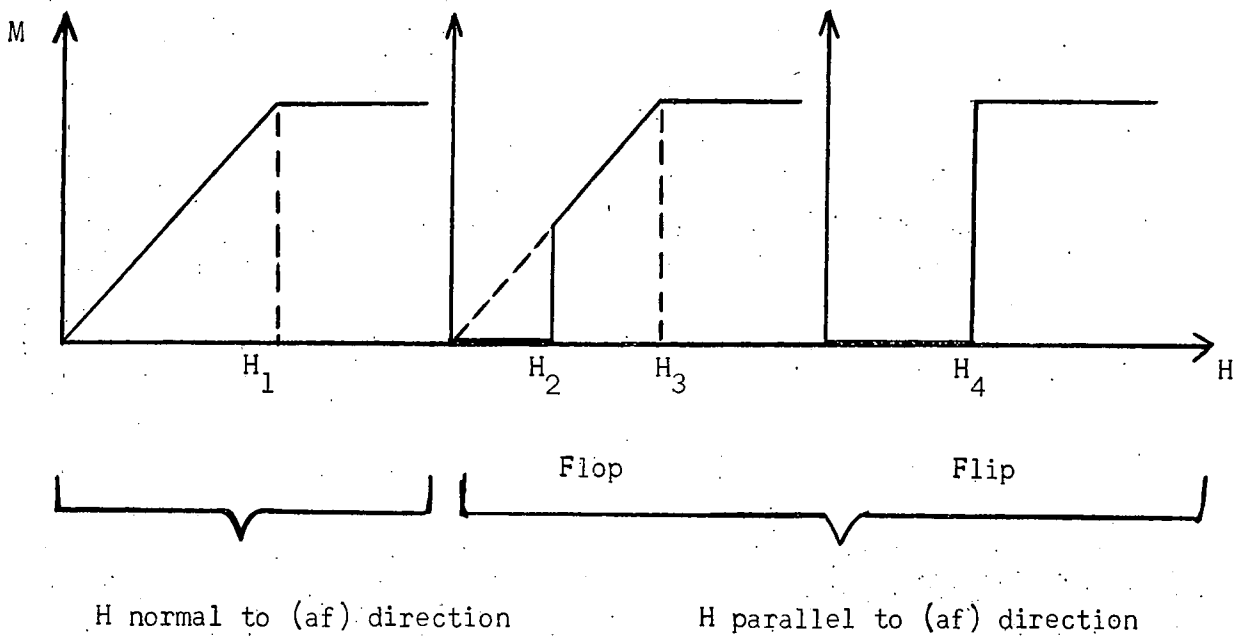


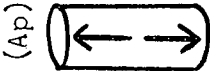
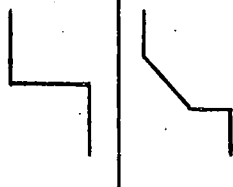
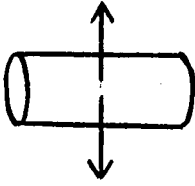
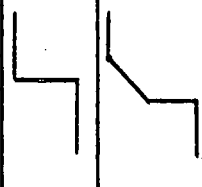
Figure 7.1 The various types of Field Induced Transition.

For fields applied parallel to the (af) direction there is initially no change in energy for small fields since no couple is exerted on the sublattice magnetizations. On increasing the field strength, a point is reached where it is energetically favourable for the spin system to undergo either of the following transitions:

- (a) Spin flip, in which the sublattice opposing the field direction reverses its magnetization direction,
- (b) Spin flop, in which the (af) direction becomes normal to the applied field, with the two sublattice magnetizations inclined towards the field direction with a component less than the saturation value M .

Spin flip is a special case of the more general spin flop. For spin flop, on further increasing the field strength above the value H_2 , the magnetization rises linearly and saturates at the field value H_3 . This linear rise extrapolates back to the origin, with a susceptibility s_p . Spin flip transitions are characteristic of materials in which the exchange is weak compared with the anisotropy. For spin flop transitions the reverse is true.

TABLE 7.1 Expressions for susceptibilities and critical fields

Anisotropy Conditions	(af) direction	s_n, h_1	Type	Form of M vs H Curve	s_p	Critical Fields
$K_0 > K_1$	(Ap) 	$s_n = \frac{1}{n(1+r')}$ $h_1 = 2(1+r')$	II III IV		— $s_p = \frac{1}{n(1-r)}$ $s_p = \frac{1}{n(1+r')}$	$h_4 = 1 + r' - r$ $h_2 = 2(1-r)^{\frac{1}{2}} r^{\frac{1}{2}}$ $h_3 = 2(1-r)$ $h_2 = 2(-r')^{\frac{1}{2}} (1-r')^{\frac{1}{2}}$ $h_3 = 2(1-r)$
$K_0 < K_1$	(An) 	$s_n = \frac{1}{n(1-r)}$ $h_1 = 2(1-r)$	V VI		— $s_p = \frac{1}{nr}$	$h_4 = 1$ $h_2 = 2(1-r)^{\frac{1}{2}} r^{\frac{1}{2}}$ $h_3 = 2r$
Ferromagnetic			I			

In table 7.1 the results of Néel's calculations are summarized in terms of the reduced variables h and r .

$$h = \frac{2H}{nM}, \quad r = \frac{2(K_0 + K_1)}{\mu_0 n M^2}, \quad r' = \frac{2(K_0 - K_1)}{\mu_0 h M^2}$$

There are five types of behaviour for the (af) system. Each type of behaviour is represented by a definite region in the (r, r') plane. The (Ap) type can undergo spin flip (type II) if $K_0 > \frac{n \mu_0 M^2}{4}$ (i.e. strong anisotropy with respect to exchange), and spin flop (type III) if $K_0 < \frac{n \mu_0 M^2}{4}$ (i.e. weak anisotropy with respect to exchange). The (An) material has three types of behaviour:

flip (type V) and flop (types IV and VI).

Type I is for ferromagnets, with which we are not concerned.

7.1.4 Some Comments on the Applicability of the Theory.

The formulae of Table 7.1 are valid at absolute zero temperature. For higher temperatures the spontaneous magnetization of the sublattice will decrease in a manner qualitatively similar to a Brillouin function, becoming zero at $T = T_N$. The magnetization directions will then spend some of their time not in the easy direction, but will have some thermal fluctuation about this direction. When a field is applied parallel to the easy direction, the ions whose magnetic moments are not in the easy direction at a given instant in time will be susceptible to magnetostatic forces. The initial susceptibility will not then be zero. Since 4.2K, the temperature at which the results were obtained, is very much less than the ordering temperatures ~ 100 K, the formulae of table 7.1 can be applied to the results.

The transitions are assumed to occur when it is energetically favourable from the point of view only of the initial and final energies (i.e. before and after the transition). The potential barrier due to anisotropy is ignored. Some sort of mechanism is therefore assumed to be present which allows the spins to by-pass this potential barrier in the transition. At low temperatures thermal activation will be insufficient. Hence some other

mechanism is required, such as tunneling.

It appears to the author that it is impossible to observe critical field transitions in (An) type uniaxial antiferromagnets. For spins confined in the basal plane, all directions in the basal plane are easy directions and are energetically equivalent. Therefore, when a small field is applied in the (af) direction it will immediately be energetically favourable for the (af) direction to rotate within the basal plane until it is normal to the applied field. \underline{M}_a and \underline{M}_b will then incline slightly towards the field direction, thus lowering the magnetostatic energy until the magnetostatic forces are balanced by the exchange forces. The total energy of the system in this situation will be lower than in the situation assumed in the theory where the (af) direction remains parallel to the applied field. We will therefore obtain a susceptibility equal to $1/n$ up to the field value required for saturation. This could be regarded as a spin flop transition with an infinitesimally small critical field H_2 . The formulae in table 7.1, for critical fields in (An) type antiferromagnets, contain the anisotropy constants K_0 and K_1 . Hence these formulae were obviously derived with the assumption that the uniaxial anisotropy had some effect in constraining the (af) direction to remain parallel to the field for field values less than H_2 or H_4 . For flop transitions it is evidently assumed (for fields just in excess of H_2) that the plane containing \underline{M}_a and \underline{M}_b be coincident with the plane containing the crystal axis and the applied field direction. It would appear, from the above consideration, that the derivation of critical field transitions for types IV, V and VI is unrealistic.

The theory has been applied with considerable success by Néel to various materials showing metamagnetic behaviour. The values of the anisotropy constants, deduced by means of this theory, are of the same order of magnitude as those measured by torque methods on some ferromagnetic materials. The magnetic behaviour of dysprosium was very well accounted for by Néel in terms of this two-sublattice theory. However, neutron diffraction techniques have since shown that dysprosium is a helical

antiferromagnet in the temperature range showing metamagnetic behaviour. The theory, therefore, evidently accounts for the grosser forms of metamagnetic behaviour, but the successful application of the theory to a given material must not be considered to be evidence of a two-sublattice magnetic structure.

From equations (1) and (2) for the paramagnetic Curie point θ_p and the Néel point T_N it is evident that T_N must be slightly larger than θ_p for the condition $n' \gg n$ to be fulfilled. On applying the theory to dysprosium Néel obtained a value of 16 for this ratio, using the formulae $s_n = 1/n$ at T_N and $n' - n = 2\theta_p/C$. From equations (1) and (2) one obtains:

$$\frac{n'}{n} = \frac{T_N + \theta_p}{T_N - \theta_p} \quad (8)$$

Using $\theta_p = 157\text{K}$ and $T_N = 178\text{K}$ this gives a value of 16 for the ratio. The two approaches are therefore consistent. Reasonable consistency was found for erbium, where $n'/n = 3.8$ using the first approach and $n'/n = 3$ using the second approach. For MnAu_2 the first approach gave $n'/n = 142$, which is particularly large, as required for the successful application of the theory. However, comparison of T_N ($= 370\text{K}$) with θ_p ($= 451\text{K}$) gives a value of $n'/n = -10$, which is entirely inconsistent with the first approach. MnAu_2 has since been shown to be a helical antiferromagnet.

7.2 The M vs H Curves of Polycrystalline Samples

The relationships derived in the theory involve quantities which are applicable to single crystals magnetized parallel or normal to the axis. Since the experimental results were obtained from polycrystalline samples, it is necessary to establish how the single crystal parameters can be related to the polycrystalline parameters before any application of the relationships to the results can be made.

7.2.1 Initial Susceptibility χ_i

In the first approximation it has been shown (ref 7.2) that the initial susceptibility of a polycrystalline sample is given by:

$$\chi_i = \frac{2}{3} s_n + \frac{1}{3} s_p.$$

This formula is not rigorous because it neglects the magnetic dipole interaction between crystallites, and also the rotation of the (af) direction on application of a field at an oblique angle to the axis of a crystallite. This latter is a second order effect. Because of its simplicity, however, we shall use this relationship. Since the results were obtained at 4.2K, which is very close to the absolute zero temperature we can neglect s_p .

$$\chi_i = \frac{2}{3} s_n. \quad (9)$$

7.2.2 The Critical Field H_c and Saturating Field H_s

There is available no satisfactory theoretical approach for relating H_c in a polycrystal with H_2 and H_4 in a single crystal. The polycrystal results show fairly sharp critical field transitions which can be assumed to have begun and ended within a small range of field values. It is reasonable to assume that the critical field H_2 or H_4 lies somewhere within this range. The error in measurement of H_c then corresponds to the extreme values of the range. The measurement of H_c was performed using the criterion already described (5.3.1).

$$H_c = H_1 \quad \text{Spin flip}$$

$$H_c = H_2 \quad \text{Spin flop}$$

For the saturating field H_s the situation is simpler. Firstly we can obviously say that saturation occurs above the critical field values H_2 or H_4 , so that neither of these can be equated to H_s . This narrows down the number of possibilities to the saturation being due either to H_3 in a flop sample or to H_1 , whichever is the greater. If we assume that the magnetic dipole contribution to the anisotropy is small with respect to the K_0 contribution, i.e. $K_1 \ll K_0$, then the easy direction of the zero field (af) state must be identical to the easy direction of the field induced (f) state. Therefore the saturation in the hard direction at a field H_1 will correspond to a higher anisotropy energy than saturation in the easy direction at a value H_2 . Since the exchange interaction is

isotropic the anisotropy excess energy in the hard direction must be supplied entirely from magnetostatic energy. Hence $H_1 > H_3$. The crystallites will reach saturation for various field values between H_3 and H_1 and therefore saturation of the polycrystalline sample will occur at H_1 .

$$H_s = H_1 \quad \text{for } K_1 \ll K_0.$$

If K_1 is not much less than K_0 the magnetic dipole interaction will play some part in the anisotropy. It is then possible that the easy direction for the zero-field (af) state may become the hard direction in the field induced (f) state. We then have the following ambiguity:

$$H_s = H_1 \text{ or } H_3 \quad \text{for finite } K_1.$$

7.2.3 Magnetization of Spin-flop materials for $H_c \ll H_s$

We shall now examine the range of fields above the field value at which all the crystallites have effectively completed their transitions, and below the field value at which saturation for some crystals is beginning. To obtain the resultant magnetization curve we must superpose two curves A and B. Curve A is the linear magnetization with susceptibility $\frac{2}{3} s_n$. Due to the sinusoidal nature of the anisotropy energy as a function of θ and θ' , the susceptibility s_n of a single crystal is linear up to H_1 . For a polycrystal this linearity will still hold up to saturation, but the saturation will not occur so sharply. Curve B will be similar to the spin flop curve of a single crystal (fig. 7.1), but the sharp corners will be rounded off in the polycrystal case. Thus in the range between H_c and H_s we must superpose two linear curves, each of which extrapolates back to the origin. The resultant polycrystal curve must also, therefore, be linear and extrapolate to the origin for a spin flop material.

7.3. Interpretation of the $Gd_3(Fe,Co)$ and $Gd_3(Co,Ni)$ Results in terms of the Neel Theory

7.3.1. Relationship between H_c and χ_1 at 4.2K.

For each type of material (II to VI) we use the expression for H_c and S_n from Table 7.1. Eliminating n in each pair of expressions, we obtained

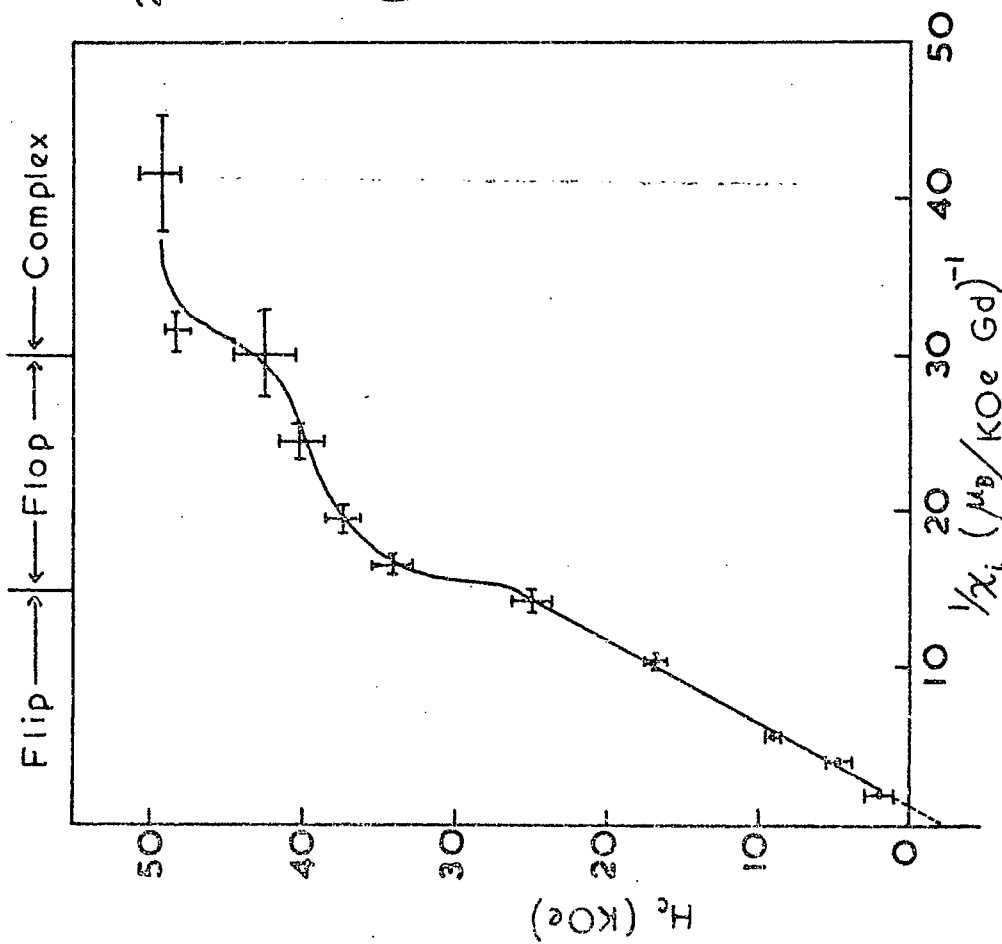


Fig. 7.2 H_c vs $1/\chi_i$ for $Gd_3(Fe,Co)$ and $Gd_3(Co,Ni)$ at 4.2 K

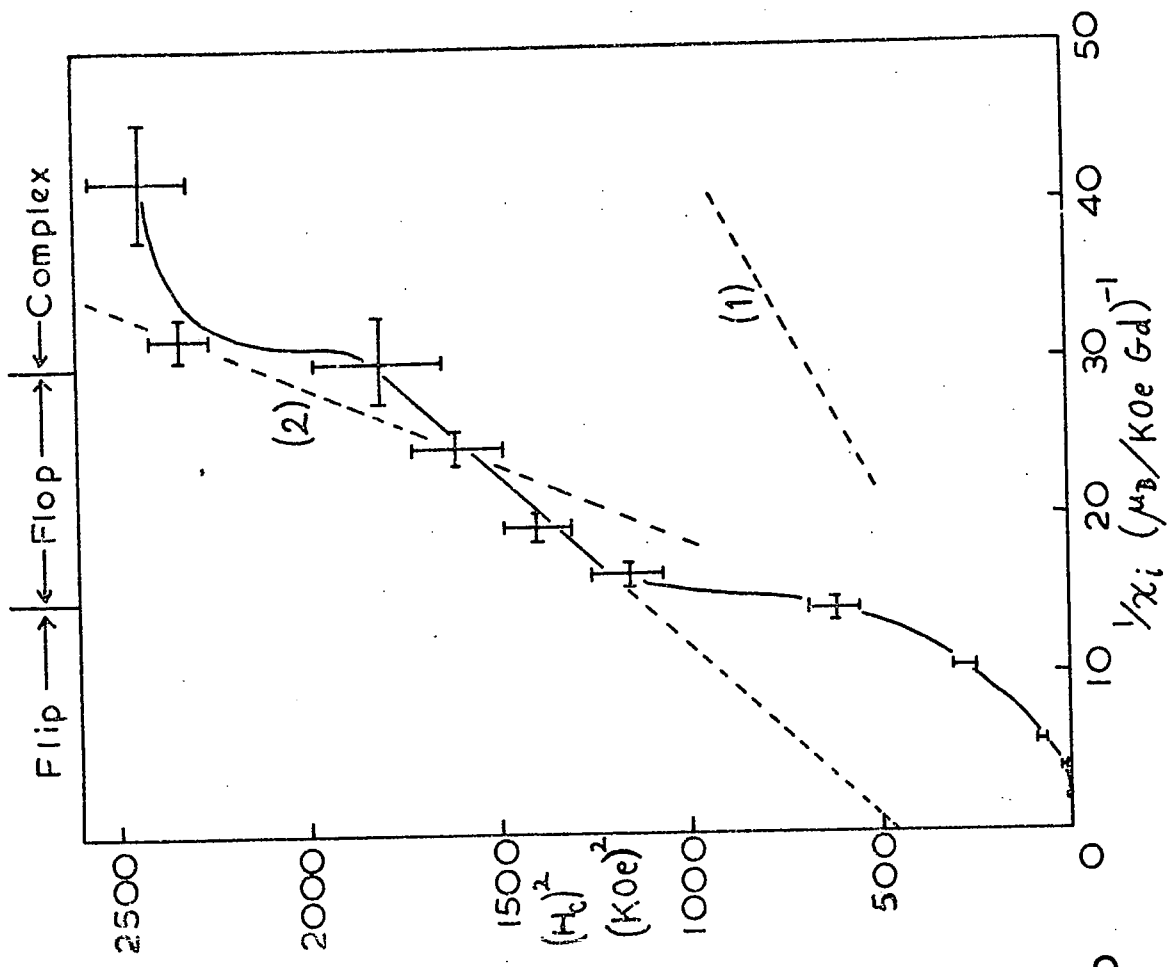


Fig. 7.3 H_c^2 vs $1/\chi_i$ for $Gd_3(Fe,Co)$ and $Gd_3(Co,Ni)$ at 4.2 K

the following:

$$\text{Spin Flip II} \quad H_c = \frac{M\alpha}{2} \cdot \frac{1}{\chi_i} - \frac{a}{2M} \quad (10)$$

$$\text{Spin Flop III} \quad H_c^2 = \alpha b \cdot \frac{1}{\chi_i} - \frac{b(a+b)}{M^2} \quad (11)$$

$$\text{Spin Flop IV} \quad H_c^2 = -\alpha b \cdot \frac{1}{\chi_i} - \frac{b(a+b)}{M^2} \quad (12)$$

$$\text{Spin Flip V} \quad H_c = \frac{M\alpha}{2} \cdot \frac{1}{\chi_i} + \frac{a}{2M} \quad (13)$$

$$\text{Spin Flop VI} \quad H_c^2 = \alpha a \cdot \frac{1}{\chi_i} \quad (14)$$

$$\text{where } a = \frac{2(K_0 + K_1)}{\mu_0} \quad \text{and} \quad b = \frac{2(K_0 - K_1)}{\mu_0}$$

If we assume that the anisotropy energies K_0 and K_1 remain constant throughout the series of compounds, then for a series of flip-type compounds H_c vs $1/\chi_i$ should be linear, and for flop-type compounds H_c^2 vs $1/\chi_i$ should be linear.

In fig. 7.2 is plotted H_c vs $1/\chi_i$ at 4.2K for the samples in the series of compounds. The curve can be divided into three portions: an initial linear portion for the smaller values of H_c from $\text{Gd}_3\text{Fe}_{0.1}\text{Co}_{0.9}$ for increasing 3d-electron concentration up to $\text{Gd}_3\text{Co}_{0.75}\text{Ni}_{0.25}$; and two non-linear portions, from $\text{Gd}_3\text{Co}_{0.5}\text{Ni}_{0.5}$ to $\text{Gd}_3\text{Co}_{0.15}\text{Ni}_{0.85}$, and the portion for the two nickel-rich compounds $\text{Gd}_3\text{Co}_{0.05}\text{Ni}_{0.95}$ and Gd_3Ni . The initial linear portion is consistent with H_c being a spin-flip transition where n varies with composition while the anisotropy remains constant. We shall call this the flip-portion.

In fig. 7.3 H_c^2 is plotted against $1/\chi_i$ for the results at 4.2K. The flip samples of course show a parabolic variation here, since they gave a linear variation for H_c vs $1/\chi_i$. The samples of the second portion of the H_c vs $1/\chi_i$, now give a linear variation of H_c^2 vs $1/\chi_i$, which is consistent with these samples having a spin-flop transition at H_c , where n varies with composition but the anisotropy remains constant. We shall call this the flop-portion.

The final portion of these curves, for the two nickel-rich compounds cannot be classified into either of the two types of transition. Because of this, and the various other strange behaviours of these two compounds,

e.g. two critical fields observed, we shall call this the complex portion.

It may be recalled, from the shapes of the M vs H curves, that these three portions correspond closely to the three qualitatively different types of M vs H curve. The flip portion corresponds to samples without any linear portion in the M vs H curves between the field values H_c and H_s . The flop portion corresponds to samples which show a linear variation in M vs H for a small range of fields between H_c and H_s , this linear portion extrapolating to the origin. This is what is expected from a flop transition, even for polycrystalline material (7.2.3). For samples showing complex behaviour, such a linear portion in the M vs H curve exists, but it extrapolates to a negative intercept on the M axis at $H = 0$. These three groups of the series of compounds will be considered in the following sections.

7.3.2 Spin-flip Behaviour

From the H_c vs $1/\chi_i$ variation we can obtain values for the sublattice magnetization and the anisotropy from the measurement of two quantities: the gradient and the intercept on the H_c axis.

From equations (10) and (13) we see that the gradient is equal to $M\alpha/2$ for both types of flip behaviour. Assuming $\alpha = \frac{2}{3}$, as is theoretically expected, we obtain:

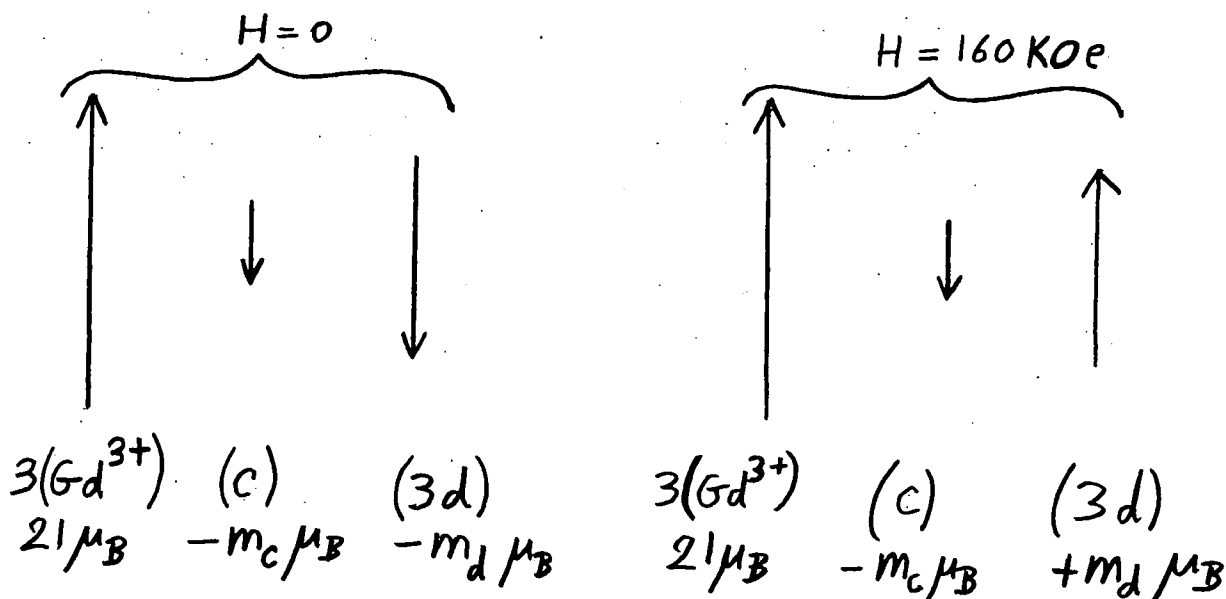
$$\begin{aligned} M &= 5.8 \pm 0.6 \mu_B / \text{Gd} \\ &= (1.51 \pm 0.15) \times 10^6 \text{ A/m} \end{aligned} \quad (15)$$

Therefore the spontaneous magnetization $M/2$ of either sublattice is:

$$M_a = M_b = (0.76 \pm 0.07) \times 10^6 \text{ A/m.}$$

If we assume that each gadolinium ion exists as a Gd^{3+} ion, contributing $7\mu_B$, this leaves $3.6\mu_B$ per transition metal atom, to be distributed among the polarizations of 3d-electrons and other conduction electrons. This is a large moment per transition metal atom and is to be compared with the excess moment above the moment expected from the Gd^{3+} ions, as obtained from the saturation magnetization in the highest field 160 KOe. This excess moment was $1 \pm 0.3\mu_B$ per transition metal atom. These two excess moments, one positive and the other negative, need not be equal in magnitude if we

arrange the moments as follows:



We divide the excess moments into m_d and m_c , the moment per transition metal atom due to the 3d electron polarization and conduction electron polarization respectively. We also assume that the 3d moment is weakly coupled to the Gd moment.

For $H = 0$ and $H = 160 \text{ KOe}$ respectively we have:

$$m_d + m_c = 3.6 \pm 1.8 \mu_B/\text{TM} \quad \text{from } H = 0$$

$$m_d - m_c = 1.0 \pm 0.3 \mu_B/\text{TM} \quad \text{from } H = 160 \text{ KOe.}$$

From these two equations we obtain:

$$m_d = 2.3 \pm 1.0 \mu_B/\text{TM}$$

$$m_c = 1.3 \pm 1.0 \mu_B/\text{TM}$$

The saturation moment of pure iron $2.2\mu_B/\text{Fe}$, and cobalt $1.7\mu_B/\text{Co}$, agree with the value of m_d within the experimental error.

The conduction electron polarization m_s corresponds to a value $0.4 \pm 0.3\mu_B$ Gd atom. The saturation moment of pure gadolinium metal is $7.55\mu_B/\text{Gd}$, leaving $0.55\mu_B/\text{Gd}$ to be accounted for by the conduction electron polarization. The two values are equal within the error. However, we have assumed that m_c is directed opposite to the Gd moment in the Gd_3B compounds, which is a negative conduction electron polarization, whereas for pure Gd metal the conduction electron polarization is positive.

The above derivation of m_c and m_d is based upon the ad-hoc assumption that the spins are arranged as illustrated above. It also depends upon the quantitative application of the Néel spin-flip formulae for H_c as a function of M , the sublattice magnetization. Since the theory is expected to be applicable only in a semi-quantitative fashion the value of M deduced from the gradient of H_c vs $1/\chi_i$ should be treated with reservation. The fact that it agrees well within an order of magnitude with the expected sublattice magnetization, $7\mu_B/\text{Gd}$, is as much as can be expected from the theory. Another reason for not treating this value of M too quantitatively is that H_c and χ_i are influenced, as will be seen later (7.3.8) by time dependence which, though it is not expected to affect the magnitude of M very much, may affect it sufficiently to invalidate the above values of m_c and m_d . The measured value of M_{160} is reliable, however, and is very close to the saturation. M_{160} for Gd_3Co agrees with that obtained by Féron et al. in static fields at 70 kOe, (ref. 7.3).

From equations (10) and (13) the intercept of the H_c vs $1/\chi_i$ curve on the H_c axis is equal to $-a/2M$ for flip II and $+a/2M$ for flip V. The measured intercept is -3 ± 1 kOe. Substituting the value of $M = 5.8 \pm 0.6\mu_B/\text{Gd}$, we obtain the anisotropy constant:

$$K_0 + K_1 = (4.5 \pm 2.2) \times 10^5 \text{ J/m}^3 \text{ flip II (A}_p\text{)}$$

$$K_0 + K_1 = -(4.5 \pm 2.2) \times 10^5 \text{ J/m}^3 \text{ flip V (A}_n\text{)}$$

This is of the same order of magnitude as the anisotropy of ferromagnetic gadolinium. It also agrees well with the anisotropy obtained by Féron et al. (ref 7.3) for Gd_3Co , $5.1 \times 10^5 \text{ J/m}^3$. They obtained n from H_c assuming the transition to be type V (flip). They then substituted this value of n , and the experimental value of χ_i at 4.2K into the expression for s_n of type V, assuming $\chi_i = \frac{2}{3} s_n$, in order to obtain the anisotropy constant $K_0 + K_1$.

7.3.3 Spin Flop Behaviour

The flop portion of the H_c^2 vs $1/\chi_i$ curve is linear and extrapolates to an intercept at 460 kOe² on the H_c^2 axis. From this intercept and the gradient the following were deduced:

$$K_0 - K_1 = \pm 9 \times 10^5 \text{ J/m}^3 \quad \begin{matrix} A_p \\ (A_n) \end{matrix}$$

$$K_0 + K_1 = \mp 38 \times 10^5 \text{ J/m}^3 \quad \begin{matrix} A_n \\ (A_p) \end{matrix}$$

These then give:

$$K_0 = \mp 14.5 \text{ J/m}^3 \quad \begin{matrix} A_p \\ (A_n) \end{matrix}$$

$$K_1 = \mp 23.5 \text{ J/m}^3 \quad \begin{matrix} A_p \\ (A_n) \end{matrix}$$

The alternative signs refer to A_p (the upper sign), and A_n (the lower sign). For A_p spin structure the type of transition must be flop III. For A_n spin structure the type of transition is assumed to be flop IV, since flop VI requires the H_c^2 vs $1/\chi_i$ curve to extrapolate to the origin. When, for the flip samples, we assumed an A_p structure, we obtained a positive ($K_0 + K_1$) value of $4.5 \times 10^5 \text{ J/m}^3$. This is opposite in sign to that obtained above and entirely different in magnitude. We also obtain a sign discrepancy assuming an A_n structure and the same difference in magnitude. This would mean that $K_0 + K_1$ changes sign as we change the composition on going from flip type to flop type behaviour. This is unlikely.

In the H_c^2 vs $1/\chi_i$ plot it is evident that the linear behaviour drawn through the experimental points is not unique, because of the large errors involved. We shall now attempt to find another linear variation which intercepts the experimental values within the error indicated on the graph, and at the same time correspond to the value of $K_0 + K_1$ as obtained in the flip region.

The equation (14) for flop VI is

$$H_c^2 = \frac{4}{3\mu_0} (K_0 + K_1) \frac{1}{\chi_i}$$

The intercept on the H_c^2 axis is zero. From the value of $K_0 + K_1$ obtained for the flip compounds, the expected linear variation for the flop compounds has been determined, and is indicated by the dashed line labelled (1) on the H_c^2 vs $1/\chi_i$ curve. Since the experimental points are nowhere near this line, we shall reject flop VI as a possible type of transition

in these compounds. For Flop VI to be applicable we would require $K_0 + K_1 = 13 \text{ J/m}^3$.

If we assume the flip compounds are type II (A_p), then the flop compounds must be type III (A_p). If we assume the flip compounds to be type V (A_n), the flop compounds must be type IV (A_n). In fig. 7.3 is shown the expected behaviour for type III (IV) using the value of $K_0 + K_1$ obtained for the flip compounds of type II (V). This expected behaviour, labelled (2), is the best fit to the experimental results, and corresponds to an assumed value of $K_0 - K_1 = 20 \times 10^5 \text{ J/m}^3$.

$$K_0 + K_1 = \pm 4.5 \times 10^5 \text{ J/m}^3 \quad \begin{matrix} A \\ (A_p) \\ A_n \end{matrix}$$

$$K_0 - K_1 = \pm 20 \times 10^5 \text{ J/m}^3 \quad \begin{matrix} A \\ (A_p) \\ A_n \end{matrix}$$

From these equations we obtained:

$$K_0 = \pm 12.3 \times 10^5 \text{ J/m}^3 \quad \begin{matrix} A \\ (A_p) \\ A_n \end{matrix}$$

$$K_1 = \mp 7.8 \times 10^5 \text{ J/m}^3 \quad \begin{matrix} A \\ (A_p) \\ A_n \end{matrix}$$

Despite the fact that these values give the best fit, the fit is not very good. It may be that the anisotropy parameter K_0 varies for the flop transition. Since the value of $K_0 - K_1$ required for the best fit is an order of magnitude larger than $K_0 + K_1$, the deduced values of K_0 and K_1 are similar in magnitude. Considering that K_0 and K_1 are a result of two entirely different sources of anisotropy, the probability of their being similar in magnitude is very low. Therefore, the values of $K_0 - K_1$, K_0 and K_1 deduced above should be treated with reservation. This remark, of course, does not apply to $K_0 + K_1$.

7.3.4 Calculation of n, the inter-sublattice exchange coefficient.

For the spin flip samples of type (A_n) the values of n can be obtained by means of either of the formulae:

$$H_c = \frac{nM}{2} \quad \text{or} \quad \chi_i = \frac{2}{3} \cdot \frac{1}{n(1-r)}$$

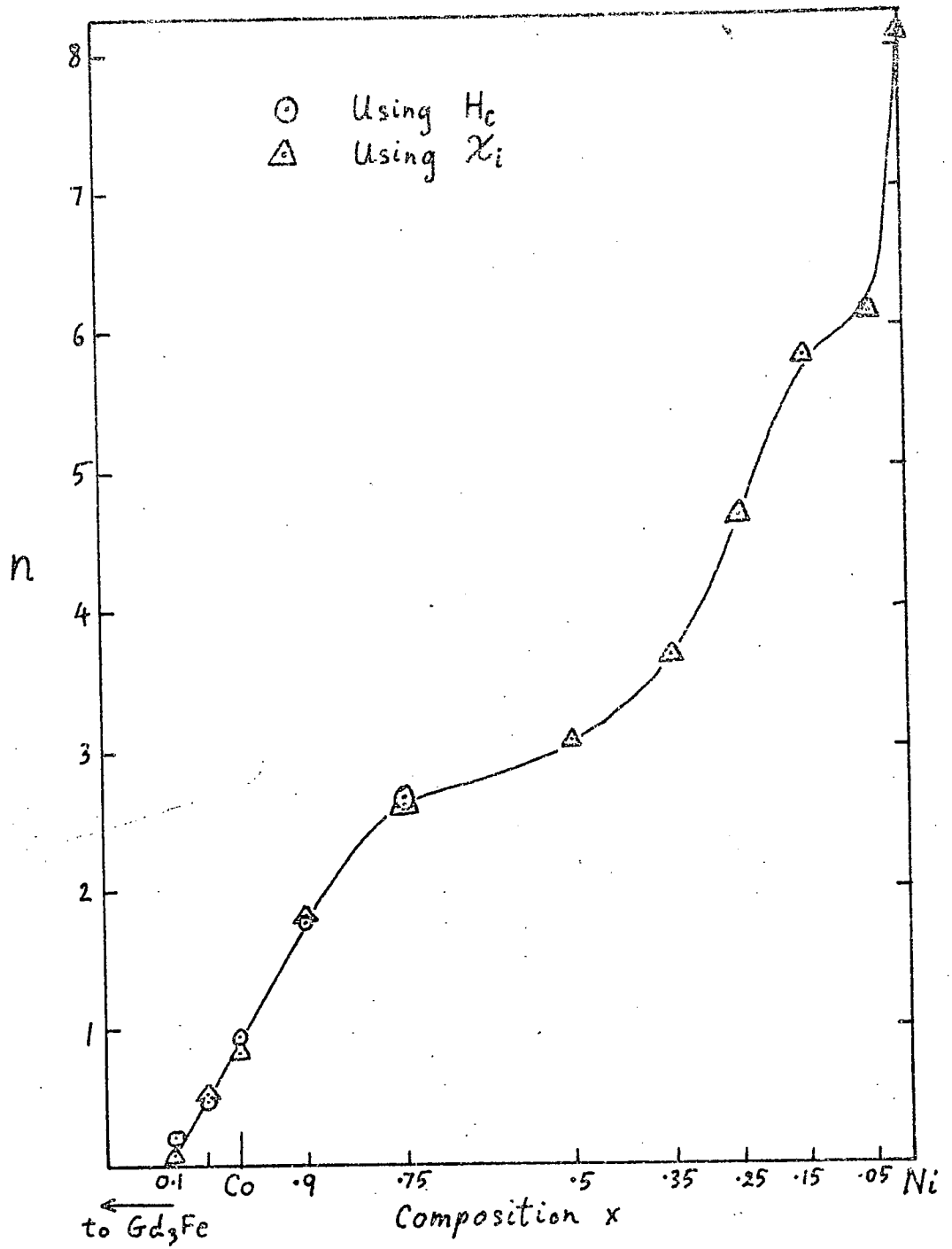


Fig. 7.4 The Exchange Coefficient n

Since M and r were obtained by combining these two formulae, the value of n for a sample calculated by means of H_c or χ_i should be identical, except for experimental scatter of results. In table 7.2 these values of n are given, together with H_c and χ_i at 4.2K, in MKS units, where χ is defined by M/H . Since the above expression for χ_i is valid for all (A_n) types the values of n for the flop samples have also been determined. It is possible that this method of obtaining n is not applicable to the complex samples, but the values obtained are also included for completeness. The values of n are plotted in fig. 7.4 as a function of composition. The exchange energy $\mu_0 M^2/4$ varies from $5.8 \times 10^5 \text{ J/m}^3$ for Gd_3Co up to $56 \times 10^5 \text{ J/m}^3$ for Gd_3Ni .

Table 7.2 n values for (A_n) spin structure

Sample	H_c ($\times 10^6 \text{ A/m}$)	χ_i	n	
			from χ_i	from H_c
$\text{Gd}_3\text{Fe}_{.1}\text{Co}_{.9}$	0.159	1.67	0.09	0.20
$\text{Gd}_3\text{Fe}_{.05}\text{Co}_{.95}$	0.358	0.792	0.53	0.47
Gd_3Co	0.716	0.584	0.83	0.94
$\text{Gd}_3\text{Co}_{.9}\text{Ni}_{.1}$	1.33	0.315	1.80	1.74
$\text{Gd}_3\text{Co}_{.75}\text{Ni}_{.25}$	1.99	0.229	2.60	2.60
$\text{Gd}_3\text{Co}_{.5}\text{Ni}_{.5}$	2.7	0.198	3.05	-
$\text{Gd}_3\text{Co}_{.35}\text{Ni}_{.65}$	2.98	0.168	3.65	-
$\text{Gd}_3\text{Co}_{.25}\text{Ni}_{.75}$	3.18	0.134	4.66	-
$\text{Gd}_3\text{Co}_{.15}\text{Ni}_{.85}$	3.38	0.109	5.80	-
$\text{Gd}_3\text{Co}_{.05}\text{Ni}_{.95}$	3.84	0.104	6.10	-
Gd_3Ni	3.92	0.079	8.10	-

7.3.5 Relationship between H_s and $1/\chi_i$ at 4.2K

From the expressions for s_n and h_1 for (A_p) and (A_n) spin structures we obtain the relationship:

$$H_1 = \frac{2M}{3} \cdot \frac{1}{\chi_i} \quad \text{for } (A_p) \text{ and } (A_n).$$

From the gradient of the H_1 vs $1/\chi_i$ plot (fig. 7.5) which is linear for the flip compounds and extrapolates to the origin, we obtain the value of the sublattice magnetization, which gives

$$M = 5.4 \pm 0.6 \mu_B/\text{Gd}.$$

This agrees, within the experimental error, with the value $5.8 \pm 0.6 \mu_B/\text{Gd}$ obtained from the H_c vs $1/\chi_i$ plot. In the H_s vs $1/\chi_i$ plot the flop samples depart from the linear behaviour of the flip samples. The first two flop samples near this departure are included in the plot.

7.3.6 Calculation of n' , the Intra-sublattice Exchange Coefficient

The Néel temperature is given by equation (2):

$$T_N = \frac{C}{2} (n' + n)$$

Values of T_N and n have already been obtained for each compound. Values of C , the Curie constant, have yet to be obtained. In the absence of paramagnetic susceptibility data, C must be calculated from the formula:

$$C = \frac{\mu_0 \mu_B^2}{3k} \sum_i n_i p_i^2$$

where p is the effective paramagnetic moment in Bohr magnetons, and n_i is the concentration (m^{-3}) of each type of magnetic ion. The suffix i refers to the i 'th type of magnetic ion. We are concerned, for these pseudobinary compounds with three types of magnetic ion. We can assume that the gadolinium ion possesses the full gJ value, $7\mu_B$, of the Gd^{3+} ion. For the transition metal ions we use the values obtained by Sucksmith and Pearce (ref 7.4) for pure Fe, Co and Ni, from the paramagnetic susceptibility.

Metal	p (effective magneton number)
Fe	3.2
Co	3.15
Ni	1.78
Gd	$\sqrt{63}$

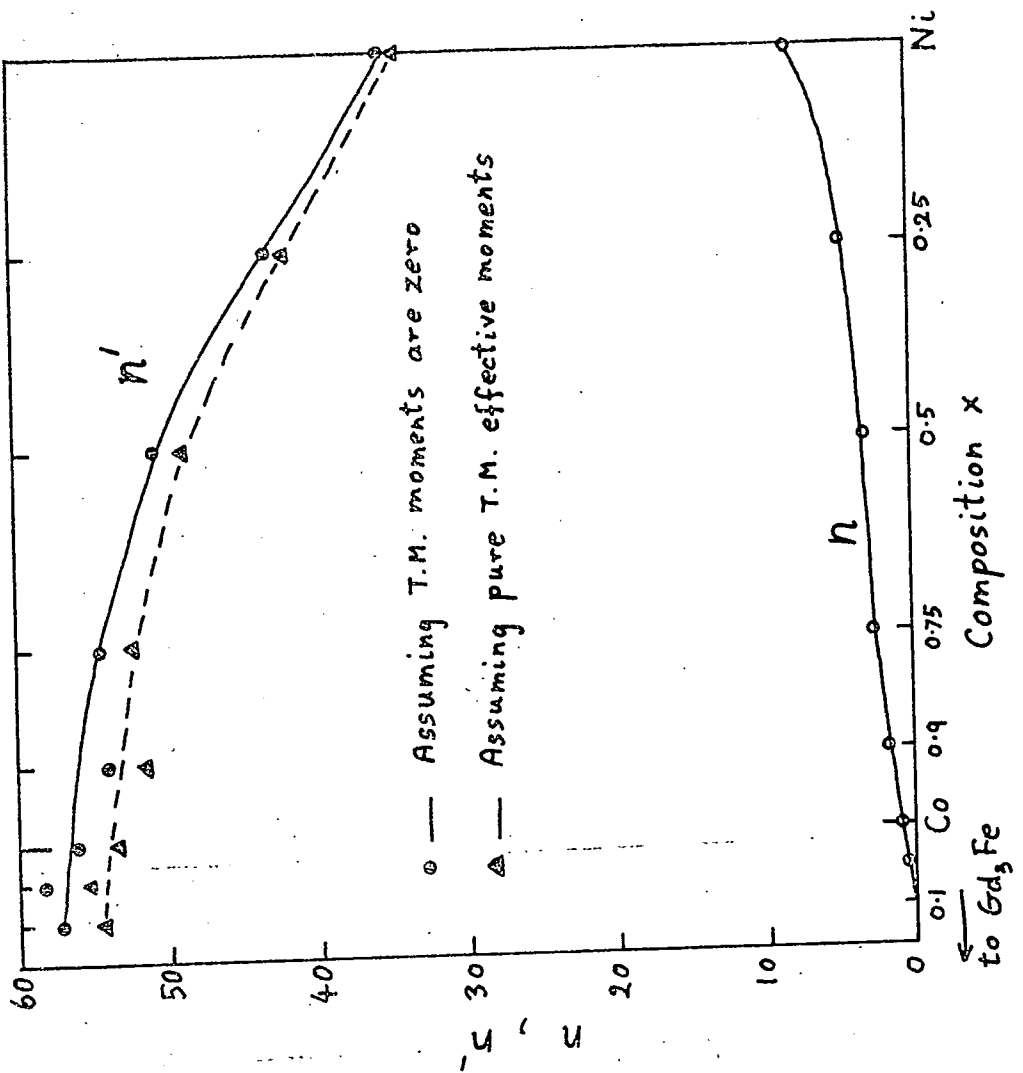
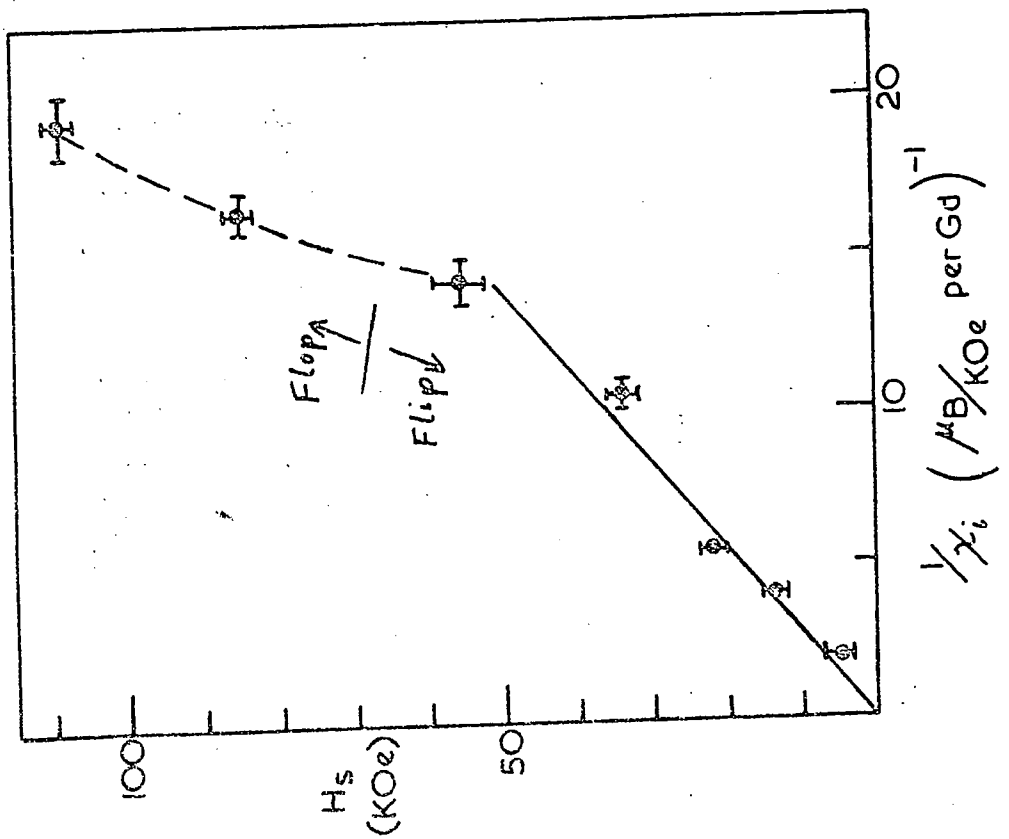


Fig. 7.5 H_s vs $1/x_i$ for Flip Compositions at 4.2K Fig. 7.6 The Exchange Coefficients n' and n .

TABLE 7.3

(Numbers in brackets are obtained assuming the T.M. moment to be zero, ie.

$$\langle p_{\text{eff}}^2 \rangle = 63, C = 4.62\text{K for all compounds})$$

Compound	$\langle p_{\text{eff}}^2 \rangle$	C(K)	$T_N(\text{K})$	$n' + n$	n	n'	n'/n
$\text{Gd}_3\text{Fe}_{.1}\text{Co}_{.9}$	66.3	4.86	132.5	54.6 (57.4)	0.1	54.5 (57.3)	545 (573)
$\text{Gd}_3\text{Fe}_{.05}\text{Co}_{.95}$	66.3	4.86	136	56.0 (58.9)	0.5	55.5 (58.4)	111 (117)
Gd_3Co	66.3	4.86	132	54.4 (57.1)	0.9	53.5 (56.2)	59 (62.5)
$\text{Gd}_3\text{Co}_{.9}\text{Ni}_{.1}$	66.1	4.84	139	53.4 (55.9)	1.8	51.6 (54.1)	29 (30)
$\text{Gd}_3\text{Co}_{.75}\text{Ni}_{.25}$	65.7	4.82	132	54.8 (57.1)	2.6	52.2 (54.5)	20 (21)
$\text{Gd}_3\text{Co}_{.5}\text{Ni}_{.5}$	65.2	4.78	124	51.9 (53.7)	3.0	48.9 (50.7)	16 (17)
$\text{Gd}_3\text{Co}_{.25}\text{Ni}_{.75}$	64.6	4.73	110	46.5 (47.6)	4.6	41.9 (43)	9 (9.5)
Gd_3Ni	64.1	4.7	100	42.5 (43.3)	8.1	34.4 (35.2)	4 (4.4)

In obtaining n_1 we use the fact that the (abc) unit cell of the crystal structure contains 12 Gd ions and 4 TM ions. For the value of the unit cell, we take the value

$$\langle abc \rangle = 424 \times 10^{-30} \text{ m}^3.$$

This is the average value of abc for Gd_3Co and Gd_3Ni . The maximum error in abc introduced thereby is only 1%. C is then calculated to be:

$$C = 0.0733 \langle p_{\text{eff}}^2 \rangle$$

$$\text{where } \langle p_{\text{eff}}^2 \rangle = 63 + \frac{1}{3} [x 3.2^2 + (1-x) 3.15^2] \quad \text{for } \text{Gd}_3\text{Fe}_x\text{Co}_{1-x}.$$

$$\text{and } \langle p_{\text{eff}}^2 \rangle = 63 + \frac{1}{3} [x 3.15^2 + (1-x) 1.78^2] \quad \text{for } \text{Gd}_3\text{Co}_x\text{Ni}_{1-x}.$$

For Gd_3Ni $\langle p_{\text{eff}}^2 \rangle = 64.1$ and for Gd_3Co $\langle p_{\text{eff}}^2 \rangle = 66.3$. If the TM moments are ignored the change introduced into C is only 1.7% for Gd_3Ni and 5% for Gd_3Co . Thus, if it is not valid to assume the TM metal moments in the Gd_3B compounds to be equal to those in pure Fe, Co or Ni, the effect upon the calculated Curie constant is small.

The values of $\langle p_{\text{eff}}^2 \rangle$, C, T_N , $n' + n$, n' , and n'/n are given in Table 7.3. Using equation (2) we obtain $n' + n$ and since n has already been calculated, we obtain n' , the intra-sublattice exchange coefficient. n' and n are plotted in fig. 7.6. The ratio n'/n is very large for the flip compounds, as required by the theory. The ratio n'/n becomes rather small for Gd_3Ni . The Néel condition, $n'/n \gg 1$, is not fulfilled for this compound, and it is therefore not expected to be explicable in terms of the Néel theory. This is, in fact, the case since Gd_3Ni shows complex behaviour.

The ratio $n'/n = 59$ for Gd_3Co . Féron et al. obtained $n'/n = 136$ for Gd_3Co . This is because their value of H_c , to which n is proportional, was obtained from static field measurements, giving $H_c = 4$ KOe approximately. This is about half the value, 9 KOe, obtained in the pulsed field measurements.

$$\frac{n'/n \text{ (static field)}}{n'/n \text{ (pulsed field)}} = \frac{136}{59} = 2.3$$

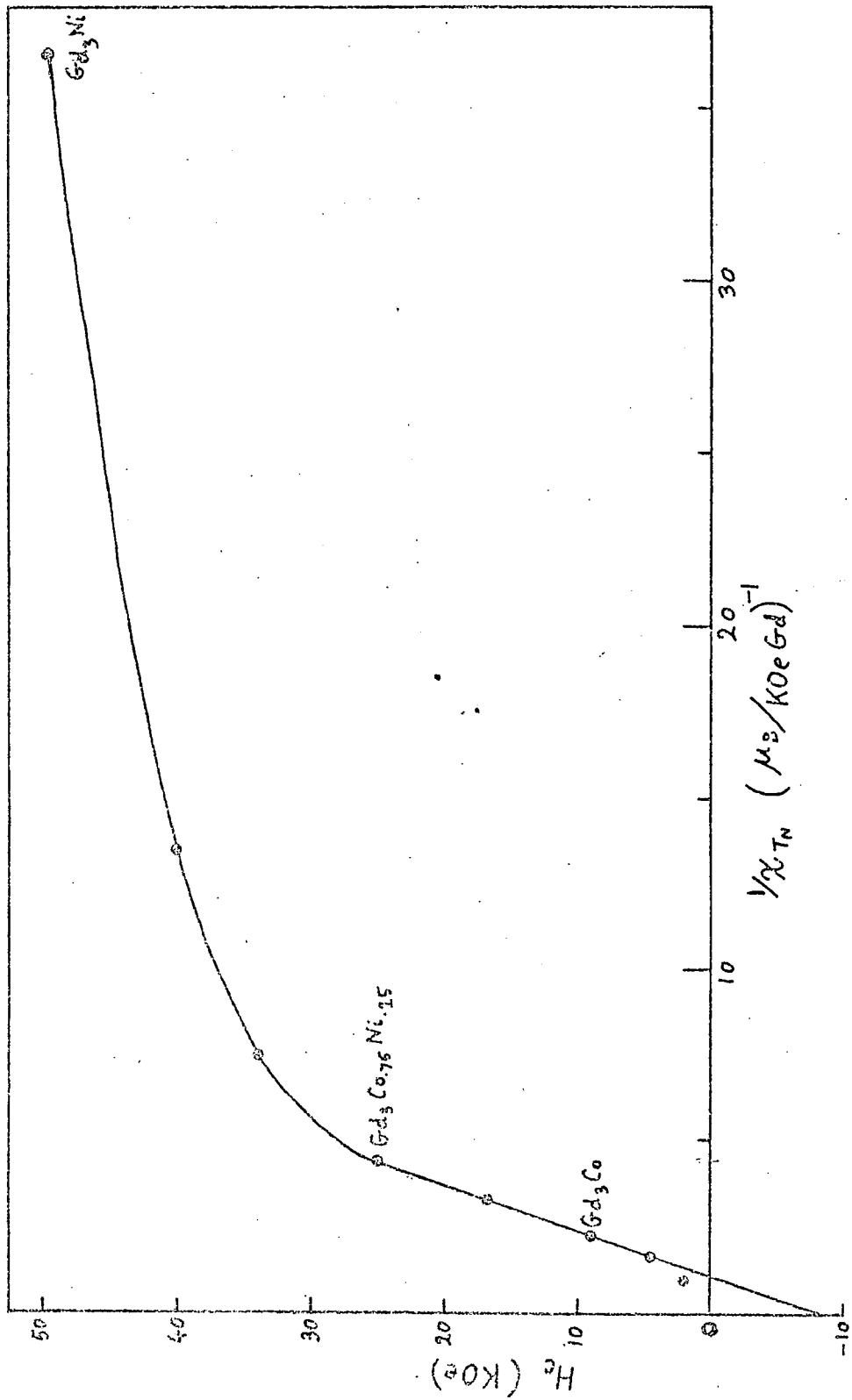


Fig. 7.7 H_c vs $1/\chi_{TN}$ for $\text{Gd}_3(\text{Fe}, \text{Co})$ and $\text{Gd}_3(\text{Co}, \text{Ni})$

$$\frac{H_c \text{ (Pulsed field)}}{H_c \text{ (Static field)}} = \frac{9}{4} = 2.25.$$

Thus the discrepancy between pulsed and static field measurements can be ascribed to the time dependent behaviour of the magnetization.

7.3.7. χ_{-T_N} , (At $T = T_N$) and its relationship with H_c at 4.2K

In fig. 5.21 the variation of $1/\chi_{T_N}$ is shown as a function of composition. From equation (3) $1/\chi_{T_N}$ is equal to n , and therefore the values of n according to χ_{T_N} are given in fig. 5.21 directly, no scaling factor being required. These values of n are appreciably different from those obtained using H_c and χ_i , both at 4.2K, assuming A_n type structure. However, the general trend is the same and the order of magnitude of the two sets of values is the same.

For flip samples we can derive the relations:

$$H_c = \frac{M}{2} \frac{1}{\chi_{T_N}} - \frac{2K_1}{\mu_0 M} \quad \text{flip II (A}_p\text{)}$$

$$H_c = \frac{M}{2} \frac{1}{\chi_{T_N}} \quad \text{flip V (A}_n\text{)}$$

Fig. 7.7 shows the variation of H_c vs $1/\chi_{T_N}$. The point for $\text{Gd}_3\text{Fe}_{0.1}\text{Co}_{0.9}$ is anomalous because of the impossibility of measuring χ_i near the Néel temperature (5.3.4). Apart from this, the flip compounds give an excellent linear variation of H_c vs $1/\chi_{T_N}$, with a negative intercept on the H_c axis. Therefore the flip samples are probably of type II, with A_p spin structure. The negative intercept gives a value for K_1 :

$$K_1 = (6.2 \pm 0.6) \times 10^5 \text{ J/m}^3.$$

Recalling the value of $K_0 + K_1$ ($= 4.5 \pm 2.2 \times 10^5 \text{ J/m}^3$), as obtained from the H_c vs $1/\chi_i$ curve for $T = 4.2 \text{ K}$, we see that these two quantities K_1 and $K_0 + K_1$ are equal within the experimental error. Therefore we can deduce that K_0 is small compared with K_1 . This is reasonable if one considers that Gd almost certainly exists as an S state ion ($L = 0$) and any interaction with the crystal field must be of second order, and therefore small compared with the magnetic dipole interaction.

If we can neglect K_0 , then the expressions for s_n reduce to the same formula:

$$s_n = \frac{1}{n \left(1 - \frac{K_1}{\mu_0 n M^2}\right)} \quad \text{for } K_0 \ll K_1.$$

Then the values of n obtained from χ_i at 4.2 K, which were valid only for (A_n) type become now valid for both (A_p) and (A_n) types.

From the gradient of the H_c vs $1/\chi_{T_N}$ curve we deduce that, according to χ_{T_N} and H_c ,

$$M = 15.5 \mu_B / \text{Gd}.$$

This is an anomalously large magnetization value, which is too large by a factor of two above the gJ value of Gd. This is probably due to the difference in the time dependent properties at 4.2K and at $T = T_N$, as will be discussed in the next section.

7.4. Effects of Various Corrections

7.4.1 Time dependence

Time dependent behaviour in magnetic materials, commonly known as magnetic after-effect, can be said to be occurring when the shape of an M vs H curve depends upon the rate at which H is varied. This means that, in order to observe the equilibrium values of M as a function of H , an experiment must be performed with a variation of H which is slow. The time taken between measurements must be large compared with some characteristic time τ which is a property of the material being studied. It can therefore be concluded that the pulsed field measurements of M vs H do not give the equilibrium curves.

The results of Féron et al. are probably closer to the equilibrium values. Their values of H_c are smaller than the pulsed field values by a factor of approximately 2. If we normalise the pulsed field H_c values by halving each value we probably can simulate the equilibrium values. Since time dependence is a phenomenon which appears only at low temperatures, the values of χ_{T_N} are probably close to the equilibrium values and hence no correction need be made.

The H_c vs $1/\chi_{TN}$ curve, when corrected for time dependence will then have a gradient which is half that of the uncorrected curve. The value of M deduced will then be half the value $15\mu_B/\text{Gd}$ obtained from the uncorrected curve. This is then close to the gJ value of the Gd^{3+} ion.

A similar correction must be made to the H_c vs $1/\chi_i$ curve for $T = 4.2\text{K}$. However, this does not necessarily reduce the gradient by half since χ_i (at $T = 4.2\text{K}$) is affected by time dependence and the values of both H_c and χ_i must be modified. The value of χ_i obtained by Féron et al. is $0.37\mu_B/\text{K0e}$ per Gd at 4.2K for Gd_3Co . The pulsed field value is $0.18\mu_B/\text{K0e}$ per Gd, which is approximately half the value obtained in static fields. Thus, in correcting for time-dependence of H_c and χ_i , both at 4.2K , H_c must be halved and χ_i must be doubled. This means that the H_c vs $1/\chi_i$, linear portion for flip materials will maintain almost the same gradient, so that the value of $M = 5.8\mu_B/\text{Gd}$ will need no correction.

The time dependence correction will halve the values of the negative intercepts on the H_c axis in the H_c vs $1/\chi_i$ curve and the H_c vs $1/\chi_{TN}$ curve. Hence the values of $K_0 + K_1$ and K_1 will both be halved, and the conclusion that $K_0 \ll K_1$ will still be valid.

A small hysteresis was observed for most samples for field values greater than H_c . $\text{Gd}_3\text{Co}_{.9}\text{Ni}_{.1}$ showed a more pronounced hysteresis than any of the other samples. This sample was therefore chosen for more detailed investigation (5.3.1). The hysteresis was found to depend strongly upon the rate of change dH/dt of the applied field (fig. 5.6). Moreover, it appeared from the linear variation of hysteresis with dH/dt that the hysteresis would become almost zero for $dH/dt = 0$, i.e. in static field experiments. This is what might be expected from time dependent behaviour. Taylor observed the time dependent behaviour of DyCoNi (ref 7.5) and found that the hysteresis increased with the rate of change of field.

The difference between this and the Gd_3B time dependent behaviour is that in DyCoNi , which is ferromagnetic, the hysteresis spans both positive and negative field values, centred symmetrically about the origin

whereas for the Gd_3B compounds the hysteresis is centred about the field value H_c . Both of these types of time dependent behaviour can be understood in terms of some mechanism, e.g. intrinsic pinning of narrow domain walls, which causes a delay in adopting the equilibrium magnetization expected for a given field. This delay will give rise to an M vs H curve which is displaced towards high field values for increasing fields, and towards low field values for decreasing fields. This appears as a hysteresis, the hysteresis being zero in very slow experiments as appears to occur in Gd_3B as dH/dt approaches zero. The static experiments of Féron et al. would be expected therefore, to give a critical field value for Gd_3Co which is equal to the average of the rising field and lowering field values of H_c obtained for Gd_3Co in pulsed fields. This is not the case, since the static H_c value is approximately half the pulsed field value. Thus the sample magnetization is delayed with respect to the equilibrium values with rising field, as expected. However, after saturation, when the field value is decreased, the sample appears to be anticipating its equilibrium magnetization values. Consider a sample magnetized to saturation; if then the applied field is decreased slowly until $H = 0$ and $M = 0$, then the state of the sample must be different from the state which it would have if the field were decreased rapidly to $H = 0$, giving $M = 0$. If this were not the case, then the sample would violate the second law of Thermodynamics. It would then be possible to have a refrigeration cycle in which negative work is done by the field. The cycle would consist of a slow field rise from the state ($H = 0, M = 0$) up to saturation, (which must be a unique state whether approached rapidly or slowly) followed by a rapid decrease of field to ($H = 0, M = 0$). Negative hysteresis would be observed in this cycle, which could then be repeated. Since such a cycle is impossible to repeat, according to the second law of Thermodynamics, the state at ($H = 0, M = 0$) must be non-unique and must depend upon the rate at which it was approached. This would involve a difference in the magnetic spin structure, in the two states at ($H = 0, M = 0$), or perhaps some other difference in the configurational entropy.

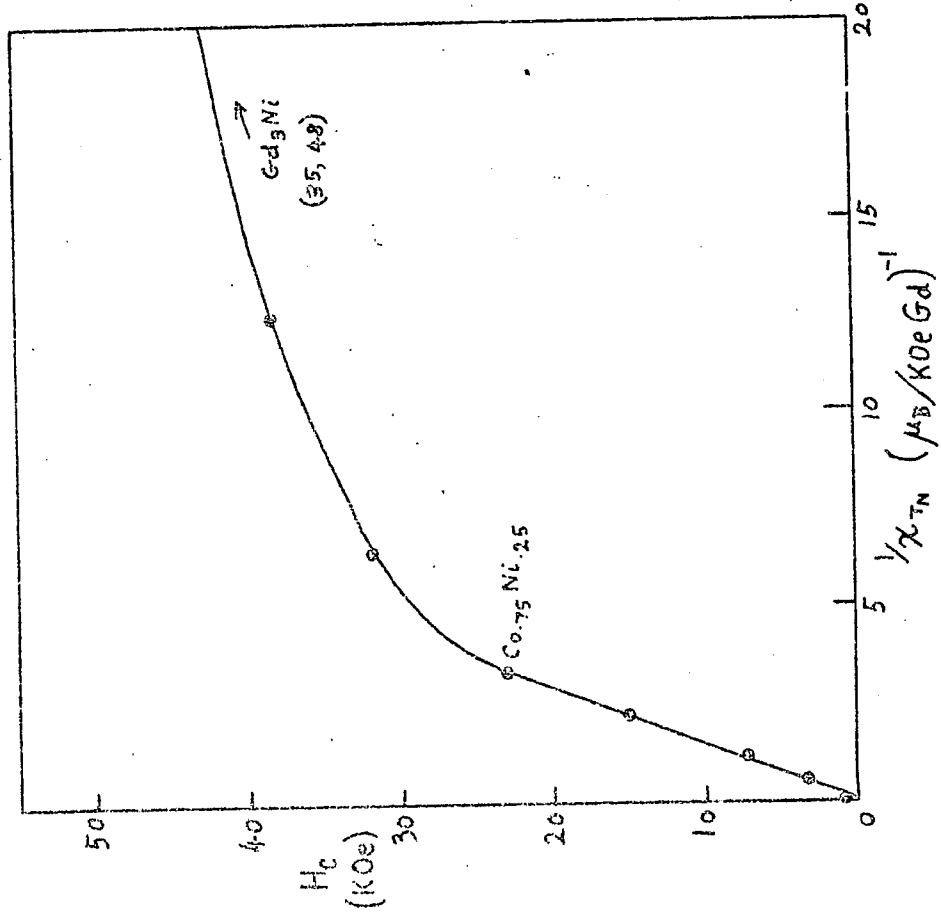


Fig. 7.8 H_c vs $1/\chi_{TN}$ with correction for demagnetizing field

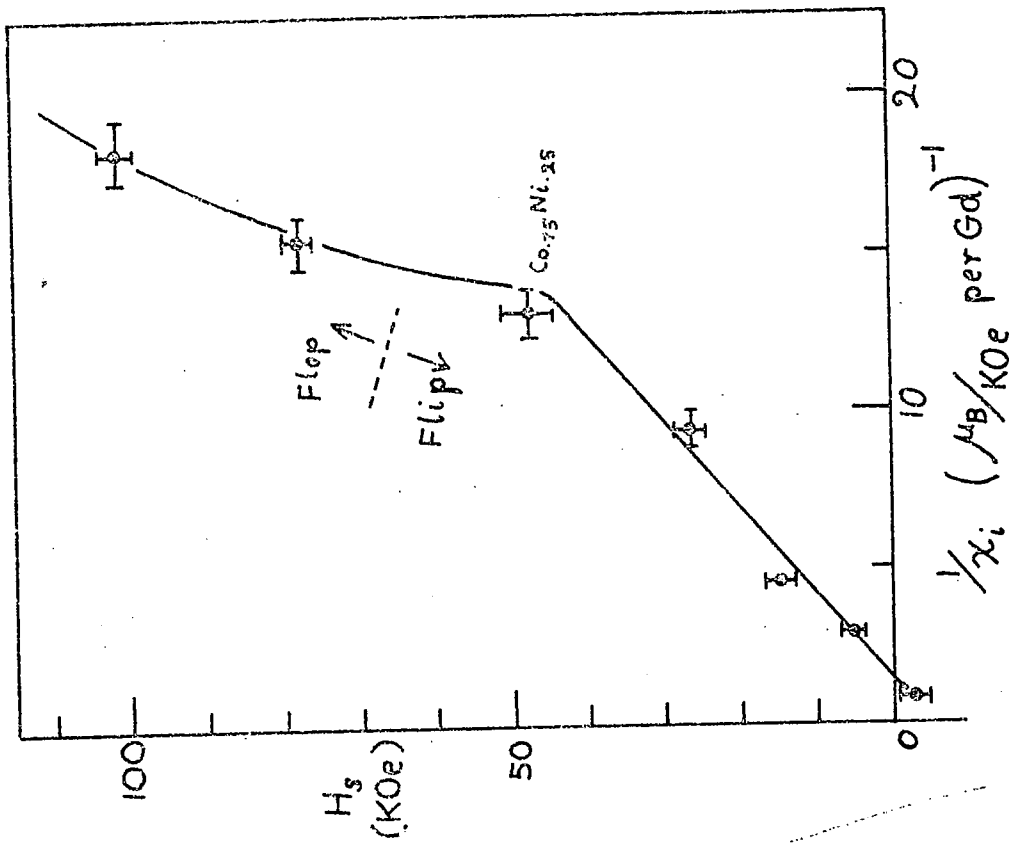


Fig. 7.9 H_s vs $1/\chi_i$ with correction for demagnetizing field

7.4.2 The Demagnetizing Field

Because of the extremely brittle nature of the specimens it was not possible to obtain spheroidal samples for magnetization measurements. This precludes any accurate estimate of the demagnetizing field. It was, however, ensured that the samples, when mounted, were oriented with the largest dimension parallel to the applied field direction in order to minimise any demagnetizing field.

Some estimate of the magnitude of the demagnetizing field is however necessary. We assume the worst possible case, i.e. that the samples are spherical. For such samples, the demagnetizing field is equal to $-\frac{1}{3} \underline{M}$ where \underline{M} is the magnetization. This corresponds to about 7KOe for a saturated sample, and about 2KOe for a sample which is about to undergo a transition to the (f) state. Thus the H_c values need a correction, which is similar in magnitude to the error of measurement. The χ_i values must also be corrected. Since $H_c \chi_i$ must be unaffected, the effect of such a correction upon the H_c vs $1/\chi_i$ curve is to shift every point towards the origin by a constant distance in the $(H_c, 1/\chi_i)$ plane. As a result, the quantity $K_0 + K_1$ changes its value from $4.5 \times 10^5 \text{ J/m}^3$ to $1.5 \times 10^5 \text{ J/m}^3$.

The effect upon χ_{TN} is larger than upon χ_i at 4.2K because χ_{TN} is a larger susceptibility. The correction shifts the H_c vs $1/\chi_{TN}$ curve so that the curve intercepts the origin (fig. 7.8). It would now be possible for the flip samples to be either of type II (with $K_1 = 0$) or of type V.

The H_s values must be decreased by 7KOe on being corrected. For the sample $\text{Gd}_3\text{Fe}_{.1}\text{Co}_{.9}$ (fig. 7.9) this results in a negative corrected value of H_s . This is physically unacceptable and shows that we have been more pessimistic than necessary when we assumed the samples to be spherical. In the absence of any reliable means of estimating the demagnetizing field we shall assume it to be considerably smaller than that for spherical samples. This is justified first, by the consideration of $\text{Gd}_3\text{Fe}_{.1}\text{Co}_{.9}$ and secondly, by the precautions which were taken in mounting the samples.

Since H_s for $Gd_3Fe_{.1}Co_{.9}$ is evidently of the same order of magnitude as the demagnetizing field it would appear that, on decreasing the 3d-electron concentration, we may be approaching a truly ferromagnetic composition, with an infinite initial susceptibility, for a little more than 10% Fe substitution in Gd_3Co .

7.4.3 Temperature Variation during a Field Pulse

The work done by the applied field in magnetizing a sample from $M = 0$ to $M = M_s$, the saturation magnetization, is given in J/m^3 by:

$$\mu_0 \int_0^{M_s} H \cdot dM$$

This is equal to μ_0 multiplied by the area in the (M, H) plane bounded by the M vs H curve, the M axis, and the line $M = M_s$. This area is largest for Gd_3Ni . We shall consider this material in order to estimate the order of magnitude of the maximum possible temperature rise during a pulse. Since only an order of magnitude value is required we approximate the M vs H curve to a straight line from the origin up to $(H = H_s, M = M_s)$. We assume the adiabatic condition in which all the work done is converted to heat which is retained by the sample.

$$\frac{\mu_0 M_s H_s}{2} = C_p \Delta T$$

where C_p is the specific heat per m^3 , and ΔT is the temperature rise. Making use of the specific heat of gadolinium metal at 4.2K, $C_p = 10$ cal/deg mole, and assuming that it is not much different from the specific heat of Gd_3Ni , we obtain, using $H_s = 100$ KOe and $M_s = 1.5 \times 10^6$ A/m,

$$\Delta T = 3K$$

This temperature rise is too small to affect the quantities measured at 4.2K to any significant extent. In addition, the flip samples will have considerably smaller temperature rises because of the smaller values of H_s .

7.5. Estimation of the Magnetic Dipole Interaction between Gd ions

In order to establish to what extent the magnetic dipole interaction can be responsible for the observed anisotropy, the following order of magnitude calculation was made. We estimate firstly the energy difference between two Gd^{3+} ions with both spins parallel and with both spins anti-parallel.

The line joining the ions is perpendicular to the spin directions, and of length R , where R is the nearest neighbour distance. This energy is

$$E_{\uparrow\uparrow} - E_{\uparrow\downarrow} = \frac{2 p^2 \mu_0}{4\pi R^3} \quad (16)$$

where p is the magnetic moment of one ion. Secondly we consider the energy difference between two parallel spins with their spin directions parallel and perpendicular to the line joining them. This energy difference is

$$E_{\uparrow\uparrow} - E_{\rightarrow\rightarrow} = \frac{3p^2 \mu_0}{4\pi R^3} \quad (17)$$

Equation (16) gives an energy difference between (af) and (f) alignment. Equation (17) gives an anisotropy energy. Since the isotropic component of interaction between a pair of dipoles is of the same order of magnitude as the anisotropic component, we would expect the value of K_1 to be of the same order of magnitude as the component of $\frac{\mu_0 n M^2}{4}$ due to the dipole term incorporated into n (7.12).

We substitute into equation (17) the following values:

$$R \approx a/2 = 3.5 \text{ \AA}, \quad p = 7 \mu_B, \text{ to obtain the value}$$

$$E_{\uparrow\uparrow} - E_{\rightarrow\rightarrow} = 197 \times 10^{-25} \text{ J. per pair of atoms.}$$

Each atom has Z nearest neighbours. In a highly symmetrical structure (e.g. simple cubic) the total field on an ion is zero, since the various components from the aligned nearest neighbours cancel out. However, for a highly asymmetric crystal structure this cancelling out does not occur and the resultant field will be a considerable fraction of Z multiplied by the field resulting from a nearest neighbour. Thus the energy of interaction of one ion with Z nearest neighbours will be $197 \times 10^{-25} Z$ Joules. Since 12

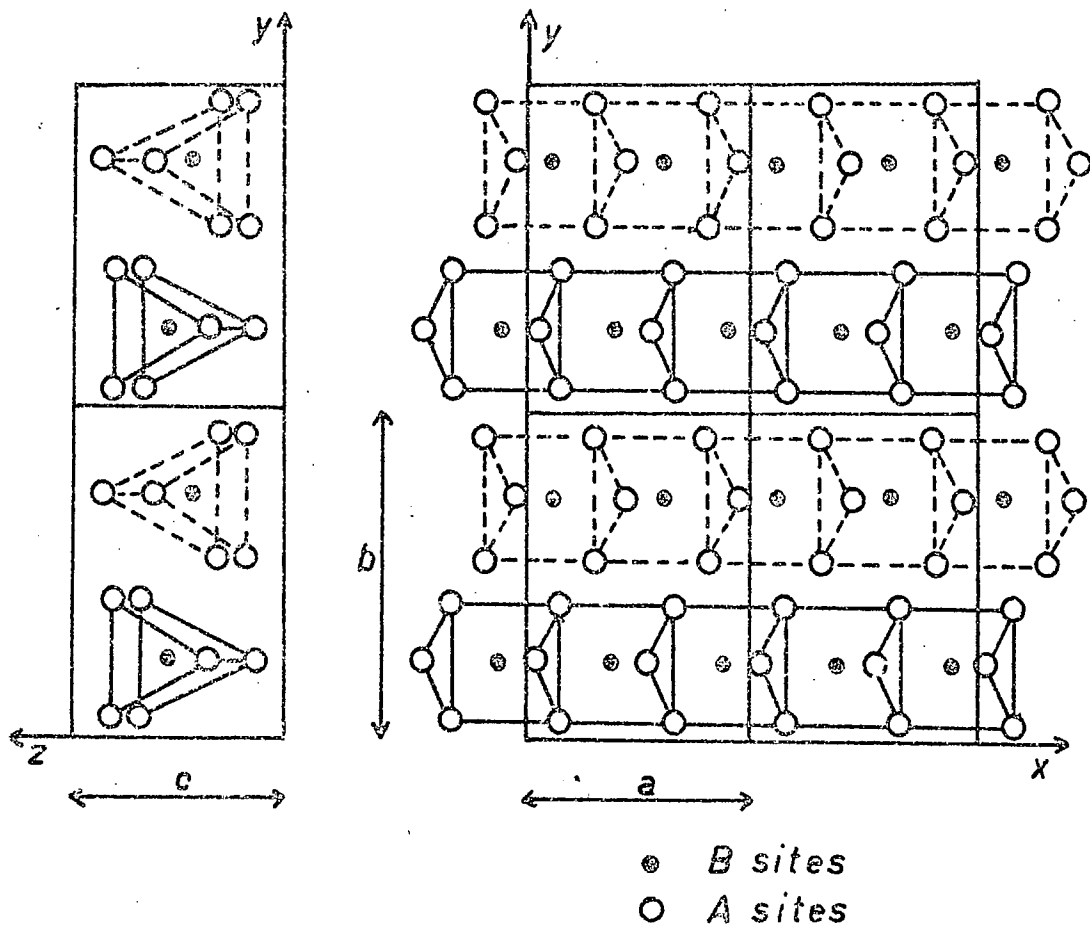


Fig. 7.10 Crystal structure of the A_3B compounds

atoms occupy $424 \times 10^{-30} \text{ m}^3$ we obtain the dipole interaction energy

$$\Delta E \approx \frac{1}{2} \cdot \frac{12 \times 197 \cdot Z \times 10^{-25}}{424 \times 10^{-30}} \text{ J/m}^3.$$

The factor $\frac{1}{2}$ appears because the interaction is between pairs of dipoles.

The result is:

$$\Delta E \approx 2.8 Z \times 10^5 \text{ J/m}^3.$$

The nearest neighbour distance is $\sim a/2$. However the next nearest neighbours are not very much further. Hence they will also exert a large influence.

Inspection of the crystal structure diagram (fig. 7.10) gives 6 as a reasonable estimate for Z . The estimate for ΔE cannot be made accurately here but, for an order of magnitude estimate we can say that ΔE is a not too small fraction of $17 \times 10^5 \text{ J/m}^3$ because of the low symmetry of the crystal structure. Therefore the magnetic dipole interaction is probably responsible for the anisotropy energy $4.5 \times 10^5 \text{ J/m}^3$.

7.6 Effect of the Average 3d-electron Concentration

Rigorously, the average 3d-electron concentration is as yet unknown.

It is generally assumed that the number of 3d-electrons increases by one if Fe is replaced by Co, or Co by Ni. If, however the 3d band is full, as may well be the case in these compounds, this extra electron will go into the conduction band and thus will probably have sp character. Since this is not definite we shall retain the above nomenclature and refer to this quantity as the "3d-electron concentration", but it must be remembered that strictly speaking what we really mean is the "Valence electron concentration". We shall not change the expression because Fe, Co and Ni are usually thought of as 3d-elements.

The result that H_c for $\text{Gd}_3(\text{Fe,Co})$ becomes zero at the same composition for which the Fe_3C structure breaks down is a remarkable coincidence. It can be concluded that, if this is not due to pure chance, the existence of the Fe_3C phase is associated with the existence of a positive value of H_c . The structural and magnetic properties are related and depend upon the average 3d-electron

concentration (hereafter referred to as A3dC). The change in A3dC will be accompanied by changes in the other unrelated parameters, which will not vary linearly with composition from Fe to Co to Ni. It was in order to examine this aspect that the $Gd_3(Fe,Ni)$ compounds were prepared and examined. It was found that the A3dC was not the only factor in determining the formation of single phase samples, because the foreign phases did not appear at the composition $Gd_3Fe_{.55}Ni_{.45}$ (which has the same A3dC as $Gd_3Fe_{.1}Co_{.9}$) but rather at $Gd_3Fe_{.3}Ni_{.7}$. However it was found that the A3dC was probably the only factor controlling the existence of an Fe_3C phase in these samples, whether or not this phase corresponds to the desired composition. This is because, after the onset of the formation of foreign phases, the Fe_3C structure, probably of composition $Gd_3Fe_{.2}Ni_{.8}$ continued to exist for increasing Fe concentrations, as shown by the fairly sharp X-ray diffraction lines, and also by the maintenance of the H_c value of this composition. These X-ray lines then rapidly became blurred between $Gd_3Fe_{.5}Ni_{.5}$ and $Gd_3Fe_{.6}Ni_{.4}$, indicating that no Fe_3C phase of any composition existed for higher Fe concentrations than that of $Gd_3Fe_{.55}Ni_{.45}$ approximately.

H_c and H_s appear to be dependent mainly upon the A3dC, as shown by the following two considerations:

- (a) On varying the composition in $Gd_3(Fe,Co)$ and $Gd_3(Co,Ni)$ from Fe to Co to Ni, the A3dC is the only parameter which varies linearly with composition, except for related parameters such as nuclear charge. Any other unrelated parameters will have a discontinuous gradient at the Gd_3Co composition. If H_c or H_s depended on one of these other parameters then the H_c and H_s curves would also have a discontinuous gradient with respect to composition at Gd_3Co . Since both vary smoothly it can be concluded that they are affected mainly by the A3dC.
- (b) Over the small range of existence of $Gd_3(Fe,Ni)$ it has been shown that H_c is the same function of A3dC in the (Fe,Ni) pseudobinaries as in the (Co,Ni) pseudobinaries. This is seen clearly in fig. 5.24. Furthermore the transition from complex to flop-type behaviour occurs at the same A3dC in the two series and H_s reaches a maximum at this A3dC value in both series.

7.7 The Exchange Interaction

It may be recalled (7.12) that the inter-sublattice interaction was not purely of exchange energy origin, but had, incorporated into it, a term derived from the isotropic component of the magnetic dipole interaction. Whilst this inter-sublattice interaction energy ($\mu_0 n M^2/4$) in Gd_3Co , which equals $5.8 \times 10^5 \text{ J/m}^3$, could be accounted for entirely by the magnetic dipole interaction, the dipole interaction is too small to account for the inter-sublattice interaction energy ($56 \times 10^5 \text{ J/m}^3$) of Gd_3Ni . The strong antiferromagnetism of the flop and complex compounds therefore indicates that the isotropic dipole component of n is only a small fraction of n in these compounds. Antiferromagnetic exchange must therefore be operating between the sublattices. Ferromagnetic exchange must be operating within the sublattices since the intra-sublattice interaction is stronger than the inter-sublattice interaction. Since we are concerned with genuine exchange interactions between rare earth ions, we are forced to consider these in terms of the concepts of the RKKY theory. This has been the most successful theory so far in accounting for the exchange interactions between localised rare earth ions. A brief outline of the theory follows.

7.7.1 The RKKY Theory (Rudermann, Kittel, Kasuya, Yosida)

The exchange mechanism in this theory was derived originally by Rudermann and Kittel (ref 7.6) in connection with the coupling of nuclear spins, and later developed by Kasuya (ref 7.7) and Yosida (ref 7.8) for the cases of exchange coupling between localised ionic spins in a lattice. The theory assumes a free electron model for the conduction electrons. A localised ion of spin S_i interacts with the conduction electrons spins by exchange. The result is that the conduction electron spins become polarized in the vicinity of the ion. This polarization is given by:

$$P_i(r) = \frac{9\pi Z^2 \Gamma S_i}{4 V^2 E_F} \frac{\sin 2 k_F r - 2 k_F r \cos 2 k_F r}{(2 k_F r)^3}$$

where r is the distance from the ion centre, Z is the atomic density of conduction electrons, V the atomic volume, E_F the Fermi energy, k_F the Fermi

wave vector modulus, Γ the exchange energy between the ionic spin and a conduction electron spin. The polarization is oscillatory, decaying as

$$\frac{\cos. 2k_F r}{(2k_F r)^3} \quad \text{at large distances.}$$

If another similar ion of spin \underline{S}_j is situated a distance r_j from the first ion, the conduction electron polarization will in turn interact by exchange with the second ion with an interaction energy

$$-\Gamma \underline{S}_j \cdot \underline{P}_i(r_j)$$

The result is that the two ions are effectively coupled, indirectly, via the conduction electrons, with an exchange interaction which varies in the same oscillatory manner as the conduction electron polarization. The oscillation wave length will depend upon k_F . Since the rare earth ions are specified by the quantum number J , rather than by S , it is necessary to replace S_i and S_j with the projection of S onto J , which is equal to $(g-1) J$. In the molecular field approximation the theory predicts a paramagnetic Curie temperature Θ_p which is proportional to the de Gennes factor.

$$\Theta_p = A (g-1)^2 J (J+1).$$

A is a function of Z , V , k_F and E_F as well as the spacial configuration of the interacting ions. For the rare earth metals, as one goes from one element to the next across the series, A will vary only slowly for a given crystal structure. This is because the extra electron added per atom from element to element across the series goes into the 4f shell, affecting the de Gennes factor, but does not go into the conduction band. Thus, the properties of the conduction band, upon which A depends, remain fairly constant for a given crystal structure.

One would therefore expect a linear relationship between Θ_p and the de Gennes factor for the heavy rare earth metals, all of which have the same crystal structure h.c.p. (except for Yb). These rare earth metals follow the expected linear behaviour remarkably well (ref. 7.9).

The band electrons in the rare earth metals are derived from 6s and 5d type orbitals. Most of the rare earth metal ions exist with a tripositive charge, e.g. Gd^{3+} and the metal contains, therefore, three conduction electrons, of sd type per atom. Band calculations on gadolinium metal give results which show an appreciable deviation from the free electron model for the conduction electrons and the Fermi surface (ref 7.9) is far from spherical. The calculated density of states curve shows a narrow energy band with a density of states about three times larger than that expected for free electrons.

This is due to the strong mixing of 6s and 5d states near the Fermi energy. Gadolinium metal has an absolute saturation magnetization which is $0.55 \mu_B$ per atom in excess of the gJ value of the Gd^{3+} ion. This is generally regarded (ref 7.10) as being due to the polarization of conduction electrons. Such a large excess cannot be accounted for by free electrons, because of their low density of states. The excess is, however, consistent with a higher density of states, as derived from band calculations. The high electronic specific heat of gadolinium also requires a high density of states model. The free electron model gives a density of states which is eight times too low, whereas the band calculation gives one which is only two times too low to account for the electronic specific heat.

The calculated density of states curve of gadolinium is an irregular shaped function of energy. Similar calculations have been made for the other rare earth metals and it was found that the density of states and the Fermi surface changed in detail only, from element to element for the hcp crystal structures. This lack of rapid change in the Fermi surface accounts for why the heavy hcp rare earth metals give the expected linear relation between Θ_p and the de Gennes function, even though the assumption of a spherical Fermi surface is wrong. The RKKY theory assumes a spherical Fermi surface, in which case A is readily calculable. For an irregular shaped Fermi surface the calculation of A is made very much more complicated. This however does not affect the validity of the Θ_p vs de Gennes function linearity as long as we maintain constant the conduction electron characteristics. Since the calculated density of states curve is an irregular function of energy, we expect

the exchange characteristics to depend strongly on conduction electron concentration which, in the pure R.E. metals, is constant. The lanthanide contraction will have some effect upon the Fermi surface shape. Therefore the exchange characteristics must vary slightly across the series.

7.8. The Conduction Electrons of Gd-rich compounds with the 3d-Elements

It is generally accepted that, if one begins with a 3d transition metal B, and alloys it with an A element, rare earth or yttrium, to make the stoichiometric compound $A_x B_{1-x}$, then the A atom, e.g. Gd, contributes electrons to the 3d band. On going progressively to rare earth richer stoichiometries, increasing x, the 3d band becomes gradually filled. The filling of the 3d band manifests itself in a decrease of the 3d moment. The problem is of course more complicated because the top of the 3d band is probably not sharp. It overlaps the much wider conduction band which probably becomes gradually 3d in character near the top of the 3d band, with no sharp dividing line.

As regards any spontaneous moment due to the non-4f electrons we can make two generalizations: On the one hand, any spontaneous moment arising from 3d band splitting has been found always to align itself antiparallel to the rare earth spin moment projection on J. This means that in the light rare earths we have ferromagnetic alignment of the rare earth and 3d moments if $L > S$ and for the heavy rare earths we have ferrimagnetic alignment, such as for Gd. On the other hand the conduction electron polarization of Gd metal is parallel to the Gd moment, giving rise to an excess absolute saturation magnetization which is $0.55 \mu_B / \text{Gd}$ in excess of the gJ value. It is reasonable to assume that, on alloying Gd with a 3d element the conduction electron polarization will still exist and that the RKKY type of coupling will not be radically changed, as long as the 3d band is full. The saturation moment will then still exceed the gJ value. If one then increases the 3d element concentration a point will be reached where the Fermi level encounters the top of the 3d band, which will then develop holes and will be able to contribute to the spontaneous

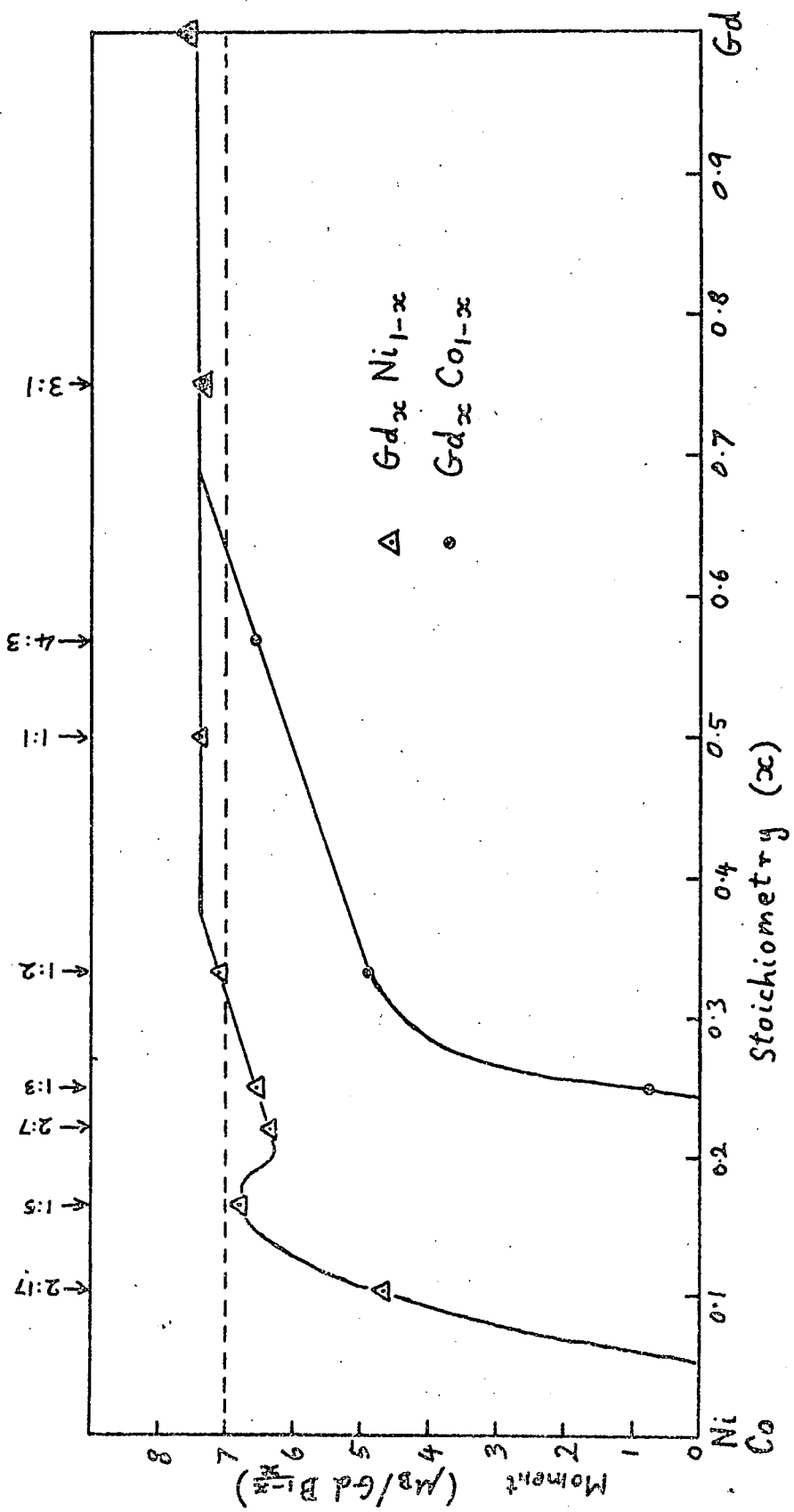


Fig. 7.11 Saturation Moment in Gd-rich Cobalt and Nickel Compounds

magnetization. This magnetization, as we have seen, opposes the Gd moment. If it exactly equals the conduction electron polarization, which we presume still exists, then the spontaneous magnetization of the material will equal that expected from the gJ value of Gd. On further decreasing x the absolute saturation magnetization will become less than the gJ value per Gd. Fig. 7.11 shows the absolute saturation magnetization per Gd atom, of the $\text{Gd Ni}_x \text{Co}_{1-x}$ and $\text{Gd Co}_x \text{Ni}_{1-x}$ compounds.

For the Ni compounds on decreasing x from 1, the magnetization remains roughly constant at a value between 0.3 and $0.5 \mu_B/\text{Gd}$ above the gJ value, for Gd_3Ni and GdNi . This can be accounted for by conduction electron polarization of the type found in Gd metal. On further decreasing x we come to Gd Ni_2 , which appears to be the type of material mentioned above, in which the 3d moment almost cancels out the conduction electron polarization to give approximately the gJ value for the magnetization. It would therefore appear that we encounter the top of the 3d band at GdNi_2 , or at least approach some conduction band levels which are developing 3d character. For the Co compounds, the excess moment above the gJ value in Gd_3Co can be accounted for by conduction electron polarization, as in Gd_3Ni and pure Gd metal. However, on a further slight decrease of x , we rapidly come to the compound Gd_4Co_3 which has a moment per gadolinium atom less than the gJ value. This suggests that the Fermi level of Gd_4Co_3 is in the 3d band, or at least so near the top of the 3d band that the conduction electrons at E_F have some 3d character. Y_4Co_3 , incidentally, is ferromagnetic, with a small spontaneous moment of $0.04 \mu_B/\text{Co}$, and supports the view that the 3d band is not quite full at the 4:3 stoichiometry of the cobalt compounds. It seems therefore that the Gd_3Co Fermi level is not far above the top of the 3d band.

7.9. The Structural Stability of Gadolinium-rich Compounds with the 3d Elements

For a given stoichiometry $\text{A}_x \text{B}_{1-x}$, if it forms a stable crystal structure with the Fermi level within the 3d band, it is postulated that this stability will be lost for the same stoichiometry with the Fermi Level above the top of the 3d band. Similarly, if another stoichiometry is stable with the Fermi

level above the 3d band, then it will be unstable for the Fermi level within the 3d band.

By means of this postulate it is possible to understand why Gd_4Co_3 exists, whereas Gd_4Ni_3 does not exist. Referring to fig. 7.11 the Fermi level appears to be within the 3d band for Gd_4Co_3 . However, for the Ni compounds the moment curve predicts a Fermi level well above the 3d band at the 4:3 stoichiometry, and therefore Gd_4Ni_3 does not exist. Similarly, $GdNi$ exists with the Fermi level above the 3d band, but the moment curve at the 1:1 stoichiometry would require the 3d band to be unfilled for $GdCo$. Hence $GdCo$ does not exist. The 3d band is by no means full in $GdCo_2$, and not quite full in $GdNi_2$, hence both these compounds exist.

It is also possible to understand, by means of the above postulate, why the Fe_3C structure breaks down when Fe is substituted for Co in Gd_3Co . It may be recalled (7.7.2) that the Fermi level for Gd_3Co is not far above the top of the 3d band (because on going from Gd_3Co to Gd_4Co_3 we acquire a 3d moment). Going from Gd_3Co to Gd_4Co_3 lowers the Fermi level by reducing the number of conduction electrons (3 per Gd atom) contributed by the Gd.

We can similarly lower the Fermi level on substituting Fe for Co in Gd_3Co . By so doing, the top of the 3d band is rapidly encountered, since the Fe_3C structure becomes unstable for only 10% Fe substitution. The Fe_3C structure of $Gd_3Fe_xNi_{1-x}$ became unstable, on increasing the Fe content, earlier than expected from the point of view of conduction electron concentration. From this point of view the Fe_3C structure was predicted to become unstable at 55% Fe, whereas it becomes unstable at 20% Fe. This might be due to the extra stresses set up in the lattice by the fact that Fe and Ni are not neighbours in the periodic table. However, the last Fe_3C compound to form, $Gd_3Fe_{.2}Ni_{.8}$, persisted for higher Fe concentrations up to approximately 55% Fe substitution, which has the same conduction electron concentration as that of $Gd_3Fe_{.1}Co_{.9}$.

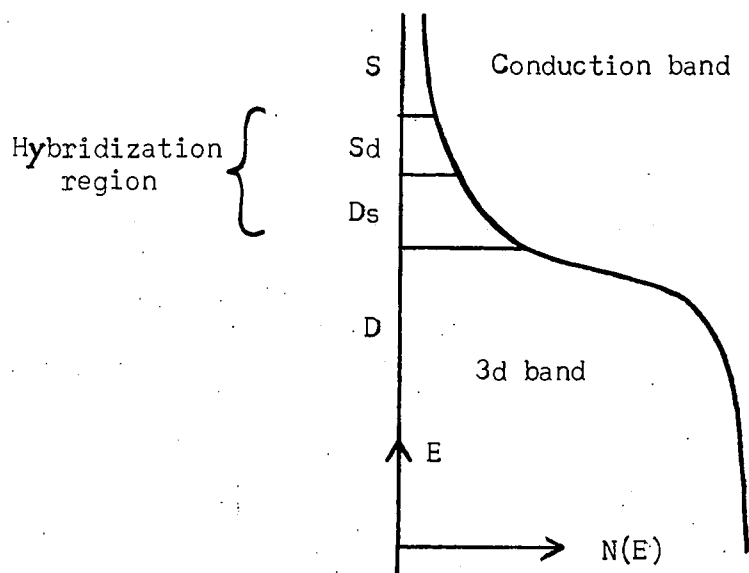
It may be that the postulate is applicable even to non-single phase material, in which the stability of any Fe_3C phase present is sensitive to the

average conduction electron concentration in the whole multiphase sample, and breaks down when the Fermi level encounters the 3d band.

7.9.1 Justification for the structural stability rule

This rule, as yet empirical, states that if a structure A is stable when the Fermi level E_F intersects the 3d band, it will probably become unstable when E_F is raised above the top of the 3d band, and will then be replaced by another structure B, or a number of new crystal structures. It also states that if a structure B is stable with E_F above the top of the 3d band, then B will probably become unstable when E_F is lowered to the top of the 3d band, and will be replaced by structure A or a number of new structures.

The physical justification approaches the problem firstly of the onset of instability in A as E_F is raised. It is well established that the 3d band in the transition metals of the iron group has a high density of states $N(E)$, and that this band is overlapped in energy by a much wider conduction band which has consequently a low density of states. The top of the 3d band will therefore not be sharp but will be characterised by wave functions which have both 3d character and non-3d (probably s) character. This hybridization region we shall divide into two parts: Sd, which has mainly s character and low density of states; and Ds, which has mainly 3d character and higher density of states. The band region well above the top of the 3d band we shall call the S region, which has a lower $N(E)$ than the Sd region. The D region is the 3d band proper with negligible s character, and highest $N(E)$.



For the structure A, stable with E_F in the D region, we can raise the Fermi level by replacing some of the atoms of a certain valency, e.g. Fe, with atoms of a higher valency e.g. Co. When E_F encounters the region with low $N(E)$ the continued addition of valence electrons is only possible with a large increase in the energy of these added electrons. Though the conduction electron energy is by no means the only factor influencing the stability of a certain structure, it is certainly one of the relevant factors. This large increase in energy will make the structure A energetically less favourable and there will probably exist another structure B which has a lower energy. If such a structure B exists, then A will become unstable and be replaced by B, which may remain stable when E_F is raised further.

Conversely, if we start with structure B stable in the S region and lower E_F , the structure B should remain stable as long as $N(E)$ remains low, since E_F will lower rapidly for a given reduction in valence electron density. When E_F encounters a high $N(E)$, there is a greater likelihood of there being some other structure A in which the total electron energy is lower than that which would be found if structure B continued to exist.

It is proposed that the Fe_3C structure of the $Gd_3(Fe,Co,Ni)$ alloys can be regarded as such a structure B, which becomes unstable somewhere in the hybridization region, perhaps between the Sd and the Ds regions. Structure B is however, not replaced by a single structure A, but a number of structures, since the alloys become multiphase, pure gadolinium being one of the phases in A.

7.10 The Exchange Interaction in the Gd_3B Compounds

Since the 3d band appears to be full for these compounds, no cooperative exchange within the 3d band can take place and hence we can have no moment from the 3d electrons. The problem is now simplified to the consideration of a material consisting of localized Gd moments in a sea of conduction electrons. Thus the RKKY type of coupling between the Gd moments must prevail, and will probably be as applicable as in pure Gd metal.

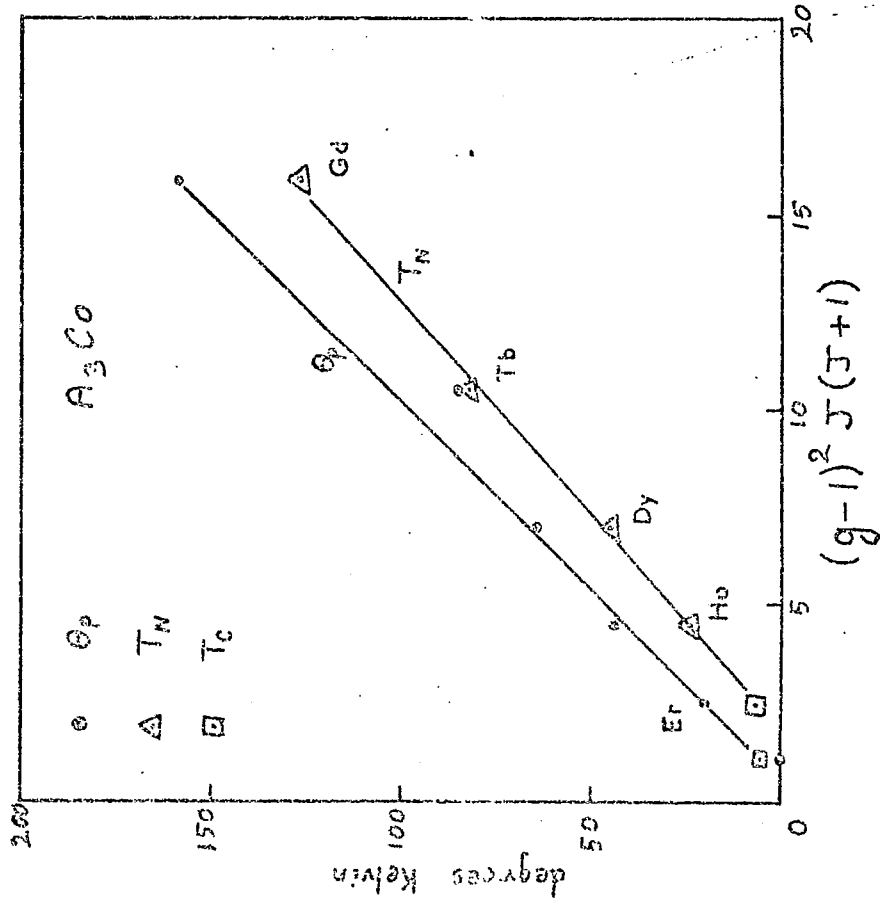


Fig.7.12 Θ_p, T_N (and T_c) for A_3Co Compounds vs the de Gennes Function

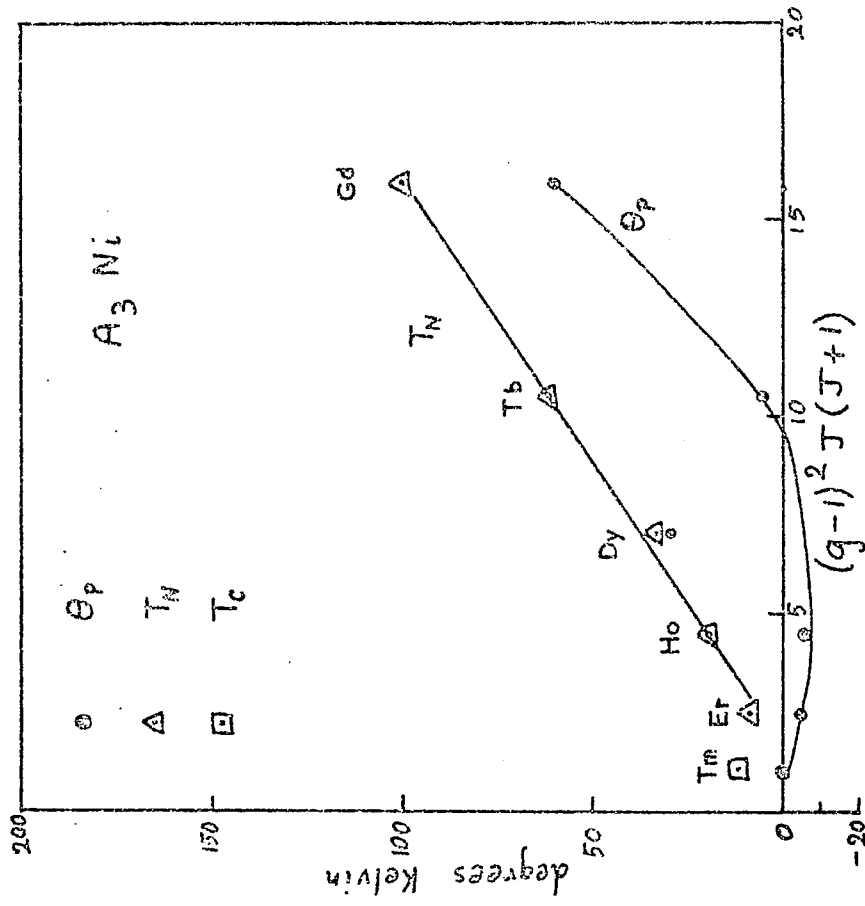


Fig.7.13 Θ_p, T_N (and T_c) for A_3Ni Compounds vs the de Gennes Function

7.10.1 Applicability of RKKY Theory to the A_3B compounds where A is a heavy trivalent Rare Earth.

The RKKY theory (7.7.1) predicts a linear relationship between Θ_p , the paramagnetic Curie temperature and G , the de Gennes function, as the rare earth ion is varied as long as the conduction band characteristics remain constant. A lanthanide contraction will, of course be present, which will cause some departure from linearity of Θ_p vs G . Fig. 7.12 and fig. 7.13 show the variations of T_c and Θ_p with the de Gennes function G for the A_3Co and A_3Ni compounds. T_c , interestingly, shows almost a linear variation in both A_3Co and A_3Ni , which the RKKY theory does not predict. The behaviour of Θ_p is approximately linear for the A_3Co compounds, suggesting applicability of the RKKY theory with constant E_F , but departs entirely from linearity in the A_3Ni compounds, becoming negative for Ho and Er. The curve is, however, smooth except for Dy, though not linear, and it may be that the smooth lanthanide contraction is affecting the linearity in the A_3Ni compounds. This would involve a change in E_F and k_F . Such sensitivity of the Fermi level suggests a low density of states at E_F . It appears therefore, that RKKY coupling may be applicable to the A_3Ni compounds, but with a lower density of states at the Fermi level than in the A_3Co compounds.

7.10.2 Application of RKKY Concepts to the Gd_3B Compounds

The Néel temperature, which is a measure of the strength of the exchange field acting on a magnetic ion, decreases on going from Gd_3Co to Gd_3Ni . This is consistent with a lowering of the density of states of the conduction band as was deduced above. A low density states will make the band less susceptible to polarization and it will therefore be less efficient as a medium via which the indirect exchange between localised ions can operate. Thus the ordering temperature must be lowered if the density of states lowers.

On varying the composition from Gd_3Co to Gd_3Ni the strong ferromagnetic intra-sublattice exchange coefficient n' decreased in strength, whilst the weak antiferromagnetic inter-sublattice exchange increased in strength. The

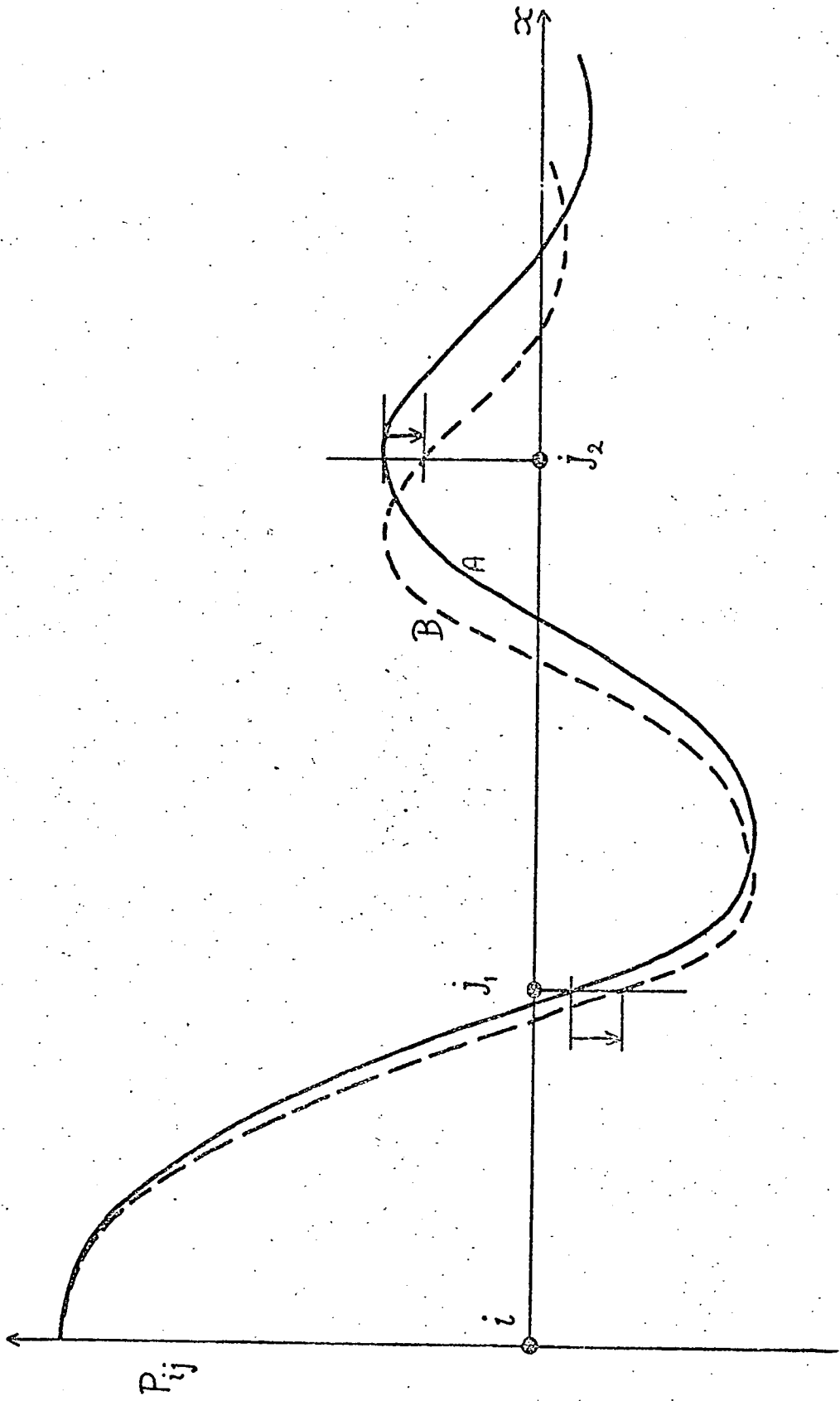


Fig. 7.14 Schematic representation of Indirect Coupling in $Gd_3(Co, Ni)$ on increasing Ni Content

RKKY theory caters for such contradictory behaviour as follows. Figure 7.14 represents schematically the conduction electron polarization P_{ij} as a function of distance x from the ion i to a nearby ion j , which is influenced by the polarization. The interaction between i and j is proportional to P_{ij} at j due to i . It is proposed that, in Gd_3Co the interaction between i and j_2 is strong and (fm) so that both belong to the same sublattice, and that j_1 is in the other sublattice, interacting weakly with i (and j_2).

Since the conduction electron concentration changes on going from Gd_3Co to Gd_3Ni the Fermi surface will change and thereby influence the indirect exchange interaction between any two ions. This involves a change in k_F the Fermi wave vector, which will directly influence the wavelength of the conduction electron polarization oscillations. Let the polarization be given by curve A for Gd_3Co and curve B for Gd_3Ni . It can be contrived, as shown in the figure, for the (fm) interaction between i and j_2 to decrease, while the (afm) interaction between i and j_1 increases. n' will therefore decrease while n increases.

It could perhaps be that the disappearance of antiferromagnetic behaviour for a composition near to $Gd_3Fe_{0.1}Co_{0.9}$ means that j_1 is near a node in the polarization oscillations for this composition. It must however be borne in mind that the real situation is far more complicated than this pictorial representation of the interaction because the Fermi surface is far from spherical, hence the value of k_F will depend on the direction of j_1 and j_2 with respect to i . Without detailed knowledge of the shape of the Fermi surface, such conjecture about the detailed nature of the exchange is hazardous.

Metamagnetic behaviour appears to exist in the Gd_xCo_{1-x} and Gd_xNi_{1-x} compounds only for the stoichiometries with a full 3d band. The RKKY type of interaction can account for the many varieties of complex spin structure in the rare earth metals. Many of these are antiferromagnetic with helical types of spin orientations through the lattice. There is no reason to expect the spin structure in Gd_3Ni to be any more simple, since we probably have an RKKY type of coupling here also. The existence of a

3d moment, however, in the compounds between rare earths and transition metals, destroys this complexity and introduces simple ferromagnetic coupling between the rare earth and 3d moments, for light RE's if $L > S$ and ferrimagnetic coupling for the heavy rare earths, both types of coupling being collinear. The reason for this is as follows. The 3d transition metal moments of Co and Ni have, for all compounds studied been found to couple ferromagnetically with each other. Such TM - TM coupling is strong as compared with the RE - RE coupling. This is deduced from the fact that, for any given stoichiometry the Curie temperature depends mainly upon the type of transition metal 3d element, and is relatively insensitive to the type of rare earth ion in the lattice, even for stoichiometries which are not particularly rich in transition metal. Since the 3d elements, Co and Ni are such strong ferromagnets, the TM - TM and TM-RE interaction will dwarf any RE - RE interaction. Since the TM moments align ferromagnetically with each other, and ferrimagnetically with the Gd moments, any tendency for a complex spin structure of Gd ions due to Gd-Gd RKKY exchange is too small to assert itself. It is suggested that, in going from Gd_3Ni to Gd_3Co , the conduction electrons are initially non-3d in character for Gd_3Ni , but gradually develop some 3d-character which tends to suppress the complex Gd_3Ni spin structure, and simplifies it into a two-sublattice collinear antiferromagnetism for the flip compounds. The next step in the simplification process is then to suppress even the two-sublattice antiferromagnetism when the top of the 3d band proper is encountered, at which point the structure becomes unstable.

7.11 Conclusion

The Néel theory was applied with reasonable success in accounting for the metamagnetism of the spin-flip Gd_3B compounds. The magnitude of the anisotropy was deduced assuming constant anisotropy energy across the series of compounds, and found to be of the same order of magnitude as that of pure gadolinium metal in the ferromagnetic state. The magnetic dipole interaction was found to be adequately large enough to account entirely for the anisotropy. Thus we did not have to resort to assuming an inter-

action of the Gd ion with the crystal field in accounting for the anisotropy. Such an interaction would probably not have remained constant across the series. However, for a given magnetic moment and for constant lattice parameters the magnetic dipole interaction cannot change across the series of compounds. Thus our initial assumption of constant anisotropy is confirmed, but its results, to be probably correct.

By considering the Gd_3B compounds in relation to the other rare earth rich stoichiometries, the empirical rule was deduced and justified, for deciding when a crystal structure is likely to become unstable. This stated that the crystal structure stability depended upon the Fermi level being either above or below the top of the 3d band. The antiferromagnetism between Gd ions depended upon the absence of 3d magnetic moments, because such moments induced a collinear simplification of the spin structure which could not cater for the Gd moments not being parallel to each other. Thus the correlation between the structural stability and magnetic behaviour was established. Such correlation was found experimentally to occur.

The time dependent behaviour of the compounds is an aspect which is as yet not understood. An understanding of this phenomenon could be arrived at by a research programme using static magnetization measurements, as well as pulsed field measurements in which the field oscillation frequency can be changed, so that a large range of rate-of-change-of-field can be investigated upon the same sample.

It would be interesting to investigate the pseudobinary systems $Gd_4(Co,Ni)_3$ and $Gd(Co,Ni)$ in order to investigate how the stability of the compounds depends upon the relative position of the Fermi level with respect to the top of the 3d band. This would provide further evidence of the applicability or otherwise of the structural stability rule mentioned above.

R E F E R E N C E S

- 1.1 van Diepen, A.M., Buschow, K.H.J., Wieringen, J.S.,
J. Appl. Phys. (Feb. 1972).
- 1.2 Vickery, R.C., Sexton, W.C., Novy, V., Kleber, E.V.,
J. Appl. Phys. 31, 366S, (1960).
- 1.3 Nesbitt, E.A., Wernick, J.H., Corenzwit, E.,
J. Appl. Phys., 30, 365, (1959).
- 1.4 Nesbitt, E.A., Williams, H.J., Wernick, J.H., Sherwood, R.C.,
J. Appl. Phys. 33, 1674, (1962).
- 1.5 Hubbard, W.M., Adams, E., Gilfrich, J.V.,
J. Appl. Phys., 31, 368S, (1960).
- 1.6 Lemaire, R., (a)
Cobalt 32, 132 (1966).
- 1.6 Lemaire, R., (b)
Cobalt 33, 201 (1966).
- 1.7 Laves, F., Witte, H.,
Metallwirtschaft, 15, 840, (1936) .
- 1.8 Lemaire, R., Paccard, D., Pauthenet, R., Schweizer, J.,
J. Appl. Phys., 39 No.2. 1092, (1968).
- 1.9 Wohlfarth, E.P.,
Phil. Mag., 40, 1095, (1949).
- 1.10 Elliott, R.P., Rostoker, W.,
Trans. A.S.M., 50, 617, (1958).
- 1.11 Lemaire, R., Berthet-Columinas C., Laforest, J., Pauthenet R., Schweizer, J.,
Cobalt, 39, 97 (1968).
- 1.12 Coles, B.R., Bitler, W.R.,
Phil. Mag., 1, 477, (1956).
- 1.13 Taylor, K.N.R.,
Phys. Letts., 29A, No.7, 372, (1969).
- 1.14 Piercy, A.R., Taylor, K.N.R.,
J. Phys. C1, 1112, (1968).
- 1.15 Piercy, A.R.,
Ph.D. Thesis, (1968).
- 1.16 Oesterreicher, H., Wallace, W.E.,
J. Less-Common Met., 13, 91, (1967).
- 1.17 Stoner, E.C.,
Repts, Progr. Phys. 11, 43, (1947).
- 1.18 Friedel, J.,
J. de Phys. et de Radium, 23, 501, (1962)

- 1.19 Cromer, D.T., Larson, A.C.,
Acta Cryst. 14, 1226 (1961)
- 1.20a Féron, J.L., Lemaire, R., Paccard, D., Pauthenet, R.,
Compt. Rend. 267B, 371, (1968).
- 1.20b Féron, J.L., Gignoux, D., Lemaire, R., Paccard, D.,
Les Elements des Terres Rares, Vol. II, CNRS, p 75 (1970).
- 1.21 Strydom, O.A., Alberts, L.,
J. Less Common Metl., 22, 503, (1970).
- 1.22 Gignoux, D., Lemaire, R.,
Sol. St. Comm. 8, 391, (1970).
- 2.1 Salmans, L.R., Strnat, K., Hoffer, G.I.,
Tech. Rep. AFML-TR-68-159 (1968).
- 3.1 Allain, Y., Varret, F., Miédan-Gros, A.,
Comptes Rendus. Acad. Sci. Paris, 260, 4677 (1965)
- 3.2 Weiss, P., Forrer, R.,
Ann. Phys. (Paris) 12, 297 (1929)
- 4.1 Gschneidner, K.A. Jr.,
Rare Earth Alloys, D. Van Nostrand, Co., Inc., Princeton, N.J., (1961)
- 5.1 Buschow, K.H.J., van der Goot, A.S.,
J. Less Common Met. 18, 309, (1969).
- 5.2 Lemaire, R., Paccard, D.,
Bull. Soc. Minéral. Cristallogr., XC, 311, (1967).
- 6.1 Buschow, K.H.J., Fast, J.F., van der Goot, A.S.,
Phys. Stat. Sol., 29, 719, (1968).
- 6.2 Kirchmayr, H.R.,
J. Appl. Phys. 39, 1088, (1968)
- 6.3 Kirchmayr, H.R., Steiner, W.,
J. de Phys. 32, C1-665, (1971)
- 6.4 Friedel, J.,
Supplemento del Nuovo Cimento, 7S, 287, (1958).
- 7.1 Néel L.,
Supplemento del Nuovo Cimento, 6S, 946 (1957)
- 7.2 Morrish, A.H.,
The Physical Principles of Magnetism, 453, (1965).
- 7.3 Féron, J.L., Gignoux, D., Lemaire, R., Paccard, D.,
Les Elements des Terres Rares, Vol. II, CNRS, p.75 (1970)
- 7.4 Sucksmith, W., Pierce, R.R.,
Proc. Roy. Soc. (London), 167A, 189, (1938).
- 7.5 Taylor, K.N.R.,
Phys. Letts. 35A, No. 3, 153 (1971)

- 7.6 Rudermann, M.A., Kittel, C.,
Phys. Rev., 96, 99, (1954)
- 7.7 Kasuya, T.,
Progr. Theor. Phys. 16, 45, 58, (1956).
- 7.8 Yosida, K.,
Phys. Rev., 106, 893, (1957).
- 7.9 Taylor, K.N.R.,
Contemp. Phys., 11 No. 5, 435, (1970).
- 7.10 (a) Dimmock, J.O., Freeman, A.J.
Phys. Rev. Letts., 13, 750, (1964).
- 7.10 (b) Watson, R.E., Freeman, A.J., Dimmock, J.P.,
Phys. Rev., 167, 497, (1968).

LIST OF FIGURESFigureCHAPTER ONE

- 1.1 The Existing Compounds in the Rare Earth-3d Metal system
- 1.2 Composition Triangles showing Existing Compounds (from literature) in Y-Fe-Co, Y-Co-Ni, Gd-Fe-Co, Gd-Co-Ni Systems
- 1.3 Saturation Moment vs x in $Gd_x B_{1-x}$
- 1.4 The AB_5 and related structures
- 1.5 Ordering Temperatures of $Y_x Ni_{1-x}$ and $Gd_x Ni_{1-x}$
- 1.6 Moments of $Y_x Ni_{1-x}$
- 1.7 Moments of $Y_x Co_{1-x}$
- 1.8 Ordering Temperatures of $Y_x Co_{1-x}$ and $Gd_x Co_{1-x}$
- 1.9 Iron Moments and Curie Temperatures in $Y_x Fe_{1-x}$ and $Gd_x Fe_{1-x}$ Compounds.
- 1.10 Transition Metal Moments in YB_2 and GdB_2
- 1.11 Curie Temperatures in YB_2 and GdB_2
- 1.12 Saturation Moments and Curie Temperatures of (Fe, Co) and (Co, Ni)
- 1.13 Magnetization vs Field Curves of A_3Co and A_3Ni Compounds
- 1.14 Moment Configuration in Er_3Ni

CHAPTER THREE

- 3.1 Photograph of Mounted Pulsed Magnet
- 3.2 Photograph of the Components of a Pulsed Magnet
- 3.3 Photograph of Pulsed Field Magnetometer
- 3.4 Circuit of Power Supply to Capacitor Bank
- 3.5 Oscillogram of H vs T
- 3.6 Schematic Cross-Section of Pulsed Magnet
- 3.7 The Integrating Circuit
- 3.8 Plot of Field along axis of Magnet
- 3.9 Lines of Induction of a Uniformly Magnetized Spherical Sample
- 3.10 Circuit of Magnetization and Field Detection System
- 3.11 The Pick-up Coil System

Figure

- 3.12 Oscillograms of Uncompensated Noise Signal
- 3.13 Oscillograms of Compensated Noise Signal
(a), (b): Without Sample; (c): With iron sample
- 3.14 Sequence of Oscillograms illustrating effect of Remanence
- 3.15 Magnetization Signal and Centering Coil output vs z
- 3.16 The Sample Holder
- 3.17 (a) Moment Calibration Graph
- 3.17 (b) M vs H Oscillograms for two bulk samples containing Iron
- 3.18 The Dewar System
- 3.19 Circuit of Constant Current Supply for Liquid Helium level Detector
- 3.20 Dewar Head and Height Adjuster
- 3.21 Vacuum System

CHAPTER FOUR

- 4.1 Lattice Parameters of Y_2B_{17}
- 4.2 M_s and T_c for Y_2B_{17}
- 4.3 Lattice Parameters of YB_5
- 4.4 M_s and T_c for YB_5
- 4.5 M vs H Curves of (a) YCo_2Ni_3 and (b) $Y_2(Co_{.4}Ni_{.6})_7$
- 4.6 Lattice Parameters of YB_3
- 4.7 M_s , M_{160} , T_c and H_c for YB_3
- 4.8 M_s , M_{160} , T_c and H_c for Y_2B_7

CHAPTER FIVE

- 5.1 Lattice Parameters of Gd_3B Compounds
- 5.2 Pulsed Field M vs H Curves of Gd_3B Compounds at 4.2K
- 5.3 Pulsed Field M vs H Curves of Ni-rich $Gd_3(Co,Ni)$ Compounds at 4.2K
- 5.4 H_c vs Composition at 4.2K
- 5.5 χ_i , H_s , H_c' , M_{160} at 4.2K
- 5.6 (a) M vs H for $Gd_3Co_{.9}Ni_{.1}$ at 4.2K
- 5.6 (b) H_c vs dH/dt at $H = H_c$, $T = 4.2K$, for $Gd_3Co_{.9}Ni_{.1}$
- 5.7 M vs H for Gd_3Co Powder at 4.2K
- 5.8 M vs H for Gd_3Ni Powder at 4.2K

Figure

- 5.9 A.C. Susceptibility Results for $Gd_3(Fe,Co)$ and $Gd_3(Co,Ni)$
- 5.10 T_N vs Composition from A.C. Susceptibility
- 5.11 χ_i, H_c, H_c' vs T for Gd_3Ni
- 5.12 χ_i, H_c vs T for $Gd_3Co_{.25}Ni_{.75}$
- 5.13 χ_i, H_c vs T for $Gd_3Co_{.5}Ni_{.5}$
- 5.14 χ_i, H_c vs T for $Gd_3Co_{.75}Ni_{.25}$
- 5.15 χ_i, H_c vs T for $Gd_3Co_{.9}Ni_{.1}$
- 5.16 χ_i, H_c vs T for Gd_3Co
- 5.17 χ_i, H_c vs T for $Gd_3Fe_{.05}Co_{.95}$
- 5.18 χ_i, H_c, M_{23} vs T for $Gd_3Fe_{.1}Co_{.9}$
- 5.19 T_N vs Composition for $Gd_3(Fe,Co)$ and $Gd_3(Co,Ni)$
- 5.20 $\chi_i, M_{160}, -M', M_s$ vs T for Gd_3Ni
- 5.21 Reciprocal Susceptibility at $T=T_N$ for Gd_3B Compounds
- 5.22 Pulsed Field M vs H Curves for $Gd_3(Fe,Ni)$ at 4.2K
- 5.23 M_{160}, M_K, χ_i vs Composition for $Gd_3(Fe, Ni)$ at 4.2K
- 5.24 H_c, H_c', H_s vs Composition for $Gd_3(Fe,Co,Ni)$ at 4.2K
- 5.25 Néel Temperature vs Composition for $Gd_3(Fe, Ni)$

CHAPTER SIX

- 6.1 Composition Triangles showing Range of Solid-Solubility of Stoichiometries in A-Fe-Co and A-Co-Ni Systems where A = Y and Gd
- 6.2 Summary Graph of Moments in Y-Fe-Co and Y-Co-Ni
- 6.3 Model to Account for Disappearance of Ordering in $Y(Co_{.2}Ni_{.8})_3$ and $Y_2(Co_{.2}Ni_{.8})_7$
- 6.4 Composition Triangles Y-Fe-Co and Y-Co-Ni showing Moment Contours
- 6.5 Curie Temperatures in Gd-Ni and Y-Ni Compounds
- 6.6 Non-Rare Earth Moment in Gd-Ni Compounds
- 6.7 Nickel Moment in Gd-Ni and Y-Ni Compounds
- 6.8 Curie Temperatures in Gd-Co and Y-Co Compounds
- 6.9 Non-Rare Earth Moment in Gd-Co Compounds
- 6.10 Cobalt Moment in Gd-Co and Y-Co Compounds
- 6.11 Iron Moments and Curie Temperatures in Gd-Fe and Y-Fe Compounds

FigureCHAPTER SEVEN

- 7.1 The Various Types of Field Induced Transitions
- 7.2 H_C vs $1/\chi_i$ for $Gd_3(Fe,Co)$ and $Gd_3(Co,Ni)$ at 4.2K
- 7.3 H_C^2 vs $1/\chi_i$ for $Gd_3(Fe,Co)$ and $Gd_3(Co,Ni)$ at 4.2K
- 7.4 The Exchange Coefficient n
- 7.5 H_S vs $1/\chi_i$ for Flip Compositions at 4.2K
- 7.6 The Exchange Coefficients n' and n
- 7.7 H_C vs $1/\chi_{TN}$ for $Gd_3(Fe,Co)$ and $Gd_3(Co,Ni)$
- 7.8 H_C vs $1/\chi_{TN}$ with Correction for Demagnetizing Field
- 7.9 H_S vs $1/\chi_{TN}$ with Correction for Demagnetizing Field
- 7.10 Crystal Structure of the A_3B Compounds
- 7.11 Saturation Moment in Gd-rich Co and Ni Compounds
- 7.12 θ_p and T_N vs de Gennes Function for A_3Co Compounds
- 7.13 θ_p and T_N vs de Gennes Function for A_3Ni Compounds
- 7.14 Schematic Representations of Polarization of Conduction Electrons about a Gd ion.

LIST OF TABLESTable

- 7.1 Expressions for Susceptibilities and Critical Fields
- 7.2 n values for (A_n) Spin Structure
- 7.3 Curie Constant, Néel Temperature, and n' values for $Gd_3 B$ Compounds.

